Innovative 3-D printed Ku- and Ka- band antenna solutions targeting cost effective satellite on the move and 5G phased arrays

Francesco Filice

To cite this version:

Francesco Filice. Innovative 3-D printed Ku- and Ka- band antenna solutions targeting cost effective satellite on the move and 5G phased arrays. Electronics. Université Côte d'Azur, 2020. English. NNT : 2020COAZ4023 . tel-03135252

HAL Id: tel-03135252
https://theses.hal.science/tel-03135252v1

Submitted on 8 Feb 2021

UNIVERSITÉ
CÔTE D'AZUR

ÉCOLE DOCTORALE
SCIENCES ET
TECHNOLOGIES DE
L'INFORMATION ET DE
LA COMMUNICATION

THÈSE DE DOCTORAT

Solutions innovantes d'antennes en bande Ku- et Ka- en technologie d'impression 3-D pour la réalisation des réseaux phasés visant des applications 5G et des communications mobiles par satellite.

Francesco FILICE

Laboratoire Polytech'lab

Présentée en vue de l'obtention
du grade de docteur en électronique
d'Université Côte d'Azur
Dirigée par : Cyril Luxey
Co-encadrée par : Frédéric Gianesello
Soutenance prévue le : 25 Mai 2020

Devant le jury, composé de :
Cedric Quendo, Professeur, UBO Brest, Président
Raphaël Gillard, Professeur, INSA Rennes, Rapporteur
Xavier Begaud, Professeur, Telecom Paris, Rapporteur
Jaime Laviada, Professeur, Universidad de Oviedo
Gilles Jacquemod, Professeur, Polytech'lab
Diane Titz, Professeur, Polytech'lab
Frédéric Gianesello, Docteur, STMicroeletronics
Cyril Luxey, Professeur, Polytech'lab

POLYTECH NICE-SOPHIA
POLYTECH'LAB

life.augmented

Solutions innovantes d'antennes en bande Ku- et Ka- en technologie d’impression 3-D pour la réalisation des réseaux phasés visant des applications 5G et des communications mobiles par satellite.

Résume : L'utilisation exponentielle d’applications mobiles entraîne une demande en constante croissance pour des débits de données de plus en plus élevés associées à des solutions de télécommunications mobiles à faible coût. Alors que les réseaux 5G en sont encore à leur début, les télécommunications mobiles par satellite (Sat-Com-On-The-Move) peuvent jouer un rôle central dans cette problématique. La bande passante disponible dans les bandes de fréquences Ku- (10,75-14,5 GHz) et Ka- (18-31 GHz) pour ces applications peut être exploitée afin de fournir une connexion internet globale à haut débit et faible coût. Des entreprises comme SpaceX déploient actuellement de grandes constellations de satellites positionnées sur des orbites terrestres basses et pouvant répondre à ces besoins. Néanmoins, le prix et le facteur de forme des terminaux utilisateurs à réflecteur motorisé existants restent les principaux goulots d'étranglement pour rendre ces technologies abordables à une grande partie de consommateurs. La bande passante opérationnelle atteignable par les éléments rayonnants intégrés à faible profil étant limité, la plupart des solutions existantes divisent la transmission (Tx) et la réception (Rx) dans deux panneaux rayonnants différents ce qui impose un coût relativement élevé pour les utilisateurs finaux. L'objectif de cette thèse consiste à développer des solutions d'antennes innovantes à faible coût et à large bande, notamment des antennes patch à couplage par fente et des antennes à guides d'ondes nervurés fabriqués avec des circuits imprimés standard (PCB) et par impression 3D en métal. Ces antennes sont censées couvrir la totalité de la bande Ku et Ka afin de permettre la création de terminaux utilisateur Sat-Com-On-The-Move à faible encombrement capables d'effectuer à la fois les fonctions Rx et Tx à l'aide d'un seul panneau antennaire.

Mots clés : Sat-Com-On-The-Move, 5G, impression 3-D, terminal utilisateur, antenne patch à couplage par fente, antennes à guides d'ondes nervurés.

Innovative 3-D printed Ku- and Ka- band antenna solutions targeting cost effective satellite on the move and 5G phased arrays.

Abstract: The increasing use of mobile applications leads to a growing demand for higher data-rates and low-cost mobile telecommunication solutions. While 5G networks are still at their early stages, a central role can be played by the mobile satellite telecommunications (Sat-Com-On-The-Move). The frequency bandwidth available at Ku- (10.75-14.5 GHz) and Ka- (18-31 GHz) bands for these applications can be leveraged in order to provide worldwide, high-speed and low-cost internet connections. Companies like SpaceX are actually deploying large satellite constellations required to work at Low Earth Orbits and offer such services. Nevertheless, the price and the form factor of the traditional motorized reflector-based user terminals remain the main bottlenecks in order to bring these technologies to the mass-market consumers. The limited operational bandwidth of the radiating elements integrated in their low-profile alternatives actually obliges to split transmission (Tx) and reception (Rx) in two different panels, keeping a relatively high cost for the end-users. The objective of this thesis is to develop innovative low-cost and wideband antenna solutions, notably microstrip aperture coupled patch and double ridged waveguide antennas, to be respectively realized by standard Printed Circuit Board (PCB) and metal 3-D printing. These antennas are meant to cover the whole Ku- and Ka-band in order to allow the creation low-profile Sat-Com-On-The-Move user terminals able to perform both Rx and Tx using a single antenna panel.

Keywords : Sat-Com-On-The-Move, 5G, 3-D printing, user terminal, aperture coupled patch antenna, double ridged waveguide antenna.

Acknowledgements

Firstly, I would like to sincerely thank my supervisors, Prof. Cyril Luxey and Dr. Frèdèric Gianesello, for their valuable guidance and support. Their engagement and help brought this work to a higher level. A special thanks goes to Dr. Nour Nachabe for her patience and advices in the first part of my experience. I also thank all the members of Polytech'lab for all their favors.

I would like to send my gratitude to the team members of the Signal Theory and Communications research group of the University of Oviedo, notably Prof. Fernando Las-Heras, Prof. Jaime Laviada Martinez and Guillermo Alvarez Narciandi, for their collaboration in order to perform the measurements of various prototypes fabricated during the thesis. A special thanks goes to the Ansys support group, notably Remy, David, Amazir and Domenico, for their technical support and their kindness.

I am very thankful to Prof. Raphaël Gillard and Prof. Xavier Begaud for having accepted to review my PhD manuscript and for their advices and corrections. My thanks go also to the other members of the evaluation committee: Prof. Cedric Quendo, Prof. Jaime Laviada, Prof. Gilles Jacquemod and Prof. Diane Titz, for their engagement.

I really appreciate the support and the friendship of all my labmates in Polytech'lab (Ana, Elsa, Zaophei) for sharing either difficult and motivating moments. Another special thought goes to all the colleagues from ST Microelectronics Crolles that contributed to make this 3-year experience invaluable: Vincent, Florence, Gerard, Romain, Cédric, Daniel, Michel, Victor, Joao, Francoise and all those I cannot cite right here. Thank you for your encouragement and your friendship.

I am grateful to all my family for the support and the encouragements in these years, and a special thought to my grandfather Silvio that would have been proud to see me achieving these results. Another special thanks goes to my extended family (Blend, Giulio M., Giulio T., Riccardo, Svetlana, Joana, Giuseppe, Francesco, Nunzio, Luca, Edoardo, Riccardo, Gabriele), to the N.K.K. association, to my schoolmates and to Fedro, for having been with me all these days. A grateful thought goes also to my teachers and friends of the Aikikai Jo-Do Grenoble, who taught me either martial arts and how to be more focused on my work.

Finally, thanks to my lifemate Mizar for being herself every day and making my life complete, nothing would have been the same without her.

Table of Contents

Table of Acronyms.

Acronym	Meaning
AUT	Antenna Under Test
ASIC	Application Specific Integrated Circuit
BW	Bandwidth
CTS	Continuously Transverse Slot
CPW	Coplanar Waveguide
CPE	Consumer Premise Equipment
DDM	Direct Digital Manufacturing
DMLS	Direct Metal Laser Sintering
DRWG	Double-Ridged Waveguide
EPFD	Equivalent Power Flux Density
EHF	Extremely High Frequency
FSS	Fixed Satellite Systems
FBW	Fractional Bandwidth
GEO	Geo Stationary Orbit
GCPW	Grounded Coplanar Waveguide
HTS	High Throughput Satellites
ITU	International Telecommunications Union
LEO	Low Earth Orbit
MEO	Medium-Earth-Orbit
ACP	Microstrip Aperture Coupled Patch
PPW	Parallel Plate Waveguide
PSTN	Public Switched Telephone Network
QRWG	Quadruple-Ridged Waveguide

Rx	Reception
Satcom	Mobile Satellite Telecommunication
Satcom-On-The-Move	Satellite Telecommunication
SLL	Side Lobe Level
SHF	Super High Frequency
SW	Surface Wave
Tx	Transmission
UHF	Ultra High Frequency
VICTS	Variable Inclination Continuously Transverse Stub
VoIP	Voice Over IP
WG	Waveguide

Introduction

Mobile communications have become highly pervasive in recent years, determining a continuous demand to increase the capacity of the actual telecommunication systems. The global amount of mobile data traffic is expected to move from the 19 exabytes per month in 2018 to a forecast of 77.5 exabytes per month by 2022 [1]. The large bandwidths available at millimeter wave frequencies for satellite communications, notably at Ku- (10.75 - 14.5 GHz) and Ka- (18 – 31 GHz) band, offer a viable solution to answer this demand. This pushes towards a paradigm shift in the field of the mobile satellite communications (Sat-Com-On-The-Move), being traditionally restrained to high-end users and applications due to the high costs related to the service subscriptions and to the user's equipment. The objective actually becomes to bring these technologies to the consumer mass-market and provide worldwide, low-cost and broadband internet connection via satellite. Moreover, the increasing demand for real-time applications requires to move from the traditional satellite constellations deployed at geo-stationary orbits to Low Earth Orbit constellations, capable to offer the level of signal latency required to guarantee a proper quality of service in this case. In this context, the use of innovative technologies such as reusable rockets, large scale 3-D printing and multi-beam satellite antennas paves the way for the creation and the deployment of large innovative high-throughput satellite constellations at reduced costs by actors like Telesat, SpaceX and Oneweb [2]. Nevertheless, the user's terminal remains a major bottleneck in order to come to the consumer mass-market: the development of innovative broadband antenna systems with wide-angle scanning capabilities and small form factors are required in order to propose low-profile and low-cost customer premises equipment (CPE) for the mass-market. Looking at the state-of-the-art of the commercial user's terminals for mobile satellite communications at Ku- and Ka- band, we can see that all the low-profile alternatives to the traditional cumbersome and expensive motorized reflector-based solutions are limited in terms of bandwidth. Hence, transmission and reception are usually split into two different antenna panels, having a direct impact over the cost and the form factor of the final products. The prime objective of this PhD work is to investigate the feasibility of low-profile and wideband antenna elements to be exploited for the realization of antenna panels for mobile satellite communication user's terminals working at Ku- and Ka- band. Proving the possibility to design such an antenna element leveraging either the standard PCB fabrication technology and a metal 3-D printing process would allow to overcome the previously mentioned limitation of the commercially available low-profile alternatives to the reflector-based user's terminals, representing a major step in order to bring the mobile satellite communications to the consumer mass-market. The envisaged antenna solution is the microstrip aperture coupled patch, to be realized in standard PCB technology and the metal double-ridged open-ended waveguide to be fabricated in 3-D printing by direct metal laser sintering. Further steps will be to propose small and medium antenna arrays integrating the designed radiating elements as unit cells to realize large antenna panels.

Chapter 1 introduces the context and the motivation of this PhD research work offering an overview of the satellite telecommunication business, from the allocated spectrum to the actually deployed systems. A particular emphasis is given to the presentation of the state-of-the-art of the commercially available user terminals for Sat-Com-On-The-Move at Ku- and Ka- band with the related antenna solutions. The challenges and the objectives of this work are detailed, underlining which characteristics are required for an effective antenna solution in order to be integrated in a compact low-cost user's terminal working with Low Earth Orbit satellite constellations.

Chapter 2 offers an overview of the planar antennas for satellite communications working at Ku- and Ka-band and introduces the working principle of the microstrip aperture coupled patch. The design of such an antenna operating at Ku-band with double linear polarization is detailed, rather than its fabrication and measurement. An analog approach is followed in order to show the design of a similar antenna working at Ka-band, a particular emphasis is given to the description of the surface wave phenomena arising at these frequencies and to the strategy to control and constructively exploit them by the use of a VIA cavity and of an additional resonating metal ring. Finally, the advantages and the drawbacks of the proposed antenna solutions are discussed and compared with the planar antennas reviewed at the beginning of the chapter.

In Chapter 3, we review state-of-the-art high-efficiency antenna arrays for mobile satellite communication at Ku- and Ka- band. The working principle of a double ridged waveguide (DRWG) antenna is discussed, rather than the design of such a radiating element able to cover the 30% of fractional bandwidth at Ku-band. The design of a 2x2 antenna array integrating the designed element with its waveguide-based feeding network is detailed, together with its fabrication from metal 3-D printing and the measurements of the prototypes. The design of a 4x4 antenna array leveraging the previous developments is also presented and the obtained results are benchmarked with state-of-the-art high-efficiency antenna arrays for Sat-Com-On-The-Move at Ku-band.

Chapter 4 proposes the development of 2x2 double ridged waveguide antenna array with its waveguide-based feeding network operating in Ka-band. A particular emphasis is given on the description of the challenges deriving from covering 50% of fractional bandwidth at these frequencies and from the will to realize a design compatible with the mechanical constraints of the direct metal laser sintering fabrication. The fabrication and the measurement of the prototypes is discussed and the possibility to integrate additional top metal patches within the structure is also investigated.

Chapter 5 concludes this work with conclusions and perspectives of this research work, notably providing an example of the simulation of a large 16x32 antenna array working at Ku-band and integrating the open-ended DRWG antenna developed in Chapter 3. Some of the main characteristics of such an antenna panel are compared with those of a commercial low-profile Sat-Com-On-The-Move user terminal working at the same frequencies.

I. LEO SATELLITE ON THE MOVE TELECOMMUNICATION TRENDS AND CHALLENGES

The continuous increase of the use of mobile applications is causing an explosion in the amount of data to be routed by mobile telecommunications networks. The global amount of mobile data traffic is expected to move from the 19 exabytes per month in 2018 to a forecast of 77.5 exabytes per month by 2022 [1]. Telecommunication industry looks at the mm-wave link in order to satisfy this demand. While the development of 5G network is still at his early stage, especially at those frequencies, mobile satellite telecommunications can play a central role providing worldwide broadband internet connection offering low-latency at an affordable price for mass-consumers. Actors like Telesat, SpaceX and OneWeb have recently gained a key position in this business, as they prompt a paradigm shift from the traditional fixed satellite systems (FSS) versus innovative high-throughput satellite systems at Low-Earth-Orbit (LEO), leveraging the bandwidth(BW) available at Ku- and Ka- bands [2]. While the fabrication and deployment costs of satellite networks have been strongly decreased, especially due to innovative technologies such as large-scale 3-D printing and reusable rockets for the injection in orbit, user's terminals still represent a bottleneck in order to reach the consumer mass-market. Being historically developed for high-end users, mobile satellite communications traditionally rely on reflector-based user's terminals solutions whose form factor and cost are not in line with the requirements of the consumer mass-market [3]. The need for a low-profile and low-cost antenna solution for these applications is therefore mandatory, in order to allow the design of an innovative user's terminal able to guarantee performance comparable with those of traditional solutions and offering an acceptable cost for the targeted end-users.

In this chapter, we briefly describe an overview of the satellite telecommunication business, from the allocated spectrum to the actually deployed systems. In this context, a particular emphasis is given to the presentation of state-of-the-art commercially available Sat-Com-On-The-Move user's terminals with related antenna solutions. Hence, we introduce the actual innovative trends in the satellite telecommunication business related to on-going deployments of High Throughput Satellites (HTS) at geo-stationary (GEO) orbit and Low-Earth-Orbit (LEO). We end this chapter with a discussion about the challenges targeted by this PhD project, related to the development of a compact low-cost antenna solution to be integrated in an innovative user terminal for LEO Sat-Com-On-The-Move communications addressing the consumer mass-market.

I.1 Satellite telecommunication business overview

I.1.1 Spectrum

There exist various standard nomenclatures defining the operating frequencies for satellite telecommunication (Satcom). The International Telecommunications Union (ITU) classifies them as UHF, SHF and EHF: [4]

- Ultra High Frequency (UHF): 300 MHz - 3 GHz
- Super High Frequency (SHF): 3 GHz – 30 GHz
- Extremely High Frequency (EHF): 30 GHz – 300 GHz

Nevertheless, it is definitely more practical to refer to the IEEE nomenclature, as shown in Table 1. The Satcom bands are given in terms of downlink (satellite-to-ground communication) and uplink (ground-to-satellite communication) frequency ranges. A wider BW is generally available at highest frequencies [5].

Band Name	Downlink	Uplink
C - Band	3.4 – 4.2 GHz	5.8 – 6.7 GHz
X - Band	7.25 – 7.75 GHz	7.9 – 8.4 GHz
Ku - Band	10.7 – 12.5 GHz	14 – 14.5 GHz
Ka - Band	18.3 – 18.8 GHz or 19.7 – 20.2 GHz	27.5 – 31 GHz
Q/V – Band *	37.5 - 43.5 GHz	47.2 - 50.2 GHz

Table 1 Main satellite telecommunication frequency bands for downlink and uplink with IEEE nomenclature, from [4] and [5]. * Frequencies are given for the experimental Q/V band satellite network based on the Alphasat TDP#5 payload, project from European and Italian Space Agencies. [6]

I.1.1.a C-Band

C-band covers a spectrum going from 3.4 GHz to around 6.7 GHz, with slight differences due to regional licensing. It has been the first one being exploited to provide satellite telecommunication services. It is particularly suitable for critical and emergency services leveraging some of the lowest frequencies designed for Satcom applications. The wide area that can be covered on the ground by a single satellite beam from a GEO satellite and a consistent robustness to harsh weather conditions in terms of radio propagation are between the benefits of working at these frequencies. C-band Satcom solutions provide mobile services for business users and industry such as mobile communications for commercial maritime, connection for ATM networks and backhaul in remote territories unserved by terrestrial networks, as required by the oil and gas sectors. These frequencies are widely exploited to deliver TV broadcasting and share critical meteorological data between governments [7]. Focusing on mobile telecommunications, it is interesting to underline that a drawback of the C-band is the size of the antennas required for the user terminals such as they cannot be mounted on very small boats or vehicles [8].

I.1.1.b X-Band

X-band frequencies are allocated between 7.25 and 8.4 GHz with slight differences due to regional licensing. They are mainly used for radar applications in terms of weather monitoring, air traffic control, maritime vessel traffic control, defense tracking and vehicle speed detection for law enforcement. These frequencies are being mostly leveraged for military applications [5].

I.1.1.c Ku-, Ka- Bands

Ku-band frequencies ranges from 10.7 to 14.5 GHz, while Ka- ones are comprised between 18.3 and 31 GHz. A larger BW is available at these frequencies if compared to C- and X- cases which are being allocated for both fixed and mobile satellite services. The aforementioned features make these bands suitable candidates to be exploited in order to deliver broadband connectivity to zones that are unserved by terrestrial infrastructures and provide mobile backhaul for maritime and aeronautical services. These bands are widely used for video distribution, live broadcasting and IP trunking applications for business and corporates. Ku-band currently dominates the market of the broadband systems for the aeronautical mobile satellite services [9]. Recent years have been characterized by the development of High-Throughput Satellite systems to work at these bands, as we will furtherly detail in this chapter. An intense debate is actually active within the community about the benefits and the drawback of leveraging either Ku- or the Ka- band for this purpose. It is interesting to underline that the propagation losses can become so consistent at high frequencies to counterbalance the benefits of having a larger BW and the opportunity to leverage a certain band must be evaluated case by case in terms of the specific user's requirements [10].

I.1.1.d Q/V- Bands

The Q/V-bands lie between 33-75 GHz, being used mainly for remote sensing, radio astronomy studies and inter-satellite links. These bands are actually being considered as the next frontier in terms of Satcom frequency bands. The objective is to allow the full exploitation of Ku- and Ka- BWs for the user link and rely on Q/V-bands for the link with the gateways. This would lead to an increased user capacity and to decrease the cost-per-bit of the service up to the forecasts of providers like Intelsat. Nevertheless, the atmospheric and rain absorption at these frequencies are such as, building a solid back-up network of terrestrial gateways is a mandatory condition in order to overcome these Q- and V-band sensitivities to weather conditions [11]. Experiments are on-going in order to test the effectiveness of a system working at these frequencies by using different coding and modulation approaches in order to help to overcome the signal propagation issues, more information can be found in [6] and [12].

I.1.2 Orbits

A satellite orbit is mainly defined by three parameters: height, representing the satellite distance from the Earth' surface; eccentricity, which refers to the different possible shapes of an orbit and particularly to its deviation from a perfect circular trajectory; and inclination, which refers to the angle of the orbit in relation to Earth's equator. Accordingly, we can identify three main classes: Geo-Stationary-Orbit (GEO), Medium-Earth-Orbit (MEO) and Low-Earth-Orbit (LEO), as shown in Figure 1. The properties of each orbit determine the satellite-to-ground signal latency, the architecture of the related telecommunication system and part of the features required for a user's terminal.

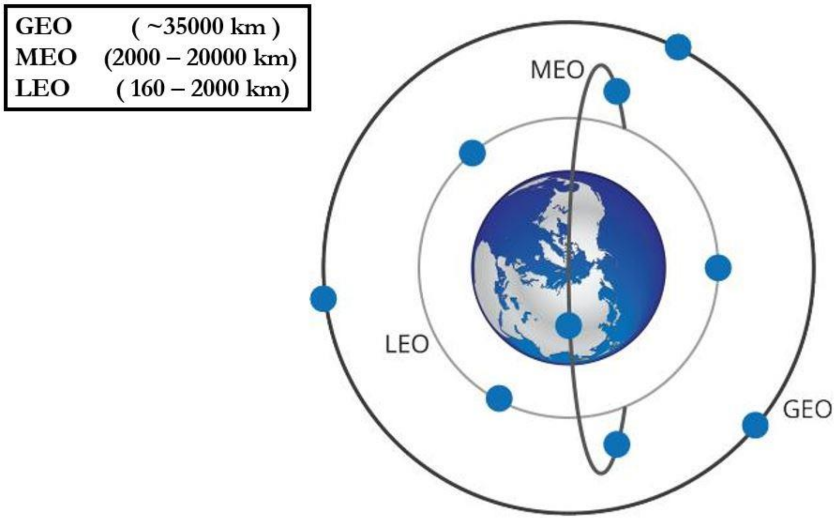

Figure 1 Drawing of the Earth with the main orbit classes, classified in terms of altitude, from [8].

I.1.2.a GEO

A geostationary orbit is a circular orbit located directly above the earth's equator. Referring to the previously introduced orbital characteristics, we can say that an ideal GEO orbit has zero eccentricity (perfectly circular) and zero inclination (perfectly parallel to equatorial belt), with an altitude of ~35000 kilometers. Nevertheless, GEO satellites withstands drifting phenomena that finally make their orbits elliptical ones. The peculiarity of this orbit is that the satellite moves in the direction of Earth's rotation with the same speed as the rotation of the Earth, resulting stationary if observed from ground perspective. This characteristic makes the GEO orbit particularly suitable for applications like the TV broadcasting, as it allows the users from a certain geographical area to continuously receive the signal without the need to reposition or re-orient its antenna. Another interesting feature is that a complete coverage of the most populated regions of the Earth can be achieved by a constellation made by just 3 satellites. The single beam produced by an opportunely shaped reflector antenna placed over a GEO satellite can cover a very wide and defined area on the ground. The drawback of working at these orbits is related to the satellite-to-ground latency of the signal, typically between 250 and 280 milliseconds [13]. These values are not compatible with most of the real-time applications such as VoIP and Skype. To give an example: ITU-T G.114 recommends a maximum of 150 milliseconds one-way latency for Voice over IP (VOIP), being equal to three fifths of the best latency we can achieve through a GEO Satcom system.

I.1.2.b MEO

The Medium Earth Orbits are characterized by a distance from the Earth' surface comprised between 2000 and 20000 kilometers. MEO orbits are almost circular with a small eccentricity and variable inclinations. A satellite flying at these altitudes moves in the direction of Earth's rotation with a higher speed that is higher than Earth's one, resulting in being not stationary if observed from ground's perspective. Hence, such a system requires user's terminals with steerable antenna solutions capable to point the satellites across the sky and hand-over from one to another. This characteristic has a direct impact over the associated infrastructure on the ground which is required to be more complex than the GEO case. The satellite-to-ground latency of the signal stays between 110 and 130 milliseconds, being almost the half if compared to GEO one. MEO systems have been traditionally developed for navigation and positioning. Current applications include delivering 4G LTE and broadband connectivity to rural and underdeveloped areas where laying fiber is either impossible or not cost effective.

I.1.2.c LEO

The Low Earth Orbits are characterized by distances from the Earth's surface comprised between 160 and 2000 kilometers. This orbital regime is a non-geostationary one, like MEO, but characterized by a higher rotational speed. Being closer to Earth a very low satellite-to-ground latency of the signal is achieved ranging from 20 to 25 milliseconds, in line with the requirements of real-time applications. If we consider the VoIP application, as did for GEO case, the one-way latency is more than six times smaller than the threshold of 150 milliseconds as recommended by ITU-T G.114 in order to achieve a satisfying quality of service [14]. Many traditional satellite providers, like Telesat, and new players, like SpaceX and Oneweb, aim at exploiting the LEO low-latency together with the large BWs available at Ku- and Ka-bands in order to maximize the achievable throughput of their satellite telecommunication systems. One of the main drawbacks deriving from the choice of such an orbital regime is that very wide constellations are required in order to guarantee a complete Earth's coverage. Being more specific: a minimum constellation of 3 GEO satellites is sufficient to guarantee Earth's coverage, excluding the polar regions, while the LEO satellite constellations under development actually count on more than 100 satellites to guarantee complete Earth coverage [15].

I.1.3 Existing systems

I.1.3.a Architecture of satellite telecommunication systems

The architecture of a satellite telecommunication system is fundamentally composed by 3 segments: space, ground and user's one. The space segment is composed by the satellites, that can be deployed at different orbit and with different payloads (i.e. on-board equipment of antennas and electronics). We can consider the space segment as the most important one as it determines the characteristics of all the other components of the system. If we look at the role of the satellite in the traditional GEO systems, they were generally not equipped with on-board processing units and they could only act as repeaters between two communication points on the ground [16]. The ground segment is fundamentally composed by gateways, remote terminals and data centers, placed in strategic geographical positions. It has functions like managing the data traffic, as every traditional satellite network needs at least one central point of management, and directing the satellite signal to terrestrial networks such as the terrestrial internet or telephone network (PSTN). The user's segment is usually defined as a set of equipment and applications associated with the exploitation of the satellite's services (i.e. TV broadcasting, mobile connectivity, Earth observation etc.) by the end-users [4]. Figure 2 shows the example of the architecture of a non-geostationary satellite telecommunication system connected to the terrestrial network by mean of gateways: the user's terminals are based on motorized-reflector antenna solutions. The various components of this basic configuration can be modified and specialized to satisfy the requirements of different applications. If the satellites are equipped with on-board processing units able to perform operations such as remodulation/demodulation, recoding/decoding and transponder/beam switching, a high-efficiency inter-satellite link can be eventually created allowing the connectivity in space without any terrestrial resource [16].

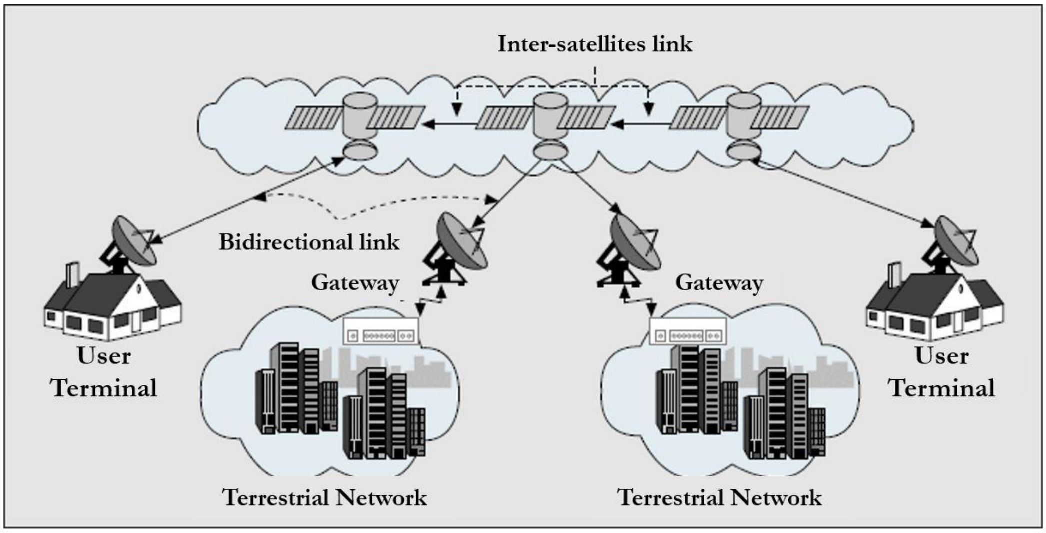

Figure 2 Architecture of a non-geostationary satellite system, from [17].

I.1.3.b Major existing systems

The author aims at providing an overview of some of the major satellite networks systems, notably belonging to operators like Eutelsat, Intelsat and Telesat. The Eutelsat system can actually count on a flying fleet of 34 GEO satellites with an almost complete coverage of the planet, as we can appreciate in Figure 3 [18].

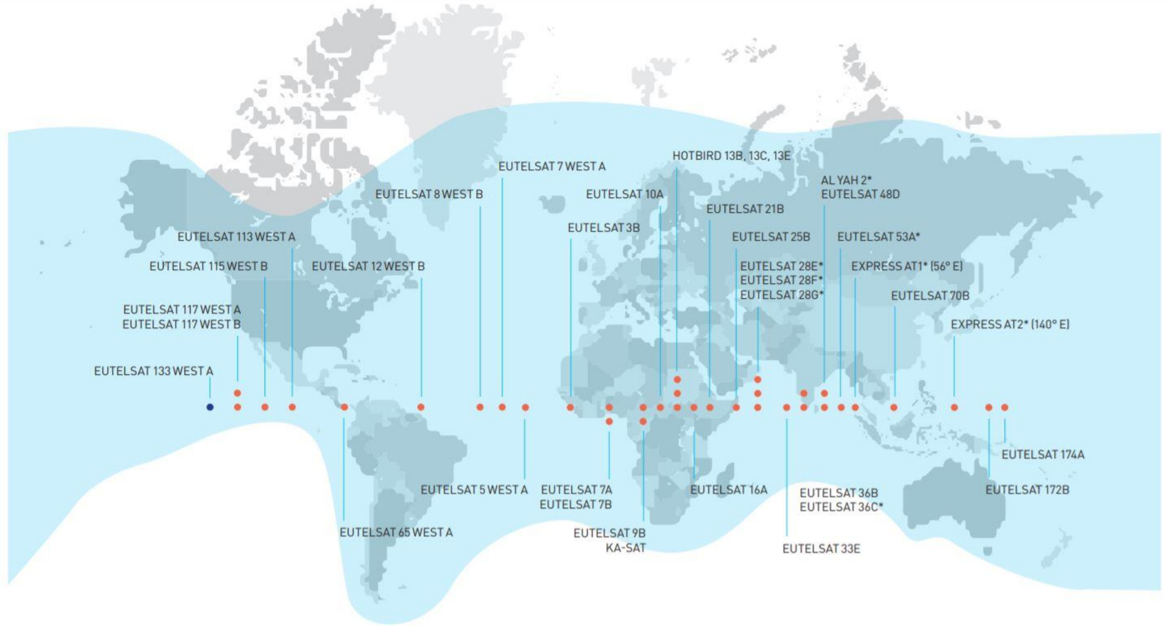

Figure 3 Eutelsat Earth’s coverage with indication of the satellites position over the Equator from [19].

The Eutelsat network is actually exploited to offer services that include TV and radio broadcasting and to provide internet connectivity to zones unserved by terrestrial networks, rather than offering aeronautical and maritime connectivity for both civil and military applications.

Intelsat can actually count on a fleet of 49 GEO satellites working at C-, Ku- and Ka- band, as shown in the map in Figure 4 [20]. This fleet is actually being reinforced by three high-throughput GEO satellites meant to be retro-compatible with the traditional systems. Their throughput is maximized by the use of technologies like frequency reuse and satellite antennas enabling the creation of multiple spot beams on the ground. The Intelsat network is actually used for media broadcasting, government and military communications, aeronautical and maritime connectivity, oil and gas industry telecommunications, rather than integrating the classical fixed and wireless operators in rural and unserved areas [21].

Accessed 29 November 2019, <http://www.intelsat.com/fleetmaps/>.

Figure 4 Map of the Intelsat GEO satellite system.

It is interesting to finally introduce the case of Telesat. This traditional satellite operator can actually count on a fleet composed by 16 GEO satellites, including 2 innovative high-throughput ones, that are exploited to provide the same services mentioned in the previous network examples at C-, Ku- and Ka-band. Moreover, Telesat is actually creating its innovative own fleet of satellites aiming at exploiting both the characteristics of the LEO orbital regime and the available BWs at Ku- and Ka-band. The objectives are to increase the number of users they can serve, the quality of service they can deliver and to be able to support real-time applications [14]. The details of the Telesat LEO project will be furtherly discussed in this chapter.

I.1.3.c Applications and market size

The revenues of the global satellite industry have been continuously increasing from 246 billions of dollars in 2014 to 277 billion in 2018, as we can see in Figure 5 a). Figure 5 b) illustrates how this industry represents the major part of the global space economy, that has reached 360 billions of dollars of revenues in 2018. The market of the satellite services reaches 126.5 billions of dollars in the same year. The most important satellite services include media broadcasting; aviation and maritime connectivity; remote sensing such as Earth science and meteorology; space science and national security. The antenna solutions that will be developed in this project are in the scope of the ground equipment market. It is worth to underline that the revenues related to this last amounted to 125.2 billions of dollars in 2018, representing ~45% of the global space economy of the same year. This category includes consumer equipment, such as TV, radio and broadcast ones with the related chipsets; and network equipment, such as gateways and network operation centers.

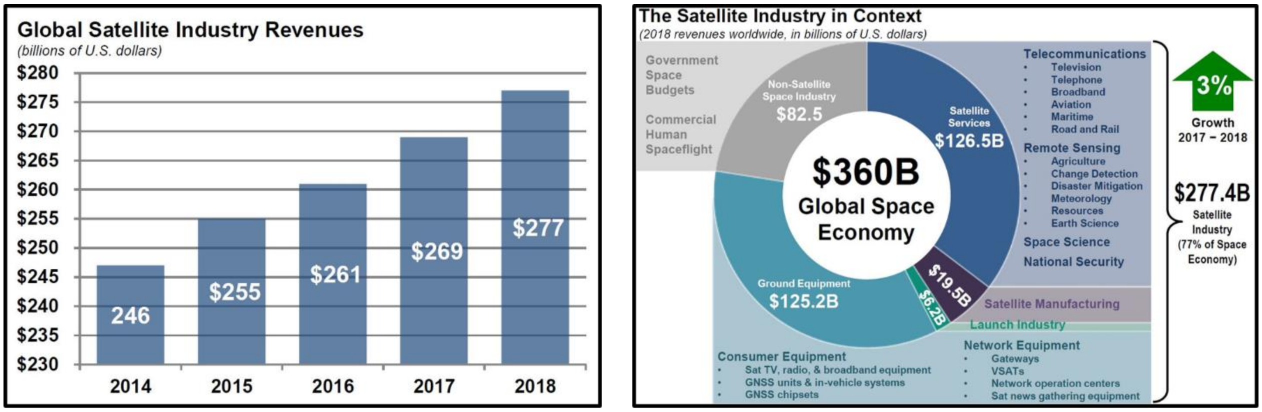

a) b)

Figure 5 a) Global satellite industry revenues from 2014 to 2018, b) Revenues of the global space economy in 2018, divided into the different categories. Both graphs are from [22].

I.2 State of the art of Sat-Com-On-The-Move antenna solutions for the user's terminals

The figures of the satellite industry market in 2018 shown in the previous paragraph prove the centrality of the ground equipment market (with the related antenna technologies) in this context. According to the scope of this work, this paragraph will be dedicated to the review of the principal antenna solutions for the commercially available Sat-Com-On-The-Move user's terminals and some of the innovative ones that are actually being developed. Our overview will start with the traditional reflector-based antenna solutions to move to the slotted waveguide antenna array-based ones and to the continuously transverse stub antenna array-based user's terminals for aeronautical applications. Finally, we will introduce some examples of innovative arrays with electronic beam forming and a benchmark of the various reviewed solutions.

I.2.1 Reflector-based antenna solutions

The reflector-based SOTM user's terminal are the traditional ones, relying on a reflector or a gimbal antenna that is usually motorized. These antennas are capable to guarantee the best performance in the market in terms of achievable BW and gain using the same aperture in order to perform both transmission (Tx) and reception (Rx). A complete scanning range in azimuth and elevation is mechanically achieved by mean of a 3- or 4- axis rotation of the antenna. One of the most important limitations of these solutions is related to their form factor: Figure 6 a) illustrates the Leonardo DRS X-38V LP designed to work at Ku-band and being one of most compact user's terminals of this class that we can find on the market. As we can see, the height of the motorized antenna solution is equal to 60 cm with a diagonal of the dish that is equal to 46 cm and a weight of 34 kg for the entire system. Moreover, these systems need to be protected with a radome, especially in the case of aeronautical and maritime connectivity applications. This is the case of the Intellian VN85-X shown in Figure 6 b) which has been designed to work either at Ku- or Ka-band. Rather than leading to issues in terms of aerodynamic drag, especially in the case of aeronautical applications, the radome has an impact on the overall form factor of the user's terminal. This last can be as high as 1.2 m with a radius of 1.1 mm and have a weight of up to 100 kg, as shown in the example in Figure 6 b). The power consumption is another important concern: if we consider the electronic system associated to the solution shown in Figure 6 a), the peak power consumption of the power amplifiers can reach 500 W [23]. The described characteristics of the motorized reflector-based user terminals makes them the proper choice for users that need to get the best and most reliable performance and being disposal to pay off in terms of form factor, power consumption and price.

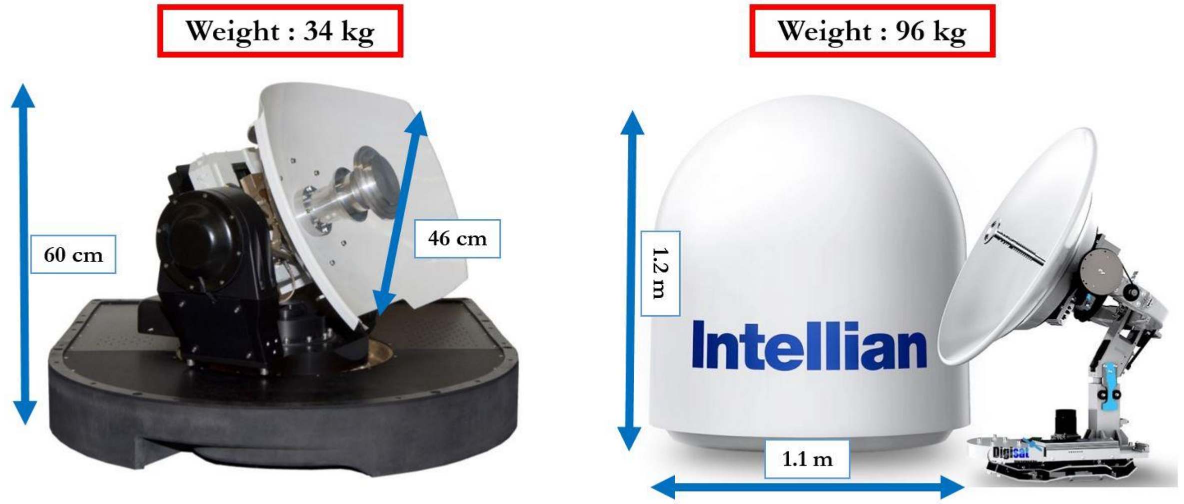

a) b)

Figure 6 Examples of commercial motorized reflectors: a) X-38V LP COTM fabricated by Leonardo DRS from [23], b) VN85-X fabricated by Intellian from [24].

I.2.2 Slotted waveguide array-based antenna solutions

The Sat-Com-On-The-Move user's terminals integrating the slotted waveguide antenna arrays have been primarily developed as an alternative to the traditional motorized reflector-based ones for all those applications that require reliable performance with a reduced form factor. This requirement becomes particularly critical for applications such as aeronautical connectivity and the mobile communications for the warfare. Considering the first case, a traditional reflector-based solution with its radome introduces a consistent impact in terms of aerodynamic drag, while it consistently increases the radar cross-section in the second one (i.e. warfare vehicle with roof-mounted user terminal). The use of the slotted waveguide antenna arrays allows to obtain solutions with a reduced height and weight, if compared to traditional motorized reflector-based solutions working at the same frequencies. One of the main limitations deriving from the use of slotted waveguide antennas is represented by the achievable operational BW of the radiators. This last is intrinsically narrower than the reflector one, obliging to split the Tx and Rx functions in two different arrays, as we can appreciate in the example of the Sanetel T65 user's terminal for Ku-band given in Figure 7 a). Focusing on this example, Figure 7 b) shows the form factor of the related antenna solution with its radome, that achieves a diameter of 1.3 m, height of 0.3 m and weight of 54 kg [25]. These values can be easily compared with those of the equivalent reflector-based solution previously shown in Figure 6 b) that was achieving a diameter of 1.1 m, a height of 1.2 m and a weight of 96 kg. It is interesting to notice that the reduced weight in the slotted waveguide array case leads to a reduced peak of the power consumption. In fact, we move from 500 W of peak power consumption in the reflector-based case to 200W for the analyzed Sanetel T65, based on slotted waveguide array antennas [25]. A complete scanning range in azimuth and elevation is mechanically achieved by a 2-axis rotation of the antenna panel.

Figure 7 Sanetel T65 SOTM user's terminal integrating slotted waveguide array antennas working at Ku-band: a) picture of the terminal from [25], b) schematic of the T65 antenna solution with radome from [25].

I.2.3 Continuously transverse stub array–based antenna solution

A special class of user's terminals has been developed for aeronautical applications in order to have the smallest achievable height for a mechanically-scanned array. The objective was to minimize the aerodynamic drag effect deriving from the mounting of the user's terminal on a fuselage, while preserving its scanning range as far as possible. Gogoair is actually dominating the market of the in-flight connectivity with its Gogo2Ku user terminal whose main innovation is a continuously transverse stub array antenna solution with a patented mechanic scanning mechanism that leverages rotating metal plates instead of the classic rotary joints. The details of the radiating elements and of the associated scanning mechanism will be given in Chapter 3. It is interesting to underline in this context that such a system achieves a profile height of 17 cm representing the smallest one between the commercially available mechanically scanned user 's terminal. It can be considered as an effectively low-profile solution for the targeted applications. The radiating elements suffer BW limitations in terms of matching and gain, leading to the necessity to split the Tx and the Rx functions in two different antenna panels as shown in Figure 8. The surface occupation of the terminal is ~ 1.6 m^2. The weight of the antenna solution is 70 kg but its impact is evaluated in terms of a specific figure of merit for aeronautical applications defined as the ratio of the weight over the aerodynamic drag, resulting better than the conventional airborne antennas [26]. The cost structure of these terminals is such as they only target high-end users.

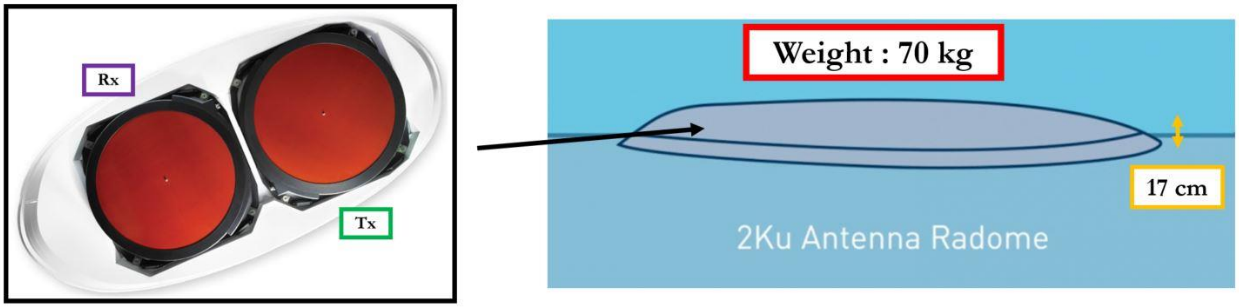

Figure 8 Picture of the Gogo2ku antenna panels and their integration scheme within the radome over the fuselage of an airplane, from [26].

I.2.4 Innovative antenna array with beamforming

The actual trend in the satellite telecommunication business is to try to bring the mobile satellite communication technology to the consumer-mass market. The on-going deployments of LEO satellite constellations that will be furtherly detailed in this chapter, aims at providing worldwide broadband internet connectivity both at Ku- and Ka-bands, keeping a price affordable by the mass-consumers. This imposes different requirements for the design of the user's terminal being cheap and low-profile becoming a primary need.

I.2.4.a Electronically-scanned phased arrays

An electronically-scanned phased array integrating a microstrip patch antenna array on PCB and the relative control electronics can guarantee a very compact form factor and the possibility to leverage a standard low-cost fabrication process. While these features are very appealing from the perspective of the industrialization for the consumer mass-market, these advantages are counterbalanced by various factors. The high losses associated to a microstrip feeding network at SOTM frequencies; the wide BW to be covered that requires patch antennas with complex stack-up and the necessity to over-size the array or use a conformal configuration in order to achieve a satisfying gain and scanning range represent some of the main drawbacks. If we look at the landscape of the commercial solutions, excluding the military ones, the most interesting electronically scanned phased array development is represented by the Phasor project. The Phasor solution guarantees a full electronic scanning over a 70° cone with no mechanical moving parts. The large BW to be covered obliges to use different modules with different patch antenna designs for Rx and Tx, respectively. An application specific integrated circuit (ASIC) is provided on the back of each patch antenna [27]. Each panel requires two PCB boards: one for the antennas and another one for the electronics. Various panels can be mounted then to form a bigger user's terminals and improve the achievable gain and the scanning range for the overall system. These characteristics rise the price of the final cost of the user's terminals for the end-users, keeping this solution far from the requirements of the consumer mass-market. Figure 9 shows the example of a conformal Phasor panel for aeronautical application integrating 6 antenna modules. We can underline that the weight of 12 kg, the surface occupation of (54 x 72) cm^2 and the panel thickness of 1.8 cm (effective thickness is higher in case of conformal panel to be mounted on fuselages) are the smallest between the reviewed examples of antenna modules for SOTM user's terminals. On the other side, the manufacturer attests a peak power consumption of 500 W that is in line with the previously reviewed traditional motorized reflector-based solutions.

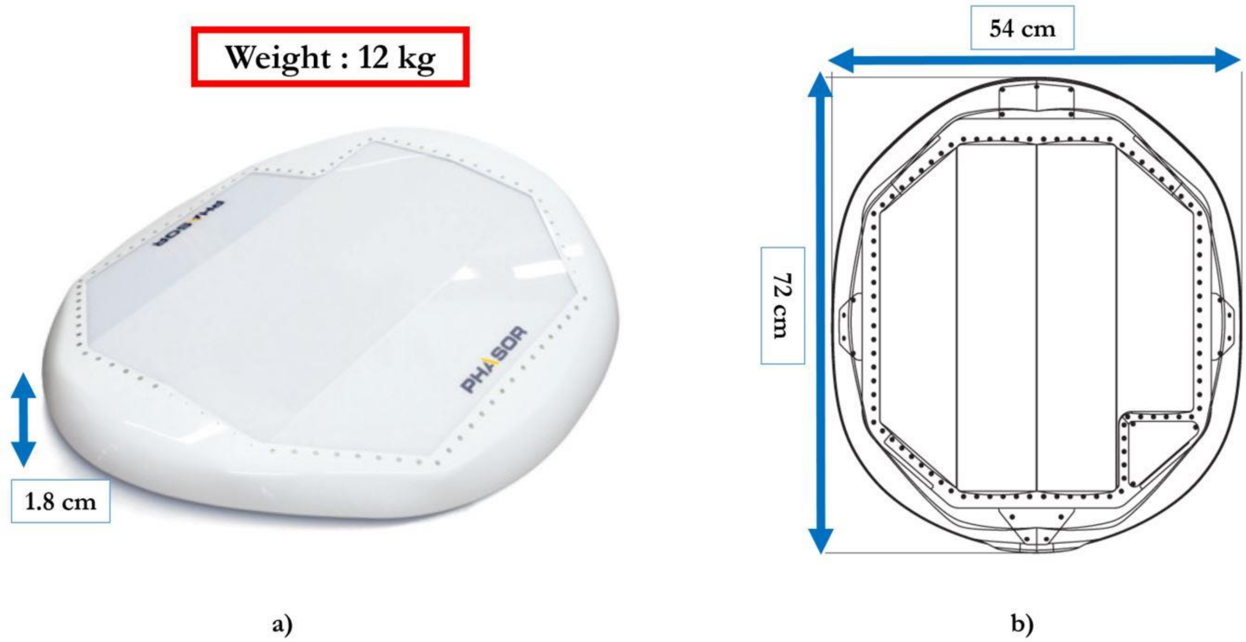

Figure 9 Example of a conformal Phasor antenna panel for aeronautical applications integrating 6 antenna modules: a) picture from [27] , b) transparent top-view of the design from [27].

I.2.4.b Metamaterials-based solutions

Another interesting line of research concerns the application of metamaterial-based antennas to realize innovative flat electronically scanned arrays, the project from Kymeta represents the most interesting example in this context. Its key features are represented by the realization of an antenna panels that has a thickness lower than 10 cm and by an innovative low-power beam scanning mechanism that relies on the properties of the metamaterials used to realize the radiating elements [28]. The weight of the panel is 9 kg with a modular approach that allows to create a system integrating various of them in order to satisfy specific demands in terms of achievable performance. The Kymeta solution guarantees a full electronic scanning over a 75° cone with no mechanical moving parts being in line with the previously reviewed Phasor. The intrinsic BW limitations of this technology oblige to split the Tx and Rx functions into different radiating elements within the antenna panel as we have already seen in the Phasor solution. The Kymeta project represents the most mature one in the landscape of the innovative flat arrays, being actually used to connect buses, trains, ships and airplanes. The major drawback is related to the price of a complete user's terminals, including the modem and all the related electronics that can reach 100 k$. This factor represents a main limitation in order to eventually address to the consumer mass-market [29].

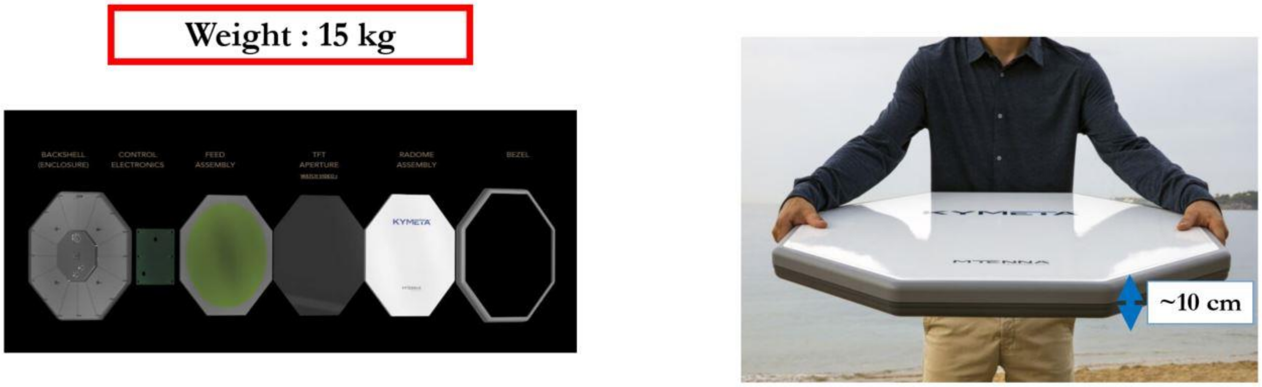

a) b)

Figure 10 a) Exploded stack-up of the Kymeta antenna panel from [30], b) picture of a Kymeta panel from [29].

I.2.5 Benchmark of state-of-the-art solutions

Table 2 synthetizes the characteristics of the reviewed commercial user's terminals for civil SOTM applications with their related antenna solutions.

User's terminal	Antenna solution	Surface (including Radome) [m^2]	Profile Height [m]	Scanning Range [Mechanic/ Electronic]	Weight [kg]	Radiating Elements Bandwidth
Intellian X-38V	Reflector	1	1.2	El: 0 - 90° M Az: 0- 360° M	96	Wide (Rx/Tx from same aperture)
Sanetel T65	Slotted Waveguide Array	1.3	0.3	El: 0 - 90° M Az: 0- 360° M	54	Limited (different designs for Rx and Tx)
Gogoair Gogo2Ku	Continuosly Transverse Stub Array	1.6	0.17	Not Available	70	Limited (different designs for Rx and Tx)
Phasor (6-modules panel)	Electronically Scanned Patch Array	0.4	0.02	El: 0 - 70° E Az: 0 - 70° E	12	Limited (different designs for Rx and Tx)
Kymeta mTenna	Electronically Scanned Metamaterials – based Array	0.64	0.07	El: 0 - 75° E Az: 0 - 75° E	15	Limited (different designs for Rx and Tx)

Table 2 Resume of some of the features of the reviewed commercial user's terminals for civil SOTM applications with their related antenna solutions, from [23], [25], [26],[27] and [28].

The weight and the form factor of the innovative user's terminals integrating electronically-scanned phased array antennas are consistently lower than those of the traditional reflector-based solutions. Nevertheless, the most compact solutions pay in terms of reduced scanning range, BW and gain (not mentioned in the table). Moreover,they have to rely on modular approaches that can provide the integration of various modules within the same antenna panels or configurations with various antenna panels. This may counter-balance the improvements achieved in terms of surface occupation and weight with the respect to the traditional reflector and slotted waveguide array-based solutions. Moreover, it is meaningful to underline that neither of the reviewed solution addresses the mass-consumers and their utilization remains constrained to high-end users.

I.3 Evolution towards higher throughput satellite systems

The traditional satellite systems rely on satellites orbiting at GEO orbit as already introduced in the previous section. These can integrate various types of antennas capable to produce a shaped beam in order to cover and provide service to a particular geographic region. This characteristic allows to have space antennas without steering mechanisms which is a remarkable benefit from the point of view of the system deployment and maintenance. Such benefits are counterbalanced by an average satellite-to-ground latency of the signal equal 265 milliseconds (that avoids to address delay critical applications), the orbit injection cost and the actual GEO orbit saturation. It is in this context that the increasing demands for system capacity, the race to provide low-cost worldwide satellite-based internet based internet connectivity and the opportunity to support real-time applications led to the design and the deployment of innovative satellite systems, such as the GEO and LEO HTS constellations.

I.3.1 HTS GEO system overview

The HTS GEO systems can be actually seen as an evolution and a partial replacement of the traditional GEO ones. These new systems are meant to leverage innovative technologies, such as the multi-beam space antennas together with the frequency re-use, in order to maximize the throughput of the overall systems and reduces the associated cost of the service for both the providers and the users [21].

I.3.1.a Multi-beam concept

The innovative HTS GEO satellites leverage space antenna technologies allowing to deploy multiple smaller beams from the same aperture instead of a traditional single wide one. Figure 11 a) illustrates the difference between the traditional single beam and the innovative HTS multi-beam approach in the coverage of a defined area, while Figure 11 b) illustrates an example of coverage of

Africa and Arabian peninsula using a GEO HTS system leveraging the multi-beam approach. Each circle represents a zone covered by one of the beams and its color represents a unique combination of frequency and polarization, that leverages a mix of frequency reuse and polarization diversity. A four-colors scheme is shown in Figure 11 b) and the principle is that two adjacent circles must not have the same color. This constraint is posed in order to avoid the possibility to have interferences between adjacent beams working with the same combination of frequency and polarization. The choice of the colors scheme is strictly related to the available polarizations and amount of spectrum allocated to the area served by the satellite [21].

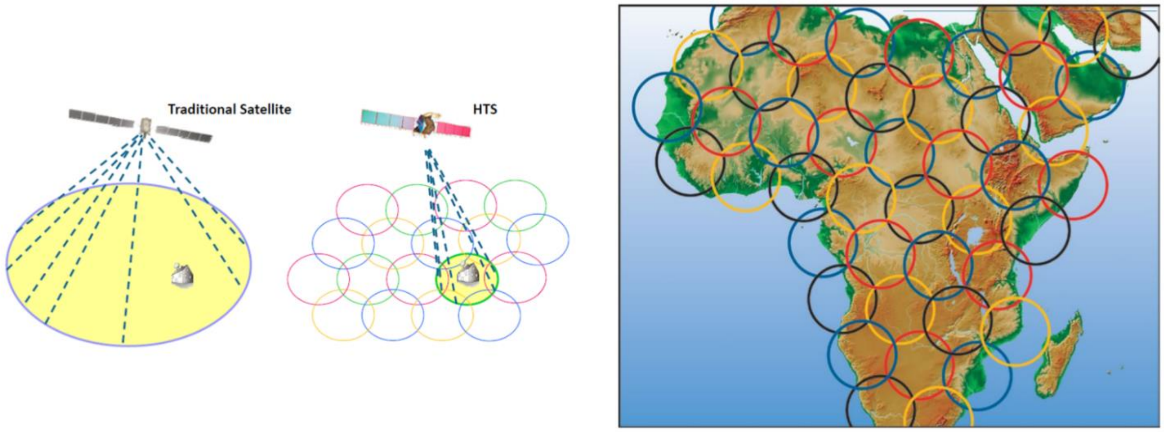

a)

b)

Figure 11 a)Difference between traditional single wide beam satellite and HTS one for the coverage of the same region from [31], b) example of coverage of Africa and Arabian peninsula using a GEO HTS system leveraging the multi-beam approach with a four-colors scheme from [21].

The BW available for a satellite is split into various sub-bands (usually two or three) and then the color scheme is built using the different available polarizations. Starting from these parameters, the total available BW of an HTS satellite can be calculated using the formula given in Figure 12. The throughput of the satellite is then calculated as the product of the total available bandwidth, as derived from the formula given in Figure 12, and the spectral efficiency. It is interesting to underline that the throughput of a such a HTS GEO satellite can absolutely outer performs that of a traditional single-beam GEO one. We can give an example citing the case of the HTS GEO ViaSat-2, that achieves a throughput of over 300 Gbps exploiting the large BW available at Ka-band. For comparison, the entire Intelsat non-HTS fleet (49 satellites working at C-, Ku- and Ka-band) has a combined throughput of about 120 Gbps [32].

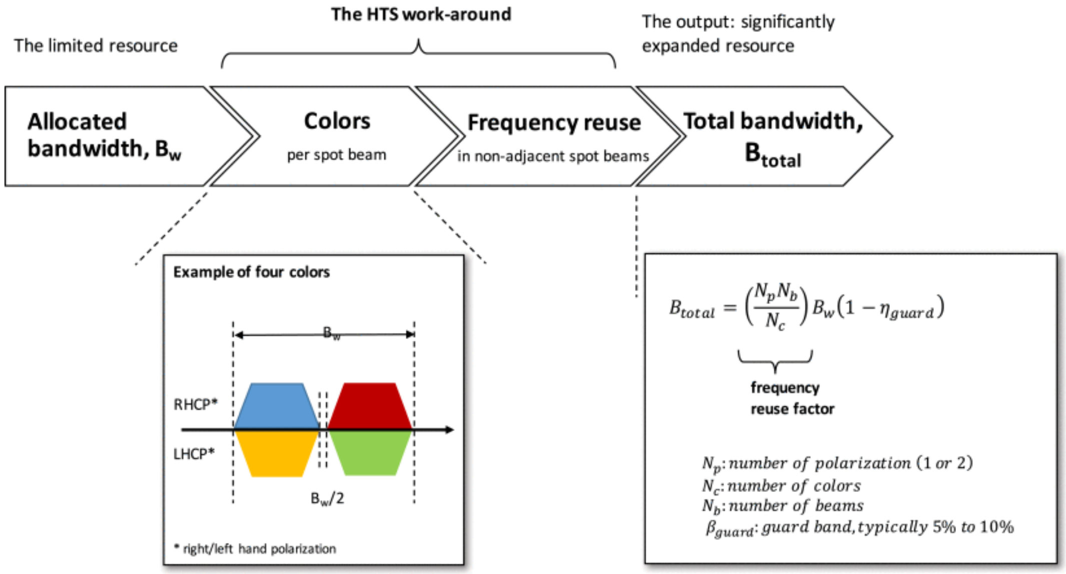

Figure 12 Details of the definition of a color scheme for a HTS satellite and calculation of the total BW from [32].

I.3.1.b Applications and key players

The deployment of these systems is envisaged in order to provide broadband internet connectivity for aeronautical and maritime users rather than residential and business ones that are located in zones that are unserved by the terrestrial network and to integrate the terrestrial networks. It is interesting to underline that the GEO altitudes, combined to the exploitation of Ku- and Ka-bands pose constraints over the required antenna gain for the user's terminal and that the HTS GEO systems cannot solve the latency issues. Hence, applications such as real-time ones and internet-of-things, where either the latency and the achievable user's terminal dimensions are critical, cannot be supported [33]. The key players are the traditional operators (i.e. Intelsat, Eutelsat, SES, Viasat) which renew their fleet in order to extend their services and erode the related prices for the end-users.

I.3.2 LEO systems emergence

The development of HTS systems at LEO actually represents a main trend in the space economy. Their emergence is driven by the possibility to guarantee worldwide low-latency connection and by the recent advances in satellite technologies, that strongly reduced their manufacturing and deployment costs.

I.3.2.a Advantages and drawbacks of LEO approach

Working at LEO altitudes implies higher orbital speeds for the satellites as they result non-geostationary. Different drawbacks derive from this feature like the need for steerable antennas, especially for the user's terminals, and the necessity of large satellite constellations in order to obtain a worldwide continuous coverage. Concerning the problematic of the number of satellites required to guarantee complete Earth's coverage: we move from a minimum of 3 satellites for a GEO constellation, with typical values staying between 30 and 50 satellites, to LEO networks composed by hundreds of satellite (i.e. 648 LEO satellites constellation planned by OneWeb) [15]. Moreover, if we consider two satellites with the same electronics and the same antenna system working at GEO and LEO, respectively, the region covered on the ground by the beam of the LEO one is significantly shrunk. On the other side, the LEO choice guarantees different advantages such as reduced path loss, if compared to a GEO system working at the same frequencies, from which a reduced link budget for the communication with the ground and the need for smaller antenna apertures. Other interesting features regard the fact that Low-Earth-Orbits are less saturated if compared to the GEO ones, rather than the visibility over the entire terrestrial surface for the orbiting constellation and the reduced orbit injection costs. The most interesting advantage consists in a satellite-to-ground delay of around 20 ms (more than ten times lower than GEO) allowing these systems to support the growing demands for real-time applications (i.e. VoIP).

I.3.2.b Key players

The most advanced projects concerning the deployment of LEO systems in the race to provide worldwide low-cost internet connectivity are actually provided by SpaceX, OneWeb and Telesat. It is remarkable to underline how this paradigm shift introduces new players, notably the first two, while withstanding the actual concrete engagement of one of the classical operators, such as Telesat [15]. Table 3 proposes a resume of the main characteristics of the three projects of LEO satellite constellations proposed by the mentioned companies and compared with the Intelsat non-HTS GEO constellation notably in terms of number of satellites and ground stations, throughput of the system and average throughput of the single satellites. If we consider the throughput of the various systems, SpaceX can guarantee 23.7 Tbps by mean of 4425 satellites being the biggest constellation with the highest throughput. Accordingly, SpaceX outperforms the Intelsat non-HTS GEO system of more than 200 times in terms of total throughput with a number of satellites that is more than 90 times higher and a number of ground stations that corresponds to almost 4 times the Intelsat one. If we consider the problem from the point of view of the average throughput per satellite and of the number of required ground stations, Telesat LEO results in the most effective system. In fact, 20 Gbps of average throughput per single satellite are achieved, corresponding to almost four times the SpaceX value, and only 40 ground stations are required, corresponding to a third of those required by the SpaceX system. Telesat LEO outperforms the Intelsat non-HTS GEO system of about ten times in terms of average throughput per satellite using a number of satellites that results three times higher than the Telesat one and a comparable number of ground stations [15]. The author tends to remark that the differences between the performances of the analyzed LEO systems are also related to particular system design choices. Interesting examples of these lasts are the satellite orbital planes, the satellite capacity, the kind of the inter-satellite links and the eventual integration of on-board processing units in the satellites, the elevation angle from the satellites to user links and many others that are not object of this discussion.

System	# of Satellites	# of Ground Stations	System Throughput [Tbps]	Average Throughput Per Satellite [Gbps]
Starlink (SpaceX)	**4425**	**123**	**23.7**	**> 5**
OneWeb	**720**	**71**	**1.56**	**> 3.5**
Telesat LEO	**117**	**40**	**2.66**	**> 20**
Intelsat GEO (non-HTS)	**49**	**34**	**0.12**	**2.4**

Table 3 Resume of the main characteristics of the LEO constellations proposed by Starlink, Oneweb and Telesat LEO and of the Intelsat non-HTS GEO constellation [15]. *LEO projects development is continuously on-going, so values may be subject to variation in time.

I.4 Challenges to be addressed during the PhD

The previous paragraph provided an overview of the actual trends of satellite telecommunications with a competition between different players in order to provide worldwide low-cost and broadband internet connectivity for mass-market consumers. In the context of the developments of the HTS systems, LEO projects have strong business potentialities due to the possibility to guarantee a latency for the satellite-to-ground communication that is in line with the requirements of the real-time applications. The actual objective of companies like SpaceX and Oneweb to bring this technology to the mass-consumers can be accomplished only if a compact and low-cost user's terminal can be proposed. Focusing on Sat-Com-On-The-Move applications, the analysis of state-of-the-art available antenna solutions for user's terminals has been summarized in Table 2. This benchmark suggested that neither of the reviewed solutions can provide the low-profile and low-cost features and offer performance comparable to those of a traditional motorized-reflector based solution (i.e. in terms of scanning range). Targeting high-end user applications, such as in-flight and maritime connectivity or the services for the oil and gas industries, developing terminals offering the maximum achievable and reliable performance had a priority over the considerations in terms of costs and form factor (i.e. surface occupation and weight). On the contrary, designing for the mass-market consumers obliges to modify this perspective giving a higher priority to the reduction of the costs and form factor, that ultimately become stringent constraints. The BW limitations of the radiating elements used in the compact alternatives to the reflector-based solutions actually oblige to split Rx and Tx into different apertures when working at Ku- and Ka-bands, respectively, with the consequent impact over the surface occupation and the cost structure of the user's terminal. We therefore consider the development of compact and low-cost wideband antenna solutions allowing to perform both Rx and Tx from the same aperture at Ku- and Ka-bands as a major innovative step in this field. Hence, the objective of this PhD project is to propose low-cost, compact and wideband antenna solutions for both Ku- and Ka-bands, to be designed exploiting either the standard PCB fabrication process and/or the innovative additive manufacturing technologies.

I.4.1 Wide band and high efficiency single aperture antenna.

The first step of this research is to assess the best performance achievable by a wideband radiating element to be realized in standard PCB technology, notably two microstrip aperture coupled patch antennas working at Ku- and Ka- bands, respectively. Chapter 2 of this manuscript illustrates the design, manufacturing and measurements of such antennas. The next step would be to develop an antenna array able to achieve the gain levels required for Sat-Com-On-The-Move applications at these frequencies. Considering a simple microstrip patch antenna with an average gain of 3 dBi at Ku-band, a 1024-elements array would be required in order to achieve the same level of Rx gain of one of the reviewed motorized reflector-based solutions [23]. The performance of such an antenna array would be strongly limited by the losses associated with the microstrip line feeding network at these frequencies and the intrinsic scanning losses for scanning ranges higher than ±30°, due to the planar radiating elements. These considerations can easily explain why the patch array antenna integrated in the Phasor user terminals leverages a signal distribution network working at baseband (exploiting a digital beamforming technique and integrating a transceiver for each antenna) and a modular approach. This last feature allows to assemble various antenna panels in order to achieve the desired levels of gain, while exploiting the conformal shape in order to help to recover the scanning losses [27]. Taking into account these limitations, it becomes difficult to envisage a patch antenna array solution achieving performance comparable to a reflector-based solution at these frequencies and a suitable price for the mass-consumers at the same time. Hence, the next step of this research will be to propose a wideband and high-efficiency antenna solution, able to reduce the losses associated to a microstrip feeding network working at these frequencies and giving the possibility to perform a ±45° electronic scanning in elevation with maximum scanning losses equal to 1 dB. If these features are provided, a single antenna panel performing both Rx and Tx could be integrated in a user's terminal requiring only a 2-axis rotary mechanics in order to guarantee a complete scanning range, instead of the 3- or 4- axis required by traditional reflector-based solutions. The impact in terms of form factor and cost of the final product would go in the direction of the design of a mass consumer-friendly LEO user terminal for Sat-Com-On-The-Move applications. A metal waveguide-based antenna could guarantee a wide

BW response with high efficiency: the open-ended metal double-ridged waveguide (DRWG) antenna configuration is considered as a suitable candidate to satisfy all the listed requirements. If compared to a standard open-ended rectangular waveguide designed to cover the same frequency range, an open-ended DRWG allows to extend its operational BW while requiring a shrunk section. The last characteristic is therefore the key feature enabling to set the required pitch element spacing for the final array in order to achieve the envisaged electronic scanning performance in elevation. Hence, Chapter 3 of this manuscript illustrates the design, manufacturing and measurements of a 2x2 DRWG antenna array working at Ku-band, rather than the design of a 4x4 DRWG antenna array with parasitic patch elements. Similarly, Chapter 4 of this manuscript illustrates the design, manufacturing and measurements of a 2x2 DRWG antenna array working at Ka-band.

I.4.2 Opportunity to leverage cost-effective technologies.

The planar antennas are envisaged to be developed using the simplest stack-up as possible and to be realized leveraging the standard PCB fabrication process taking into account the will to contain their cost, as detailed in Chapter 2 of this manuscript. Considering the waveguide-based solution, we target the opportunity to leverage the possibilities offered by the innovative additive manufacturing technologies such as direct metal laser sintering. The 3-D metal printing technologies have already represented one of the factors allowing to decrease the overall manufacturing cost of the satellites and paving the way for this new era of very large constellation project, such as the SpaceX one [2]. The idea is that these technologies may be leveraged in our case in order to realize such waveguide-antenna arrays and part of their complex waveguide-based feeding networks in a single block. These structures would require various fabrication and assembly steps if a traditional metal fabrication technology (i.e. machining, milling) is exploited, which would contribute to keep a relatively high cost for complete process [34]. On the other side, on-going researches suggest that the metal 3-D printing technology can be leveraged in order to build complex designs with a single fabrication step. This may contribute to decrease the cost of the user's terminals for the end-users and to realize a further step in order to bring the mobile satellite telecommunications to the large public. Chapter 3 and Chapter 4 detail the challenges and the constraints related to the possibility to leverage such a process in order to build a small wideband DRWG antenna array with its complex waveguide-based feeding network in single aluminum block.

I.4.3 Envisaged specifications.

Figure 13 a) presents a resume of the features of some of the reviewed commercial user terminals for civil SOTM applications from Table 2, and the envisaged specifications for a consumer-friendly one. Focusing on this last, the envisaged BW for the radiating elements of the antenna panel and its scanning range should be in line with those of traditional reflector-based solutions. The main difference is the envisaged hybrid scanning mechanism that should completely rely on the electronic steering for the elevation plane while keeping the rotary mechanics only for the azimuthal steering. The envisaged profile height and weight are in line with those of the slotted waveguide array – based solution and of the Phasor's one. Concerning the evaluation of the maximum allowed surface, Figure 13 b) shows a top-view of a Mini Cooper subcompact car produced in 2014 with its dimensions ([35]), and the indications of the biggest surface that would be theoretically available for the placement of a circular shaped Sat-Com-On-The-Move user's terminal. A compact car accessible to the large public has been properly selected in order to provide a suitable practical example. Concerning the pricing of the final product, the actual commercial solutions are intended for high end-users with costs that can reach 100 k$ for a complete Kymeta system ([29]). A reasonable price of a user's terminal intended for consumer mass-market should reach a maximum amount of 1 k$ which corresponds to the VIASAT hardware for satellite vehicle tracking [36]. Table 4 gives an overview of the envisaged electrical performance of an antenna panel for such a user's terminal in the Ku- and the Ka- cases. An antenna array is required for each case, whose radiating elements will be designed and dimensioned during this thesis aiming to satisfy the fixed operational BW constraints as primary objective, and then the form factor and scanning range requirements.

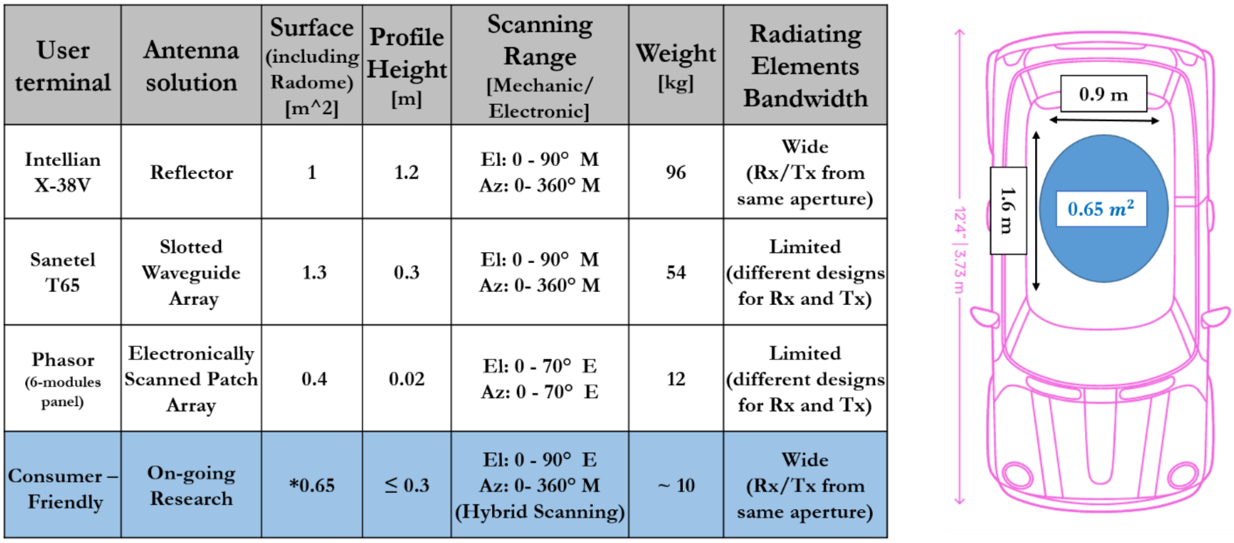

User terminal	Antenna solution	Surface (including Radome) [m^2]	Profile Height [m]	Scanning Range [Mechanic/ Electronic]	Weight [kg]	Radiating Elements Bandwidth
Intellian X-38V	Reflector	1	1.2	El: 0 - 90° M Az: 0- 360° M	96	Wide (Rx/Tx from same aperture)
Sanetel T65	Slotted Waveguide Array	1.3	0.3	El: 0 - 90° M Az: 0- 360° M	54	Limited (different designs for Rx and Tx)
Phasor (6-modules panel)	Electronically Scanned Patch Array	0.4	0.02	El: 0 - 70° E Az: 0 - 70° E	12	Limited (different designs for Rx and Tx)
Consumer – Friendly	On-going Research	*0.65	≤ 0.3	El: 0 - 90° E Az: 0- 360° M (Hybrid Scanning)	~ 10	Wide (Rx/Tx from same aperture)

a)

b)

Figure 13 a) Resume of the features of some of the reviewed commercial user's terminals for civil SOTM applications and envisaged ones for a consumer-friendly user's terminal, b) Top-view of a 2014 Mini (BMW) Cooper subcompact car with its dimensions from [35] and indications of the max. surface available for a circular shaped Sat-Com-On-The-Move user's terminal. *Surface value for consumer-friendly user's terminal is given from the values given in b).

Band	Frequency Range [GHz]	Fractional Bandwidth [%]	Electronic Scanning Range (Elevation)	Antenna Panel Rx Gain [dBi]	Antenna Panel Tx Gain [dBi]	Polarization
Ku-	**(10.75 – 14.5) *Rx: 10.9-12.75 *Tx: 13.75-14.5**	**30**	**±45° (max scan loss of 1 dB)**	***35.8 @ 12.5 GHz**	***36.2 @ 14.5 GHz**	**Dual Linear**
Ka-	**(18 – 31) **Rx: 19-21 **Tx: 29-31**	**53**	**±45° (max scan loss of 1 dB)**	****45 @ 20 GHz**	****38.5 @ 30 GHz**	**Dual Circular**

Table 4 Envisaged electrical specifications of an antenna panel to be integrated in a consumer-friendly user's terminal. * Values from Sanetel T65 datasheet [25]. ** Values from TAIPAN-48 datasheet [37]

II. WIDEBAND, DUAL POLARIZED KU- AND KA-BAND PLANAR ANTENNAS ACHIEVED ON PCB TECHNOLOGY

In the previous chapter we have presented the trends and the challenges of Low-Earth-Orbit SOTM telecommunications at Ku- and Ka-band and the objectives of our work. The aim was to propose an antenna solution to be leveraged in order to propose an innovative low-profile user's terminal, able to guarantee the same performance as the traditional bulky reflector–based solutions with a price affordable by mass-consumers. Compact alternatives are already available, but they keep a relative high cost for the end-user being characterized by the use of two different antenna panels in order to perform Rx and Tx functions [3]. As we detailed in Chapter 1, this is due to the fractional bandwidth (FBW) required by SOTM application at Ku-band (10.75 - 14.5 GHz), equal to the 30%, and Ka-band (18 - 31 GHz), equal to 53%. Hence, the development of a low-cost and wideband antenna solution, allowing to develop a low-profile panel integrating both Rx and Tx functions into the same antenna aperture has been recognized as a major innovative step in the field. The objective of this part of the work is to assess the maximum performance achievable by planar antennas to be realized with the traditional low-cost PCB fabrication processes. The idea is to cover the targeted bandwidths (BWs) of interest while keeping the simplest and cheapest fabrication stack-up as possible. Designed antennas are meant to achieve performance in line with the state-of-the-art, notably in terms of achieved impedance bandwidth, realized gain and capability to support a dual circular polarization. Developed antennas could be eventually integrated in large arrays, achieving the gain levels required by SOTM applications.

We begin this chapter with the introduction of state-of-the-art planar antennas operating at Satcom frequencies with a particular attention to the designs offering the largest bandwidths that have been reported in literature. Following this analysis, the working principle of the microstrip aperture coupled patch (ACP) antenna is introduced, highlighting the versatility of this configuration coming from its many design parameters and the opportunity to be leveraged for wideband applications. The design of an ACP antenna working at Ku- band is detailed, starting from a design supporting a single linear polarization moving to a complete prototype with connectors that supports dual linear polarization. The relative simulated performance is shown, as well as the fabrication of 4 samples and their measurements. Finally, a benchmark with the state-of-the-art of the best reported designs of wideband ACP antennas working at Ku-band is proposed. The next part will present a similar approach for the design of a wideband dual polarized ACP antenna working at Ka-band. While following the same kind of methodology from the design to the benchmark of the prototypes, a particular attention will be given to the description of the surface waves (SWs) phenomena arising at these frequencies due to the use of thick substrates. The method applied in order to use the generated SWs in a constructive way for radiation will be detailed. The chapter ends with the discussion of the benefits and limitations of the planar antenna solutions for SOTM applications.

II.1 Satcom planar antenna state-of-the-art

The existing low-profile commercial alternatives to the traditional reflector-based user terminals for SOTM applications at Ku- and Ka-band rely on two distinct antenna panels to perform Rx and Tx communications. Each panel usually integrates a radiating element (i.e. microstrip patch) optimized to work in the sub-range of frequency assigned to Rx and Tx, respectively. Figure 14 shows an example of such a user's terminal for small aircrafts (HiSat-35TR from [38]), working at Ku- band). The scanning range required by LEO SOTM communications is achieved by a mixture of electronic and mechanical beam steering in this case.

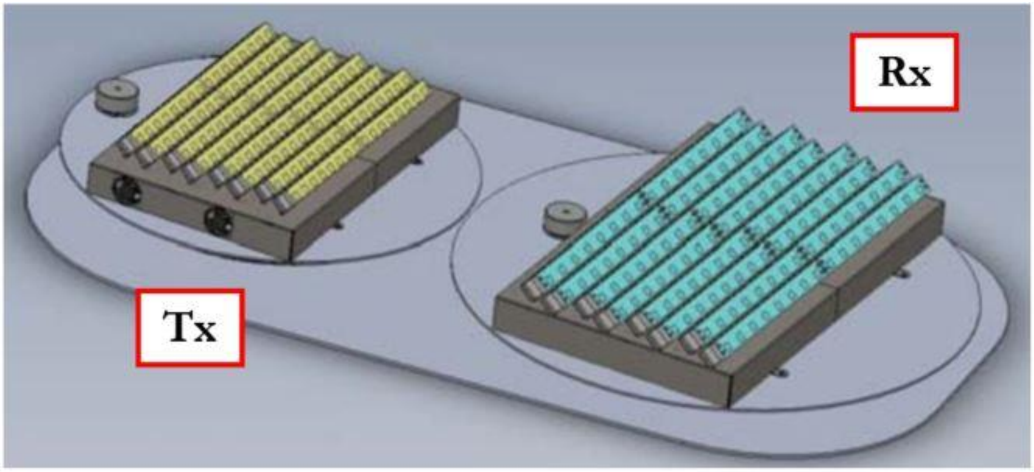

Figure 14 HiSat-35TR antenna panels for Rx and Tx at Ku-band from [38].

Developing a compact low-cost planar antenna offering the large operational BW required to cover both Rx and Tx sub-bands at these frequencies would represent a major innovation. The form factor of the user's terminals could be reduced moving from a double to a single antenna panel, decreasing the overall final cost for the end-users. PCB antennas able to cover such wide operational bandwidths have already been reported in literature both at Ku- and Ka-bands [39] [40]. The drawback comes from the fact that either complicated stack-ups and non-conventional fabrication processes have been used in order to extend the operational bandwidth, representing a main limitation for a possible large-scale production oriented to the mass-consumer market. Moreover, the form factor of these antennas is such that their possible integration in an array is usually limited to configurations characterized by small scanning angles or fixed beam applications. The following sub-paragraphs synthetize the state-of-the-art of the most interesting examples of planar wideband antennas working at these frequencies that have been reported in literature.

II.1.1 Ku-band

An interesting example of planar wideband antenna working at Ku-band can be found in [39], where an ACP antenna is presented covering ~30% of fractional bandwidth around the center frequency of 15 GHz. The minimum measured broadside realized gain is equal to 3 dBi, as we can see in Figure 15 d), with a matching oscillating around -10 dB at the frequencies of interest, as we can see in Figure 15 c). The prototype is printed by direct digital manufacturing (DDM), illustrated in Figure 15 b). The relative stack-up is detailed in Figure 15 a), comprising three layers of metal and three layers of a plastic polymer (acrylonitrile butadiene styrene) with different densities, used as dielectrics. The appealing performance of this antenna is counter-balanced by the use of a non-conventional fabrication process which may limit a possible industrialization of this prototype for low-cost applications. The size of the complete design is not available, but the edge dimension of the patch is equal to a third of the wavelength at the highest operational frequency. This suggests that an array with a spacing of at least λ at the highest operational frequency may be created, offering fixed beam functionalities avoiding grating lobes.

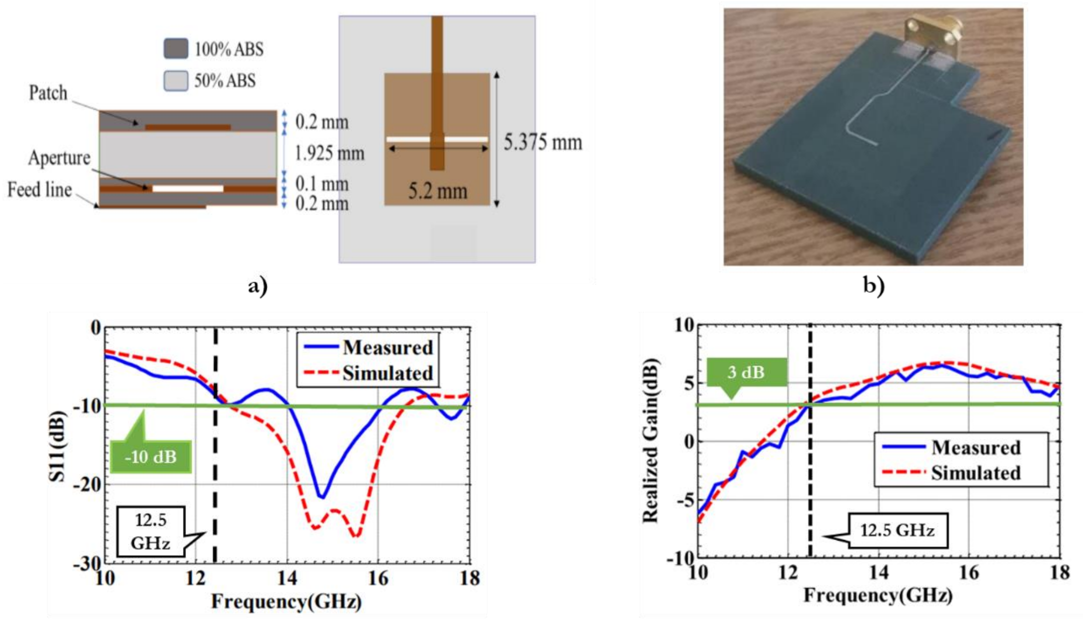

a) b)

c) d)

Figure 15 ACP antenna working at Ku-band with 30% of fractional bandwidth around the center frequency of 15 GHz, , from [39]: a) stack-up and transparent top-view with dimensions, b) prototype, c) simulated and measured S_{11} versus frequency, d) simulated and measured broadside realized gain versus frequency.

Another interesting design can be found in [41], where a single-fed multilayer circularly-polarized aperture-coupled patch antenna is presented. The exploded stack-up of the antenna is shown in Figure 16 a) and the simulated matching versus frequency is shown in Figure 16 b): -10 dB impedance bandwidth is achieved from 13.5 to 19 GHz, corresponding to ~33% bandwidth around the center frequency of 16 GHz. Lower than -3 dB axial ratio is ensured from 15.5 to 16.4 GHz, providing a minimum peak gain of 5.8 dBi within the band. The stack-up of the structure is complicated by the presence of an air cavity within the patch substrate and by the use of a parasitic patch and a bottom ground layer. The final stack-up consists of 4 dielectric layers, 5 metal layers and two series of vias. The size of the patch is equal to $(0.57*\lambda_{19GHz})*(0.57*\lambda_{19GHz})$, where λ_{19GHz} is the free-space wavelength at the highest frequency of the BW.

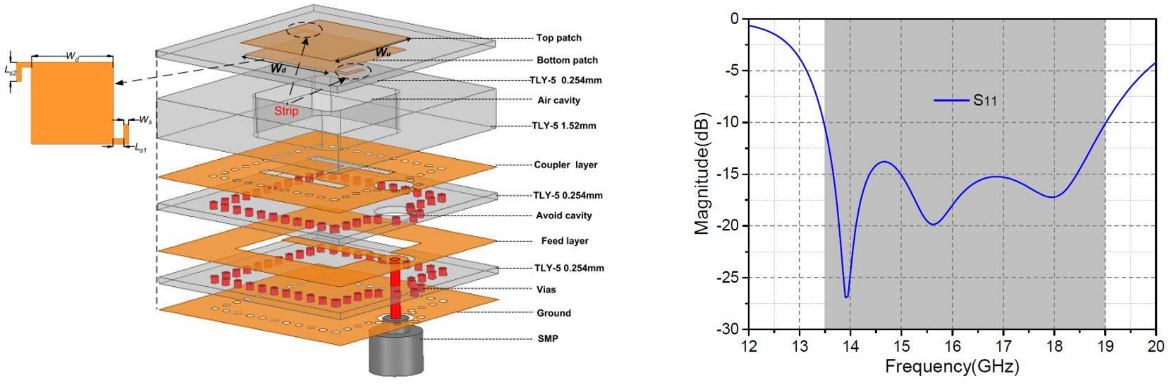

a) b)

Figure 16 Single –fed multilayer circularly polarized planar aperture- coupled antenna, from [41]: a) exploded stack-up from [41], b) simulated S_{11} versus frequency from [41].

The main characteristics of the already discussed designs are synthetized in Table 5. The thickness of the PCB and the -10 dB impedance bandwidths are equivalent in the 2 cases. The minimum broadside realized gain of the circularly polarized ACP antenna is almost the double of the single polarized one. This is due to the use of a parasitic patch, a cavity and an additional ground plane at the bottom of the structure which strongly improves the front-to-back ratio [42]. These works prove the feasibility to achieve the 30% fractional bandwidth required by Ku-band for SOTM applications using planar wideband antennas such as ACP configurations. Nevertheless, these results are achieved either using a direct digital manufacturing process with plastic polymers, for which low-cost large-scale production has to be proven, or by a traditional PCB fabrication process with a complicated stack-up.

Authors	Configuration	Polarization	-10 dB Impedance BW → Fractional BW	Min Broadside Realized Gain	Fabrication Process	Thickness
Kacar et al, 2017.	**Aperture Coupled Patch**	**Single Linear**	**(12.5 – 18) GHz →(~30%)**	**3 dBi (along the -10 dB Impedance BW)**	**Direct Digital Manufacturing (Plastic polymers)**	**~ 2.4 mm**
Liu et al., 2018	**Aperture Coupled Patch**	**Left-Hand Circular**	**(13.5 – 19) GHz →(~33%) Simulated**	**5.6 dBi (Simulated in the -3 dB Axial Ratio BW: → 5% of fractional BW)**	**Simulated →Envisaged PCB**	**~ 2.4 mm**

Table 5 Resume of the best reviewed wideband planar antennas working at Ku-band [39], [41].

II.1.2 Ka-band

An interesting example of planar wideband antenna working at Ka-band can be found in [40], using an aperture coupled stacked patches configuration. The exploded build-up can be appreciated in Figure 17 a), while the simulated matching and mutual coupling between the two ports are illustrated versus frequency in Figure 17 b). The simulated -10 dB impedance bandwidth ranges from 17.7 to 30.3 GHz, corresponding to more than 52% of fractional bandwidth centered around the frequency of 24 GHz. The very large operational bandwidth is achieved by the use of 2 stacked patches and a foam layer. The resulting stack-up has a thickness of 4.2 mm, which could be a serious issue if low-cost design is targeted. The overall surface of the antenna is $(1.12*\lambda_{30.3GHz})*(1.12*\lambda_{30.3GHz})$, where $\lambda_{30.5GHz}$ is the wavelength at the highest operational frequency. It is then not possible to realize an array for fixed beam applications whose functionality could be guaranteed at the highest frequency of interest avoiding the apparition of grating lobes. Another interesting example of planar wideband antenna working at Ka-band is reported in [43], consisting of an aperture coupled oval patch with a single L-shaped feeding network and an L-shaped coupling slot as we can see in Figure 18 a). The stack-up can be appreciated in Figure 18 b): only 3 metal layers are used with different dielectric substrates for the microstrip line and the patch, achieving a final stack-up thickness of 0.9 mm. The reflection coefficient is lower than -19 dB over a wide range of frequencies from 27.5 to 30.5 GHz corresponding to 17% of fractional bandwidth around the center frequency of 29 GHz, as shown in Figure 18 c). The minimum simulated broadside realized gain is 7 dBi and the antenna supports a right-handed circular polarization.

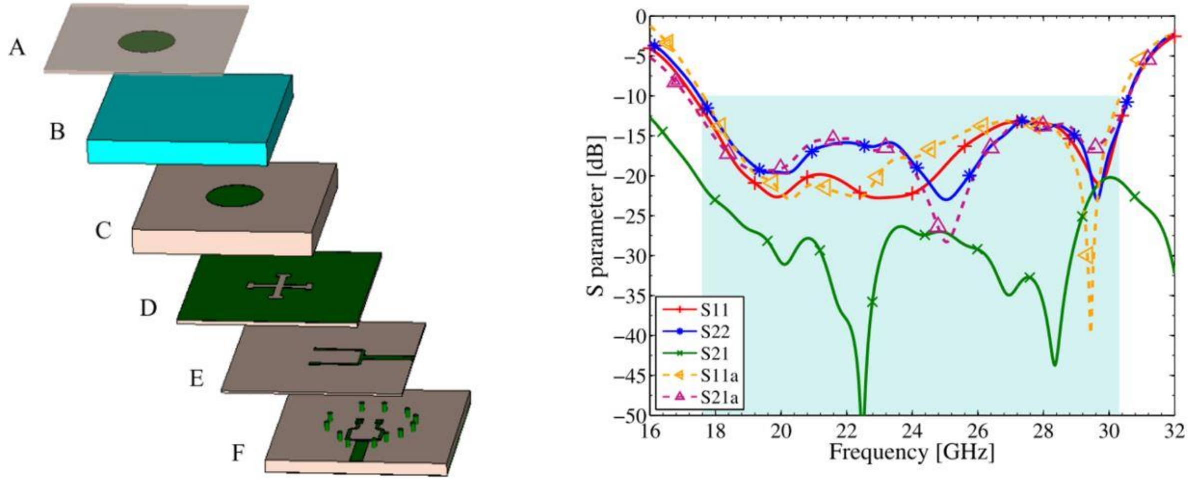

a)

b)

Figure 17 ACP antenna working at Ka-band using aperture coupled stacked patches and fork-based feeding network in asymmetric stripline technology, from [40]: a) antenna element composed by six thin layers fed by two fork lines. Copper is highlighted with green color, dielectric layers with brown and foam layer with blue). Layers thicknesses are: A – 0.787, B – 0.127, C - 0.254, D – 1.575, E – 1.5, F – 0.254 [mm] from [40], b) simulation results of the S- and S-active parameters of the proposed antenna versus frequency from [40].

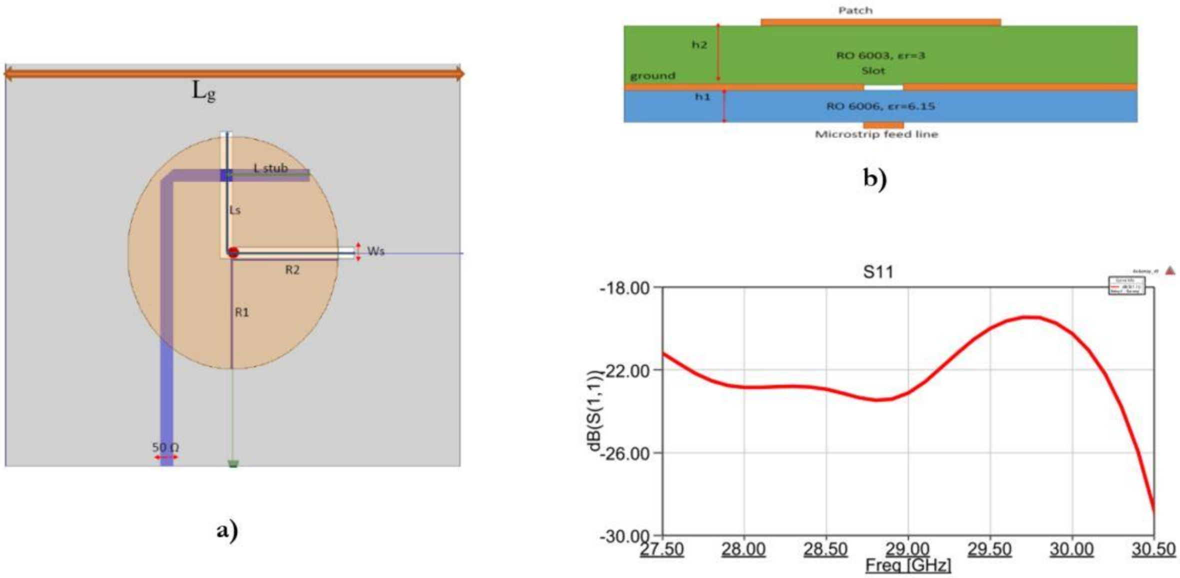

a)

b)

c)

Figure 18 Aperture coupled oval patch antenna working at Ka-band, from [43]: a) transparent top-view from [43], b) cross-section view from [43], c) simulated S_{11} versus frequency from [43].

The main characteristics of the already discussed designs are synthetized in Table 6. It is interesting to underline that the aperture coupled antenna with stacked patches manages to cover the frequency range from 17.7 up to 30.5 GHz supporting a dual circular polarization with reflection coefficients lower than -19 dB at both ports. This proves that it is possible to achieve a planar design covering both Rx and Tx Ka-bands used for SOTM applications. Nevertheless, this result is achieved by using a very thick stack-up (4.2 mm) that includes a series of VIAs, a stacked patch and a layer of foam representing a drawback for an eventual low-cost large-scale production (due to its complexity).

Authors	Configuration	Polarization	-10 dB Impedance BW → Fractional BW	Min Broadside Realized Gain	Fabrication Process	Thickness
Gorsky et al, 2015.	**Aperture Coupled Stacked Patches**	**Dual Circular Polarization**	**(17.6 – 30.3) GHz →(~52%)**	**N.A.**	**Simulated →Envisaged PCB with a foam layer.**	**~ 4.6 mm**
Hussam et al., 2015.	**Aperture Coupled Oval Patch**	**Right-Handed Circular Polarization**	**(27.5 – 30.5) GHz →(17%)**	**7 dBi**	**Simulated →Envisaged PCB with 2 different dielectrics.**	**0.9 mm**

Table 6 Resume of the best reviewed wideband planar antennas working at Ka-band [40], [43].

II.2 Aperture coupled patch antenna concept

As we have already seen in the previous paragraph, the ACP antenna configuration seems a very interesting option when designing wideband planar antennas targeting SOTM applications. This configuration that allows to feed a microstrip patch antenna without requiring a direct connection between the antenna and the feedline has been firstly introduced by Pozar in [44]. The basic configuration can be appreciated in

Figure 19: the patch and the feeding line lay on two different metal layers, each one with its own substrate that can be independently optimized with the possibility to use two different dielectric materials, as we have seen in [39] and [43]. A metal ground plane is placed in the middle of the stack-up, separating the feeding line and the patch metal layers, avoiding any possible spurious radiations originated by the feeding line to impact the radiation pattern of the antenna. This represents one of the advantages of this configuration if compared to those providing a feeding line placed in the same metal layer as the patch [44]. The signal driven by the feeding line is magnetically coupled to the patch by means of a slot in the ground plane and a stub is usually optimized at the level of the feeding line in order to improve the matching. The shape of the slot can be customized in order to improve the coupling level. To give an example: a rectangular aperture can provide a coupling that is ten times stronger than a circular one with equivalent surface. [45] The described configuration provide two

resonances coming from the patch and the slot, respectively. The back-radiation is an intrinsic issue of this kind of design, mainly due to the slot resonance and radiation. The slot is usually dimensioned in order to resonate at frequencies higher than the targeted ones, in this way most of the forward radiated power is due to the patch and the front-to-back ratio can be set to about 15-20 dB in the frequency range of interest [45].

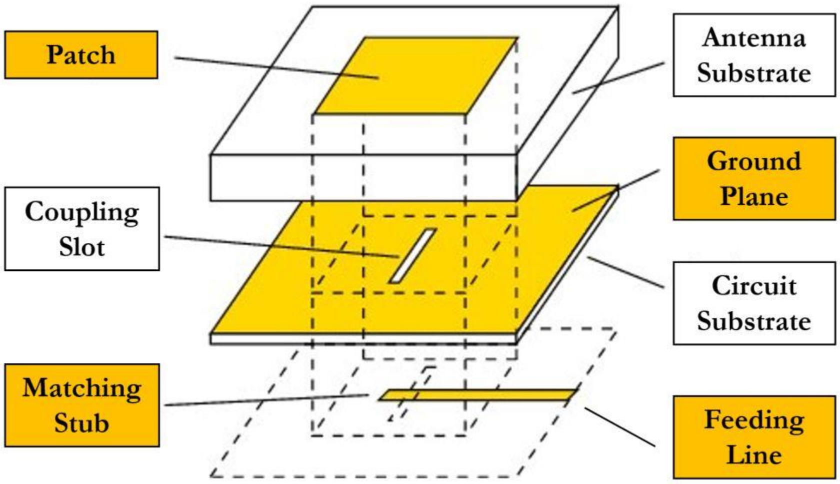

Figure 19 Exploded stack-up of the basic concept of an ACP antenna, from [46].

The basic configuration can be modified by adding a second feeding line and a second aperture, in order to support a dual polarization feature. It is possible to alleviate the back-radiation issue by dimensioning the slot in order to upshift its resonance very far from the operational bandwidth. This approach can be considered without sacrificing some operating bandwidth by the introduction of a new resonance inside the targeted BW. An additional metal layer is added on the top of the stack-up, where a stacked patch is designed, rather than a related additional substrate, as shown in Figure 20 a) [47]. It is also possible to furtherly improve the performance by adding another metal layer with the relative substrate below the feeding lines at the bottom of the stack-up. This enables to add a shielding ground plane that definitely blocks the radiation in the backward direction, as shown in Figure 20 b) [42]. Finally, we can conclude that the ACP offers a very versatile configuration for the design of a wideband planar antenna. Nevertheless, a particular attention must be paid on the trade-off between the envisaged performance and the complexity of the stack-up, which will have a direct impact on the fabrication costs. This consideration becomes critical in the case of SOTM applications where the required levels of gain are such that large array are needed for the eventual integration in a user's terminal.

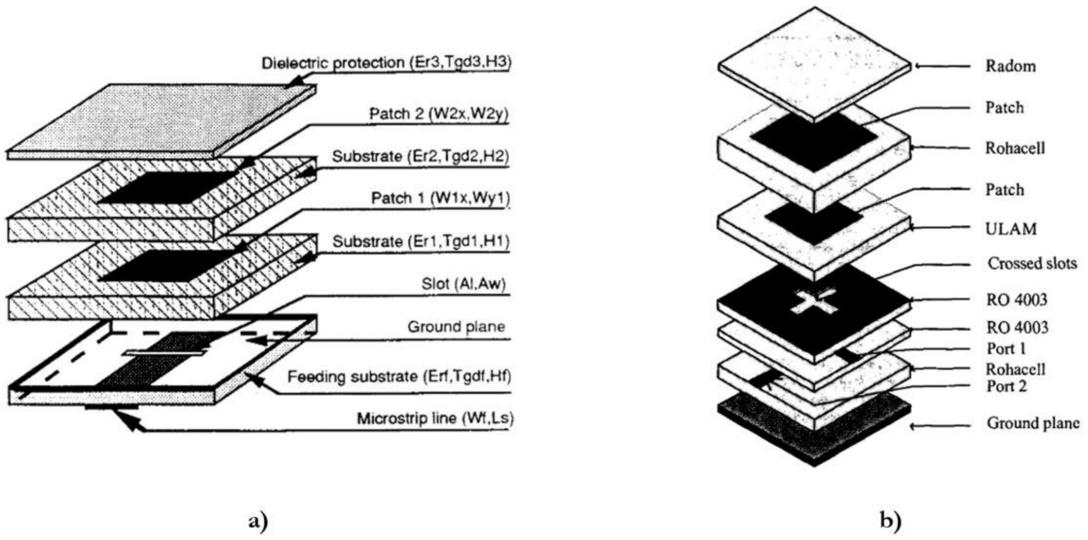

Figure 20 Exploded stack-up of ACP antenna configurations: a) stacked aperture coupled patch with single linear polarization, from [47], b) stacked aperture coupled patch with additional ground plane supporting dual polarization and with improved front-to-back ratio, from [42].

II.3 Wideband Ku-band dual polarized microstrip aperture coupled patch antenna design

Following the discussion of the previous paragraphs, the microstrip aperture coupled patch antenna architecture is chosen to design a planar antenna working at Ku-band (10.75-14.5 GHz) with ~30% fractional bandwidth and supporting dual linear polarization. As we have seen in [39], a planar antenna capable to offer the 30% of FBW at Ku-band has already been proposed supporting a single linear polarization and requiring a DDM fabrication process with two plastic substrates with different densities. We envisage to propose an antenna with similar performance able to support a second polarization while keeping the simplest stack-up as possible, to be compatible with a low-cost standard PCB fabrication process. The first step will consist in presenting the design of an ACP antenna supporting a single linear polarization. Hence, we discuss the integration of a second feeding line and a second slot in order to support a second orthogonal polarization and finally the integration of the connectors required for the measurements of the prototypes. The prototyping and the test results will be discussed before concluding with the benchmarking of the performance of the proposed solution compared to the state-of-the-art.

II.3.1 Single polarization design

A NELCO 4000 – 13 Si EP substrate ($\varepsilon_r = 3.7$, $tg(\delta) = 0.009$) is chosen (being a cost effective standard FR4 material grade) and an initial antenna supporting single linear polarization is designed. The transparent top-view of the design can be appreciated in Figure 21 a) and the relative exploded stack-up is shown in Figure 21 b), detailing the different components and the main design parameters.

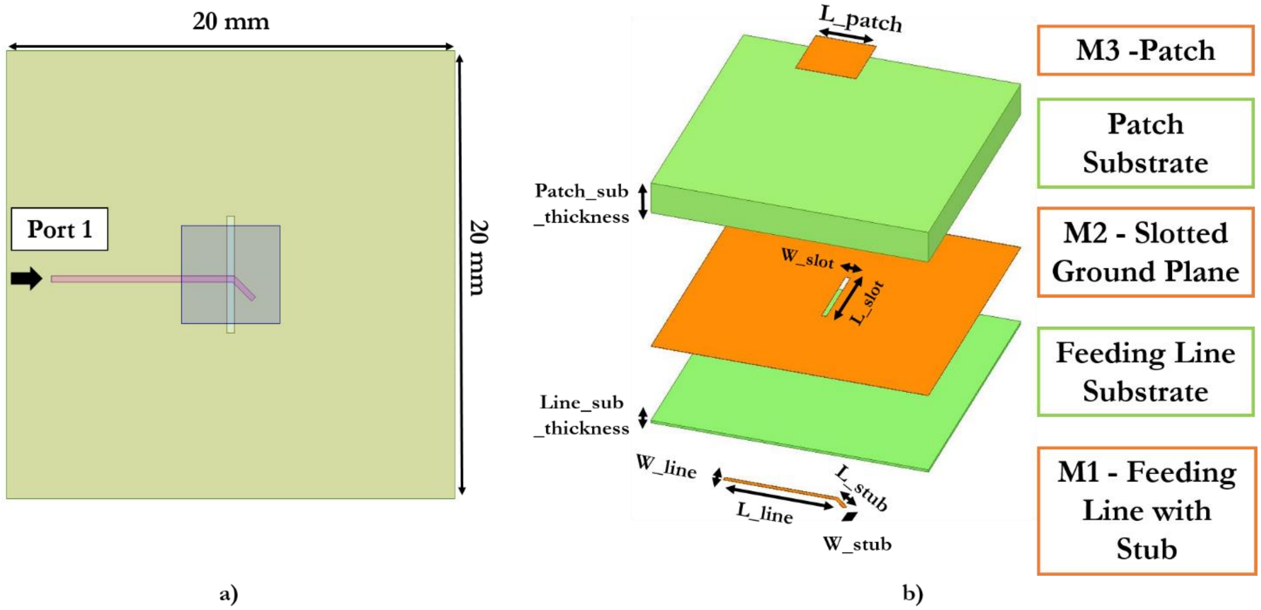

Figure 21 Designed ACP antenna working at Ku-band and supporting a single linear polarization: a) transparent top-view, b) exploded stack-up detailing the different components.

Table 7 shows the dimensions of the most important design parameters highlighted in Figure 21 b). A very thin substrate for the feeding line is chosen and the microstrip feeding line is dimensioned in order to offer a characteristic impedance of 50 Ω at the central frequency of 12.6 GHz. Taking into account the necessity to accommodate a second feeding line on the same metal layer in order to support a second polarization, the line is positioned with an offset of 0.6 mm from the center of the edge of the PCB board on the first metal layer and a diagonal stub is designed, as we can appreciate in Figure 21.

L_patch (mm)	Patch_sub _thickness (mm)	L_slot (mm)	W_slot (mm)	Line_sub _thickness (mm)	L_line (mm)	W_line (mm)	L_stub (mm)	W_stub (mm)
4.4	2.4	5.2	0.35	0.18	8.2	0.2	1.33	0.28

Table 7 Dimensions of the design parameters of the ACP antenna working at Ku-band shown in Figure 21 b).

The length and the width of the stub are optimized via simulation in order to improve the matching along the wide targeted operational bandwidth. A square patch is chosen to support a second polarization. The size of the patch and the thickness of the relative substrate are calculated aiming to get a resonance around 13.5 GHz. The dimensions of the slot in the ground plane are optimized via simulation in order to set its resonance at lower frequencies, instead. The strategy aims to exploit these two resonances to guarantee the functionality of the device over the 30% of FBW. Moreover, we target a low-cost design with the simplest stack-up as possible without the need for additional elements, like the stacked patch seen in Figure 20. It is worth to underline that simulation results indicate that the two resonances are intrinsically interconnected, so it is not possible to independently tune one of them without simultaneously affecting the other. The simulated performance of the antenna are plotted in Figure 22 in terms of matching, total efficiency, directivity and broadside realized gain versus frequency. Figure 22 a) shows that the targeted frequency range is covered with a matching lower than -10 dB, except for the high edge of the band where it increases to -8 dB, and a total efficiency being higher than 90% except at the high edge of the band where it drops to ~80%. Figure 22 b) illustrates that the simulated broadside realized gain stays between 5.7 and 6.3 dBi and the directivity between 6.1 and 6.5 dBi in the operational BW. The simulated radiation patterns of the realized gain are plotted at three different frequencies: 10.75, 12.5 and 14.5 GHz, for the H- and E- planes and they can be appreciated in Figure 23 a) and b), respectively. The simulated 3-D radiation pattern of the realized gain at 14 GHz is plotted in Figure 24 a) (transparent isometric view) and b) (front-view).

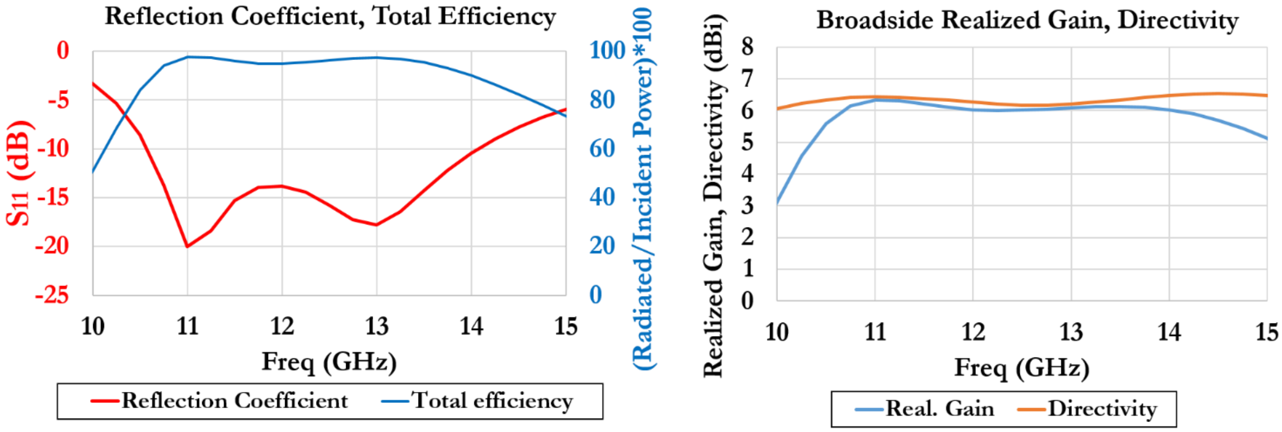

a) b)

Figure 22 Simulated performance of the designed ACP antenna with single polarization versus frequency: a) reflection coefficient, total efficiency, b) broadside realized gain, directivity.

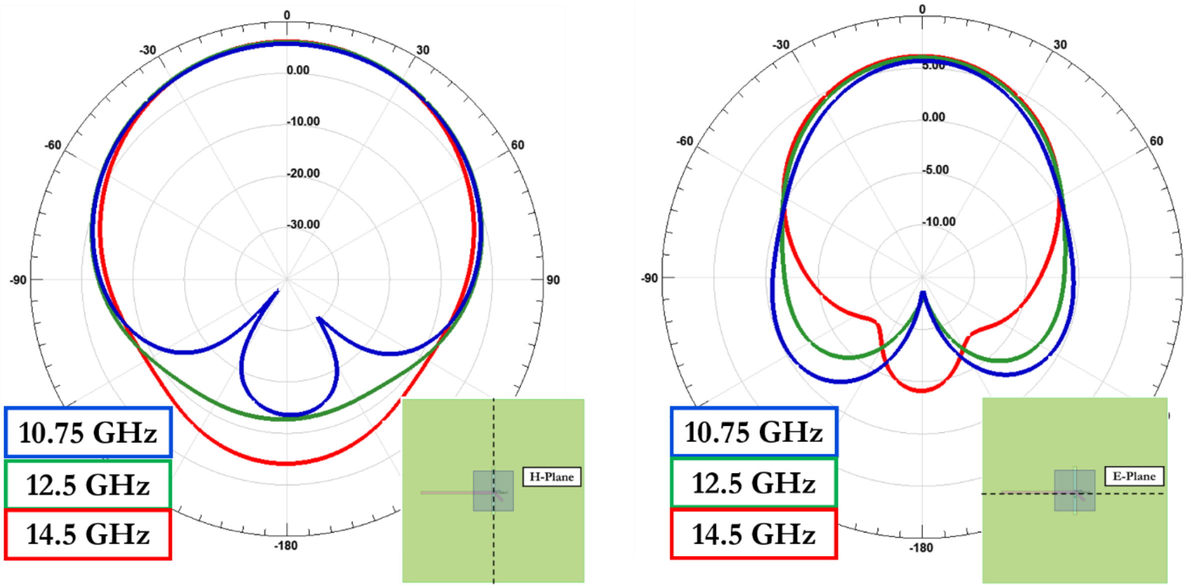

a)

b)

Figure 23 Simulated realized gain radiation patterns in dBi at 10.75 GHz, 12.5 GHz and 14.5 GHz for a) H-plane and b) E-plane.

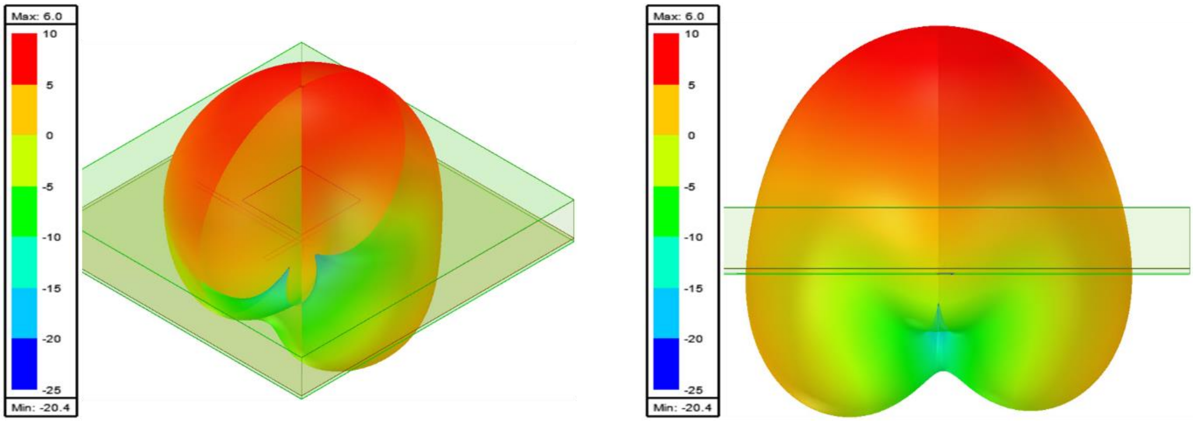

a)

b)

Figure 24 Simulated 3-D radiation patterns of the realized gain at 14 GHz, in dBi: a) transparent isometric view, b) transparent front-view.

II.3.2 Dual polarization design

We wanted to modify the previous design in order to support a second linear orthogonal polarization, so we proceeded by adding a second feeding line on the first metal layer and a second orthogonal slot in the ground plane, accommodated in the second metal layer, as shown in Figure 25.

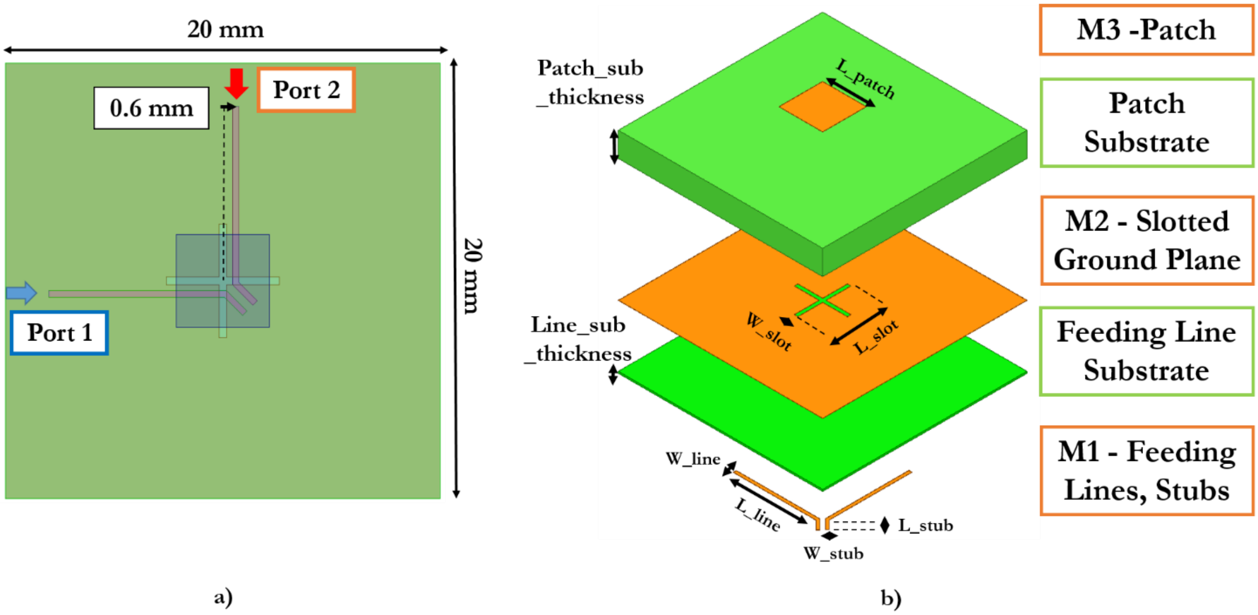

Figure 25 Designed ACP antenna supporting dual linear polarization: a) transparent top-view, b) exploded stack-up detailing the different components.

The dimensions detailed in Table 7 are kept symmetric for the two microstrip lines and the two slots, respectively. The simulated matching of the dual polarized design is plotted versus frequency in Figure 26 a): the S_{11} and the S_{22} are superimposed with the matching of the single polarization design. As we can see, there is a deterioration of the performance in both cases: the responses are shifted in frequency with a maximum drop of 9 dB of the S_{22} in correspondence of 11 GHz. Figure 26 b) shows the simulated broadside realized gain versus frequency when only port 1 is fed and when only port 2 is fed, compared with that of the single polarization design. The deterioration of the performance is evident ranging from 0.4 dBi to a maximum of 2 dBi at 14.5 GHz when only port 2 is fed.

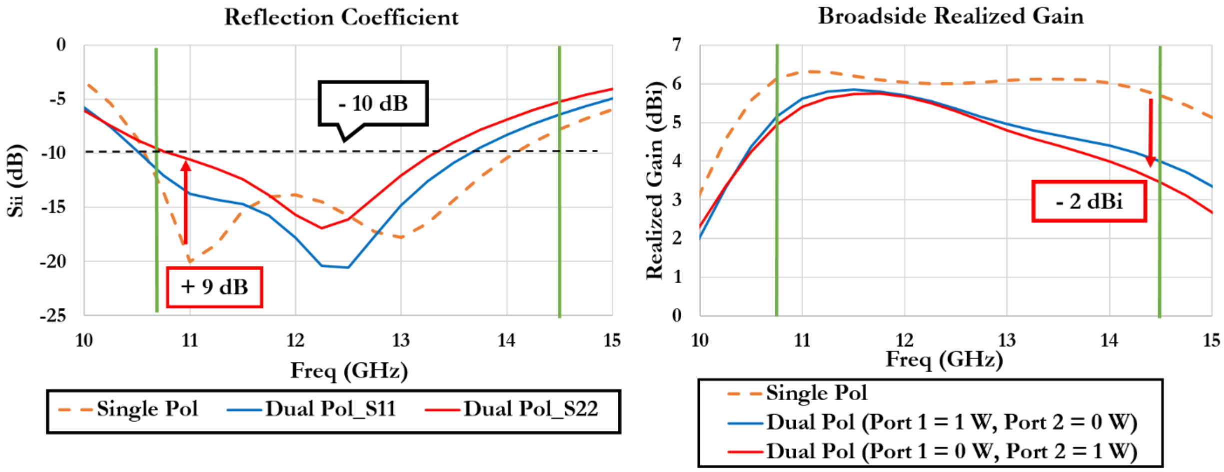

a)

b)

Figure 26 Simulated performance of the designed dual polarized ACP antenna versus frequency, compared with those of the single polarization design: a) S_{11} and S_{22} of the dual polarized design, compared with the matching of the one supporting single polarization, b) total broadside realized gain when only Port 1 is fed and when only Port 2 is fed, compared with that of the single polarization design.

To improve the performance of the dual polarization design, the size of the patch has been reduced from (4.4 x 4.4) mm^2 to (4.275 x 4.275) mm^2 in order to slightly shift its resonance to a higher frequency and the stub has been tuned in order to optimize the overall response of the antenna. The values of the final design can be appreciated in Table 8.

L_patch (mm)	Patch_sub _thickness (mm)	L_slot (mm)	W_slot (mm)	Line_sub _thickness (mm)	L_line (mm)	W_line (mm)	L_stub (mm)	W_stub (mm)
4.275	**2.4**	**5.2**	**0.35**	**0.18**	**8.2**	**0.2**	**1**	**0.28**

Table 8 Optimized dimensions of the parameters of the dual polarized ACP antenna shown in Figure 25 b).

The simulated reflection coefficients of the obtained design are shown in Figure 27 a) for both ports versus frequency and compared with the results of the initial design. As we can see, S_{11} is lower than -10 dB over the whole frequency range of interest, same thing for the S_{22} except for an increase at -8 dB at higher frequencies. The simulated S_{11} and S_{22} plotted on a Smith chart for both the initial and the optimized designs are illustrated in Figure 27 b) in the frequency range of interest at Ku-band.

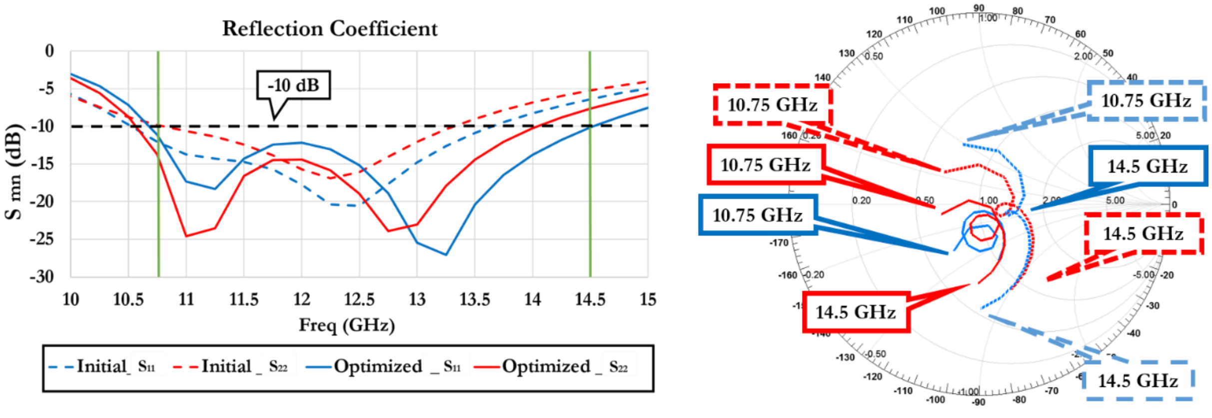

a) b)

Figure 27 a) Simulated S_{11} and S_{22} versus frequency at Ku-band, compared with those of the initial design, b) simulated S_{11} and S_{22} of the initial and the optimized designs on a Smith chart.

Figure 28 shows the simulated broadside realized gain and the directivity that we obtain for the optimized design when port 1 and port 2 are fed. Performance is pretty similar with a broadside realized gain staying between 4 and 5.8 dBi and a directivity oscillating around 6.3 dBi. The simulated radiation patterns for the realized gain are plotted in Figure 29 for the H- and E- planes at the lowest and highest frequencies of interest when port 1 and port 2 are fed. These simulations prove that the respective radiation patterns obtained when feeding the two ports are practically symmetric. It is interesting to underline this feature, taking into account how the feeding lines are accommodated on the first metal layer applying a position offset with reference to the center of the PCB board. The simulated 3-D radiation pattern of the realized gain obtained when feeding port 1 is plotted at 14.5 GHz in Figure 30 a) and b).

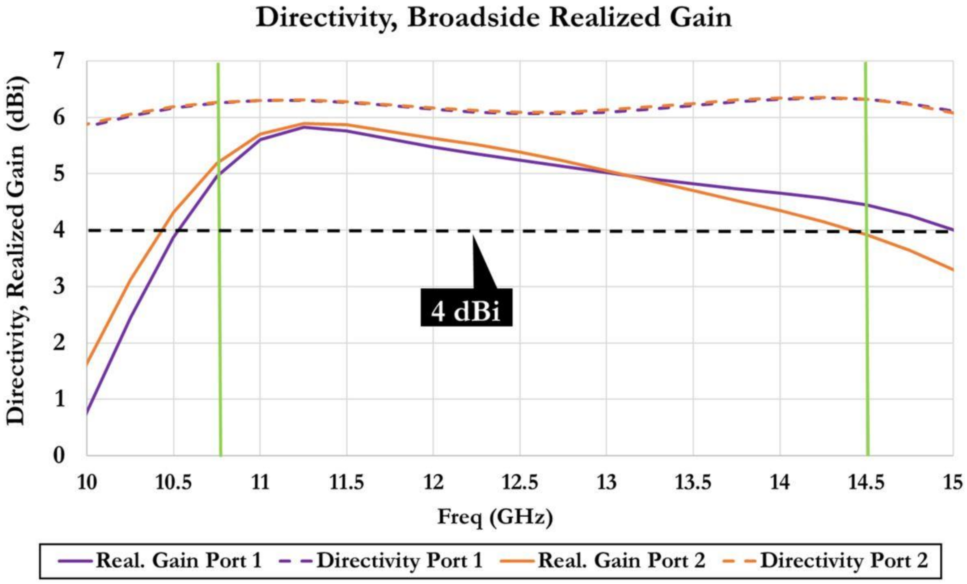

Figure 28 Simulated broadside realized gain and directivity versus frequency at Ku-band obtained when port 1 and port 2 are fed.

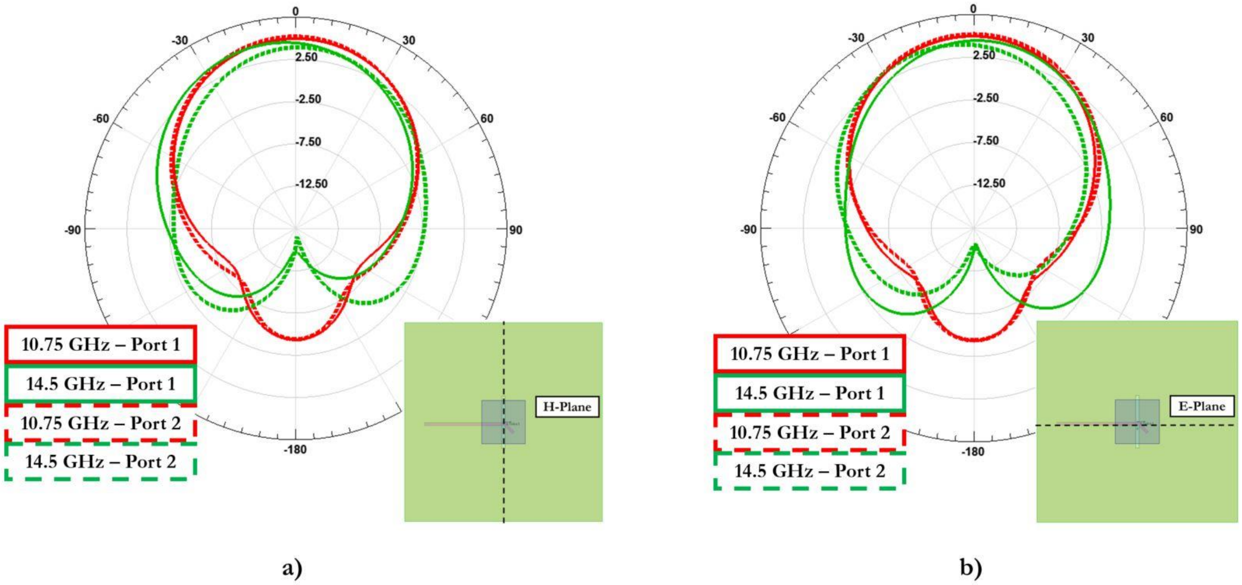

Figure 29 Simulated realized gain radiation patterns in dBi at 10.75 GHz and 14.5 GHz when feeding port 1 and port 2 : a) H-plane and b) E-plane.

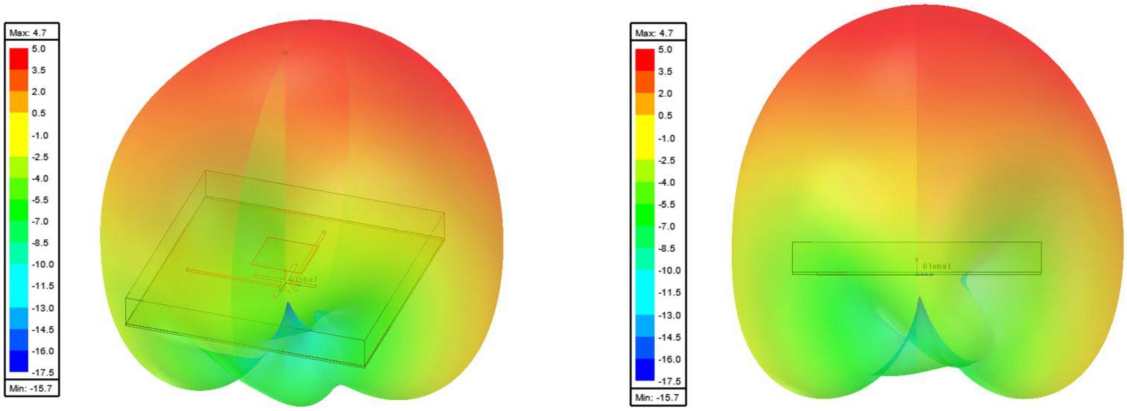

a)

b)

Figure 30 Simulated 3-D radiation patterns of the realized gain at 14 GHz when feeding port 1, in dBi: a) transparent isometric view, b) front-view.

II.3.3 Dual polarized design with connector pads

An Hirose HK-LR-SR2 connector is chosen in order to allow the connection and the test of the designed antenna, as shown in Figure 31 a). This connector has an operational bandwidth going from DC to 40 GHz, which makes it a suitable choice for both this design and those we are going to develop at Ka-band. This is an edge-mounted connector, as we can see in Figure 31 b), and it requires a pad and two screws to allow its integration , as depicted in Figure 31 c). The patterning of the connector pad , given by the manufacturer in Figure 31 c), fixes a coplanar waveguide (CPW) at the edge of the PCB and the dimensions of the ground pads. The use of the transmission line simulator in ADS allows to assess that the dimensions of the CPW are such as it offers ~100 Ω of characteristic impedance at the central frequency of 12.6 GHz in our case.

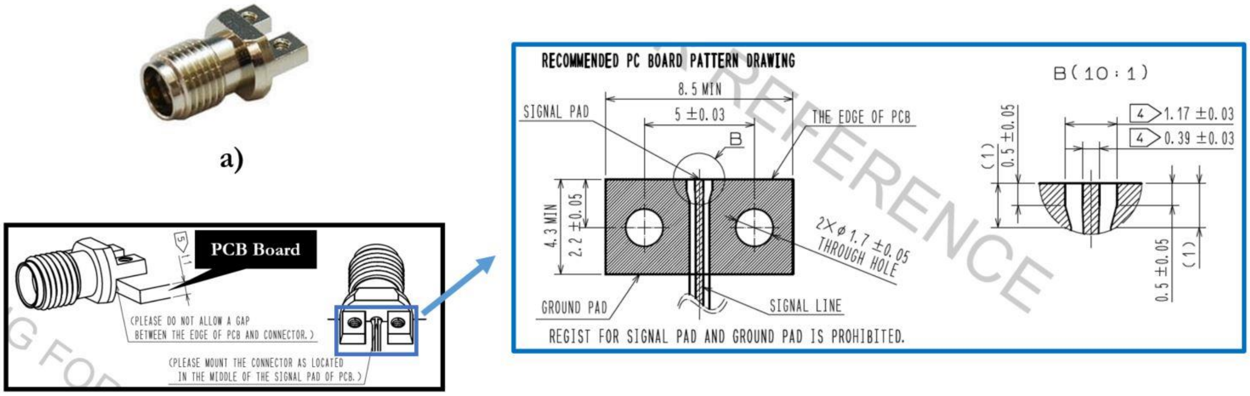

a)

b)

c)

Figure 31 Chosen edge-mounted HK-LR-SR2 connector, from [48]: a) connector picture, b) assembly scheme of the connector on the PCB, c) recommended pad patterning with dimensions in mm.

Starting from the mentioned constraints, the pad integration has to be properly designed in order to allow the integration of the connectors without deteriorating the overall performance of the antenna. The design of the pad is optimized using ADS and a quarter-wave impedance transformer is added : the CPW section fixed by the manufacturer is completed by 3.3 mm of grounded coplanar waveguide (GCPW), designed in order to offer ~75 **Ω** of characteristic impedance at the central frequency of 12.6 GHz, as we can see in Figure 32 a). Consequently, the model is drawn and simulated in HFSS, as illustrated in Figure 32 b): the ground plane is tapered in correspondence of the edge of the PCB in order to guarantee the functionality of the input coplanar waveguide and a series of VIAs is used to ground the connector pads. It is worth to underline that these VIAs are meant to be realized by laser and pass only through the substrate of the feeding line, in order to not interfere with the radiation of the patch at the edge of the PCB board. The simulated S_{11} and S_{21} of the connector pad, obtained from HFSS and ADS, are plotted versus frequency in Figure 32 c). The simulated matching in HFSS stays between -14 and -12.5 dB and the losses between 0.3 and 0.45 dB. A consistent difference is found between the two simulation results: the matching simulated in HFSS is ~5.5 dB better than the one resulting from schematic at 10.75 GHz. Such discrepancy may be explained by the fact that the schematic takes into account only a theoretical model of the transmission lines, simulated taking into account the thickness and the dielectric properties of our line substrate, as shown in Figure 32 a). On the other side, the HFSS model provides a series of VIAs that connect the pads to ground, which could not be taken into account in the schematic simulation, as shown in Figure 32 b). Simulations show that the position and the number of these elements can influence the impedance bandwidth of the overall design.

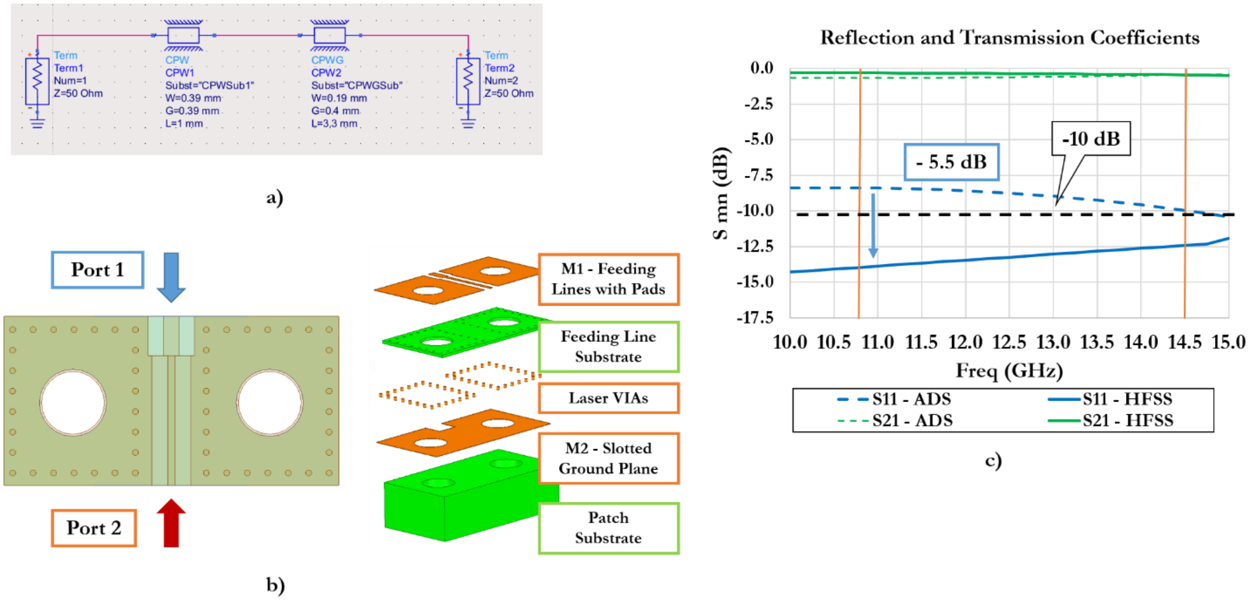

a)

b)

c)

Figure 32 a) ADS schematic of the designed pad for the connector, b) transparent top-view of the HFSS model of the pad for the connector with exploded stack-up, c) comparison of the results of the HFSS and schematic simulations of the connector pad: S_{11} and S_{21} are plotted versus frequency.

The achieved connector pad is integrated in the dual polarization design, as shown in Figure 33 a). A small section of microstrip line that offers 66 **Ω** of characteristic impedance at 12.6 GHz has been added in order to improve the matching, being highlighted in Figure 33 a). The simulated S_{11} and S_{22} plotted on a Smith chart versus frequency are illustrated in Figure 33 b). The simulated S_{11} and S_{22} of both the complete model and the model without pads are superimposed in Figure 34 a) versus frequency at Ku- band. It is interesting to notice that the final performance is improved in the central part of the band, while being deteriorated at the highest and lowest frequencies. This phenomenon can be explained taking into account that the matching of either the connector pads and that of the overall design has been optimized using various transmission lines dimensioned at the central frequency of the operational bandwidth. The simulated broadside realized gain of either the complete model and the model without pads are plotted versus frequency at Ku- band in Figure 34 b) when port 1 and port 2 are fed, respectively. The performance of the antenna with connector pads is deteriorated at lowest frequencies, where the realized gain obtained from feeding port 1 is decreased of a maximum of 1.7 dBi, and at highest frequencies, where the maximum decrease of the realized gain obtained from feeding port 2 is 2 dBi.

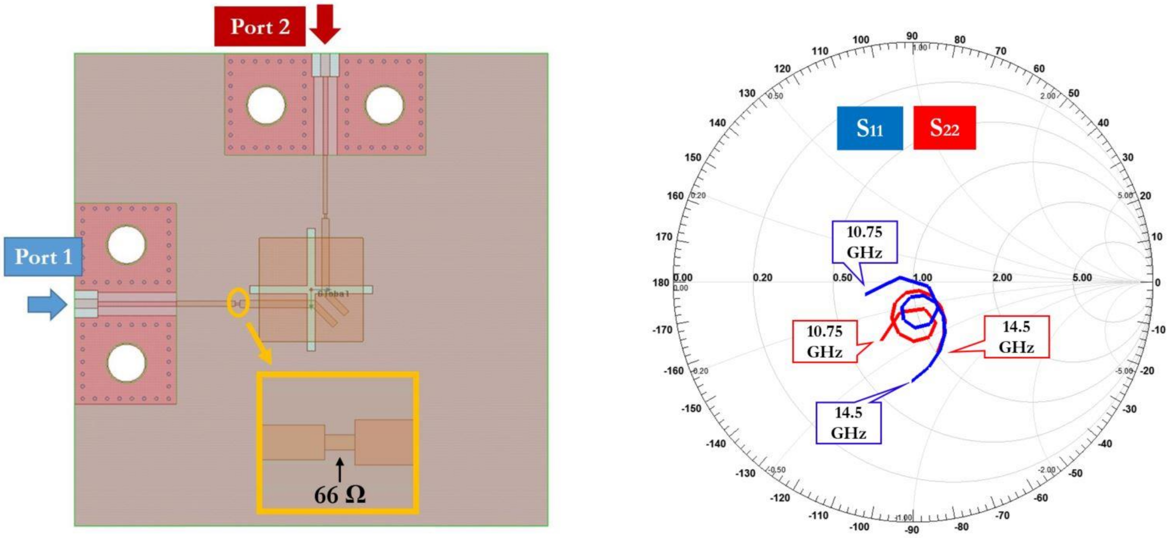

a)

b)

Figure 33 a) Transparent top-view of the complete dual polarized ACP antenna with connector pads and particular of the short line used to improve the matching, b) simulated S_{11} and S_{22} plotted on a Smith chart versus frequency at Ku- band.

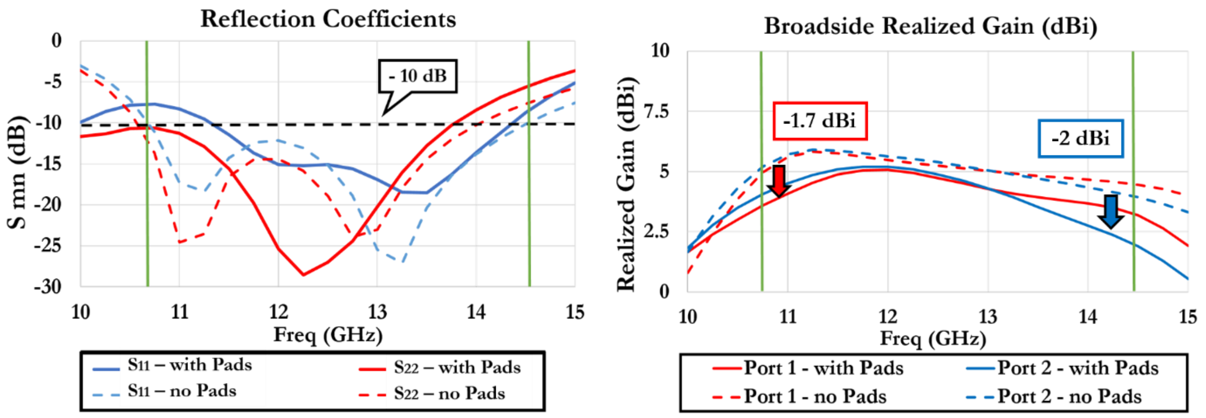

a)

b)

Figure 34 a) Simulated S11 and S22 of the complete model and the model without pads versus frequency at Ku-band, b) simulated broadside realized gain of the complete model and of the model without pads versus frequency at Ku- band when port 1 and port 2 are fed.

The stack-up of the design to be prototyped using a traditional PCB fabrication process is shown in Figure 35. Ten layers of metal can be appreciated: only three of them are needed for the antenna, while the others consist of dummies imposed by the fabrication constraints. 4 samples have been fabricated and the isometric view of one of them can be appreciated in Figure 36 a) , while the related top- and bottom-views are shown in Figure 36 b) and c), respectively.

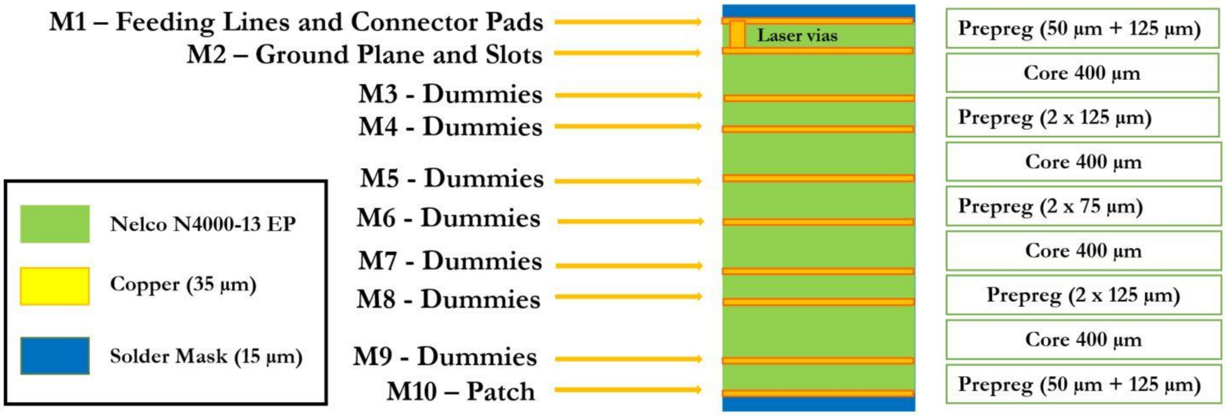

Figure 35 Stack- up for PCB prototyping.

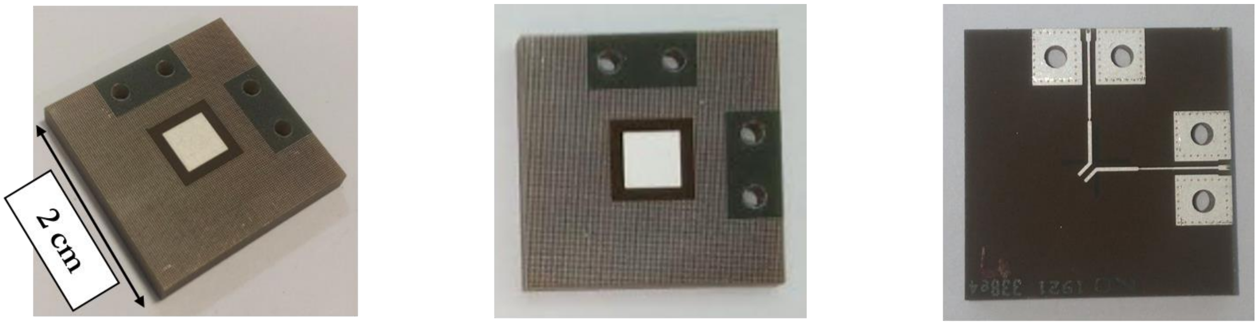

a) b) c)

Figure 36 Pictures of a fabricated sample: a) isometric-view, b) top-view, c) bottom-view.

.

II.3.4 Measurements

The measurement of the prototypes has been performed in the context of a collaboration with the University of Oviedo (Spain) leveraging the expertise of Prof. Jaime Laviada Martinez and Guillermo Alvarez Narciandi. The matching of the prototypes is measured using an Agilent PNA-X N5247A, from 10 GHz up to 15 GHz [49]. These results are shown and compared with simulation results in Figure 37 a), in terms of S_{11}, and b), in terms of S_{22}. A good agreement is achieved between simulations and measurements with values that remains lower than -10 dB for both ports along the whole bandwidth for most of the samples. We can appreciate the main differences between simulation and measurements around 10.8 GHz and 13.3 GHz for the S_{11} and at highest frequencies for the S_{22}. Such differences between simulations and measurements can be attributed to the presence of the connectors with their metal screws, as only the relative pads were considered in the simulations.

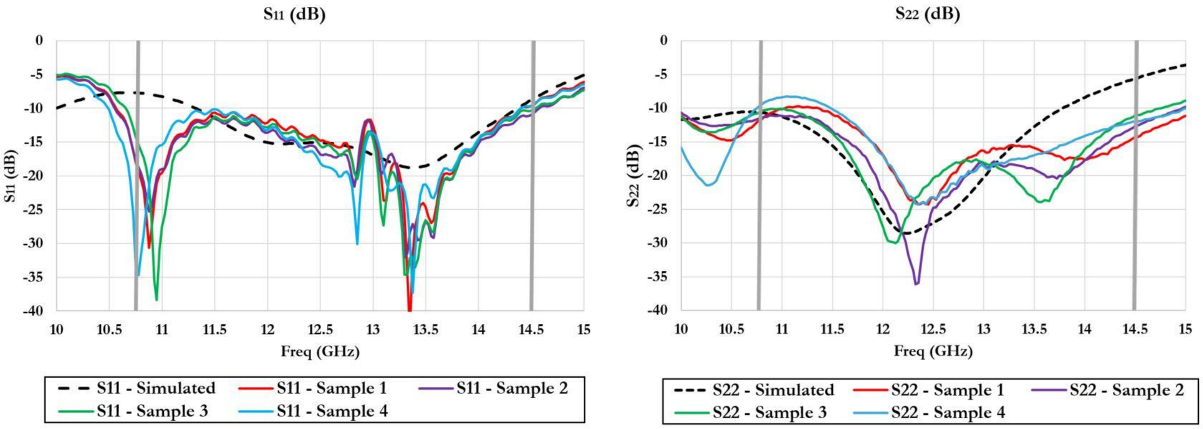

a) b)

Figure 37 Simulated and measured reflection coefficient of the prototypes versus frequency: a) S_{11}, b) S_{22}.

Figure 38 illustrates the simulated and measured levels of S_{ij} between the feeding lines, underlining that the poor port-to-port isolation represents a limitation for this kind of antenna configuration. We notice a very good agreement between measurements and simulations with the measured values of S_{12} and S_{21} that stay between -12.5 and -5.5 dB along the targeted operational bandwidth. Nevertheless, the isolation between the ports remains one of the major drawbacks of this design, considering that a commercial low-profile Sat-Com-On-The-Move user's terminal working at Ku-band can guarantee at least 25 dB of isolation between the polarizations [25]. The strong mutual coupling seems to be related to the use of two orthogonal feeding lines placed on the same metal layer [50].

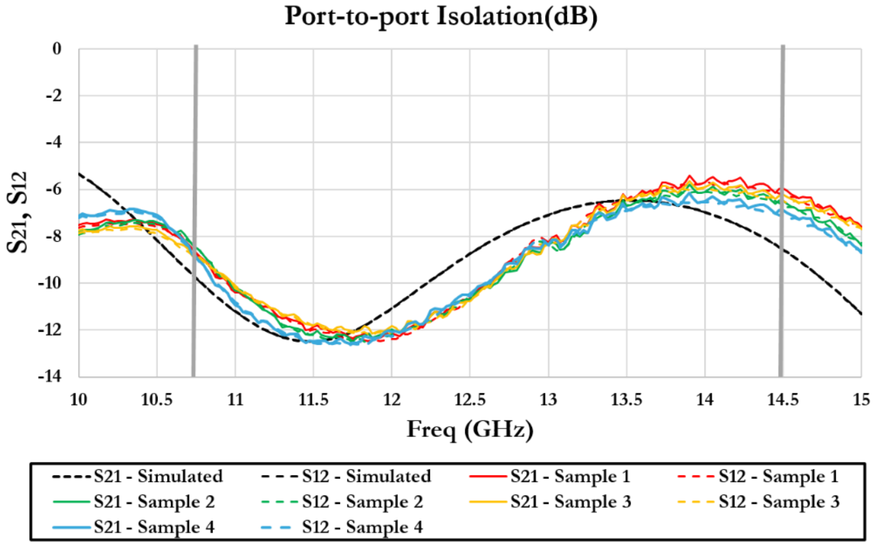

Figure 38 Simulated and measured Sij of the prototypes versus frequency.

The antennas are furtherly tested in an anechoic chamber in order to assess their performance in terms of gain and directivity versus frequency and acquire the realized gain radiation patterns at different frequencies. The anechoic chamber at the University of Oviedo implements a spherical range: the measurements are accomplished by placing the antenna under test (AUT) on a platform that allows rotations about two orthogonal axis, as shown in Figure 39. Considering the azimuth axis, the AUT positioner moves at a constant speed and the radiated field is acquired at a constant rate. This axis enables to measure different radiation patterns, corresponding to sweeps along the elevation angle θ of the spherical coordinates system. Considering the roll axis (still referring to Figure 39), the AUT positioner accomplishes a step scan. Thus, after each azimuth measurement, this positioner is turned a fixed amount and a new acquisition is performed. This axis usually matches the azimuthal angle φ of the spherical coordinates system. A third positioner is installed in the probe side, being used in order to turn the probe and allow to measure two orthogonal polarizations. A far field distance of 5 m is set between the antenna under test and the probe and the antennas are fixed on a foam support, backed by a panel of electromagnetic absorbers, as shown in Figure 40 a). Measurements are performed with a reference system where ϕ=0° is aligned with the feeding line of the port 1, as shown in Figure 40 b).

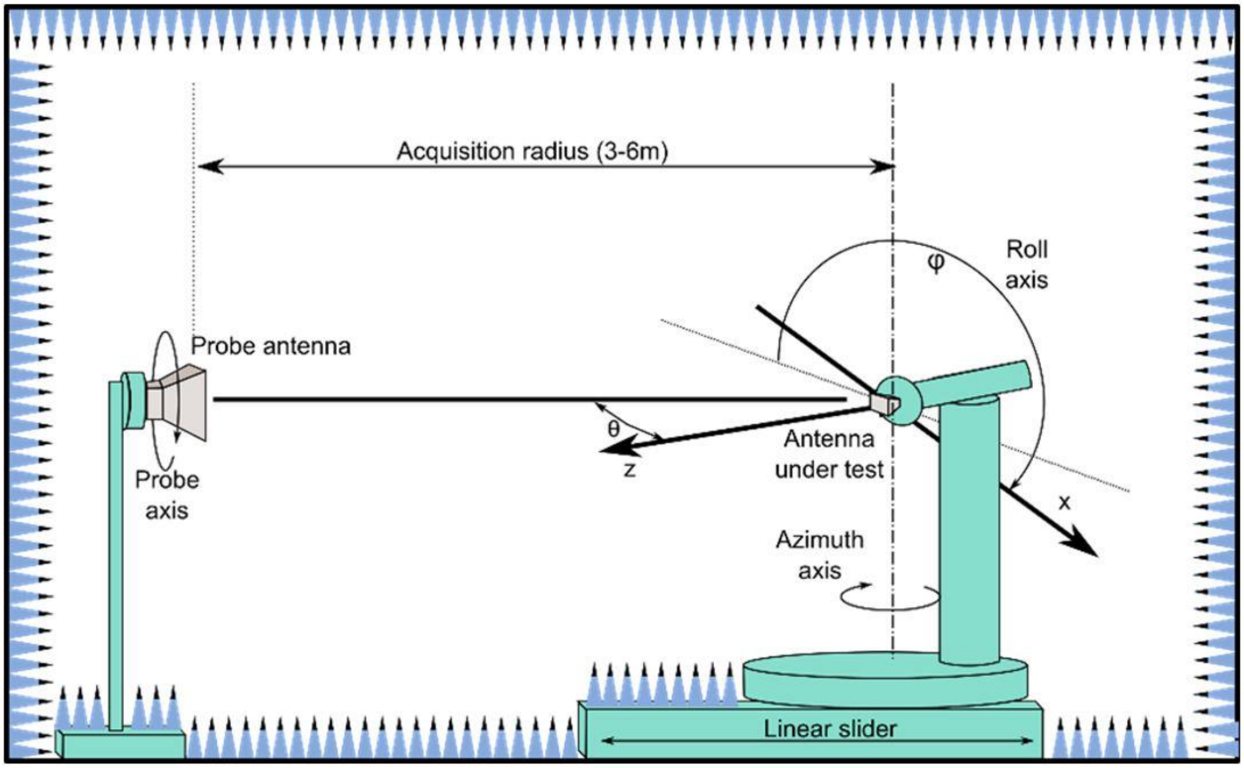

Figure 39 Scheme of the measurement setup in the anechoic chamber [Courtesy of the university of Oviedo and Prof. Jaime Laviada Martinez].

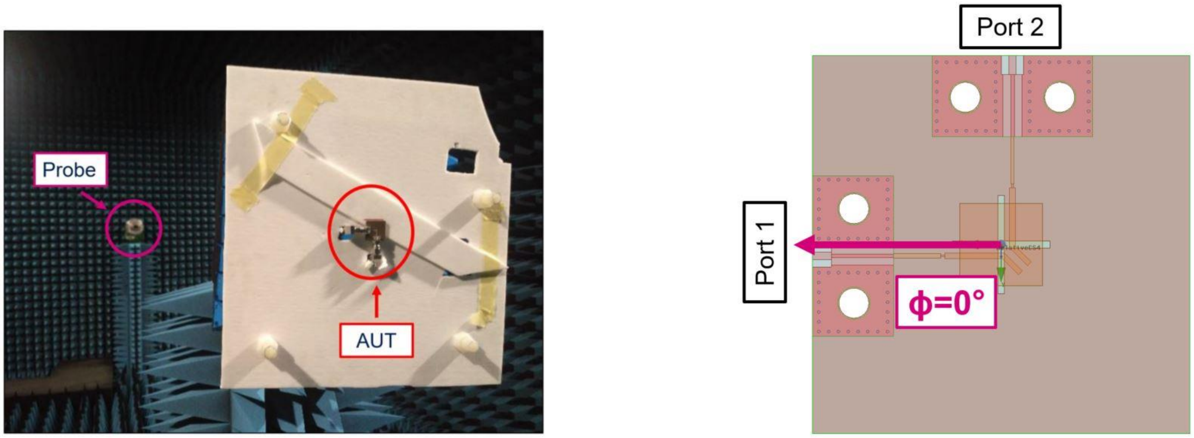

a) b)

Figure 40 a) Picture of the sample in the anechoic chamber, b) measured and simulated directivity of a sample versus frequency.

Figure 41 shows the comparison of the measured and simulated peak realized gain versus frequency including measurement uncertainty bars (±0.3 dB) for all the samples, when port 1 and port 2 are fed, respectively. Measured values are lower than simulated ones at lowest and highest frequencies. Considering the central part of the band of interest, the measured values are higher than simulated ones reaching a maximum difference of (1±0.3) dB around the central frequency of 12.6 GHz. These unusual results may suggest the possibility of having unwanted radiations (i.e. due to the resonance of a cable) or reflections in the anechoic chamber. Another hypothesis could be related to the accuracy of the HFSS model used for the simulations and will be verified later in this paragraph.

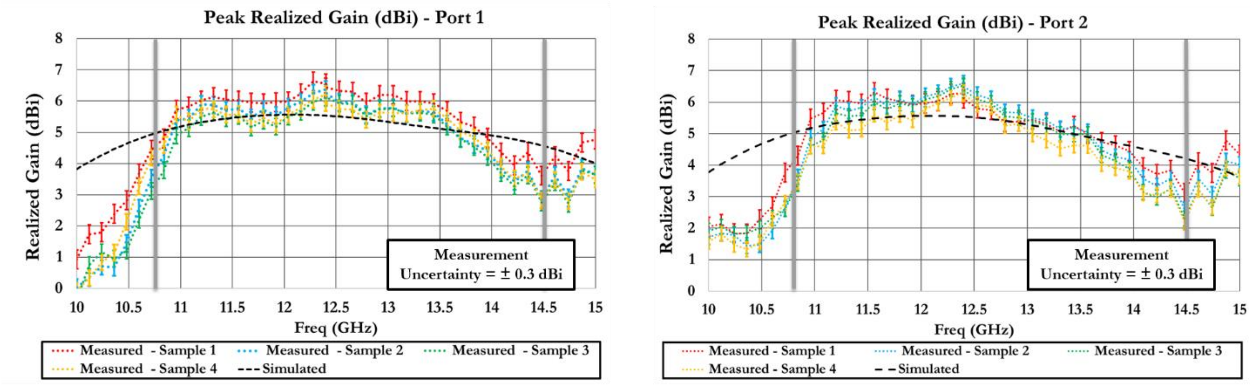

a) b)

Figure 41 Simulated and measured peak realized gain in function of frequency, including measurement uncertainty bars, obtained feeding: a) port 1, b) port 2.

Figure 42 and Figure 43 show the simulated and measured θ and ϕ components of the realized gain obtained when feeding port 1 for ϕ=0° and ϕ=90°, respectively, as a function of θ at 14 GHz. Only one measured sample is shown for sake of readability in both cases, this choice is justified by the fact that the measurements of the different samples are reproducible. As we can see, the measured radiation patterns result pointed away from the broadside direction, which can be partially attributed to the fact that the two feeding lines are offset from the geometric center of the PCB board creating a small intrinsic asymmetry within the structure. Moreover, the accentuated differences from the simulations suggest that these last are not accurately reproducing the real radiation patterns.

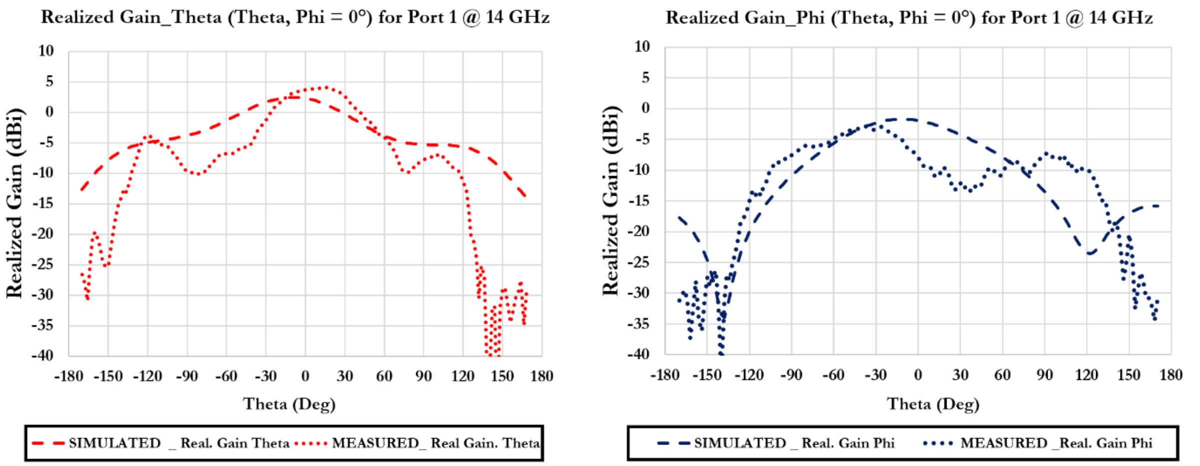

a) b)

Figure 42 Simulated and measured realized gain for ϕ=0° as a function of θ at 14 GHz, obtained feeding port 1: a) θ component, b) ϕ component.

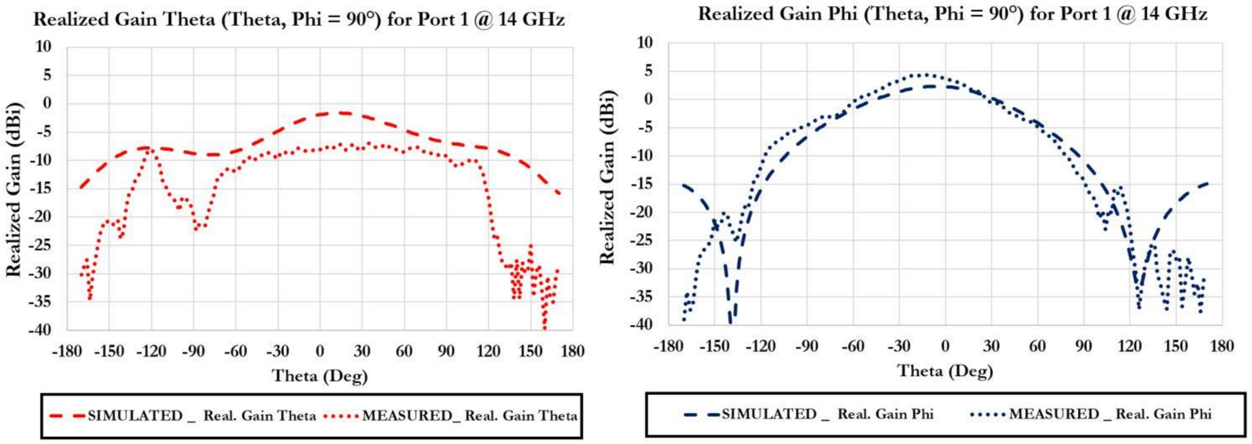

a) b)

Figure 43 Simulated and measured realized gain for ϕ=90° as a function of θ at 14 GHz, obtained feeding port 2: a) θ component, b) ϕ component.

Figure 44 and Figure 45 show the simulated and measured θ and ϕ components of the realized gain obtained when feeding port 2 for ϕ=0° and ϕ=90°, respectively, as a function of θ at 14 GHz. The behavior is pretty symmetric if compared to the previous, as expected due to the symmetry of the structure. The previous considerations about the measured beam de-pointing from the broadside direction remain valid, as well as the inaccuracy of the simulations in order to reproduce this phenomenon.

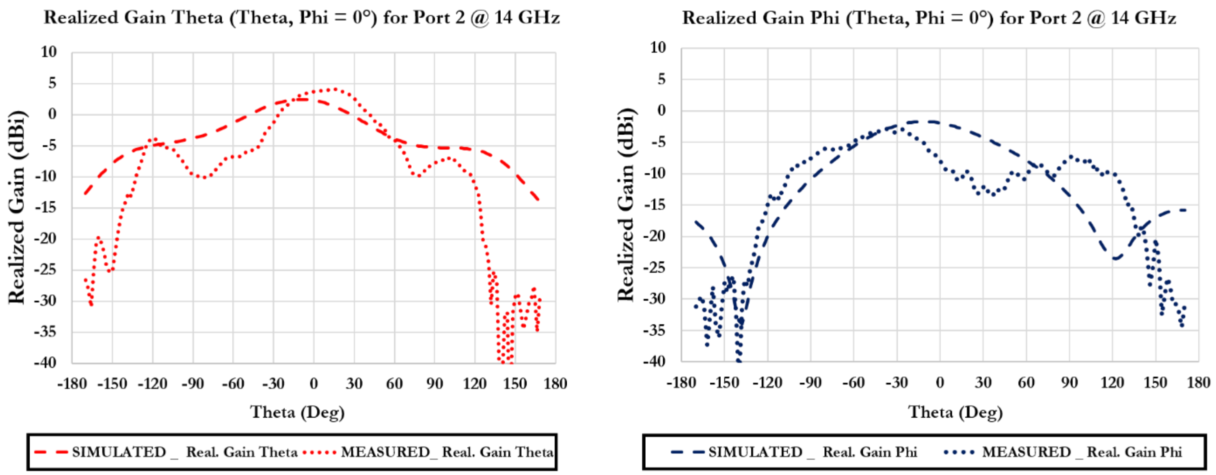

a) b)

Figure 44 Simulated and measured realized gain for ϕ=0° as a function of θ at 14 GHz, obtained feeding port 2: a) θ component, b) ϕ component.

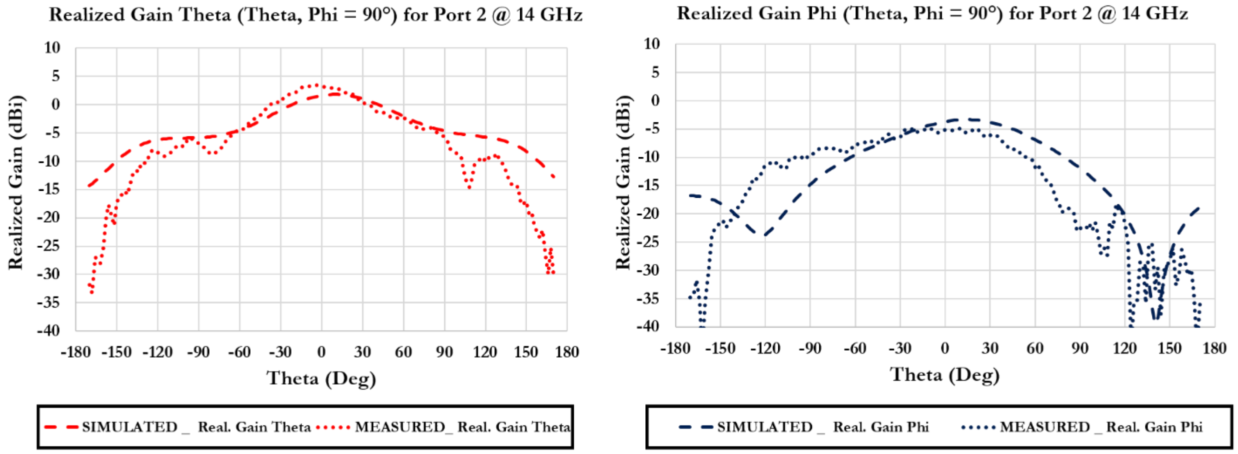

a) b)

Figure 45 Simulated and measured realized gain for ϕ=90° as a function of θ at 14 GHz, obtained feeding port 2: a) θ component, b) ϕ component.

The large bandwidth and the thickness of the patch substrate may have led to the excitation of surface waves that were not expected. The choice to simplify the simulated connectors model by including only their pad in the HFSS design was supported by the hypothesis that there were no surface waves travelling along the substrate that could cause unwanted interactions and radiations. Moreover, the space waves radiated by the patch may hit the connectors, being located in the near-field zone of the patch and create a secondary radiation source. Hence, we proceed modifying the design and using an encrypted model of the complete connector provided by the manufacturer, as shown in Figure 46. This last, in fact, accurately takes into account both the mechanic and electrical characteristics of the edge-mounted connector. Simulations confirm that the coaxial input port of the connector model, as provided by the manufacturer, offers 50 Ω of characteristic impedance at 12.6 GHz. Figure 47 shows the comparison of the measured data and the simulated ones concerning both the previous HFSS design with only the connector pads and the new one integrating the complete connector model, in terms of peak realized gain versus frequency. As we can see, the results of the two simulations differs both at lowest and highest frequencies suggesting that the connectors have an effect over the overall behavior of the antenna and the eventual impact of surface waves not taken into account in the initial simulations. Nevertheless, the new simulation is not capable to reproduce the measured data, suggesting that the measurement environment may also play a role generating effects that cannot be predicted by the simulations of the single antenna. Figure 48 and Figure 49 show the measured realized gain radiation patterns at 12 and 14.5 GHz, respectively, compared with the simulated ones concerning either the initial HFSS design integrating only the connector pads and the one with the complete connectors. The radiation patterns are given in terms of θ component of the realized gain as a function of θ, obtained in the plane ϕ=0° by feeding port 1 and ϕ component of the realized gain as a function of θ, obtained in the plane ϕ=90° when feeding port 1. As we can see, even the new simulations are not likely to reproduce the measured response of the antenna. Moreover, it is interesting to underline how the simulations integrating only the connector pads can fit the measurements for ϕ=90°.

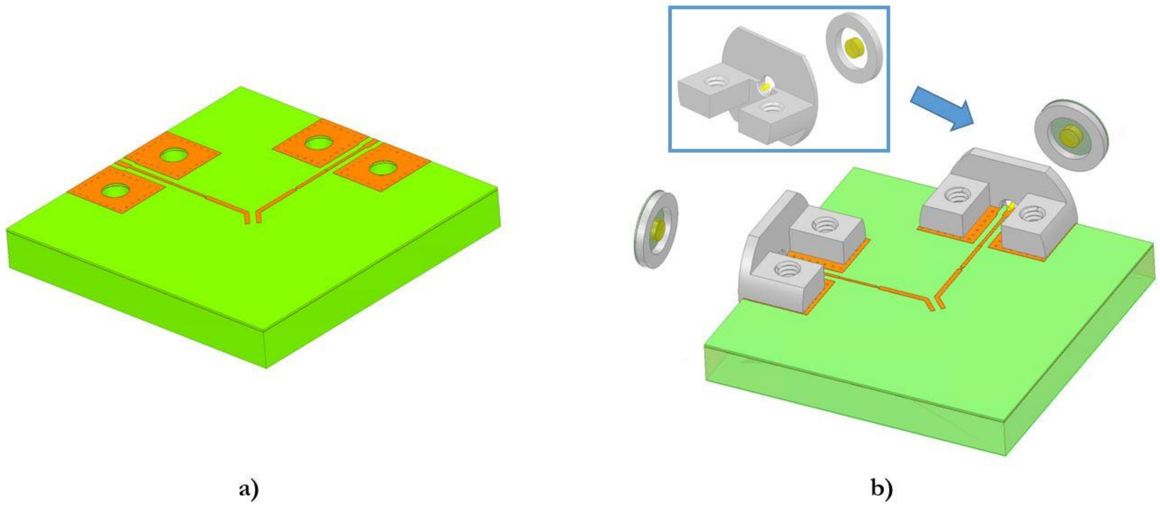
a) b)

Figure 46 a) Previous HFSS design containing only the connector pads: isometric view from feeding lines side, b) HFSS design with connectors pads and complete connector models (encrypted) from the manufacturer: isometric view from feeding lines side.

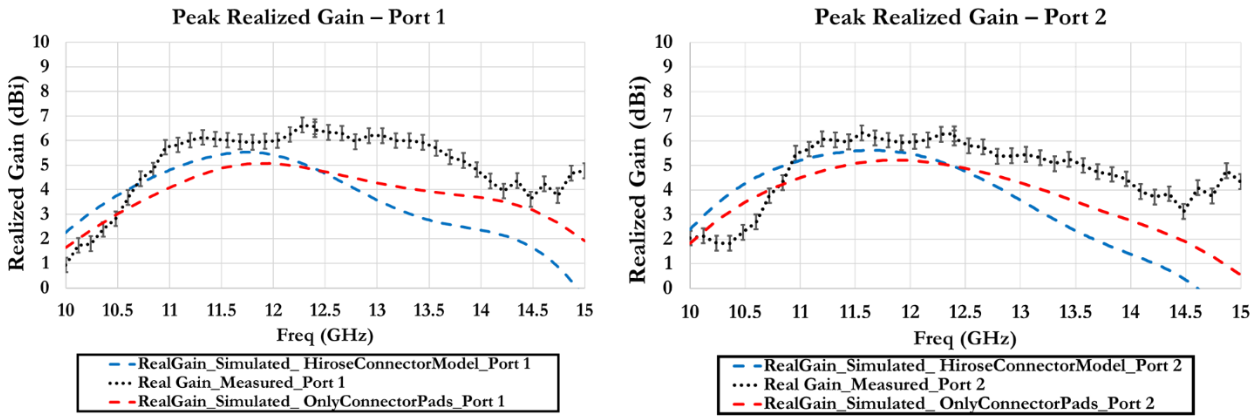

a) b)

Figure 47 Comparison of the peak realized gain versus frequency obtained from measurements (including uncertainty bars) and simulations either integrating only the connector pads and the complete connector models from the manufacturer, results are obtained feeding: a) port 1 and b) port 2.

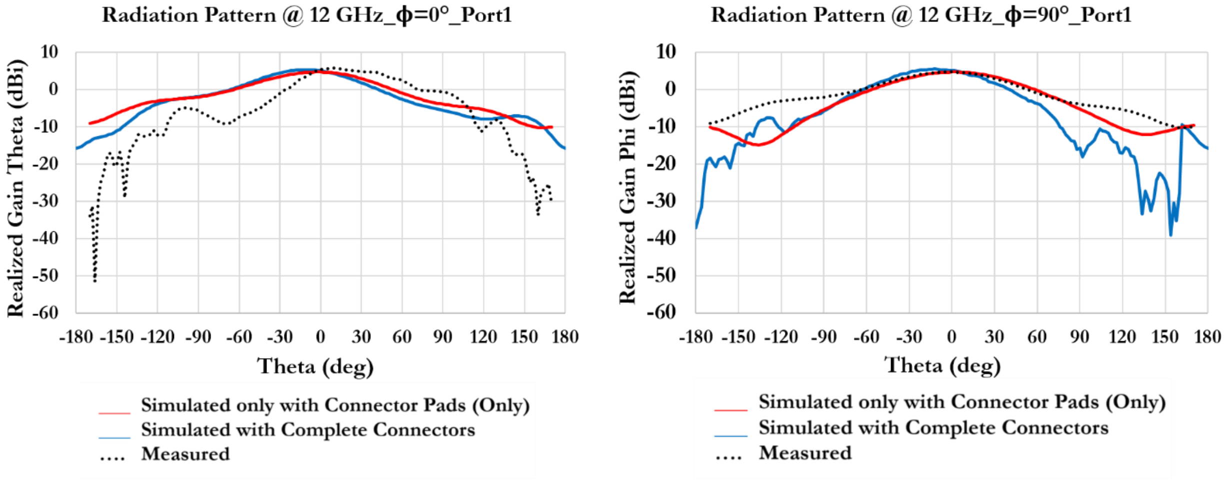

a) b)

Figure 48 Comparison of the measurements results and simulated ones concerning both the design integrating only the connector pads and the one integrating the complete connector model from the manufacturer, obtained when feeding port 1: a) θ component of the gain at 12 GHz as a function of θ in the plane ϕ=0°, b) ϕ component of the gain at 12GHz as a function of θ in the plane ϕ=90°.

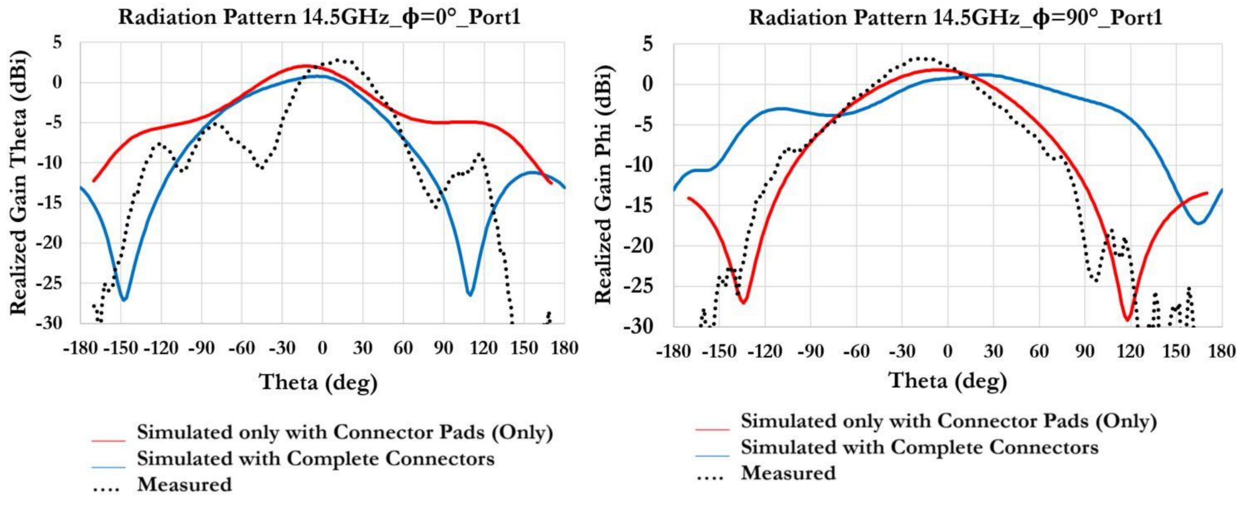

a) b)

Figure 49 Comparison of the measurements results and simulated ones concerning both the design integrating only the connector pads and the one integrating the complete connector model from the manufacturer, obtained when feeding port 1: a) θ component of the gain at 14.5 GHz as a function of θ in the plane ϕ=0°, b) ϕ component of the gain at 14.5 GHz as a function of θ in the plane ϕ=90°.

II.3.5 Benchmarking

Table 9 shows the benchmark of the designed antenna with the best reviewed planar wideband antenna working at Ku- band [39]. Using the same antenna configuration, we manage to support a second linear polarization. We leverage a traditional PCB fabrication process, which is very useful in the perspective of an eventual large-scale production, instead of a direct digital manufacturing process. The same stack-up thickness as the prototype from the reviewed paper is obtained [39].

Authors	Configuration	Polarization	-10 dB Impedance BW → Fractional BW	Min. Measured Broadside Realized Gain	Fabrication Process	Thickness
Kacar et al, 2017.	Aperture Coupled Patch	Single Linear	(12.5 – 18) GHz → (~30%)	3 dBi (along the -10 dB Impedance BW)	Direct Digital Manufacturing (Plastic polymers)	~ 2.4 mm
This work	Aperture Coupled Patch	Double Linear	(10.75 – 14.5) GHz → (~30%)	1.9 dBi (along the -10 dB Impedance BW)	Traditional PCB Fabrication	~ 2.4 mm

Table 9 Benchmark of this work with the best reviewed planar wideband antenna working at Ku-band [39].

II.4 Wideband Ka-band dual polarized microstrip aperture coupled patch antenna design

Fifty percent of fractional bandwidth is required for an antenna able to perform both in Rx and Tx for SOTM applications at Ka-band (18-31 GHz). As we have seen in [40], a planar antenna capable to offer such a wide operational bandwidth at Ka-band has already been proposed supporting a dual circular polarization. The drawback of this configuration was the complicated stack-up reaching a thickness of 4.6 mm and requiring a layer of foam plus a stacked patch. Moreover, the size of the antenna avoided its integration in an array. We target to design a wideband planar ACP antenna capable to cover the targeted bandwidth supporting a dual linear polarization using the simplest stack-up as possible while being compatible with a standard low-cost PCB fabrication process. The first step will be to present the design of an ACP antenna supporting a single linear polarization. The challenge of the Ka-band is that wide bandwidth and the use of relatively thick substrate leads to the excitation of surface waves at these frequencies. The technique applied in order to manage this phenomenon by creating a cavity in the patch substrate and an additional metal ring on the patch layer will be detailed. Hence, we discuss the integration of a second feeding line and a second slot in order to support a dual polarization and the integration of the connectors required for the measurement. The prototyping and the measurement are finally illustrated before concluding with the benchmarking of the performance of the proposed solution, compared to the state-of-the-art wideband planar antennas working at Ka-band.

II.4.1 Single polarization design

An initial ACP design is proposed in order to work in the (18 - 31) GHz frequency range using a NELCO 4000 – 13 Si EP substrate (ε_r =3.7, tg(δ) =0.009) and following a similar approach as the one described for the Ku-case. An initial single polarization design is proposed, whose transparent top-view can be appreciated in Figure 50 a). Its exploded stack-up is illustrated in Figure 50 b), where the different components and the main design parameters are detailed. The dimensions of the various design parameters are given in Table 10. The microstrip feeding line is dimensioned in order to offer 50 **Ω** characteristic impedance at the central frequency of 24.5 GHz over a thin substrate of 0.18 mm and the stub is optimized via simulation in order to achieve the best matching along the targeted wide operational frequency range. A square patch is used taking into account the goal to support a dual linear polarization, its dimensions and the related substrate thickness are chosen in order to obtain a resonance in the high part of the band around 27 GHz. The slot is made longer than the patch targeting to place its resonance in the lower part of the band, instead. This choice takes into account the excitation of SWs and the will to design a cavity and a ring working at high frequencies in order to constructively manage them, as we detail in the next paragraph. The dimensions of both the slot and the patch are furtherly optimized via simulations in order to improve the performance of the antenna along the wide band. Similarly, to what we have seen for the development at Ku-band, the electromagnetic behavior of the structure is such as the two resonances are intrinsically coupled and they cannot be independently modified.

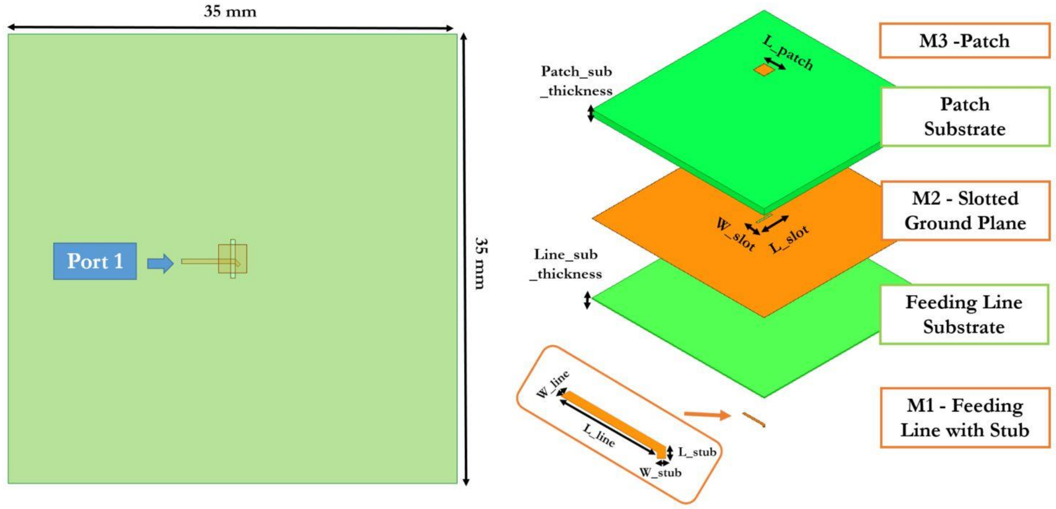

a) b)

Figure 50 Designed ACP antenna working at Ka-band and supporting single polarization: a) transparent top-view, b) exploded stack-up detailing the different components.

L_patch (mm)	Patch_sub _thickness (mm)	L_slot (mm)	W_slot (mm)	Line_sub _thickness (mm)	L_line (mm)	W_line (mm)	L_stub (mm)	W_stub (mm)
2.2	**1.2**	**3**	**0.35**	**0.18**	**4**	**0.37**	**0.6**	**0.3**

Table 10 Dimensions of the design parameters of the ACP antenna working Ka-band shown in Figure 50 b).

The use of a thick substrate for the patch leads to the excitation of surface waves as we will detail in the next paragraph, so the size of the PCB board becomes the first design parameter we can leverage in order to manage this phenomenon. The chosen size is almost the double of the one used in the Ku-case, moving from (20 * 20) mm^2 to (35 * 35) mm^2. This size has been fixed via simulation, representing an optimum trade-off between form factor and performance, as illustrated in Figure 51 where we show the simulated broadside realized gain for different PCB sizes versus frequency. The simulated matching and total efficiency of the antenna designed over the (35 * 35) mm^2 board are plotted versus frequency in Figure 52 a). The reflection coefficient stays below -5 dB over most of the bandwidth with an increase at highest frequencies up to -3 dB. The total efficiency is above the 70% moving down to 50% at the highest frequencies of the bandwidth. Figure 52 b) shows the simulated broadside realized gain versus frequency, staying between 3 and 7.5 dBi while directivity stays between 4 and 9 dBi, except for a consistent drop around 24.5 GHz. The origin of this behavior can be found in the mentioned generation of surface waves that propagate in the patch substrate towards the edges of the board, evidenced by the plot of the magnitude of the simulated H-field at 24.5 GHz in the patch substrate in Figure 53 a). The radiation of the SWs when they meet the edges of the substrate produces ripples in the radiation pattern, as illustrated by the 3-D plot of the simulated realized gain at 24.5 GHz given in Figure 53 b) and c). The amount of generated SWs can be adjusted by a proper choice of the substrate thickness and this phenomenon can be leveraged in a constructive way from radiation's perspective in order to enlarge the gain operational bandwidth of the antenna as we detail in the next sub-paragraph.

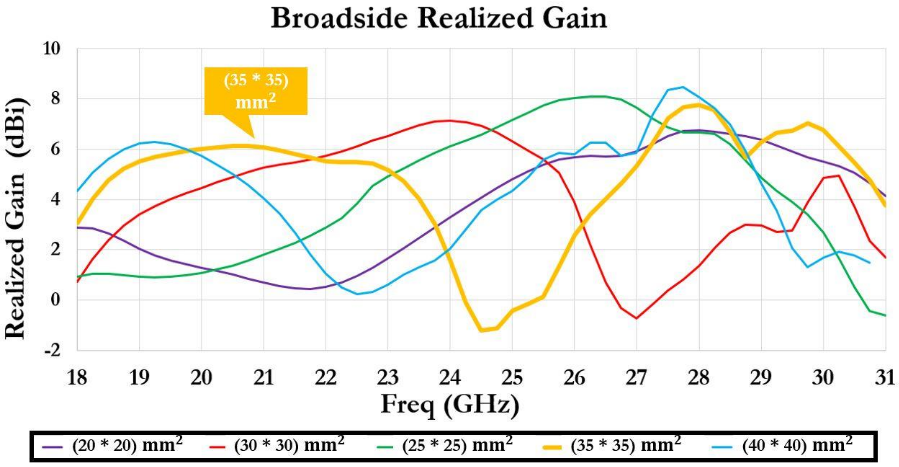

Figure 51 Simulated broadside realized gain of the design shown in Figure 50 with the dimensions given in Table 10 versus frequency, for different PCB sizes.

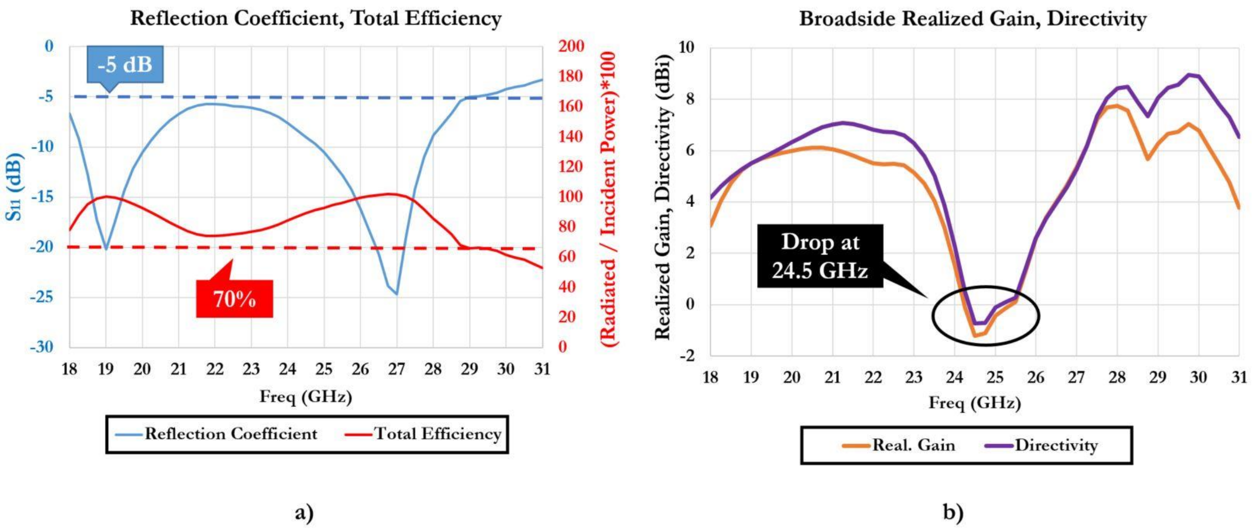

a)

b)

Figure 52 Simulated performance of the designed ACP antenna working at Ka-band with (35*35) mm^2 PCB versus frequency: a) reflection coefficient, total efficiency, b) broadside realized gain, directivity.

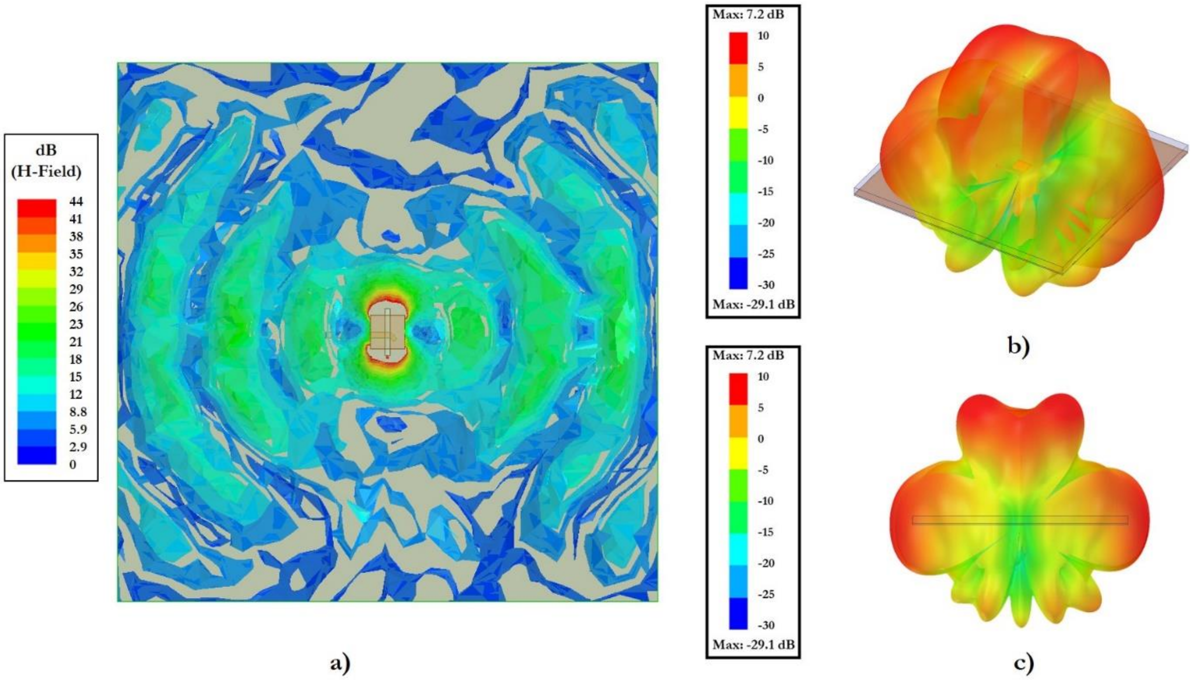

Figure 53 a) Simulated magnitude of the H-field in the patch substrate at 24.5 GHz evidencing the presence of surface waves propagating towards (and back from) the edge of the PCB, 3-D radiation pattern of the realized gain in dBi at 24.5 GHz: b) isometric view, c) front-view.

II.4.2 Surface wave generation and use of a cavity and a metal ring

Surface waves can be generated when a wave propagating in a dielectric medium impinges at the interface with another one that is characterized by a lower dielectric constant ($\varepsilon_1 > \varepsilon_2$), as shown in Figure 54 a). In this case a critical incidence angle (θ_c) for which a total reflection is obtained can be derived from the third law of Snell-Descartes, as shown in Figure 54 b). Considering our case, the total reflection can occur at the interface between the patch substrate ($\varepsilon_1 = 3.7$) and the air ($\varepsilon_2 = 1$). The wave impinging at this interface with an angle equal or greater than the critical one undergoes a total reflection, being trapped between the metal ground plane and the air and creating a surface wave. The SW propagates inside the patch substrate and travels toward the PCB edge where it is partly radiated and partly reflected back, as shown in Figure 55. The degenerative effects of these unwanted radiations can be appreciated in the 3-D plot of the simulated realized gain of the ACP antenna working at Ka-band, previously given in Figure 53 b) and c).

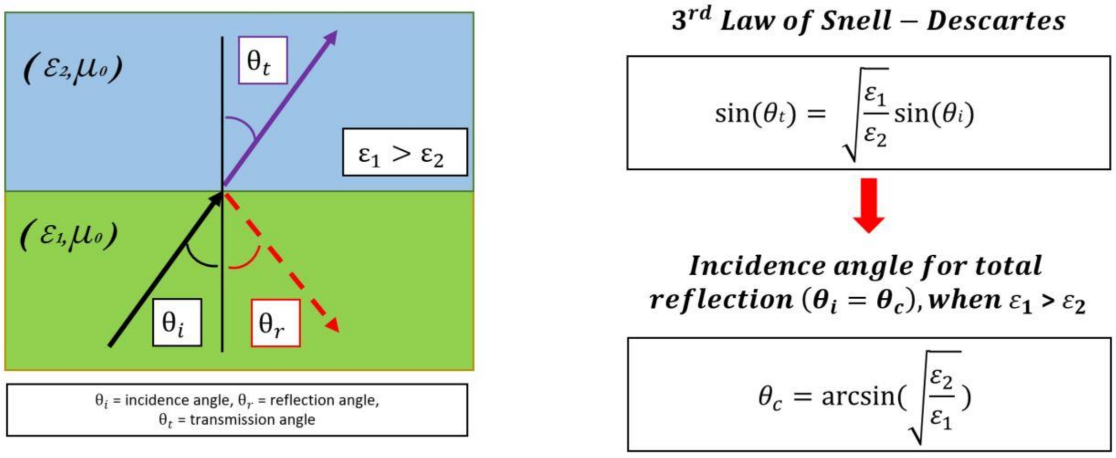

a) b)

Figure 54 a) Example of a wave traveling from a higher to a lower dielectric constant medium, b) third law of Snell - Descartes and derivation of the critical incidence angle generating the total reflection when $\varepsilon_1 > \varepsilon_2$.

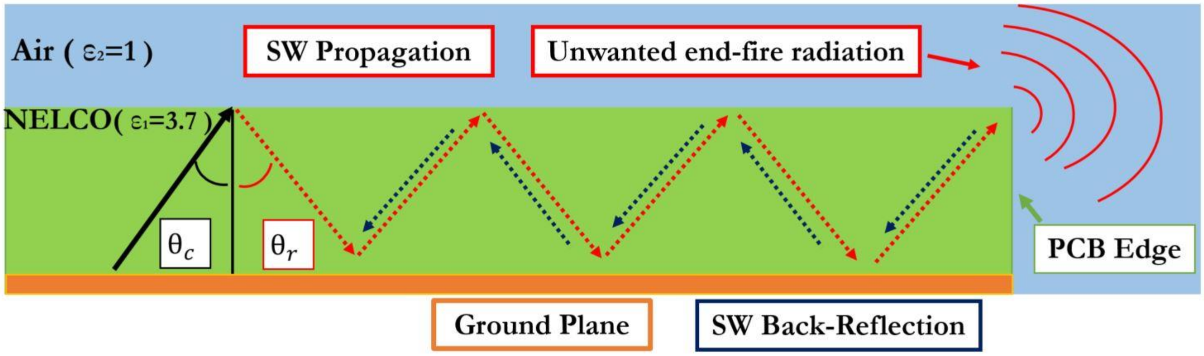

Figure 55 Example of the total reflection at the interface between the patch substrate and the air with propagation of the surface wave toward the PCB edge, producing unwanted end-fire radiation and back-reflection.

The conventional approach is to avoid the generation of the SWs using a thin or low permittivity substrate or to suppress them by the use of an electromagnetic bandgap substrate, a series of pin or different techniques [51] [52]. The possibility to use the SWs in a constructive way has been proven in [53], [54] and [55]. The idea is to keep a thick substrate such as the surface waves are generated and then create a cavity inside the patch's substrate in order to stop them from propagating towards the PCB edges. The next step is to redirect them to an additional metal ring placed on the patch metal layer, this ring will be further acting as an additional resonator. The opportune dimensioning of the cavity and ring allows to enlarge the operational bandwidth of the antenna. Different surface wave modes can be excited along the patch substrate whose normalized propagation constants can be calculated following the method given in [53]. The normalized propagation constants of the lowest 4 surface wave modes in the patch substrate with ground plane are computed in Matlab according to the method given in [53]. The results are plotted in Figure 56 a) as a function of the thickness of the substrate, normalized to the central wavelength at 24.5 GHz. As we can see, our working point is such as only the TM_0 mode seems to be excited. Figure 56 b) shows the simulated magnitude of the H-field in the patch substrate at 24.5 GHz, illustrating the direction of propagation of the TM_0 SW mode towards its edges.

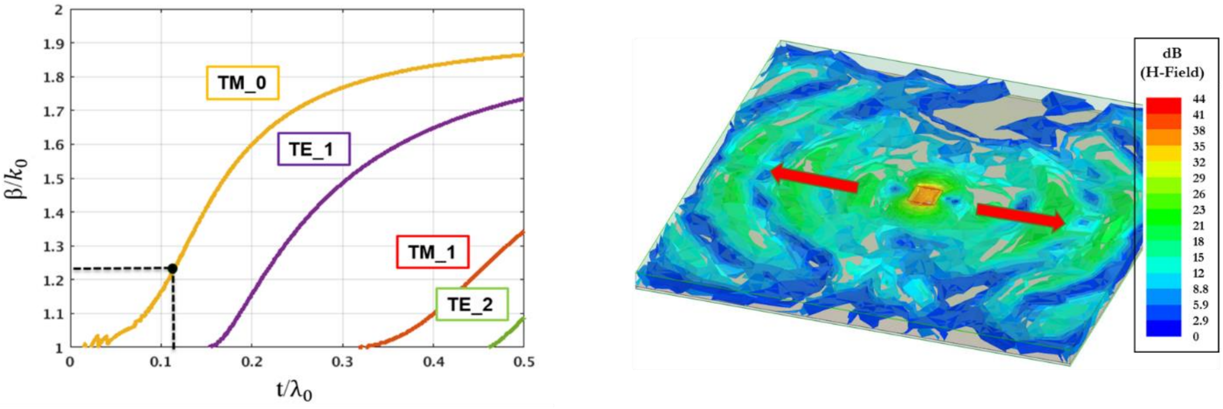

a)

b)

Figure 56 a) Computed normalized propagation constants of the surface wave modes in a substrate with ground plane as a function of the thickness of the substrate, normalized to the central wavelength(the operational point corresponding to our case is indicated), b) simulated magnitude of the H-field in the patch substrate at 24.5 GHz, highlighting the direction of propagation of the TM_0 SW mode.

The exploded stack-up of the antenna with the cavity and the ring is shown in Figure 57 a), the square cavity is realized by VIAs passing through all the PCB layers and it can be appreciated in Figure 57 b). The first layer of metal comprising the patch and the ring is illustrated in Figure 57 c). The cavity length and the width of the ring represent the most important design parameters in this case. The first one is optimized by simulation in order to maximize the directivity of the antenna at 30 GHz. The width of the ring is dimensioned in order to collect surface current in-phase with those of the patch at this frequency following the method given in [53]. Once these dimensions are fixed, the patch size is slightly increased in order to bring its resonance to lower frequencies in correspondence of the central part of the band. The final dimensions of the various design parameters are given in Table 11.

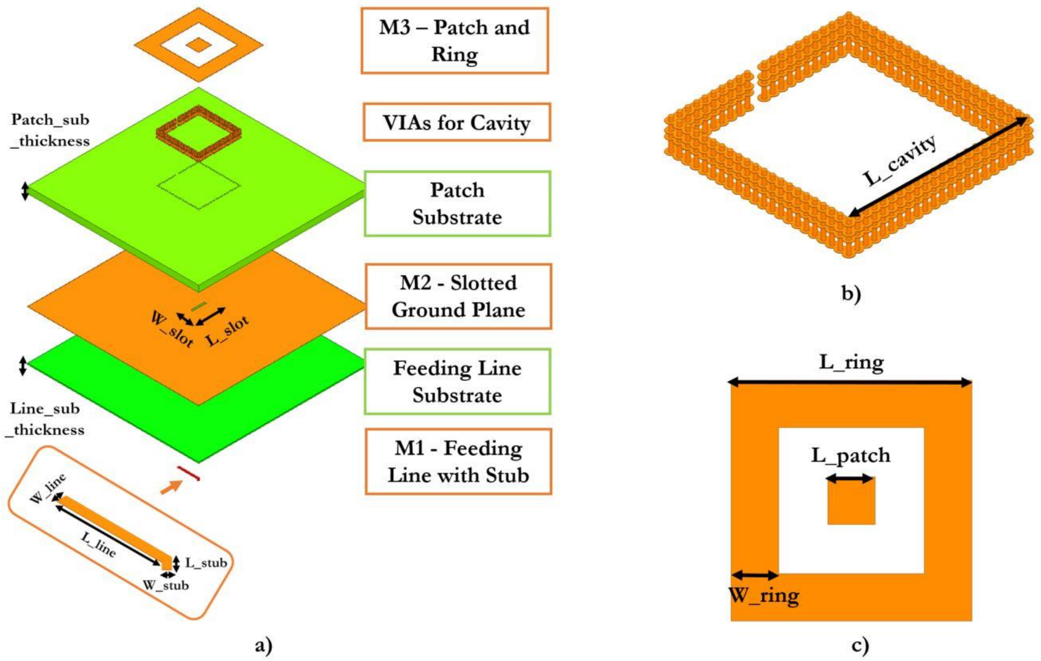

Figure 57 Single polarization ACP antenna with cavity and ring designed to operate in Ka-band: a) exploded stack-up, b) isometric view of the VIA series for cavity, c) top-view of the patch with metal ring.

L_patch (mm)	Patch_sub _thickness (mm)	L_slot (mm)	W_slot (mm)	Line_sub _thickness (mm)	L_line (mm)	W_line (mm)	L_stub (mm)	W_stub (mm)	L_cavity (mm)	L_ring (mm)	W_ring (mm)
2.6	**1.25**	**2.8**	**0.35**	**0.2**	**4**	**0.37**	**0.6**	**0.3**	**13.2**	**8.4**	**2.6**

Table 11 Dimensions of the main design parameters of the single polarization ACP antenna with ring and cavity, as depicted in Figure 57.

The simulated broadside realized gain and directivity are plotted versus frequency at Ka-band in Figure 58 for both the achieved design with cavity and ring and the previous one. As we can see, the performance is strongly improved around 24.5 GHz: the directivity is increased by 9 dBi and the broadside realized gain by about 8.2 dBi. Moreover, the directivity of the design with cavity ring results almost flat in the rest of the bandwidth with values that are increased of 2 up 3 dB, if compared to the initial ones. A similar behavior is observed in terms of realized gain starting from 19.5 GHz, with an increment of 0.5 up to 3.5 dB if compared to the initial values. The magnitude of the H-field is plotted inside the patch substrate at this frequency in Figure 59 for both the designs. The cavity cannot completely block the surface waves from propagating outside itself, but drastically reduces the amount of them that travels towards the PCB edges. Figure 60 shows the comparison of the 3-D radiation patterns of the two designs, with and without cavity, in terms of realized gain at 24.5 GHz. The use of the cavity solves the problem of the unwanted radiated lobes caused by the diffraction of the surface waves at the edges of the PCB. It is worth to underline that the resulting 3-D radiation pattern is analog to that of a traditional microstrip patch antenna.

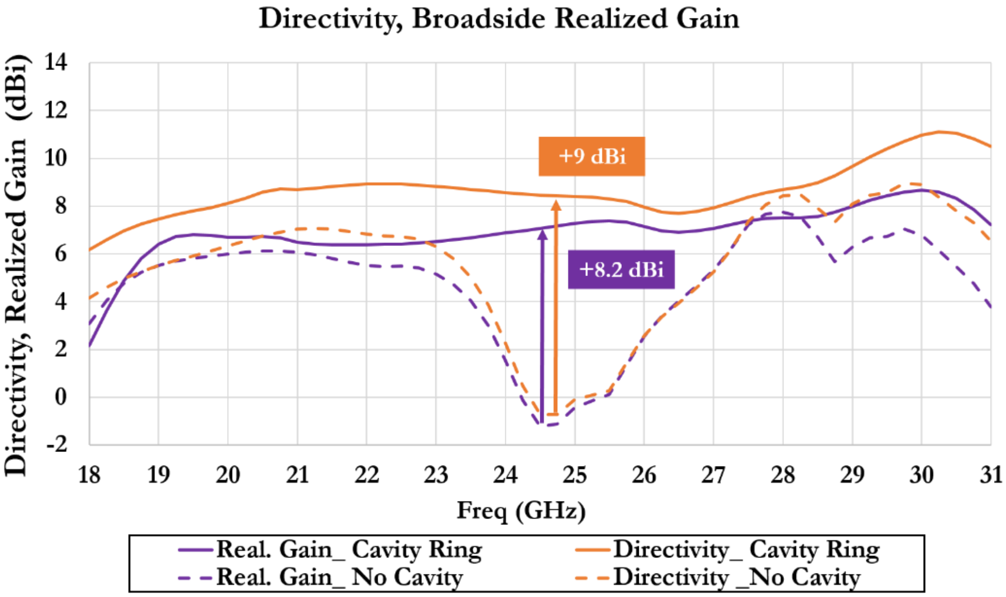

Figure 58 Simulated broadside realized gain and directivity of the designed ACP antenna with and without cavity and ring, versus frequency at Ka-band.

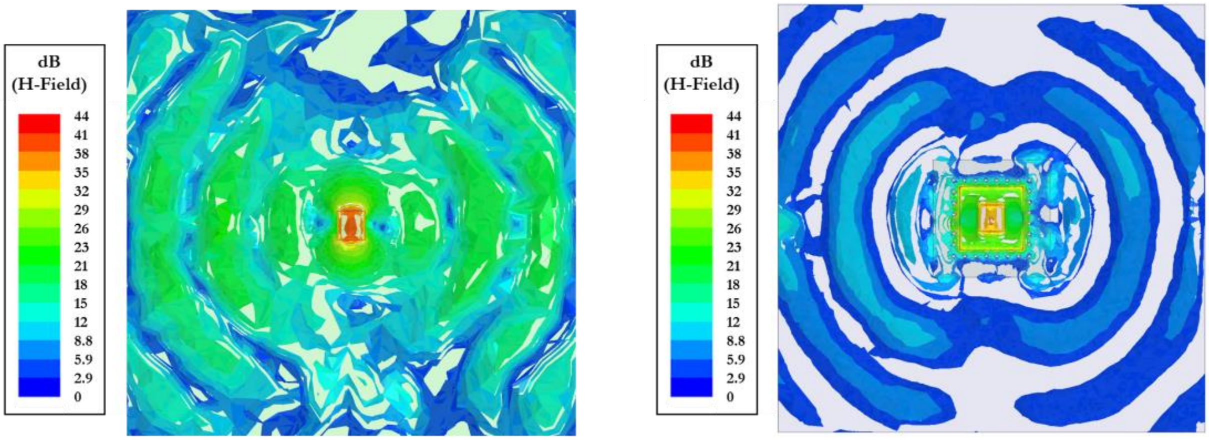

a)

b)

Figure 59 Simulated magnitude of the H-field in the patch substrate at 24.5 GHz for: a) design without cavity and ring, b)design with cavity and ring.

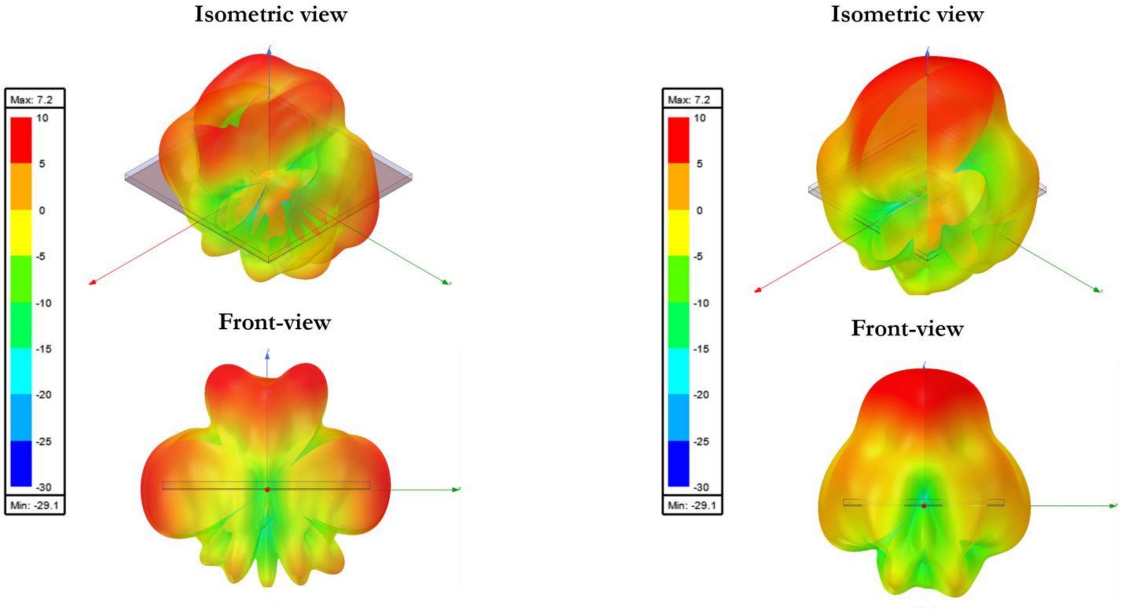

a) b)

Figure 60 3-D radiation pattern of the realized gain in dBi at 24.5 GHz: a) design without cavity and ring, b) design with cavity and ring.

II.4.3 Dual polarized design with connector pads for fabrication

The obtained design with cavity and ring is modified by adding a second feeding line and a second slot, in order to support a dual linear polarization. Following the method given in [42], the second feeding line is buried inside the feeding line's substrate in order to alleviate the mutual coupling between the lines that would deteriorate the performance of the ACP antenna at these frequencies. Envisaging the use of the same Hirose HK-LR-SR2 connectors used for the Ku- case, a proper connector pad is designed following the same method applied to develop the Ku- connector pads [48]. The connector pads are placed on the first metal layer and connected to ground by series of VIAs. Figure 61 a) shows the transparent top-view of the final antenna, while its exploded stack-up is illustrated in Figure 61 b).The buried microstrip line is connected to a section of microstrip line at the output of the related connector pad on the first metal layer by the use of a VIA to be realized by the use of a laser, as shown in the particular of Figure 61 a). Figure 62 shows the simulated S_{11} and S_{22} plotted on a Smith chart versus frequency. Figure 63 a) shows the simulated reflection versus frequency for the two input ports and their isolation. The matching oscillates around -10 dB for both ports increasing to -3 dB around 18 and 29 GHz. The port-to-port isolation stays below -15 dB along the whole bandwidth, except for an increase at -7 dB around 18 GHz. Figure 63 b) illustrates the simulated broadside realized gain and directivity, highlighting that performance is strongly deteriorated below 19.25 GHz. Excluding this part of the band from the current analysis, the directivity stays between 5.2 and 8.2 dBi and broadside realized ranges from 2 up to 5.43 dBi.

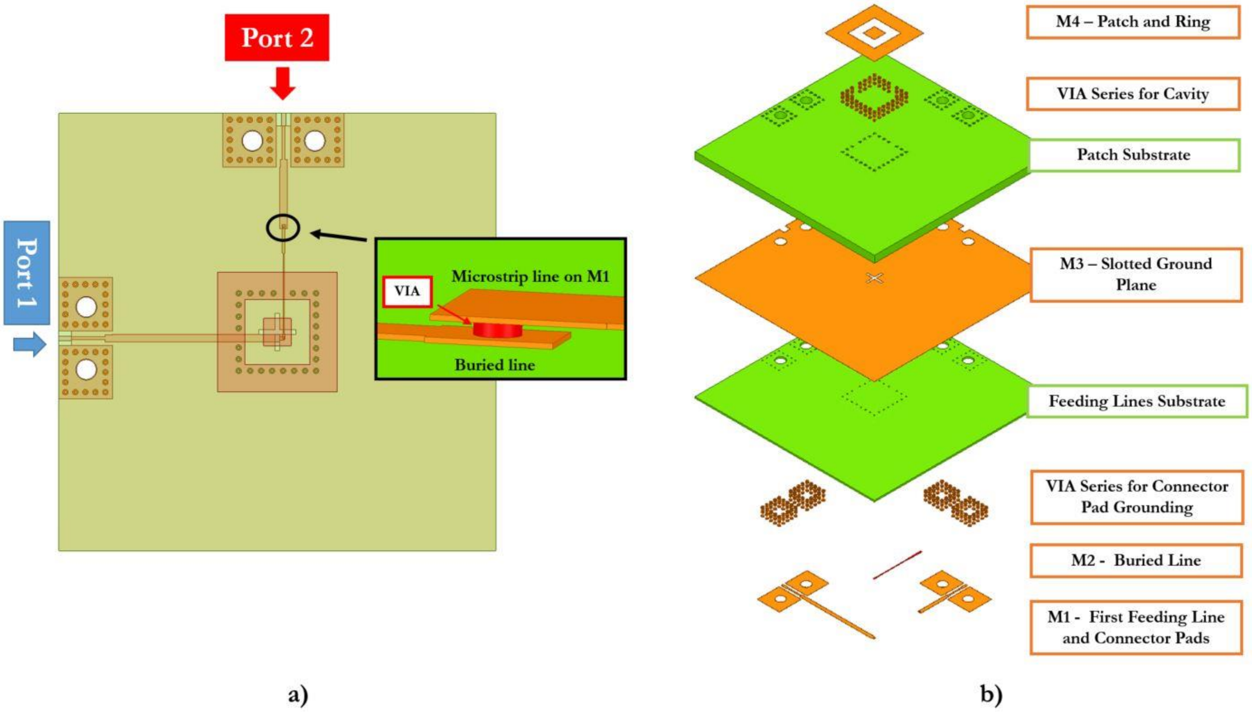

Figure 61 Dual polarized ACP antenna with connector pads working at Ka-band: a) transparent top-view with particular of the connection of the buried feeding to the output of the second connector pad first metal layer by the use of a VIAs, b) exploded stack-up detailing the various layers.

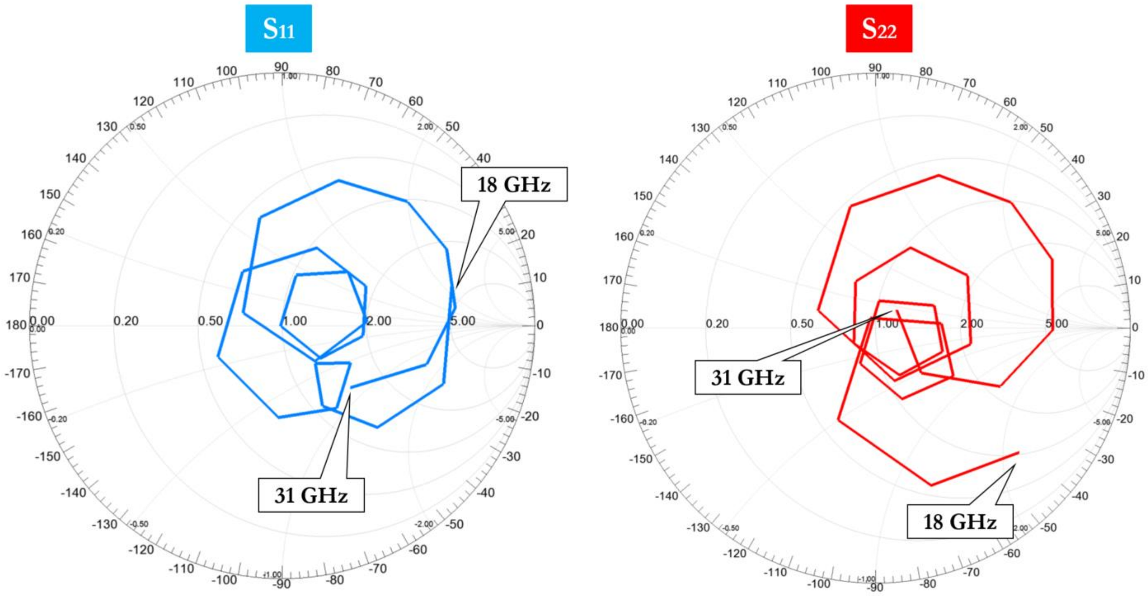

Figure 62 Simulated S_{11} and S_{22} plotted on a Smith chart of the complete dual polarized design versus frequency at Ka-band.

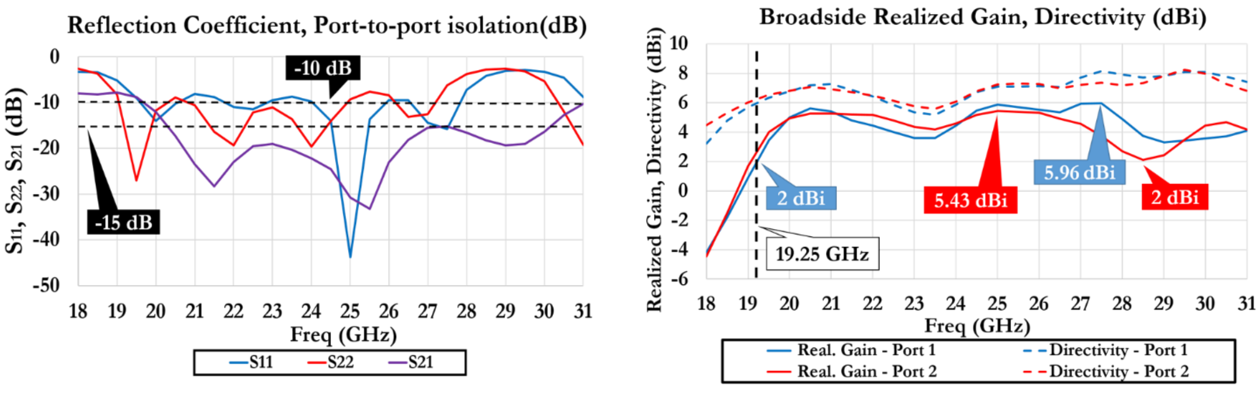

a) b)

Figure 63 Simulated performance of the dual polarized ACP antenna versus frequency: a) reflection coefficient and port-to-port isolation, b) broadside realized gain and directivity.

The simulated radiation patterns obtained when feeding port 1 and port 2 are plotted in Figure 64 in terms of realized gain at 24.5 and 30 GHz for both the E- and the H- planes. The final stack-up for the fabrication is shown in Figure 65 a), including the additional metal layers with dummies required in order to comply with fabrication constraints, notably in terms of copper balance. Four samples have been fabricated, the isometric, top and the bottom-view of a fabricated sample can be appreciated in Figure 66 a), b) and c), respectively.

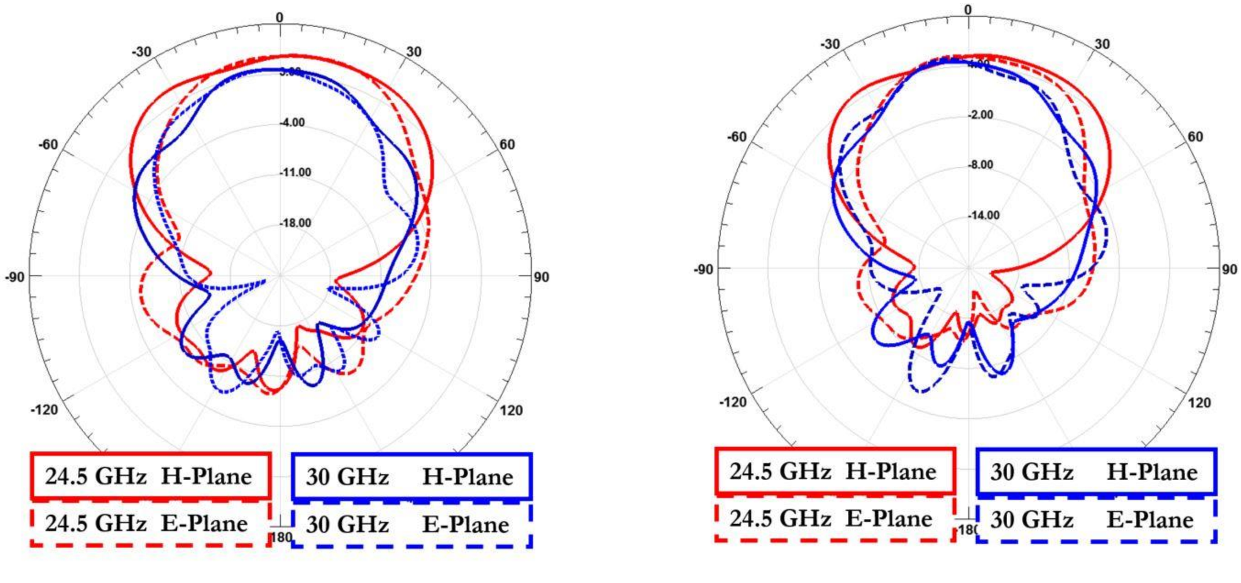

a) b)

Figure 64 Simulated realized gain radiation patterns at 24.5 GHz and 30 GHz for both E- and H- planes, obtained when feeding: a) port 1, b) port 2.

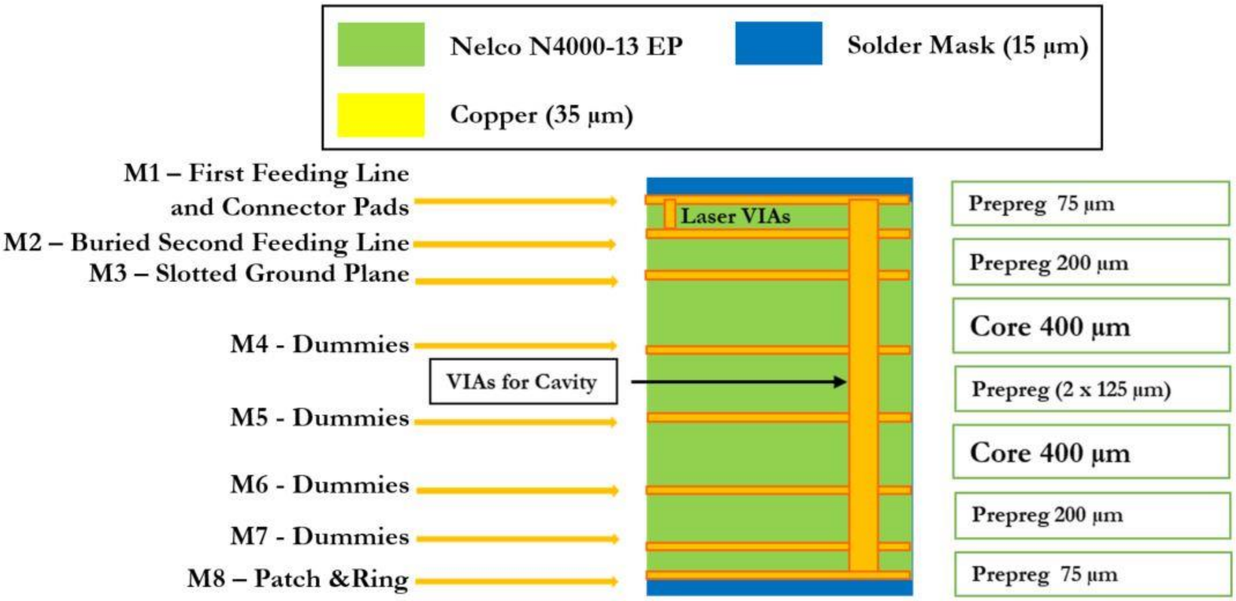

Figure 65 a) Dual polarized antenna stack-up for PCB fabrication.

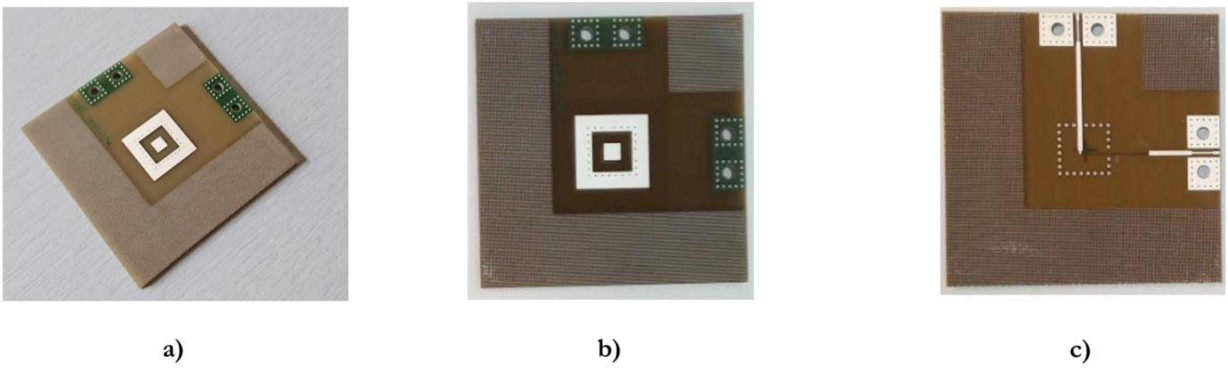

Figure 66 Pictures of a fabricated sample: a) isometric sample, b) top-view, c) bottom-view.

II.4.4 Measurements

The measurements of the prototypes have been performed in the contest of the collaboration with the University of Oviedo (Spain), as done for the samples working at Ku- band. The matching of the prototypes is measured using an Agilent PNA-X N5247A, [49] from 18 GHz up to 31 GHz. The results are compared with the simulated ones in Figure 37 a), in terms of S_{11}, and b), in terms of S_{22}. The asymmetry in the behavior of the ports is primarily due to the fact that the second feeding line is buried and connected to its connector pad by mean of a laser VIA. If we focus on port 1, we can appreciate an acceptable agreement between simulated and measured matching for the four samples, staying below -6 dB from 19 to 27.5 GHz and from 29.5 to 31 GHz. If we look at the second port, the matching stays below -6 dB from 22.2 to 28.5 GHz. Figure 68 shows the simulated and measured port-to-port isolation of the prototypes versus frequency. Values stays below – 15 dB from 18 to 25 GHz and from 28 to 30 GHz and below -10 dB along the rest of the bandwidth.

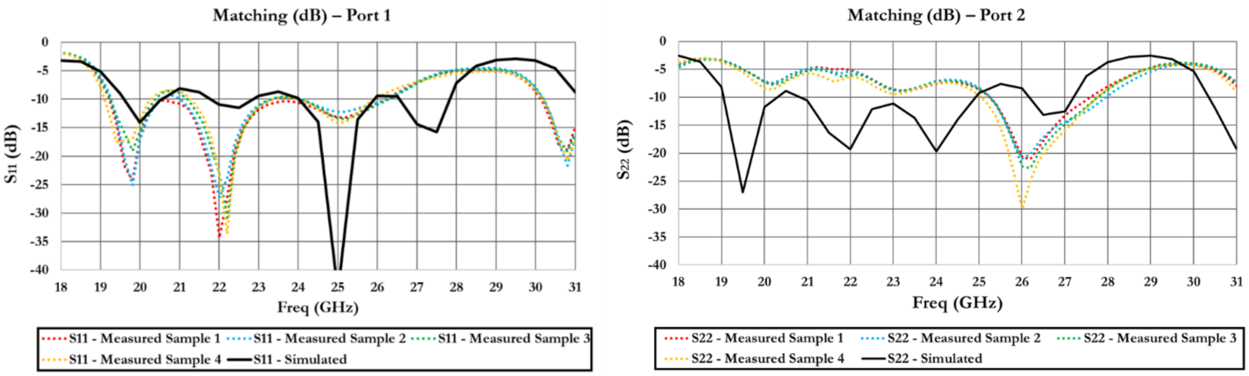

a)

b)

Figure 67 Simulated and measured reflection coefficient of the prototypes as functions of frequency: a) S_{11}, b) S_{22}.

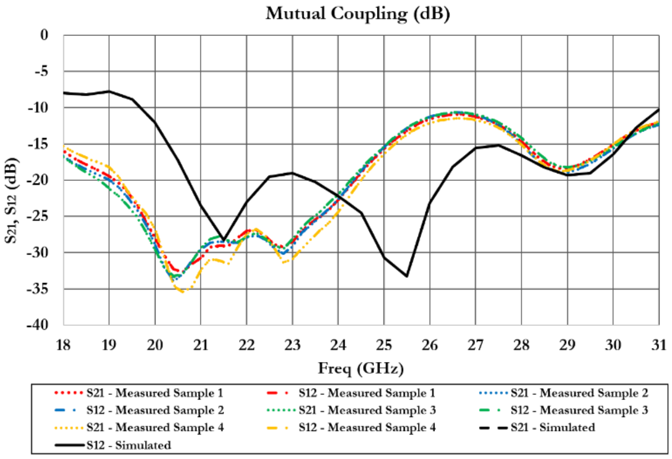

Figure 68 Simulated and measured port-to-port isolation of the prototypes versus frequency.

Figure 69 shows the simulated and measured peak total realized gain versus frequency obtained when feeding port 1 and port 2, including measurement uncertainty bars (±0.4 dB). A good agreement between simulation and measurements is found. Except for the drop below 19 GHz, the measured realized gain stays between 3 and 7 dBi for port 1 and between 2.2 and 6.5 dBi for port 2. The measured values result higher than the simulated ones along part of the operational BW, especially concerning port 2. This unusual behavior has already been noticed analyzing the measurements of the Ku- samples, previously in this chapter. A first hypothesis could be related to the inaccuracy of the

HFSS model and setup used for the simulations. The simulations performed in the Ku- case underlined that a better agreement between measured and simulated results could not be obtained, even using a HFSS design integrating a more complex connector model provided by the manufacturer. Moreover, the correctness of the simulation setup has been verified with the support of the HFSS engineers. The other hypothesis concerns the possibility of having unwanted radiations (i.e. due to the resonance of a cable) or reflections in the anechoic chamber.

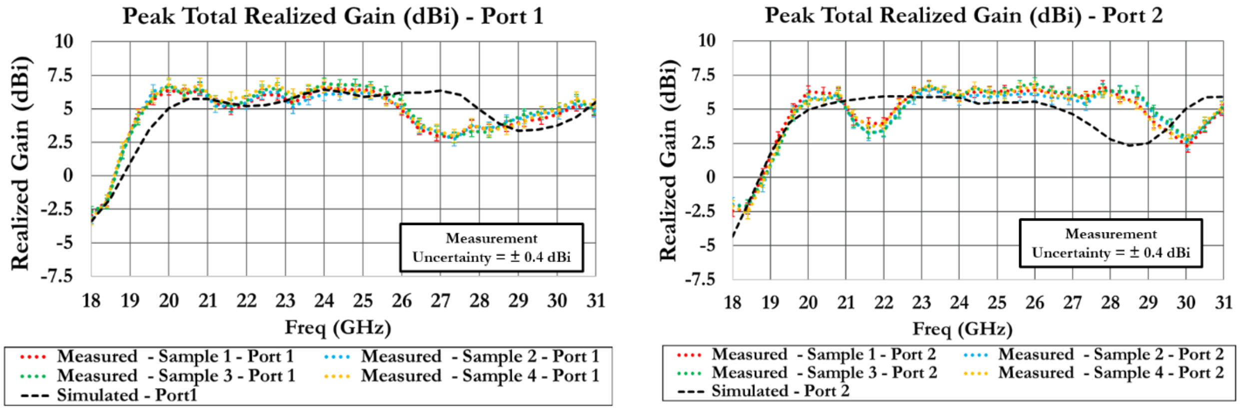

a)

b)

Figure 69 Simulated and measured peak total realized gain versus frequency, including measurement uncertainty bars: a) port 1, b) port 2.

The simulated and measured realized gain radiation patterns obtained when feeding port 1 and port 2, are plotted for one sample as a function of θ for ϕ = (0, 90°). Similarly to Ku- band, the strong reproducibility of the measurements is such as we can show the results concerning a single sample without affecting the integrity of the information. Figure 70 shows the curves for ϕ =0° at 24 GHz, Figure 71 shows the curves for ϕ = 90° at the same frequency.

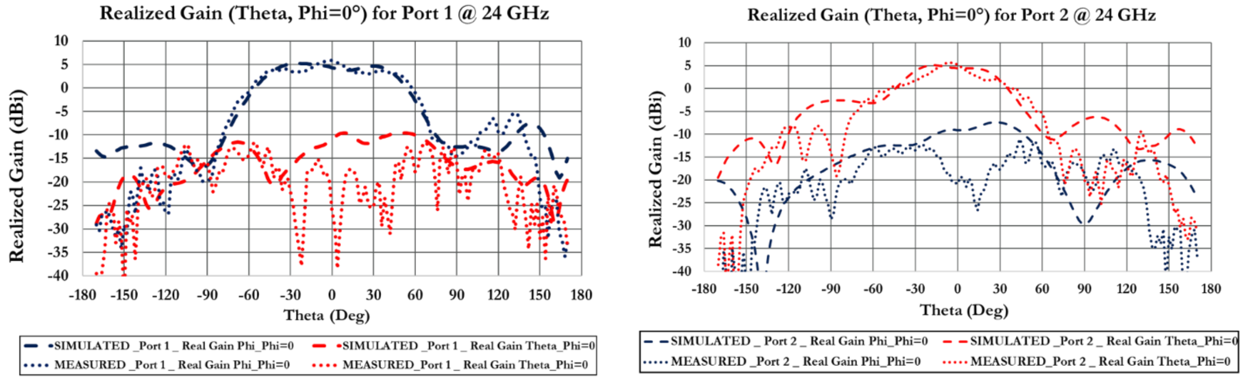

a)

b)

Figure 70 Simulated and measured realized gain for ϕ=0° as a function of θ at 24 GHz, obtained when feeding: a) port 1, b) port 2.

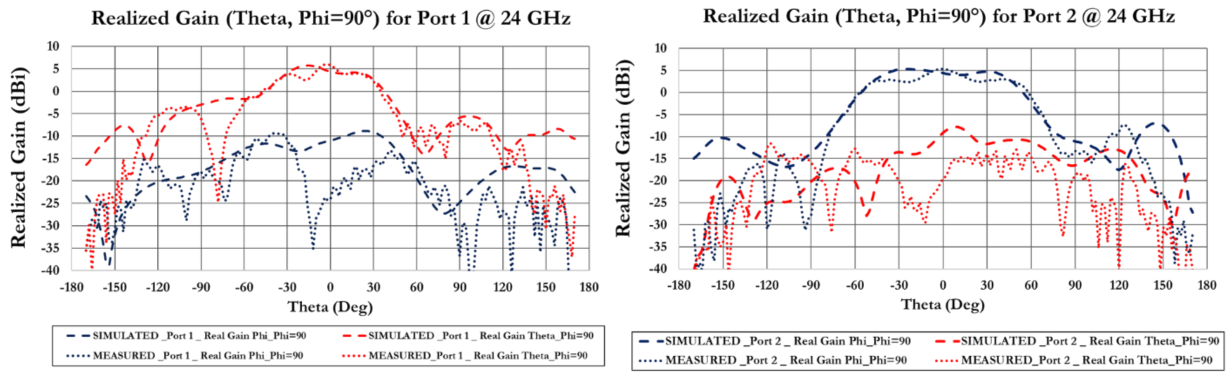

a)

b)

Figure 71 Simulated and measured realized gain for ϕ=90° as a function of θ at 24 GHz, obtained feeding: a) port 1, b) port 2.

The very large operational bandwidth obliges to show the same dataset for at least another frequency, so the same curves are plotted at 30 GHz for ϕ = 0° in Figure 72 and for ϕ = 90° in Figure 73. It is interesting to underline that we have a good agreement between measurements and simulations in all cases, except for the cross-polarization of port 2, as shown in Figure 72 b) and Figure 73 b). Looking at Figure 69 b), we can appreciate that the differences between simulated and measured broadside total realized gain at this frequency were more consistent when feeding port 2, if compared to port 1. Taking into account this phenomenon and provided hypotheses about its possible origins, we can consider these results as coherent with the previous ones.

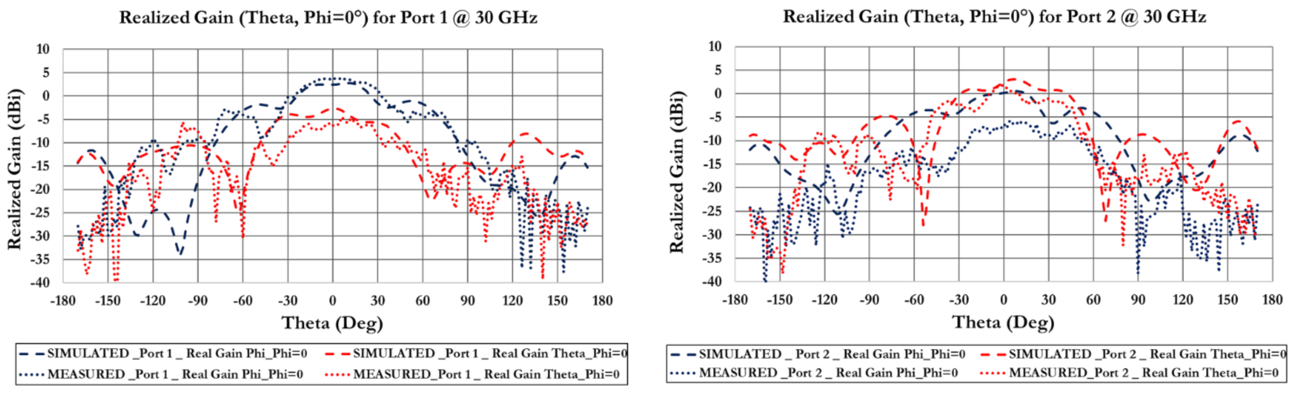

a)

b)

Figure 72 Simulated and measured realized gain for ϕ=0° as a function of θ at 30 GHz, obtained feeding: a) port 1, b) port 2.

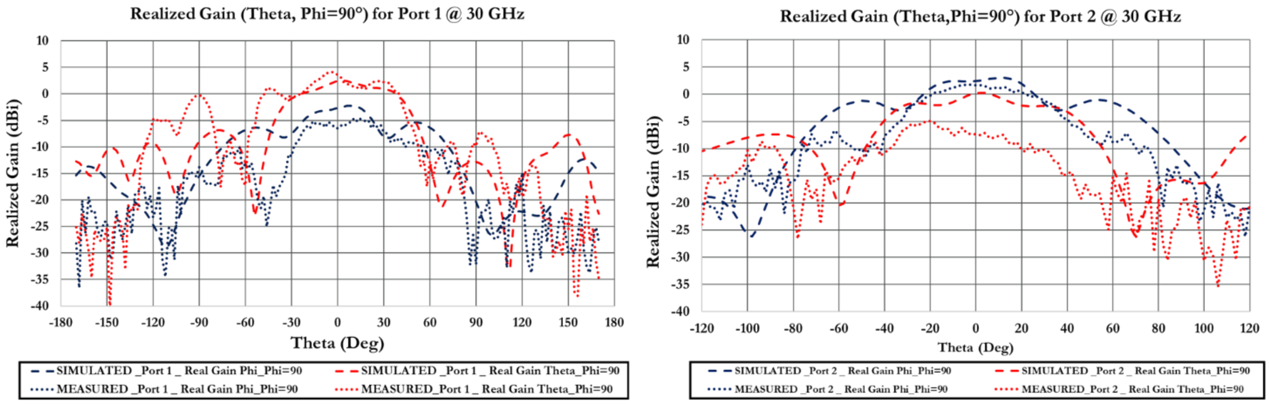

a) b)

Figure 73 Simulated and measured realized gain for ϕ=90° as a function of θ at 30 GHz, obtained feeding: a) port 1, b) port 2.

We don't perform the simulations with the complete connector models, as done in the previously illustrated Ku-case, as the presence of the cavity reduces the propagation of the SWs along the PCB and, therefore, the possible impact of the connectors over the radiation properties of the device. Moreover, considering the Ku- designs, entitled to be more sensitive to the SW propagation due to the lack of cavity, the simulations integrating the complete connector models were not able to consistently improve the capacity to reproduce the measured response of the antennas.

II.4.5 Benchmarking

Table 12 shows the benchmark of the designed antenna with the best reviewed planar wideband antenna working at Ka- band [40]. Using a similar antenna configuration without the necessity for a stacked patch and a foam layer, we manage to support a double linear polarization instead of a double circular one. The reviewed paper proposes a simulated -10 dB fractional impedance bandwidth of 52%, from 17.6 to 30.3 GHz. In our case, we guarantee a measured -6 dB impedance bandwidth from 19 to 27.5 GHz and from 29.5 to 31 GHz referring to port 1. We can underline that the reviewed paper proposes simulated results with a PCB board that has a thickness of 4.6 mm and including a foam layer. In our case, the samples have been fabricated through a standard PCB process without foam achieving a thickness of 1.7 mm for the board, being almost a third of the reviewed one.

Authors	Configuration	Polarization	-10 dB Impedance BW → Fractional BW	Min Broadside Realized Gain	Fabrication Process	Thickness
Gorsky et al, 2015.	Aperture Coupled Stacked Patches	Dual Circular Polarization	Simulated (17.6 – 30.3) GHz →(~52%)	N.A.	Envisaged Standard PCB Fabrication with a foam layer.	4.6 mm
This work	Aperture Coupled Patch with Cavity and Ring	Dual Linear Polarization	Below - 6 dB: (19 - 27.5 GHz), (29.5 – 31 GHz) For Port 1	Measured 3 dBi, From 19 GHz For Port 1	Standard PCB Fabrication	1.7 mm

Table 12 Benchmark of this work with the best reviewed planar wideband antenna working at Ka-band [40].

II.5 Open discussion concerning the limitation of planar antenna solution

The bibliographic review and the design work developed in this chapter allow to underline some of the main characteristics of the planar antennas for SatCom mobile telecommunications. As already detailed, the target to bring this technology to the mass consumer-market poses particular constraints, especially in terms cost, weight and complexity of the possible antenna solutions. The aperture coupled patch configuration emerges as the main approach for its possibility to leverage different design parameters starting from a relatively simple stack-up including only 3 metal layers. Realizing a wideband antenna capable to cover the wide fractional bandwidth required at Ku- and Ka-band would allow to reduce the cost and the complexity of a user's terminal for the consumer mass-market, by moving from the traditional planar solutions comprising of two distinct panels for Rx and Tx, respectively, to a single antenna panel per module. The versatility of this approach allows its modification by the addition and the reshape of various design elements. Nevertheless, a trade-off must be made between the complexity and the cost of the radiating and its performance in terms of bandwidth and realized gain. As we have shown, it is possible to realize low-cost radiating elements for the Ku-band that covers the whole targeted bandwidth with satisfying performance. Ka-band requires different considerations, as the 50% fractional bandwidth required to perform Rx and Tx using the same element inevitably leads to the excitation of surface waves, requiring a more complex stack-up in order to be managed and constructively leveraged. The levels of gain required by SOTM communications require the realization of large arrays, but the dimensions of the devices are such that it is possible only for the Ku- design. Assuming to be able to obtain 10 dB of gain from the RF electronics at these frequencies, an array integrating the ACP here designed to work at Ku- band would require 512 elements to achieve the 35 dBi of realized gain and comply with the SOTM transmission link budget. An eventual planar antenna solution would require making a trade-off between the achievable bandwidth and gain, with the consequent impacts in terms of complexity of the stack-up and its costs. Moreover, looking at the emerging LEO systems the user terminal will be required to have a complete scanning range in elevation in order to guarantee the continuity of the service in a mobile environment (i.e. connected car). Restraining our scope to the Ku- case, it would be theoretically possible to realize an antenna array guaranteeing an inter-element spacing equal to λ/4 at the highest frequency of interest and provide a grating-lobe electronic scanning in elevation. Nevertheless, the scanning limitations of such solution array would require mechanical scanning mechanism in order to provide full coverage both in azimuth and in elevation, as required by LEO Sat-Com-On-The-Move requirements

III. INNOVATIVE 3D-PRINTED WIDEBAND AND HIGH-EFFICIENCY KU- BAND ANTENNA ARRAYS

In the previous chapter we have presented the design of wideband aperture coupled microstrip patch antennas for Sat-Com-On-The-Move applications at Ku- and Ka- band. As explained, the goal is to achieve a compact user terminal able to guarantee the same performance as a traditional reflector – based solution. Moreover, proposing a user terminal for mobile satellite communications with a price affordable for mass-consumers (< 1 k$) actually represents the main bottleneck to bring this technology to the mass-market. Microstrip patch arrays would be able to guarantee a very low profile for the final user terminal and they could rely on well consolidated low-cost fabrication processes for printed circuit boards, which would represent an appealing feature looking from the perspective of the large-scale production. The simplicity, low-cost and ease of fabrication are payed in terms of efficiency of the antenna solution. The level of gain required by this kind of satellite communications impose the use of large arrays (i.e. 16x16 or 32x32) and complex microstrip-based feeding networks, whose efficiency would be highly reduced by the microstrip line losses at these frequencies. Moreover, as introduced in the previous chapter, the surface wave phenomenon may represent a serious concern for the creation of large microstrip arrays causing an increase of the mutual coupling between elements and pattern degradations due to the scan blindness phenomenon.

The possibility to leverage advanced and low-cost additive manufacturing processes actually represents an appealing approach for the innovations in this field. Metal antennas and complex feeding networks, traditionally requiring to be fabricated in different pieces by using machining methods, can actually be fabricated in a single piece. In this chapter we propose innovative high-efficiency, low-profile and wideband waveguide-based arrays to be fabricated by direct metal laser sintering (DMLS) technique to work at Ku-band (10.75 - 14.75 GHz). The chapter begins with the state-of-the-art of the slotted waveguide, horn and continuously transverse slot (CTS) antenna arrays. Those actually proposed as low-profile and high-efficiency alternatives to the traditional motorized reflectors, used as antenna solution for the SOTM user terminals at Ku- and Ka- bands. Hence, the opportunity to exploit the open double-ridged waveguide antenna configuration is discussed. The aperture of a traditional waveguide (WG) covering the Ku-band can be shrunk, allowing to design a wideband radiating element that can guarantee high efficiency while fitting the inter-element spacing of an array able to scan ±45° at 14.5 GHz, avoiding grating lobes. The design of the aforementioned antenna is detailed, as well as its integration in the design of 2x2 and 4x4 arrays. The prototyping and the tests of the designed 2x2 antenna array is detailed. Finally, the advantages and the drawbacks of the proposed solutions are discussed.

III.1 Slotted waveguide and horn antenna array challenges and state-of-the-art

The need for compact and low-cost Sat-Com-On-The-Move user terminals pushes towards the development of innovative antenna solutions able to fit the requirements of the consumer mass-market in terms of cost, form factor and performance. The microstrip patch antenna arrays theoretically answers these demands leveraging the low-cost PCB fabrication process and an intrinsic low profile. Unfortunately, microstrip feeding networks have a strongly degenerative impact over the performance of large arrays like those required for these applications. Radiation and ohmic losses of the microstrip feeding lines are proven to strongly limit the impedance and gain bandwidth of an eventual large array working at these frequencies [56]. Hence, the most diffused planar alternatives to the traditional reflector-based user terminals leverage different low-profile solutions. Slot waveguide antenna arrays and horn antenna arrays represent the most appealing considered solutions of antennas used in satellite communications [3]. Slot waveguide and CTS arrays offer the advantage of their high efficiency and the intrinsic drawback of their narrow bandwidth (BW). Horn antennas offer the benefits coming from large achievable operating BW, high-efficiency and easily achievable double polarization [57]. However, their form factor is such as it results difficult to create arrays with inter-element distance allowing to realize the wide-angle electronic scanning required to track LEO satellites.

III.1.1 Slotted waveguide antenna array

We can explain the working principle of a slot antenna considering a narrow rectangular slot in a conducting surface. The described element radiates an electromagnetic field if its long side interrupts currents occurring in the surface, since these can be continued within the slot as a displacement current, as shown in Figure 74 a). An array can be easily created by creating a series of slots in the wall of a rectangular waveguide, as shown in Figure 74 b) from [58]

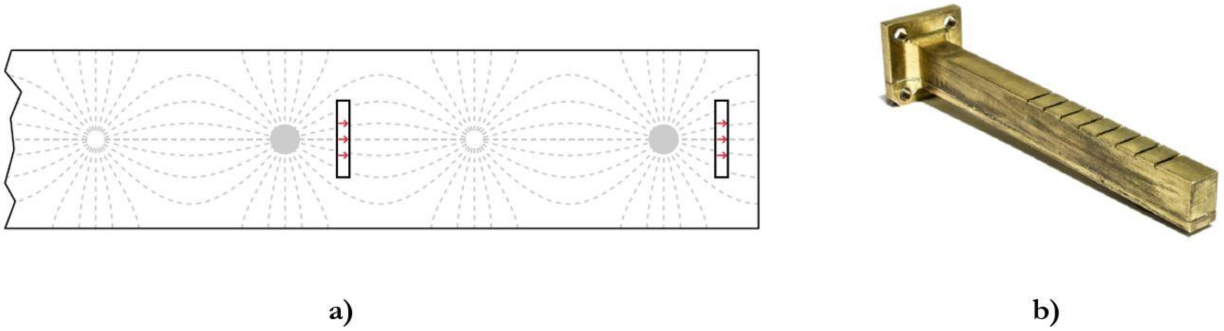
a) b)

Figure 74 a) TE10 electric field distribution (red, within the slot) and displacement currents on the broadside wall of a rectangular waveguide with transversal slots from [58], b) Example of slotted rectangular waveguide array from [58].

A typical advantage of this kind of antenna is the radiation efficiency which can exceed 90%. [59] The fractional bandwidth (FBW) represents an intrinsic limitation instead, being typically equal to 3-5 %

[60] [61]. These values are far from the 33% and 50% of FBW required to cover the Ku- and Ka-bands, respectively. Hence, SOTM user terminals integrating slotted waveguide array as an antenna solution, like the one proposed in the framework of the LOCOMO project (Figure 75), split Tx and Rx paths into two different panels with a direct impact on the form factor and the final cost of the solution [62].

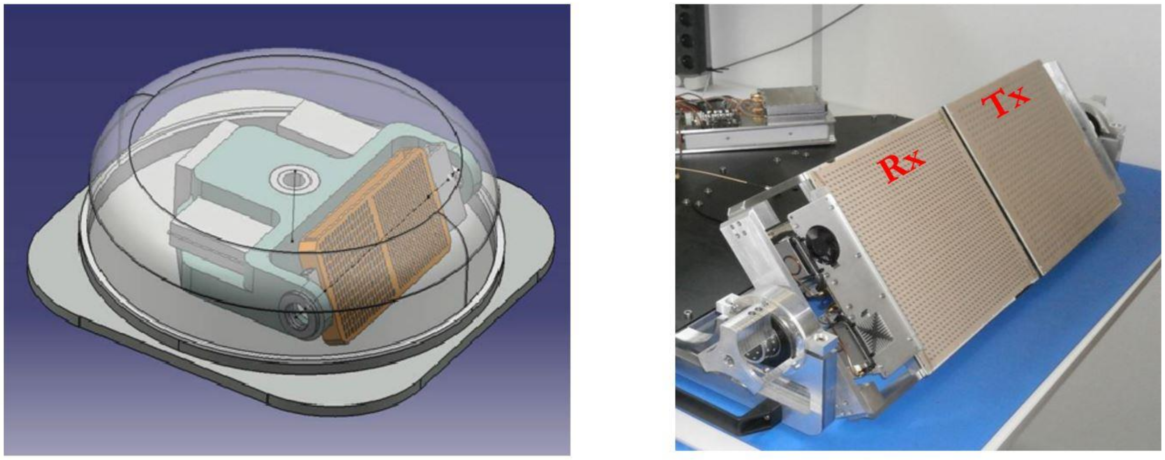

a) **b)**

Figure 75 a) LOCOMO user terminal for Ka-Band from [63], b) Particular of the antenna panels for Rx and Tx, integrated in LOCOMO prototype from [64].

III.1.2 Horn antenna array

We can define a horn antenna as a device able to make a transition from waves propagating in a waveguide into electromagnetic signals transmitting in another open medium, such as free space [57]. A typical advantage of this configuration comes from the flaring aperture that can easily realize a wideband impedance matching, being an appealing feature for SOTM applications. Unfortunately, the same characteristic becomes the main drawback of this kind of antenna looking from the perspective of the design of an electronically scanned array. The intrinsic large radiating aperture avoids in fact to impose the inter-element distance required to create an electronically scanned phased array with wide – angle scanning capabilities, as required by LEO systems. In this case, a mechanically scanned approach becomes mandatory. Figure 76 a) shows an example of a horn array with double linear polarizations for SOTM applications at Ku-band [65]. Figure 76 b) shows the integration of the array in the final user terminal: as we can see, two motors are used to mechanically scan in azimuth and elevation. Other interesting benefits of this approach are represented by the possibility to support a double linear polarization by creating a square or circular aperture and the high efficiency.

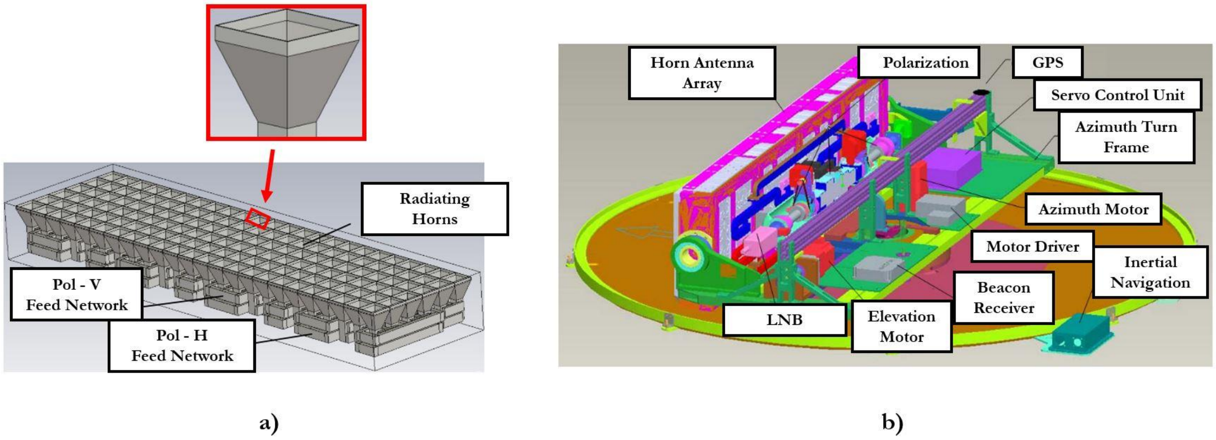

a) b)

Figure 76 a) Horn antenna array with double linear polarization and particular of the horn from [65], b) Complete prototype of a user terminal with 2- axis mechanical scanning from [65].

III.1.3 Continuously transverse stub antenna array

Continuously transverse stub (CTS) antenna array exploits broad, continuous radiating stubs that are connected to a low-loss parallel plate waveguide (PPW) which is cropped along the direction parallel to their large side and excited by a primary line source, as shown in Figure 77 a). The stubs block the longitudinal currents within the PPWs radiating a linearly polarized field [66]. The feeding network and the radiators can be adapted to work with a double linear polarization and a radiation efficiency higher than 80%, a thickness of less than 4.5 cm has been reported in literature for such a prototype working in the (26.5 – 40) GHz band [34]. The complexity of the feeding network leads to complex and expensive stack-up requiring laborious manufacturing and assembly processes, while the narrow BW of the radiators imposes to use different antenna panels for Rx and Tx in the case of SOTM applications [34]. Starting from this concept, ThinKom has developed its own variable inclination continuously transverse stub (VICTS) antenna solution, which exploits a system of rotating plates to mechanically scan the beam. The Gogo2Ku terminals, shown in Figure 77 b), dominates the in-flight connectivity market.

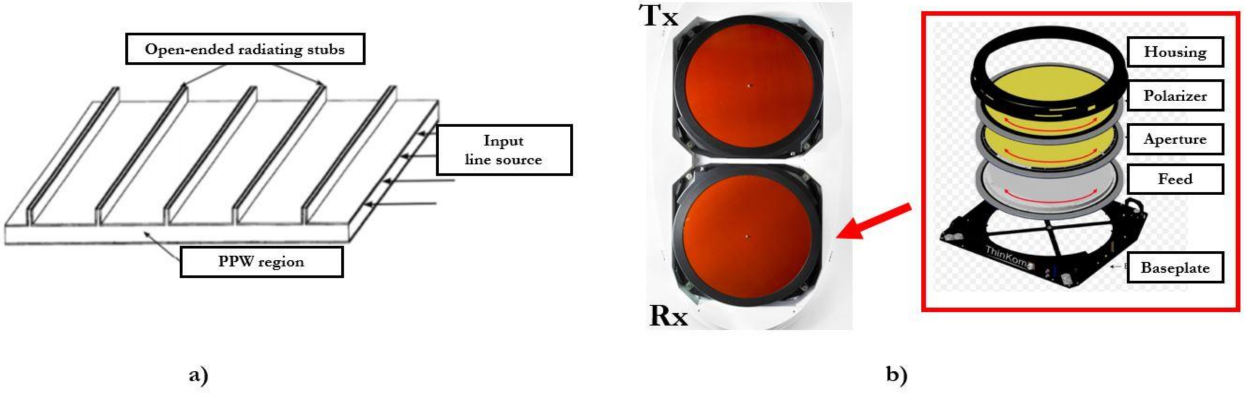

a) b)

Figure 77 a) CTS architecture from [66], b) Gogo2Ku terminal with exploded stack-up of a panel from [67].

III.1.4 Summary of the state-of-the-art

Table 13 synthetizes the characteristics of the most interesting antenna arrays made by slotted waveguides, CTS and horns working at Ku- and Ka-band found in the literature. These solutions actually represent the non-planar alternatives to the traditional reflector-based SOTM user terminals.

Antenna Type	**Measured Gain (dBi) (N.A. for "Not Available")**	**Number of elements (i.e. 16x16)**	**Antenna Size (l*w *h) [mm] (N.A. for "Not Available")**	**Frequency**	**Scanning (Mechanic/ Electronic, N.A. for "Not Available")**	**Technology (N.A. for "Not Available")**
Horn array [65], [68],[69]	36.1 (Max) [35.6 - 36.1]	144	504*504*N.A.	Ku- Band (Tx)	El: 0 - 90° M Az: 0- 360° M	N.A.
	35 (Max)	256	300*300*N.A.	Ka- Band (Rx)	El: 0 - 90° E Az: 0- 360° M	Milling
	40.7 (Max)	1024	400*400*N.A.	Ka- Band (Tx)	El: 0 - 90° E Az: 0- 360° M	Milling
Slot Array with Polarizers [70]	27.5 (Max)	128	N.A.	Ku- Band (Rx)	El: 0 - 90° M Az: 0- 360° M	Machining
Conformal Slot Array [71]	18 (Max)	44	N.A.	Ku- Band (Rx)	N.A.	DMLS
Cavity - Backed Slot Array [72]	25.9 (Max)	64	N.A.	Ku- Band (Tx)	N.A.	Simulated (Envisaged Milling)
Multilayered Slot Array [73], [63],[59], [74]	30 (Max)	256	N.S.	Ku- Band (DUPLEX)	N.A.	Simulated (N.A)
	N.A.	16	270*270*N.S.	Ka- Band (Rx)	El: 0 - 90° M Az: 0- 360° M	Milling
	N.A.	64	270*270*N.S.	Ka- Band (Tx)	El: 0 - 90° M Az: 0- 360° M	Milling
CTS Stub Array, [34]	28.9 (Max)	16	N.S.*N.S*45	Ka- Band (Tx)	El: 0 - 40° M Az: N.A.	Milling and Electrical Discharge Machining

Table 13 Previously reported Ku- and Ka- band slotted waveguide, horn and CTS antenna arrays. [Mechanical scanned terminals are consistently higher than individual antenna panels (h)]

III.2 Open double ridge waveguide antenna array opportunity

The targeted characteristics of a consumer-friendly SOTM user terminal for LEO applications have been introduced in Chapter 1, notably being low profile, low-cost and able to guarantee performance comparable with those of a traditional reflector-based solution in terms of gain, scanning angle and operational BW. Considering the reviewed antenna solutions for SOTM user terminals, neither of them allows to satisfy all these conditions at the same time.

Hence, a high-efficiency radiator able to guarantee ± 45° of electronic elevation scanning for a final array avoiding grating lobes and working over the whole Ku-Band would represent a major innovation in the field. In fact, such features would allow to use a single aperture for both Rx and Tx decreasing the overall cost structure. Moreover, the mechanical scanning would be restrained to the azimuth plane, keeping a moderate complexity for the final system to be proposed to the users. In addition, the possibility to prototype the radiators and part of the feeding network in a single piece using the additive manufacturing technologies would ease the fabrication and assembly processes. The open-ended DRWG antenna array is identified to be an appealing candidate due to the intrinsic high-efficiency of the waveguide-based radiators and the possibility to guarantee wideband features. The shrunk aperture of the elements allows to fit the inter-element spacing required to obtain the targeted scanning in the elevation plane for the final array. This configuration has been proven to be suitable for an additive manufacturing process like DMLS [54].

III.2.1 Theory

The working principle of the ridged waveguides relies on the possibility to add one or two ridges on the bottom and/or top walls of a rectangular waveguide, as shown in Figure 78.

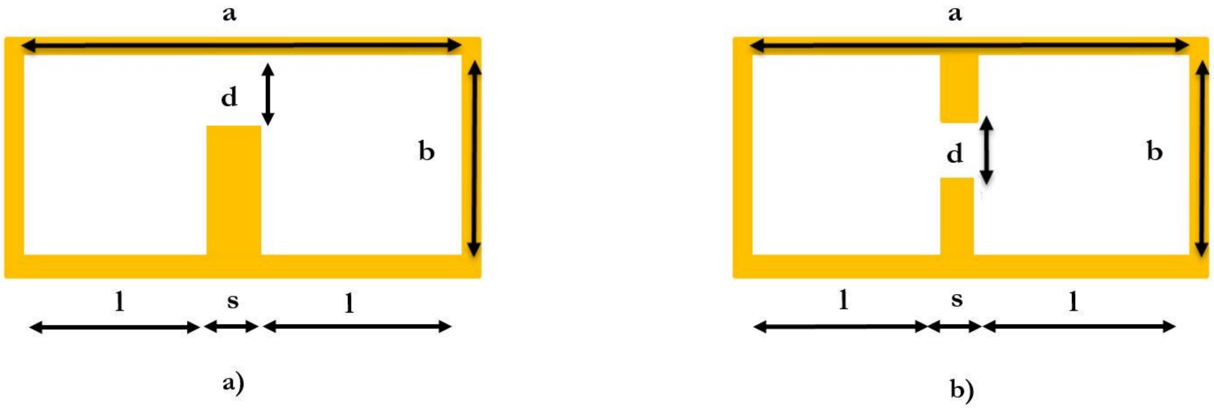

Figure 78 a) Single ridged waveguide and b) DRWG cross sections from [75].

A unit length of a ridged waveguide can be modeled as a lumped-constant equivalent circuit over a frequency band, made by the parallel made by 2 capacitances and an inductance, as shown in Figure 79.

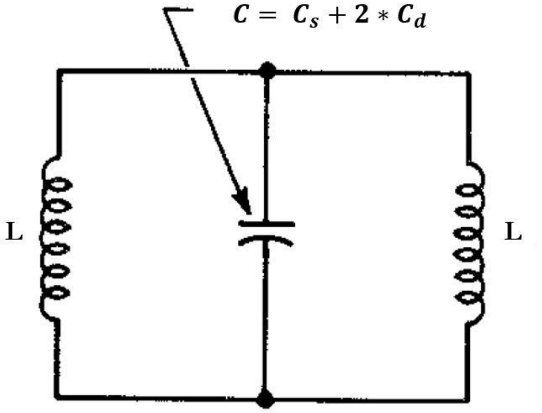

Figure 79 Equivalent lumped circuit of a unit length of a ridged waveguide from [76].

The values of the inductance and the capacitances can be computed by the following formulas, given in [76]:

$$C_s = \frac{\varepsilon * s}{d} \tag{1}$$

$$C_d = \frac{\varepsilon}{\pi}\left\{\frac{(\frac{d}{b})^2 + 1}{d/b} cosh^{-1}\left[\frac{1 + (\frac{d}{b})^2}{1 - (\frac{d}{b})^2}\right] - 2\ln\left[\frac{4 * \frac{d}{b}}{1 - (\frac{d}{b})^2}\right]\right\} \tag{2}$$

$$L = \left[\frac{\mu * (a - s)}{2}\right] * b \tag{3}$$

where ε and μ are the electric permittivity and the magnetic permeability of the medium, respectively. Once the inductance and capacitance values s are computed, the cut-off frequency of the fundamental mode of the ridged waveguide can be evaluated as:

$$f'_c = \frac{1}{2\pi\sqrt{(L/2)(C_s + 2C_d)}} \tag{4}$$

The ridges lower the cut-off frequency of the dominant mode, if compared to a traditional rectangular waveguide with the same section. A rectangular waveguide with (a = 2*b) has a BW of an octave as the cut-off frequency of the TE_{20} mode is equal to the double of the cut-off frequency of the dominant TE_{10} mode [77]. Considering a ridged configuration, and in particular a DRWG one, the ratio of the cut-off wavelength of the fundamental TE_{10} mode to that of the TE_{20} mode can be higher than 5. [75] The improvement of the achievable operational BW from 1 octave to a maximum of about 5.5 is paid in terms of attenuation, which can be up to 20 times higher than the attenuation of a traditional rectangular waveguide with the same aperture [75]. Design curves are given in [75]: DRWG dimensions are calculated taking the parameters of a rectangular WG with a ($\frac{b}{a}$) form factor equal to 0.45 as reference. Different design curves are given for fixed values of the ridges gap d, normalized to b, as a function of the width of the ridges s, which is normalized to a. Figure 80 a) presents the design curves allowing setting the normalized cut-off wavelength of the fundamental mode for the double-ridged waveguide. Figure 80 b) gives the design curves for the BW, defined as the ratio of the cut-off wavelength of the fundamental to that of the first higher order mode. The origin of the vertical axis is fixed at 2 in both cases, corresponding to the case of a traditional rectangular waveguide. The maximum $\frac{\lambda_{c\,TE10}}{a}$ value is 5.5, obtained with $\frac{d}{b} = 0.1$ and $\frac{s}{a} = 0.45$, and the maximum $\frac{\lambda_{c\,TE10}}{\lambda_{c\,TE20}}$ is 6.25, obtained with $\frac{d}{b} = 0.1$ and $\frac{s}{a} = 0.3.$ Once the DWRG ridge width is fixed, an increment of the height of the ridges leads to an increase of either the bandwidth or the normalized cut-off wavelength of the fundamental mode.

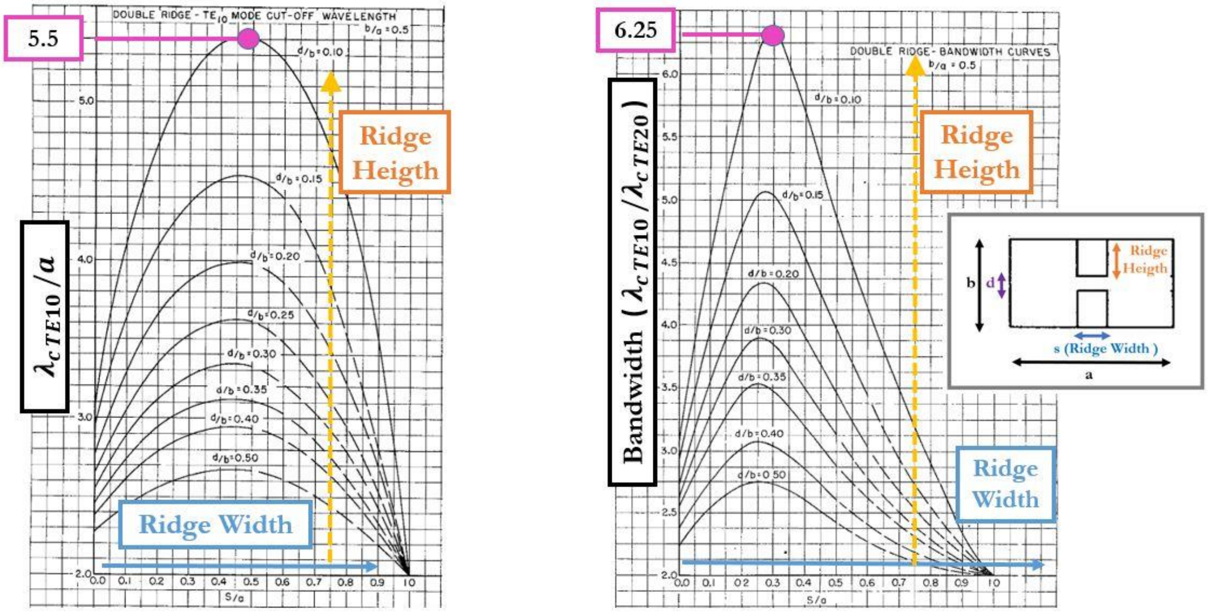

a)

b)

Figure 80 Design curves of DRWG: a) cut-off wavelength of fundamental TE_{10} normalized to “a” as a function of the ridge’s width normalized to “a” for various ridge distance normalized to “b”, from [75], b) BW as a function of normalized ridge’s width for various d/b values, from [75].

Figure 81 shows the attenuation of a DRWG, normalized to that of a rectangular WG with the same section, versus the normalized ridge's width and for various theoretical bandwidth values. It is clearly shown that larger bandwidth values lead to higher level of attenuation, up to a normalized value of 21.

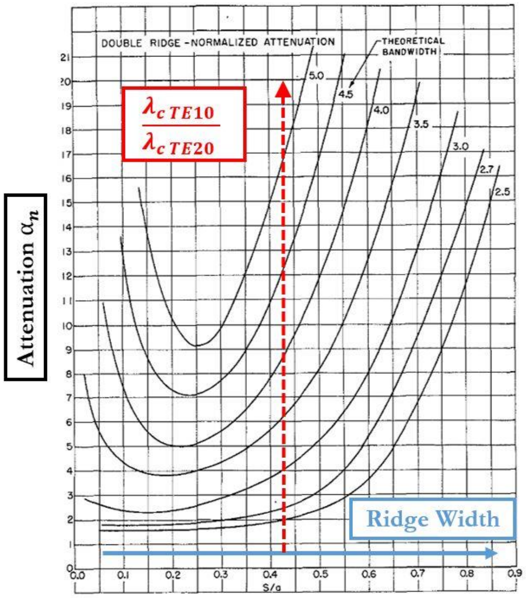

Figure 81 Design curves of DRWG normalized attenuation as a function of normalized ridge's width for various d/b values, from [75].

III.3 Open-ended Ku- band DRWG antenna design

The starting point of the design was to evaluate the inter-element distance required to design a phased array that achieves ±45° of electronic beam steering without grating lobes at 14.5 GHz, representing the high edge of our operational BW at Ku- Band. According to [78], this value can be evaluated by the following formula:

$$d_{max} = \frac{\lambda}{1 + \sin\left(\theta_{max}\right)} \tag{5}$$

where λ is the wavelength at 14.5 GHz, θ_{max} is set to be equal to 45° and d_{max} results equal to 12.1 mm. Considering the objective to build the whole array in a single metal block, a minimum thickness of 0.6 mm for the sidewalls shared between adjacent elements must be guaranteed in order to fit the mechanical constraints of the chosen DMLS fabrication technique, the resulting maximum aperture dimension is 11.5 mm [79]. Figure 82 a) shows the corresponding rectangular WG, Figure 82 b) shows the propagation constant of the fundamental TE_{10} mode as a function of frequency for this configuration. It is obvious that using a rectangular WG design it would not be possible to cover the targeted operational bandwidth.

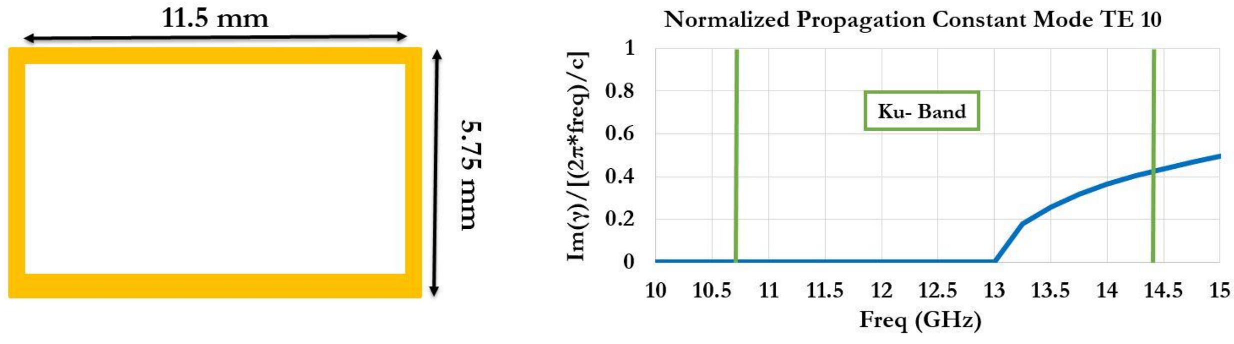

a) b)

Figure 82 Rectangular WG: a) Section with dimensions [mm], b) Normalized propagation constant of TE_{10} mode versus frequency.

A DRWG was designed using the previously shown design curves in order to cover the targeted operational BW (10.75 – 14.5 GHz). Figure 83 a) shows the section of the designed DRWG with relative dimensions. The propagation constants of the fundamental modes of the DRWG and the equivalent rectangular WG are shown in Figure 83 b) as a function of frequency. The effect of the presence of the ridges is such that the designed DRWG starts to work below the range of frequency of interest. A traditional rectangular WG would have required a 63% bigger section to achieve the same results without complying with the spacing requirements for the final array.

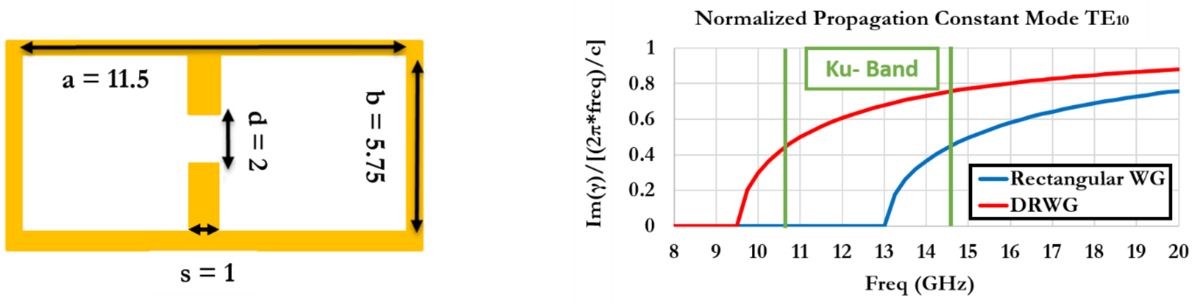

a) b)

Figure 83 DRWG: a) Section with dimensions [mm], b) Normalized propagation constants of TE_{10} modes of the DRWG and of the rectangular waveguide with same dimensions versus frequency.

The simulated electric field distribution of the TE_{10} mode at 14.5 GHZ is shown in Figure 84 for the designed open-ended DRWG (b) and an open-ended rectangular WG with the same section (a). As we can see, the ridges have a strong capacitive loading effect and the electric field is strongly concentrated in the gap between them.

a) b)

Figure 84 Simulated electric field distribution of the fundamental TE_{10} mode at 14.5 GHz for b) the designed open-ended DRWG antenna and a) open-ended rectangular WG with equivalent section.

The simulated performance of the DRWG in open-ended configuration is shown in Figure 85: we can appreciate a reflection coefficient that stays below -5 dB along the wide bandwidth and a total efficiency (calculated as the ratio of the radiated power to the total incident power) higher than 70%. The broadside realized gain is ~3.5 dBi and directivity is ~ 5 dBi. Taking into account the various fixed constraints and the fractional bandwidth of 30% to be covered, these performances are promising.

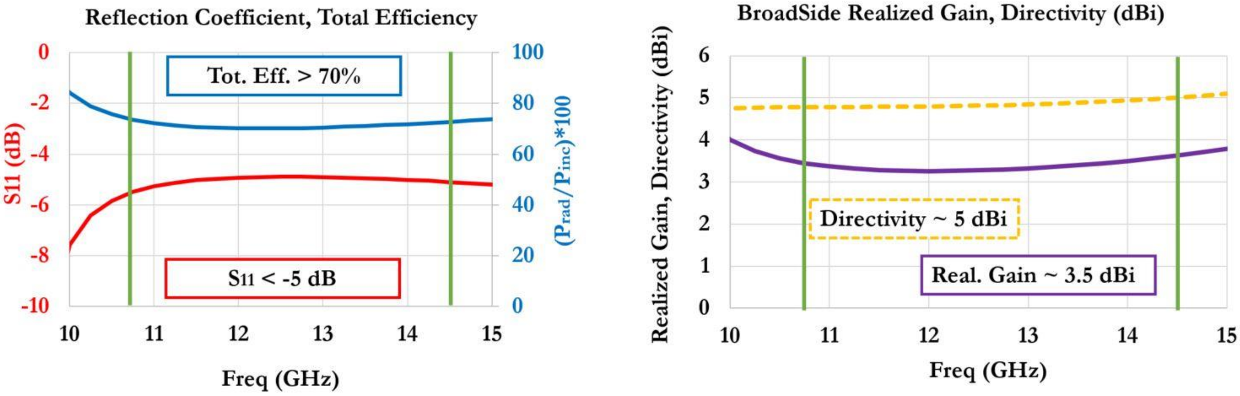

a) b)

Figure 85 Simulated performance of the designed DRWG: a) reflection coefficient and total efficiency as a function of frequency, b) broadside realized gain and directivity as a function of frequency.

The simulated realized gain radiation patterns of the designed antenna are shown in Figure 86 at 10.75, 12.5 and 14.5 GHz for both E and H planes. If we consider the E-plane, the angle such as realized gain (θ,90°) = {max [realized gain (θ,90°)] – 1 dB} is θ ≥ 45° for each frequency. Taking into account that the far-field pattern of an array is equivalent to the convolution of the array factor and pattern of the single radiating element, a final array integrating the designed element could be able to realize a ±45° steering in the E-Plane with maximum theoretical scanning loss of 1 dB in the whole frequency range [80].

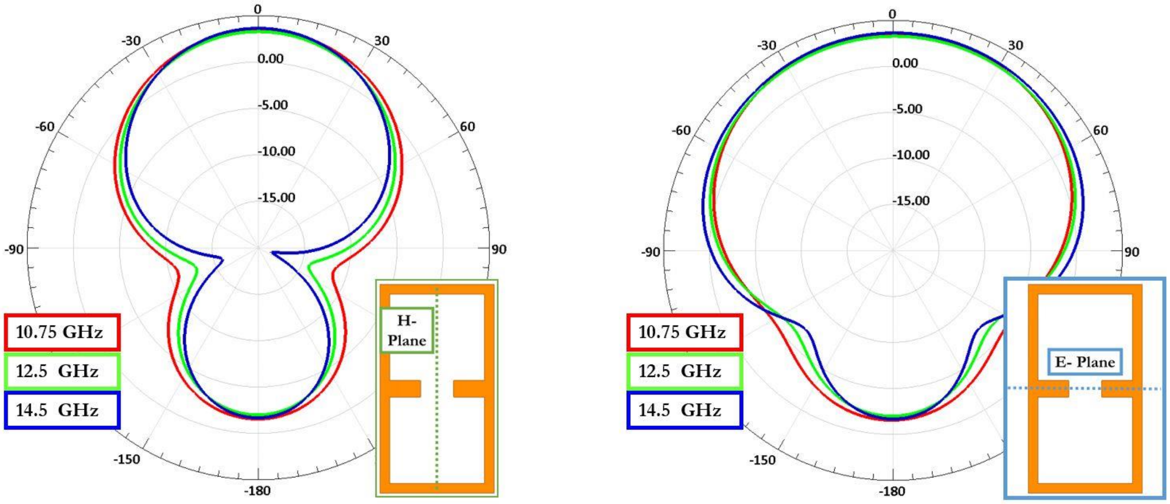

a)

b)

Figure 86 Simulated realized gain radiation patterns of the DRWG antenna at 10.75, 12.5 and 14.5 GHz: a) H-Plane, b) E-Plane.

III.4 Innovative 2x2 Ku-band DRWG antenna array

The goal is now to create a 2x2 sub-array with corporate feeding network leveraging the designed DRWG antenna (to be used in next step as unit cell for the development of large arrays). The envisaged integration scheme is shown in Figure 87: as we can see, a uniform 1:4 DRWG – based power divider represents the core of the feeding network while a DRWG-to-WR-75 standard waveguide transition and a WR-75 flange will be used to allow connection and test. The realization of the sub-array allows to assess benefits and drawbacks of the chosen approach, prove the feasibility and the robustness of the selected fabrication technology and validate the complete workflow by measuring the samples and comparing achieved results with simulated ones.

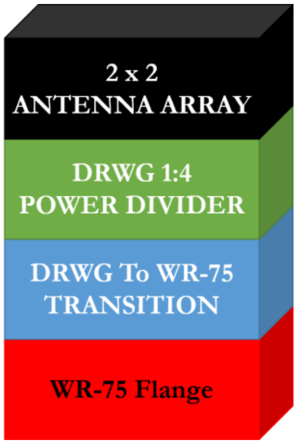

Figure 87 Integration scheme for the 2x2 DRWG sub-array with corporate feeding network and WR-75 flange.

III.4.1 2x2 DRWGs simulation

A 2x2 array is created, according to the previously fixed inter-element distance, and simulated with HFSS. Each element is fed in phase with the same amount of power. The designed 3D model is shown in Figure 88 a) and the simulated broadside realized gain and directivity are shown in Figure 88 b) and compared with those of the single DRWG antenna. The broadside realized gain of the array is ~9 dBi with an improvement of ~5.3 dBi if compared to the single antenna. The directivity of the array increases with frequency from 9.7 up to 10.8 dBi with an expected improvement of ~6 dBi, if compared to the single antenna. The simulated realized gain radiation patterns of the array are shown in Figure 89 for E and H planes at 10.75, 12.5 and 14.5 GHz, according to the reference system in Figure 88 a).

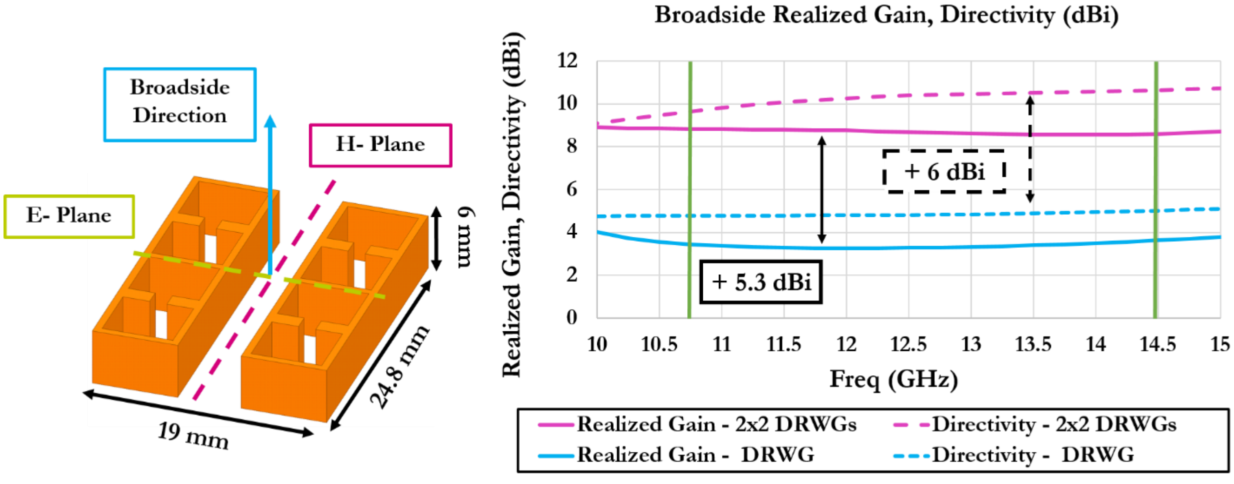

a) b)

Figure 88 2x2 DRWG array: a) 3D Model, b) Simulated broadside realized gain (continuous line) and directivity (dashed line) as a function of frequency, compared with the performance of the single DRWG.

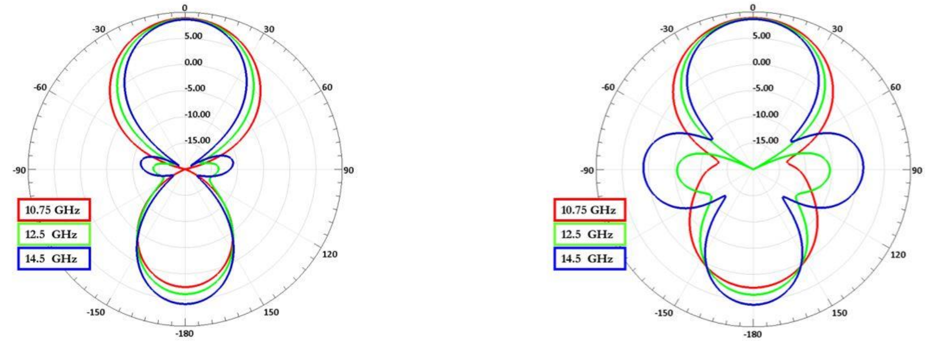

a) b)

Figure 89 Simulated realized gain radiation patterns of the 2x2 DRWG array at 10.75, 12.5 and 14.5 GHz: a) H-Plane, b) E-Plane (according to reference system shown in Figure 88 a)).

III.4.2 1:4 power divider design

The 1:4 power divider represents the core of the envisaged corporate feeding network for the 2x2 array. The wide FBW to be covered represents a challenge, as the traditional cavity-based power dividers cannot offer enough bandwidth [81]. A tapered cavity with ridges is designed following the method proposed in [54]. The heigth of the cavity, defined as "h_c", is set to be equal to $\lambda_c/4$, where λ_c corresponds to the central wavelength at 12.65 GHz. The proper operational bandwidth is set by adding ridges in the E-plane whose form factors are defined by the width "w_r" and the length "l_r". Moreover, the structure is chamfered introducing a difference between the top and the bottom widths of the cavity and between its top and the bottom lengths, equivalently. Ridges, chamfers and cavity parameters are optimized by simulations in order to achieve the best performance over the targeted Ku- band. The designed cavity can be appreciated in Figure 90 a), the design is integrated as a 5-port model including 1 input and 4 output DRWGs, each one terminated with a waveport in order to perform the HFSS simulations, as shown in Figure 90 b).

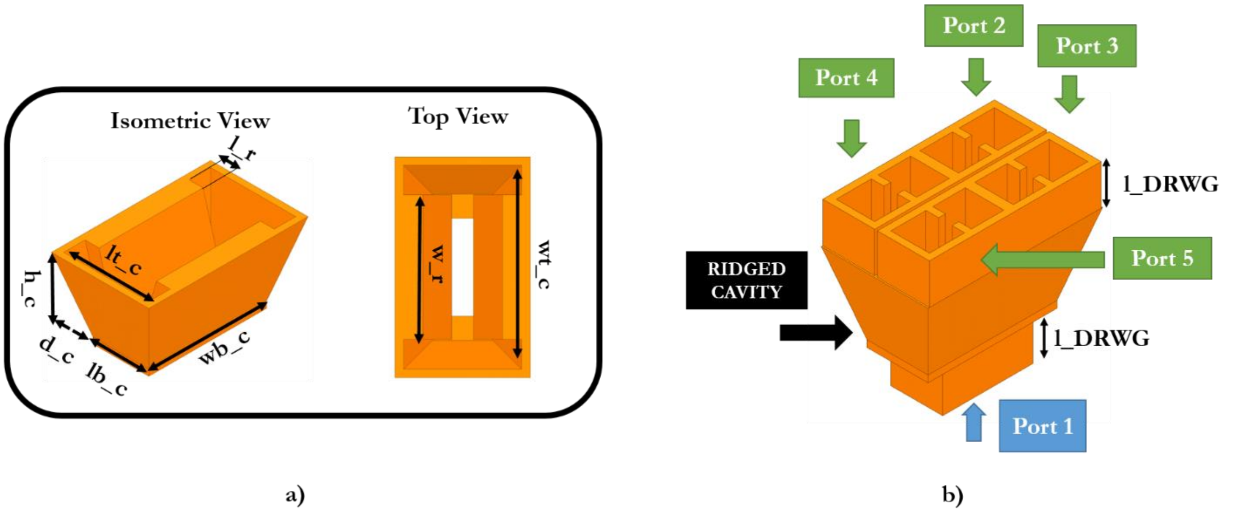

Figure 90 a) Designed chamfered cavity with ridges with dimensions (mm) in Table 2, b) 5-port model of the uniform 1:4 power divider with input and output DRWGSs for the simulation.

Table 14 specifies the dimensions of the most important important design parameters of the ridged cavity.

h_c	d_c	lb_c	wb_c	lt_c	wt_c	w_r	l_r
12	3.4	9.1	17.2	13.9	24	17	2.5

Table 14 Dimensions of the main design parameters of the chamfered ridged cavity in mm.

The designed 5-ports model is simulated feeding port 1 with 1 W and the relative performance is shown in Figure 91, in terms of matching and transmission. The simulated magnitude of the S_{11} stays between -23 and -11 dB, while the transmission coefficients are equal considering the four outputs and they oscillate around the value of -6 dB. This confirms that the uniform four-way power splitting is well achieved with maximum additional losses of 0.4 dB at highest frequencies for each port.

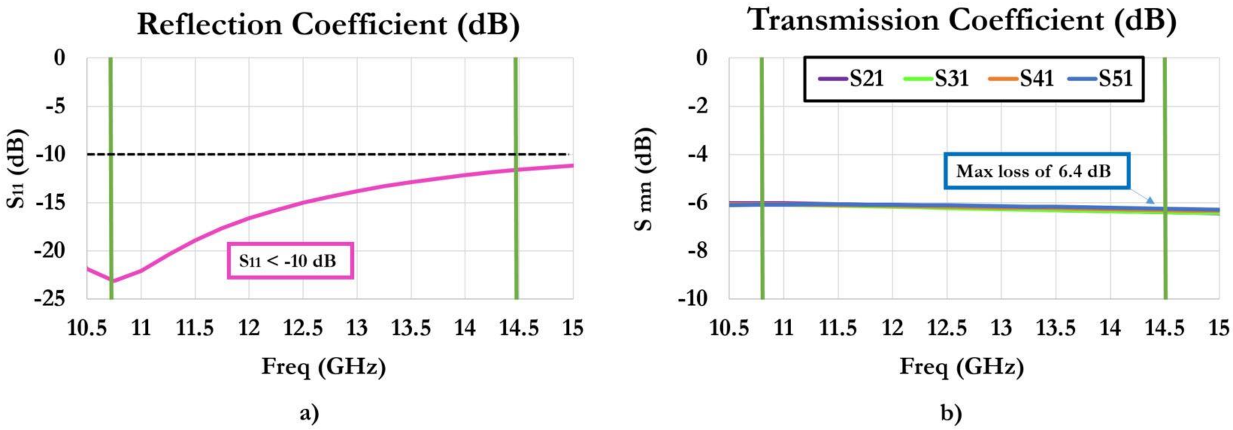

Figure 91 Simulated performances of the 5-port model of the uniform 1:4 power divider in function of frequency: a) reflection coefficient, b) transmission coefficients.

III.4.3 WR-75 transition and flange design

A DRWG-to-WR-75 transition and a flange are required in order to allow the connection and the test of the final 2x2 sub-array with corporate feeding network. The transition is designed starting from the section of the DRWG by chamfering the walls and progressively reducing the thickness of the inner ridges, until the section of a standard rectangular WR-75 waveguide is obtained. The height of the transition is set as design parameter and the value of 24 mm, corresponding to the center wavelength of the operational BW, is found to be the optimum trade-off between achieved performance and form factor. A standard WR-75 flange is designed according to [82] and assembled with the transition, as shown in Figure 92 a) and b). The simulated performance is shown in Figure 92 c): resulting S_{11} stays between -18 and -11 dB, while the transmission losses are between 0.08 and 0.4 dB at lowest frequencies.

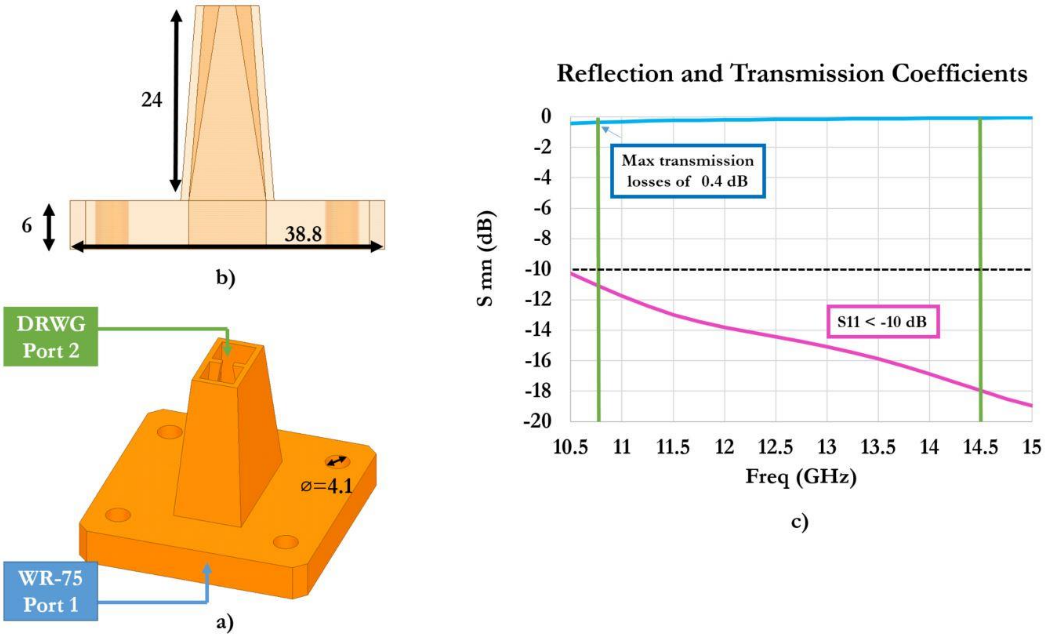

Figure 92 Designed WR-75 flange with DRWG-to-WR-75 transition: a) isometric view with dimensions (mm), b) transparent side-view with dimensions (mm), c) simulated reflection and transmission coefficients.

III.4.4 Simulation of the complete 2x2 array

The previously designed components are assembled in the model of the 2x2 array with corporate feed, as shown in

Figure 93.

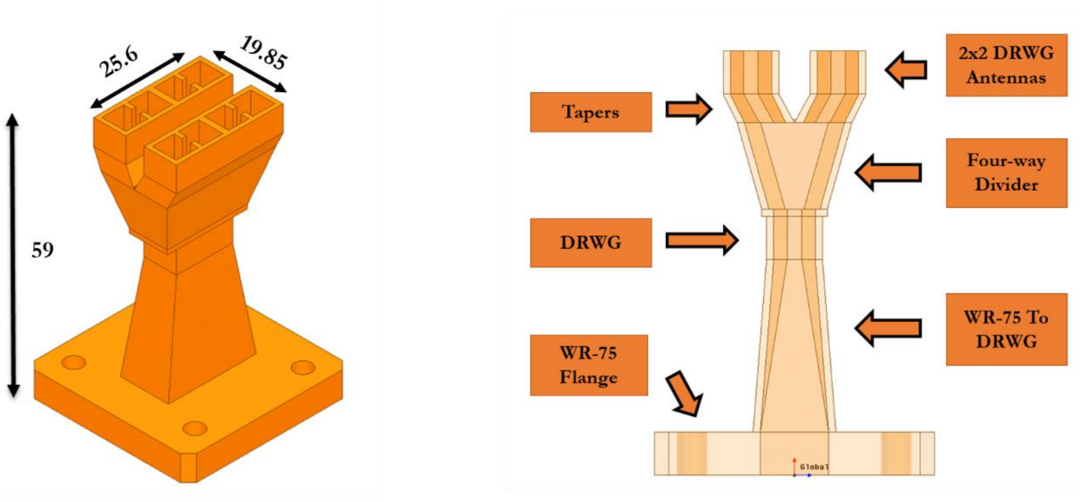

a)

b)

Figure 93 Complete 2x2 array with feeding network: a) isometric view with dimensions (mm), b) transparent side-view with indications of the different components.

DRWG tapers are introduced to connect the four-way power divider to the 4 antennas and respect the initially calculated inter-element distance for ±45° steering. The scattering matrixes of the single components shown in

Figure 93 b) are extracted and used to define a circuit model of the complete array with corporate feeding network in ADS. The obtained ADS schematic is shown in Figure 94.

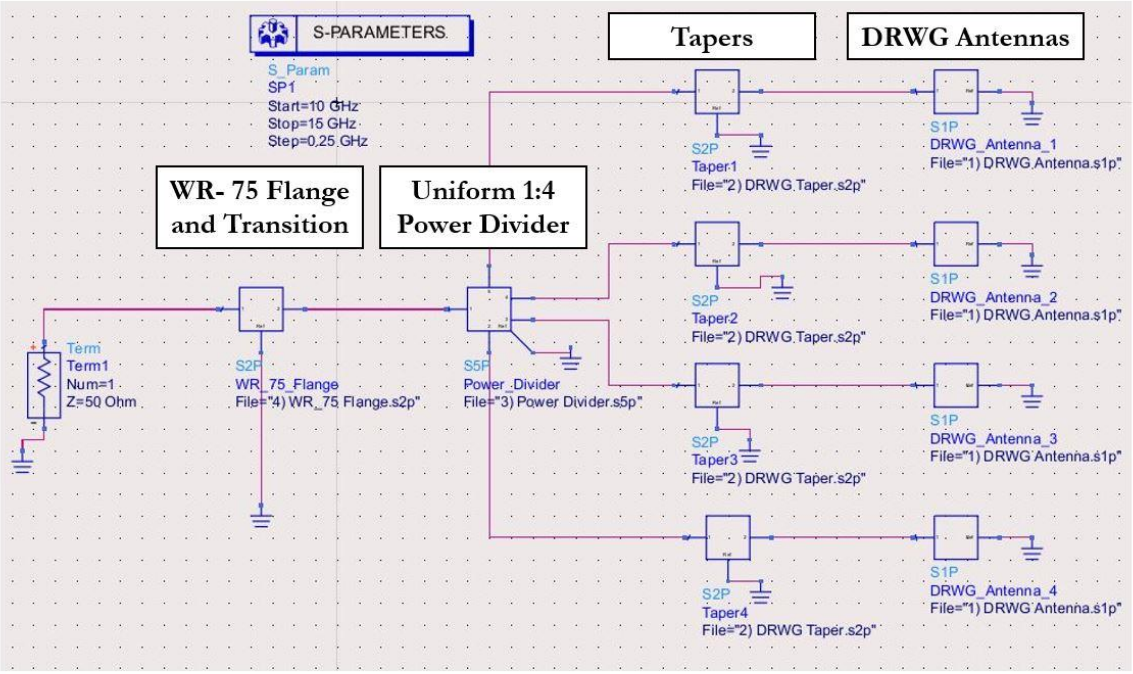

Figure 94 ADS schematic of the complete 2x2 array with corporate feeding network and WR-75 Flange.

Figure 95 shows the results of the schematic (using S-parameters of each building blocks) and HFSS simulations of the complete 2x2 array, in terms S_{11} of versus frequency. HFSS values oscillate around -5 dB, reaching -3 dB at 11.25 GHz.

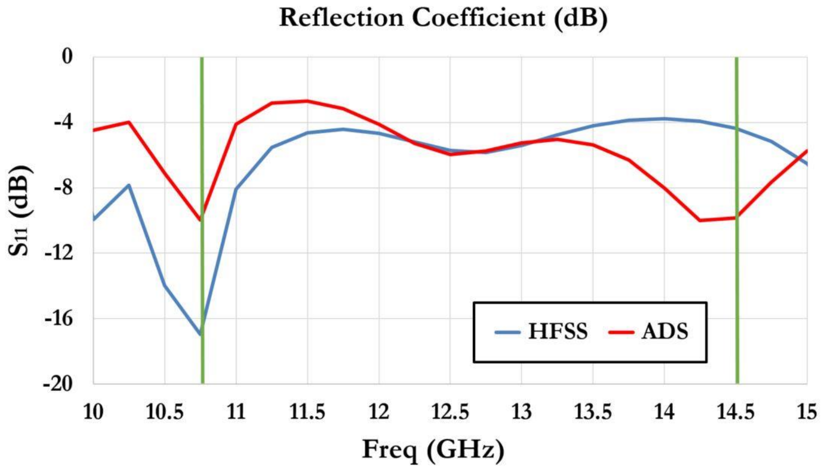

Figure 95 Simulated reflection coefficient of the complete 2x2 array versus frequency, in ADS and HFSS.

ADS simulation manages to model the complete array with a satisfying agreement with HFSS complete model, which suggests that this technique may be used to evaluate the matching of more complex array starting from the scattering matrix of the single blocks and speed up the design flow.

Figure 96 a) shows the simulated total efficiency calculated as the ratio of the radiated power from the structure to the incident one, which stays above 50% along the whole bandwidth. Figure 96 b) shows that the simulated realized gain and directivity oscillate around the mean values of ~9 dBi and ~11 dBi, respectively.

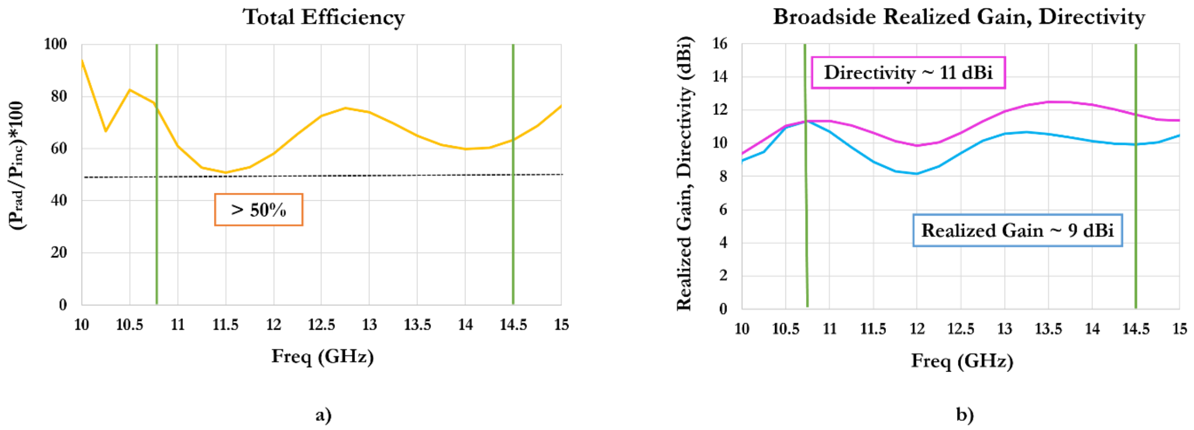

a) b)

Figure 96 Simulated performance of the 2x2 array versus frequency: a) total efficiency, b) directivity and broadside realized gain.

III.4.5 Prototyping using DLMS 3D printing technology

Direct metal laser sintering has been chosen as a low-cost additive manufacturing process to fabricate the designed 2x2 array with corporate feeding network in a single block. The available material from the chosen manufacturer is AlSi10Mg, being the most common aluminum alloy for this technique due to its mechanical and thermal properties [83]. The use of a traditional milling process would have required to realize the structure in different pieces to be assembled together, raising the final cost and the complexity of the fabrication. The principle of the direct metal laser sintering by powder-bed method is illustrated in Figure 97 a). A dispenser contains the metal powder, which represents the raw material, and it is lifted by a piston. A recoater arm places a layer of powder onto the adjacent build platform, where the part of interest is sintered by laser in order to create a single layer of the final structure. Once a layer is sintered, the powder dispenser raises again and the build platform descends of the same height to restart the operation. This iterative process continues until the complete piece is fabricated [84]. Unfortunately, this process poses stringent mechanical constraints: inner surfaces that are parallel to the build platform in the direction of printing cannot be fabricated. Each layer needs to withstand the next one, so parallel surfaces must be replaced by 45° chamfers. Hence, the array model has been modified to comply with those manufacturing constraints and an example of one of these modifications can be appreciated in Figure 97 b).

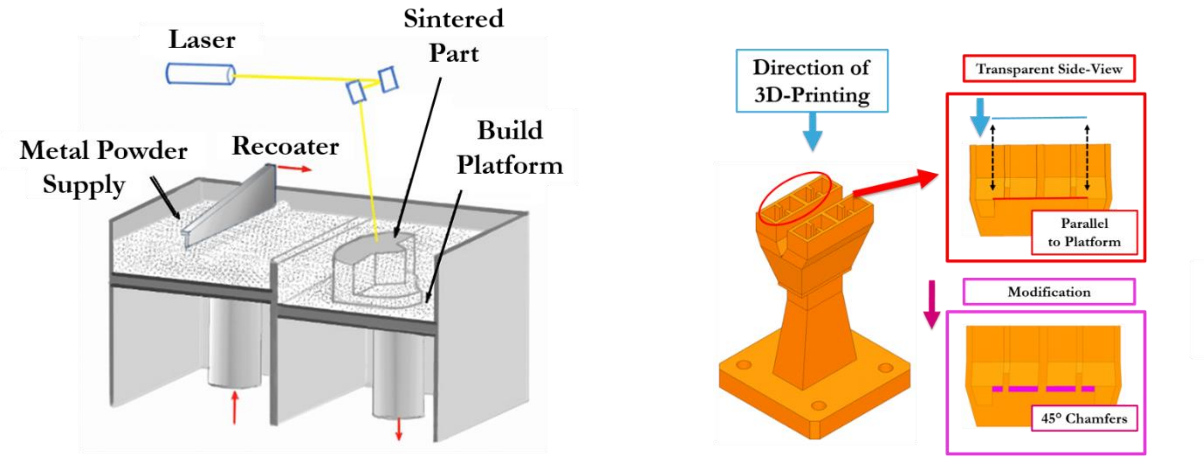

a)

b)

Figure 97 a) DMLS working principle from [84], b) example of a modification of the array model, required to fit the fabrication process.

Figure 98 a) shows the simulated reflection coefficient and total efficiency of the modified model, compared with the performance of the initial one that was not complying with the fabrication constraints. Added chamfers are cause of mismatching, especially at low frequencies, and a consequent decrease of the total efficiency. Three same prototypes were fabricated in aluminum and an example can be appreciated in Figure 98 b).

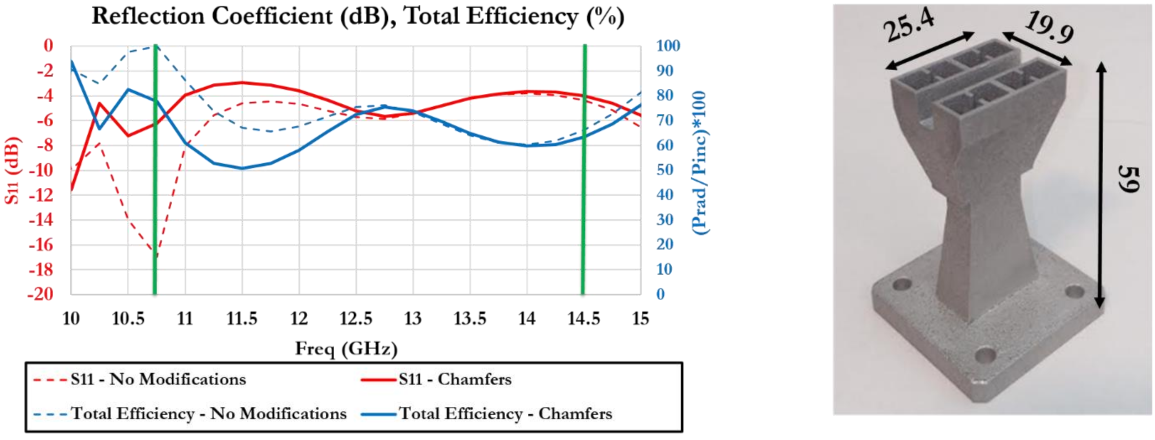

a)

b)

Figure 98 a) Simulated reflection coefficient and total efficiency of the modified array model versus frequency and comparison with the simulated performance of the previous model, b) Picture of the DMLS-fabricated prototype with dimensions in mm.

III.4.6 Measurements

The measurement of the prototypes has been performed in the contest of a collaboration with the University of Oviedo (Spain), leveraging the expertise of Prof. Jaime Laviada Martinez and Guillermo Alvarez Narciandi. The matching of the prototypes is measured using an Agilent PNA-X N5247A, [49] from 10 up to 15 GHz. The results are shown in Figure 99: measured S_{11} values range from a minimum of -9 dB at lowest frequencies to a maximum of -3 dB at 11.25 GHz. A good agreement is found between simulations and tests and it is interesting to underline the robustness of the fabrication process, as the measured responses of the three prototypes are really identical.

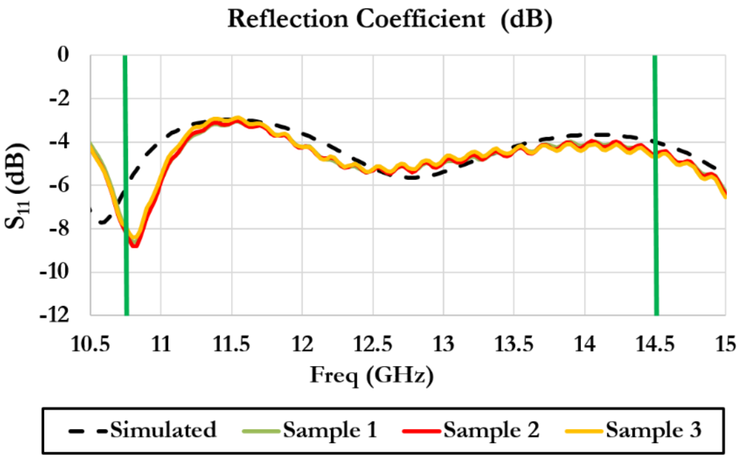

Figure 99 Simulated and measured reflection coefficient of the prototypes versus frequency.

A planar measurement set-up, modified in order to perform far-field measurements, was used to test the radiation performance of the prototypes [85]. The wide measurement band obliges to split the measurements into two sub-bands: (10 – 12.4) GHz and (12.4 – 15) GHz. Two standard Narda 640 and Narda 639 waveguide horns are used as acquisition probes for the low and high sub-bands, respectively [86]. Figure 100 b) shows the table used to evaluate the minimum far-field distance of 10 cm, according to the maximum dimension of the radiating aperture which is shown in Figure 100 a). The antenna under test is placed over a plastic support at a distance of 70 cm from the probe, as shown in Figure 100 c). The polarization is given by the relative alignment of probing antenna and the AUT. The AUT is 360° rotated around the vertical axis (dotted red in Figure 100 c) while the probe stays in the fixed position, in order to acquire a single radiation pattern. Once a first acquisition is completed, the AUT is independently rotated around its horizontal axis (dotted orange in Figure 100 c) up to 360°, with a step of 15°. The first acquisition is repeated for each one of these angular positions in order to extract the complete 3-D radiation pattern. Finally, the measurements are repeated using reference antennas as AUTs and the results are compared with the previous ones in order to calculate the levels of realized gain and directivity. Figure 101 a) shows the measured broadside realized gain of the 3 samples versus the simulated ones, as function of frequency. The measured levels are between 7 and 11.2 dBi with a maximum difference of ~3 dBi from the simulated values at 12.6 GHz. It is worth to underline that the discontinuity we appreciate for measured responses at around 12.4 GHz is in correspondence of the separation between the two sub-frequency bands. The directivity has been measured for only one of the 3 samples, as shown in Figure 101 b). Measured values are between 9.5 and 13.2 dBi, showing a good agreement with simulation results. It is interesting to underline that the measured directivity values are higher than the simulated ones in the frequency range of interest.

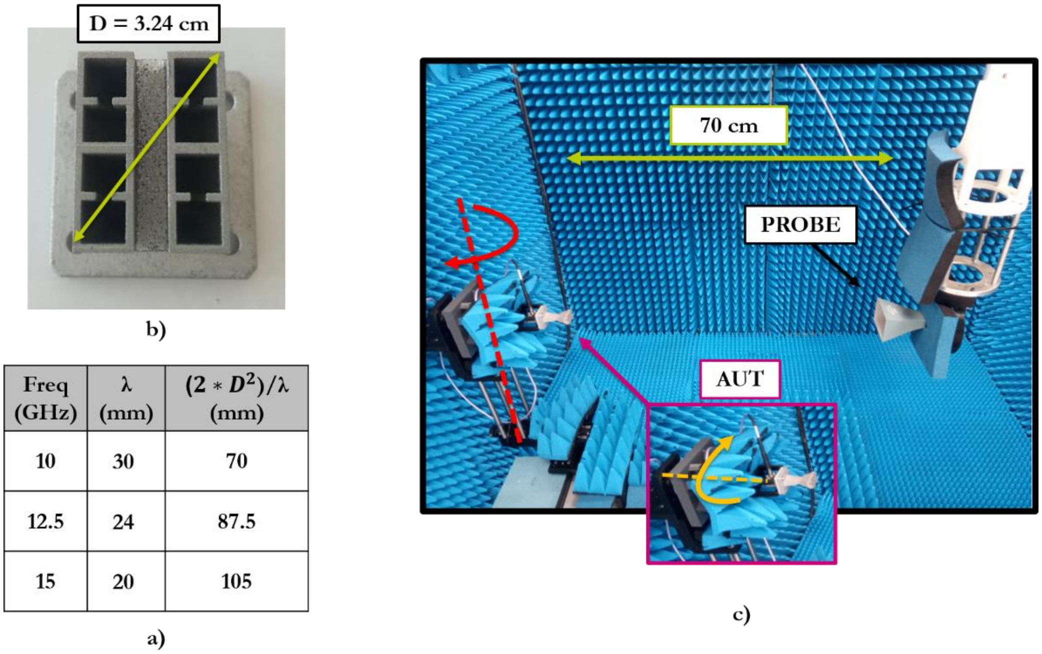

b)

Freq (GHz)	λ (mm)	$(2 * D^2)/\lambda$ (mm)
10	30	70
12.5	24	87.5
15	20	105

a)

c)

Figure 100 a) Top-view of the prototyped array with indication of the maximum dimension of the aperture, b) calculated far-field distances for low, middle and high frequencies of the measurement band, c) picture of the sample and the probe within the measurement range with indications of the rotation axis of the AUT.

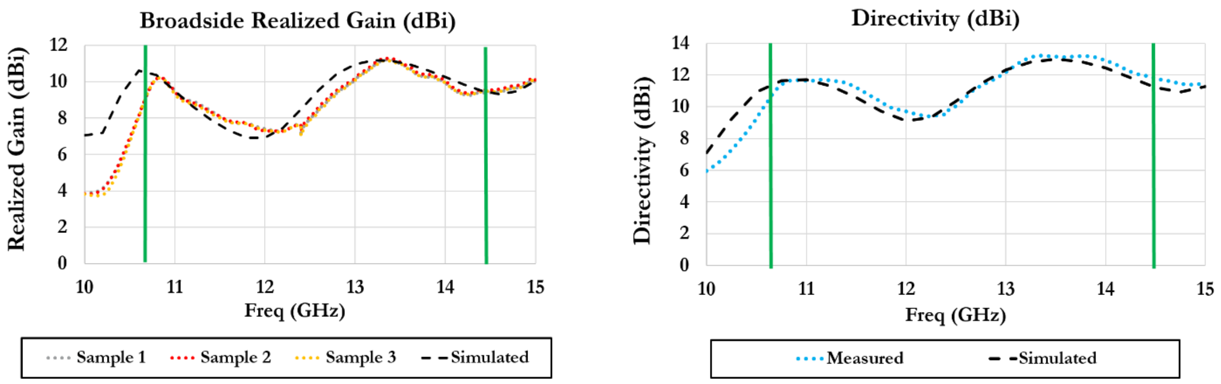

a)

b)

Figure 101 Measured and simulated performance of the prototypes versus frequency: a) broadside realized gain, b) directivity for a single sample.

Figure 102 a) shows the reference system for the measurement of the realized gain patterns, in terms of E- and H-plane. Figure 102 b) shows the measured realized gain patterns at 12.5 GHz in both E and H planes, for co- and cross-polarizations. According to the setup shown in Figure 100 c), the polarization is defined by chosen alignment of the probe with respect to the sample. We can appreciate a good agreement between simulated and measured patterns, the x-pol data are less reliable due to the very low levels but the measured ones stay below -20 dB.

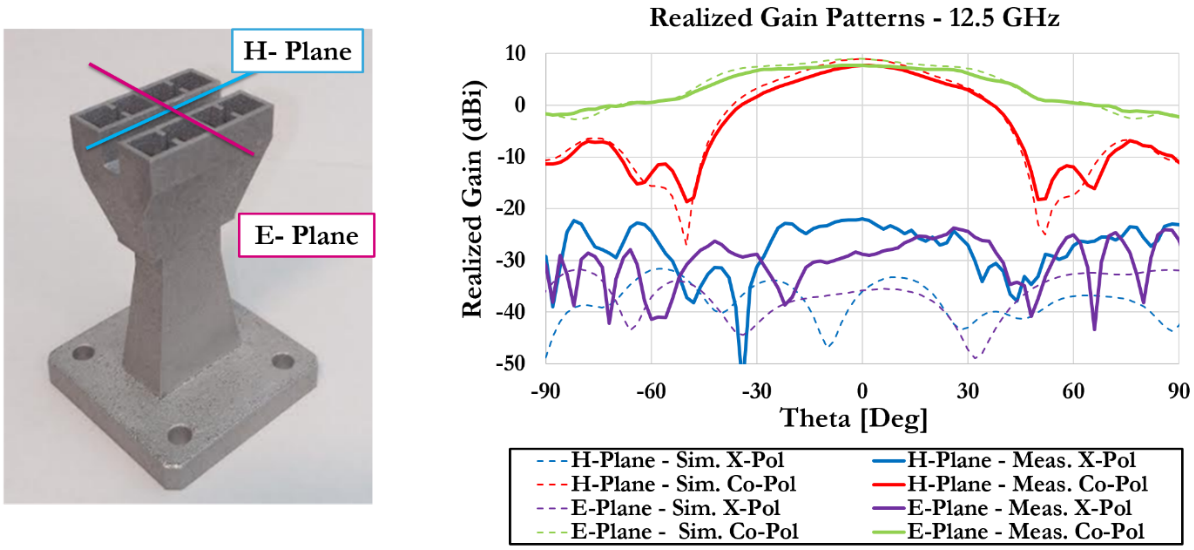

a)

b)

Figure 102 a) Picture of one Prototype with reference system for radiation pattern measurements, b)Simulated and measured realized gain in E and H Planes at 12.5 GHz (Co-Pol and X-Pol are defined by the relative alignment of probe).

III.4.7 Benchmarking with state-of-the-art antenna solutions

It is not possible to make an exhaustive comparison of simulation or test results with any high-efficiency 2x2 antenna array working at the same frequencies. Up to our knowledge, there are not enough data in literature about such a small array configuration allowing to perform a consistent benchmarking. Table 15 gives a comparison of the measured peak gain, bandwidth, fractional bandwidth and polarization of our 2x2 array prototype with some of the works reviewed at the beginning of this chapter. Unfortunately, the data given in the related publications are restrained to the measurements of larger array configurations, so the presented measured peak gain values have been extrapolated by the application of the array factor formula. It is worth to underline that this kind of extrapolation leads to values that are generally lower than those that could be obtained analyzing a 2x2 unit cell by itself. Even taking into account the limitation of this approximation, it is evident that the proposed solution is in line with state-of-the-art solutions and over performs some of them. Considering the BW, there are no reported examples in literature nor commercial solutions conceived to cover the whole Ku- bandwidth with high-efficiency. Table 15 shows that the fractional bandwidth of our solution corresponds almost the double of the reviewed example with the largest operational bandwidth. The envisaged possibility to merge Rx and Tx functionalities using a single antenna already represents a major innovative step even if the design will need to be furtherly modified in order to support a double linear polarization feature.

Antenna Type	Measured Peak Gain For 2x2 Array	Bandwidth	Fractional Bandwidth	Polarization
CONFORMAL SLOTTED WAVEGUIDE (Guennou-Martin et al., 2017)	**4.6***	**N.A.**	**N.A.**	**Single Linear**
SLOTTED WAVEGUIDE WITH POLARIZERS (K.Son et al, 2006)	**9.5***	**(11.7 – 12.75) GHz**	**8%**	**Dual Circular (Mechanical Pol. Switch)**
DRWG (This work)	**11.7**	**(10.75 – 14.5) GHz**	**30%**	**Single Linear**
HORN (K.S.Feng et al., 2014)	**15.1***	**(12.25 – 14.5) GHz**	**17%**	**Dual Linear**
CAVITY-BACKED SLOTTED WAVEGUIDE (G.L.Huang et al., 2012)	**15.9***	**(14 – 16.5) GHz**	**16%**	**Single Linear**

Table 15 Measured peak gain, bandwidth, fractional bandwidth and polarization of the fabricated 2x2 DRWG array working at Ku-band, compared to the most relevant high-efficiency antenna arrays working at Ku- band reported in literature in 2x2 configuration [11], [17], [18], [19]. *Peak gain values have been extrapolated by mean of the array factor formula from the measurements performed over larger arrays: 44 elements for the conformal slotted waveguide array, 128 for the slotted waveguide array with polarizers and 256 for the horn array.

III.5 Innovative 4x4 Ku-band DRWG antenna array

The goal is now to create a 4x4 array with corporate feeding network leveraging the designed 2x2 DRWG sub-array. The envisaged 4x4 array is meant to have a single input with a WR-75 flange and transition, as done before. The aim is to prove the scalability of the concept and the possibility to apply the additive manufacturing process to a bigger and more complicated structure.

III.5.1 Feeding network overall strategy

The immediate approach would be to design the 4x4 array starting from the previously developed 2x2 sub-array by adding a second level of 1:4 power dividers and using DRWG tapers to connect them to the antennas while keeping the required spacing. As shown in Figure 103, the main drawback of this approach would be the height of the complete structure resulting to be equal to ~10 cm. The height of the design is strongly increased by the necessity to add a level of DRWG connection and by the height of the power dividers. Taking into account the requirements for the final user terminal depicted in Chapter 1, we propose the integration scheme shown in Figure 104. Its maximum height is 7 cm and it requires the design of new components such as DRWG 90° bends and DRWG tee-junctions for both E and H planes.

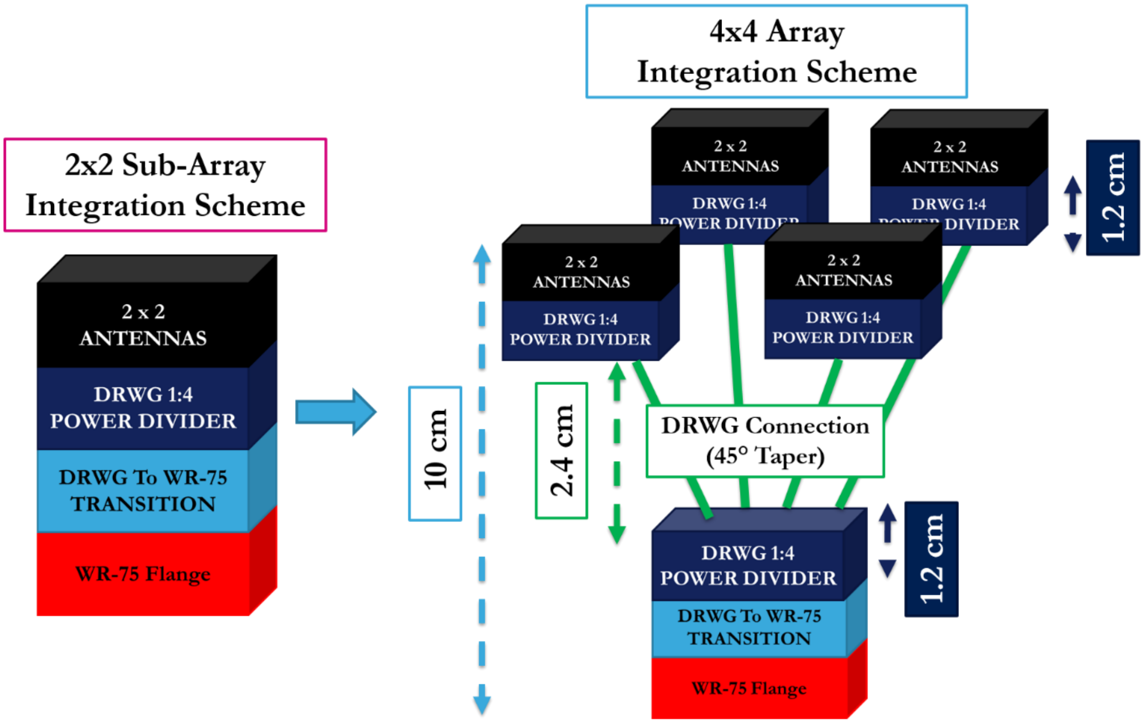

Figure 103 Possible integration scheme of the 4x4 array starting from the previously developed 2x2 sub-array and adding a second level of 1:4 power dividers and antennas (not in scale).

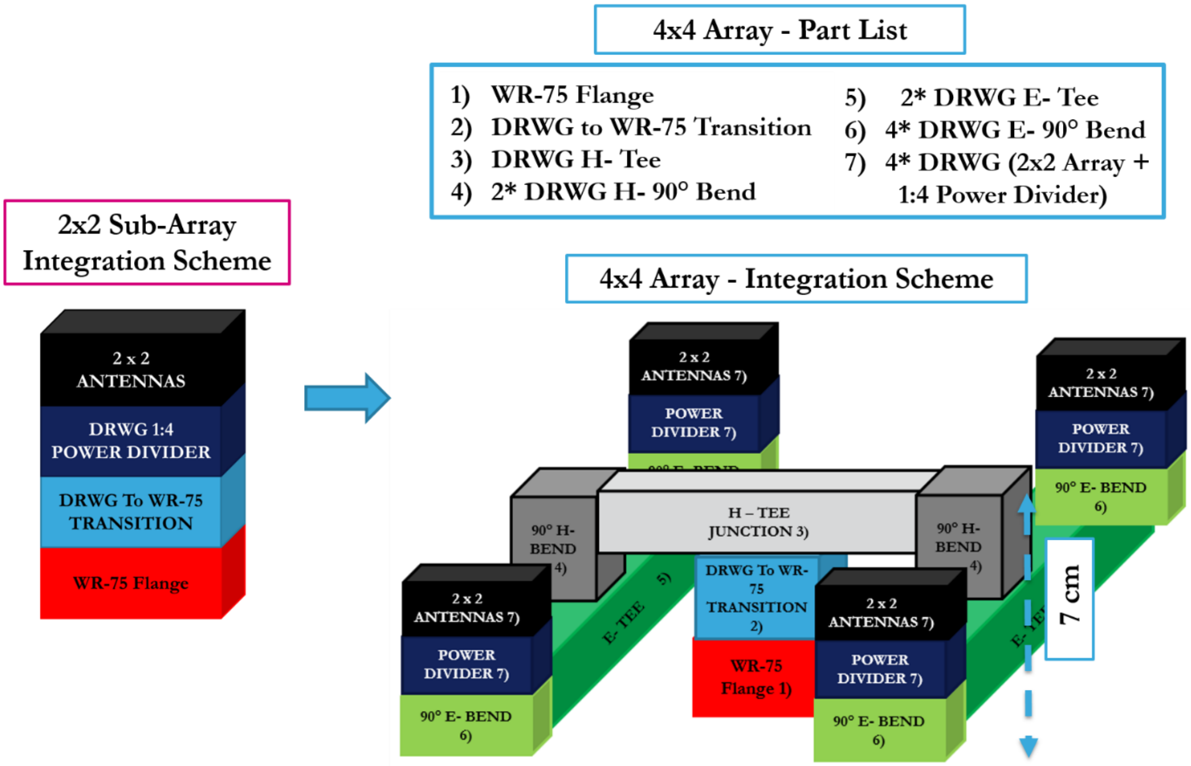

Figure 104 Envisaged integration scheme and list of parts required for the design of a 4x4 array with corporate feeding network, leveraging the previously designed 2x2 sub-array (not in scale).

III.5.2 DRWG Tee-junction for H- Plane

A DRWG tee-junction working in the H-Plane is the first part required by the corporate feeding network of the 4x4 array according to the scheme in Figure 104. An initial design was obtained crossing two DRWGs in the H-plane, as shown in Figure 105 a) and b). The simulated matching is shown in Figure 105 c) for the three ports, staying between -4 and -9 dB in all cases. The simulated losses are shown in Figure 105 d), resulting in higher values than 4 dB in all cases and in the whole bandwidth of interest. The maximum loss is equal to 5 dB at the lowest frequency, resulting in 2 dB worse than the expected theoretical 3 dB in order to realize half-power splitting. Hence, we modified the design adding an iris along the H- plane direction in the central section of the junction following the method proposed in [87] as it can be appreciated in Figure 106 a) and b). The dimensions of the iris have been optimized via simulation in order to obtain the best performance in the frequency range of interest. Simulated matching performance are shown in Figure 106 c): S_{11} is below -20 dB with a consistent improvement if compared to the previous case where the value stood between – 4 and -7 dB. Simulated S_{22} and S_{33} of the model with iris are ~-6 dB, while they stood between – 4 and -9 dB in the previous case. Simulated transmission losses of the new model are shown in Figure 106 d) with a maximum value of 3.1 dB, being 0.1 dB higher than the 3 dB required for the uniform 1:2 power splitting. The improvement is consistent, if compared to the previous case where transmission losses stood between 4 and 5 dB.

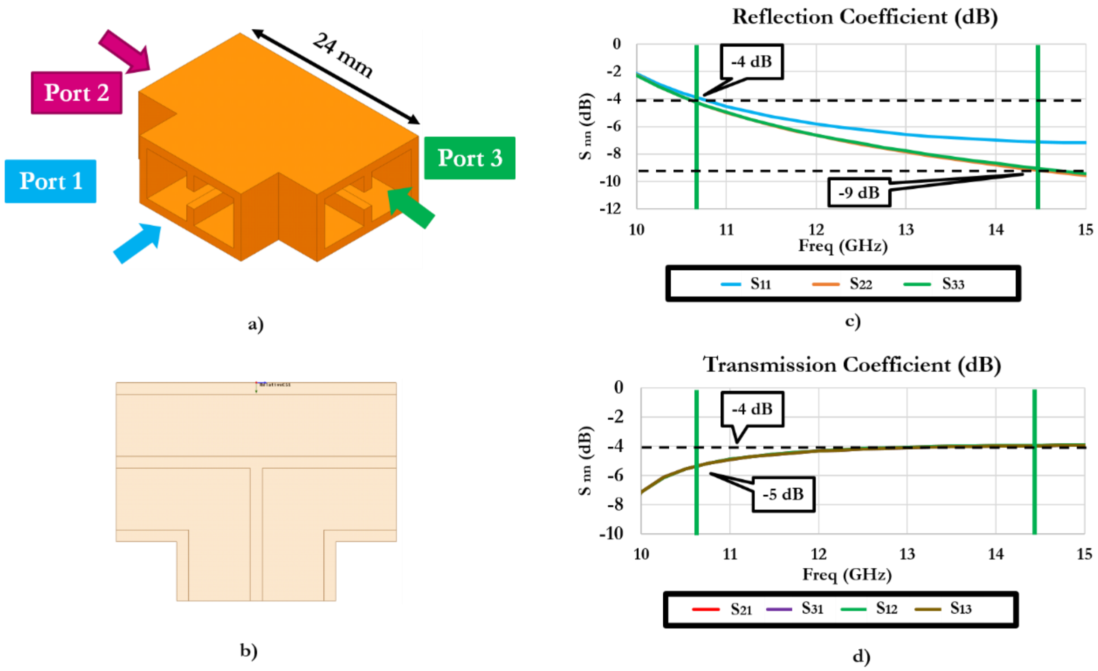

Figure 105 Initial design of the DRWG tee-junction for the H-Plane: a) isometric view, b) transparent side-view, c) simulated reflection coefficients, d) simulated transmission coefficients.

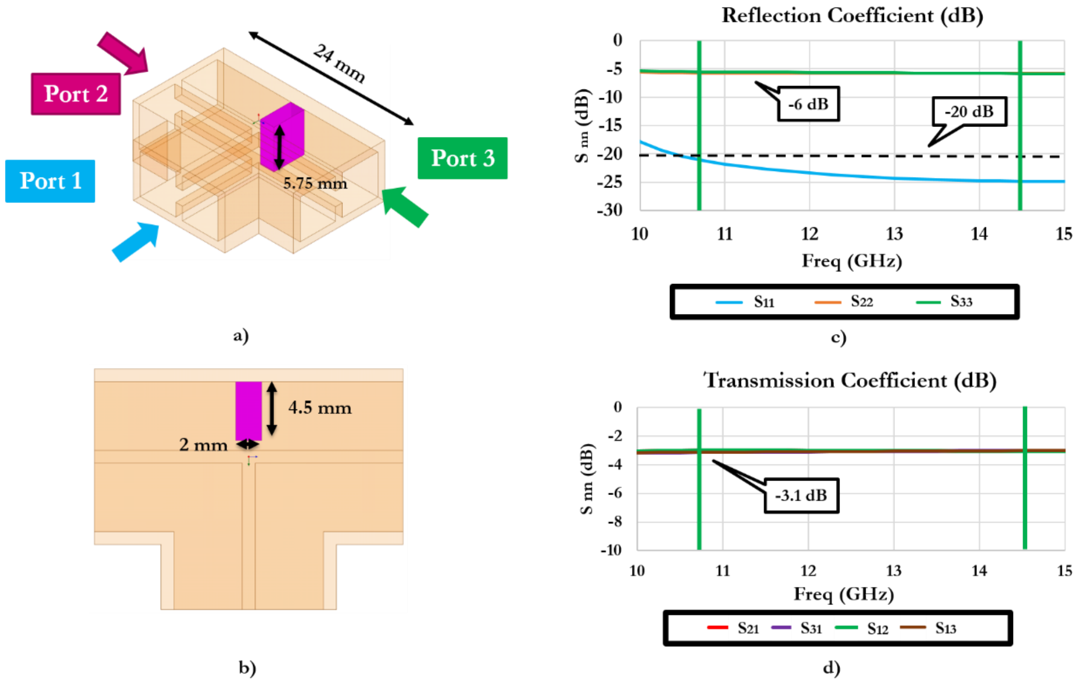

Figure 106 Modified design of the DRWG tee-junction for the H-Plane with iris: a) isometric view, b) transparent side-view, c) simulated reflection coefficients, d) simulated transmission coefficients.

III.5.3 90° DRWG bend design for H-Plane

Figure 107 shows the designed DRWG 90° bend for the H-plane and its simulated performance: the S_{11} is better than -30 dB along the bandwidth of interest with maximum transmission losses of 0.06 dB at lowest frequencies.

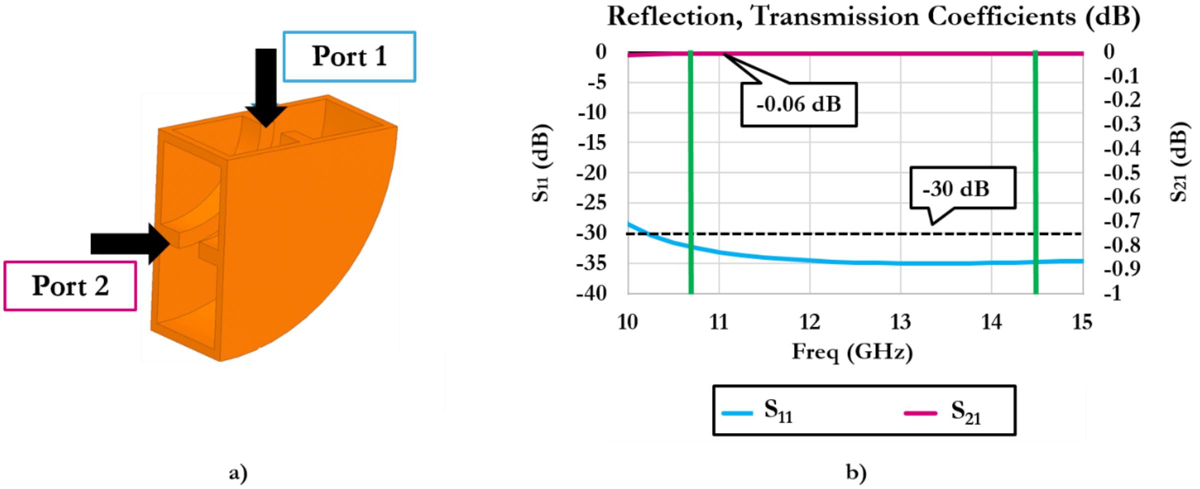

Figure 107 a) Designed DRWG 90° bend for the H-plane, b) simulated reflection and transmission coefficients of the designed structure versus frequency.

III.5.4 DRWG Tee-junction for E- Plane

A DRWG tee-junction working in the E- plane was designed crossing two DRWGs in the E-plane, as shown in Figure 108 a). The alignment of the electric field line is shown in Figure 108 b), resulting in 180° phase difference at the output ports. The issue is solved by the use of 90° DRWG bend for the E-plane in the final structure. As we can see in Figure 108 c), the matching of the three ports is symmetric staying between -6 and -9 dB. Transmission performance is shown in Figure 108 d) with maximum losses of 4 dB. Taking into account the 3 dB required for the targeted uniform 1:2 splitting, we get 1 dB of additional losses for each branch which is considered to be not satisfying. Hence, the performance of this part is not improved by modifying the design according to the approach suggested in [87]: an iris is added along the E- plane next to port 1, as shown in Figure 109 a) and b). Its dimensions and position are optimized via simulation in order to obtain the best performance in the frequency range of interest. Matching can be appreciated in Figure 109 c): S_{11} is below -15 dB along most of the bandwidth, while S_{22} and S_{33} stay ~ -7 dB. Transmission losses are symmetric considering the two output ports with maximum loss of 3.3 dB at highest frequencies, which represents an improvement of 0.7 dB for each branch if compared to the initial design.

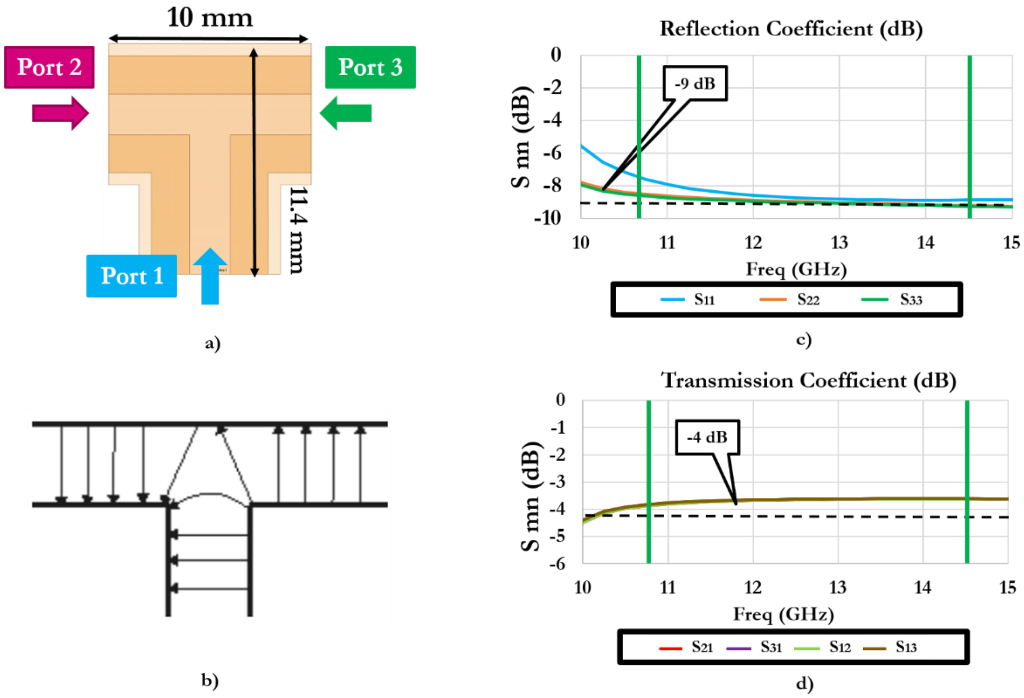

Figure 108 Design of the DRWG tee-junction for the E-Plane: a) Transparent side-view, b) electric field lines in the tee-junction, from [88], simulated performance: c) reflection and d) transmission coefficients.

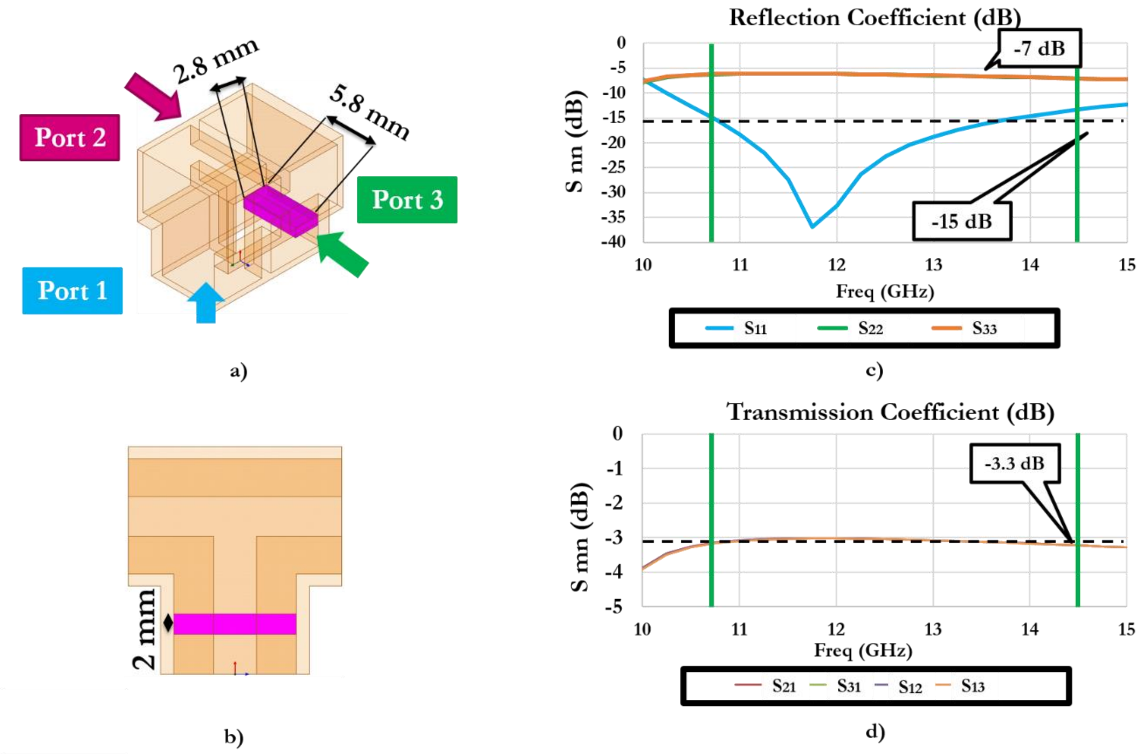

Figure 109 Modified DRWG tee-junction for the E-Plane: a) transparent isometric and b) transparent side-view with highlighted iris, simulated performance: c) reflection and d) transmission coefficients.

III.5.5 90° DRWG bend design for E-Plane

Figure 110 shows the designed DRWG 90° bend for the E-plane and its simulated performance: the S_{11} is better than -15 dB along the BW of interest with maximum losses of 0.06 dB at 10.75 GHz.

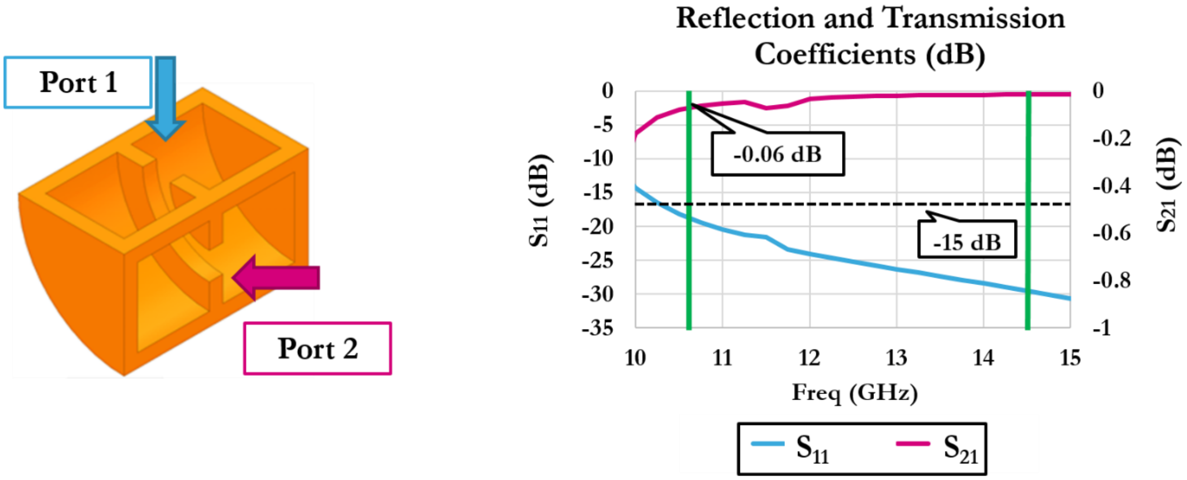

a)

b)

Figure 110 a) Designed DRWG 90° bend for the E-plane, b) simulated reflection and transmission coefficients of the designed structure versus frequency.

III.5.6 4x4 array with corporate feeding network

The previously designed parts have been assembled to create the 4x4 array with corporate feeding network as shown in Figure 111. It can be noticed in Figure 111 c) that we needed to redesign the 3D model of the tee-junction for the H-Plane in order to fit the size constraints while keeping the performance in line with what was reported in Figure 106. The scattering matrix of each one of the components shown in Figure 111 a) is extracted from the HFSS simulations in the frequency range of interest and used to create a schematic model of the complete 4x4 array with feeding network in ADS as shown in Figure 112 a). The simulated reflection coefficient versus frequency is shown in Figure 112 b): the results of the schematic and the HFSS simulations are overlapped. The HFSS simulation shows a peak of the return loss at 14.25 GHz with S_{11} ~-2 dB. The best matching is at 11.75 GHz where the S_{11} results equal to – 22 dB. The average value of the S_{11} results is equal to -7 dB along the range of interest. The complex structure leads to non-negligible interactions between the other parts of the complete array that cannot be modeled using the schematic simulation. Taking into account the last consideration and the wide FBW, we can appreciate a good agreement between the two simulations. Looking at ADS results, we can see that the matching is better at high frequencies and worse at lower ones, with an average value of -6.7 dB that results in comparable values as the – 7 dB from the HFSS case.

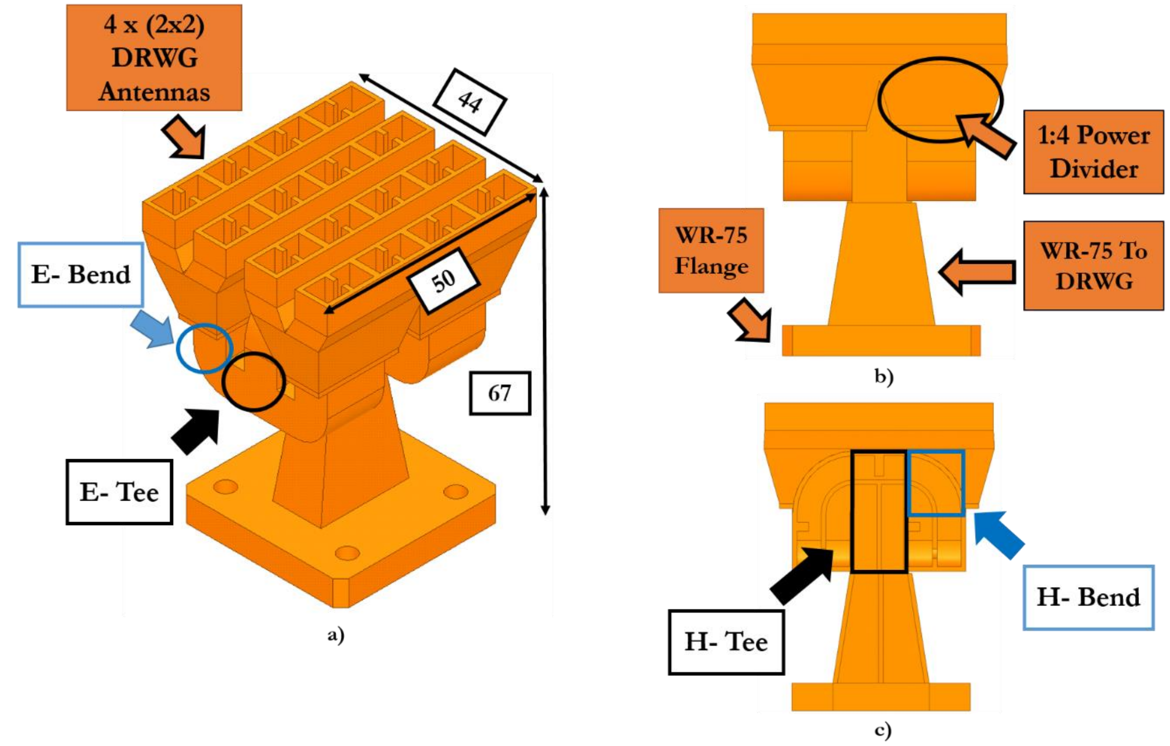

a)

b)

c)

Figure 111 Assembled 4x4 Array with feeding network: a) isometric view with dimensions in mm, b) side-view, c) side-view (cut).

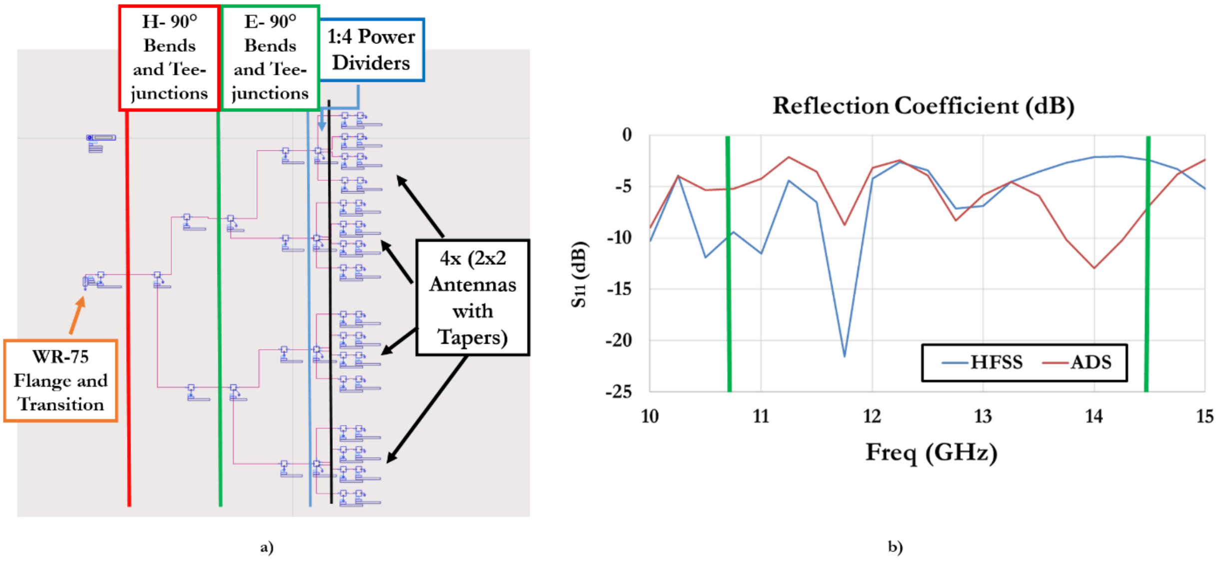

a)

b)

Figure 112 a) ADS schematic of the complete 4x4 array with its feeding network, b) Simulated reflection coefficient of the complete 4x4 array with its feeding network versus frequency in ADS and HFSS.

Figure 113 shows the simulated broadside realized gain and directivity of the complete 4x4 array with feeding network versus frequency compared with those of the complete 2x2 array with feeding network. The broadside realized gain of the 4x4 array oscillates around 15 dBi with an average improvement of 6 dBi if compared to the 2x2 array. The directivity is around 16.5 dBi, with an average improvement of 5.5 dBi.

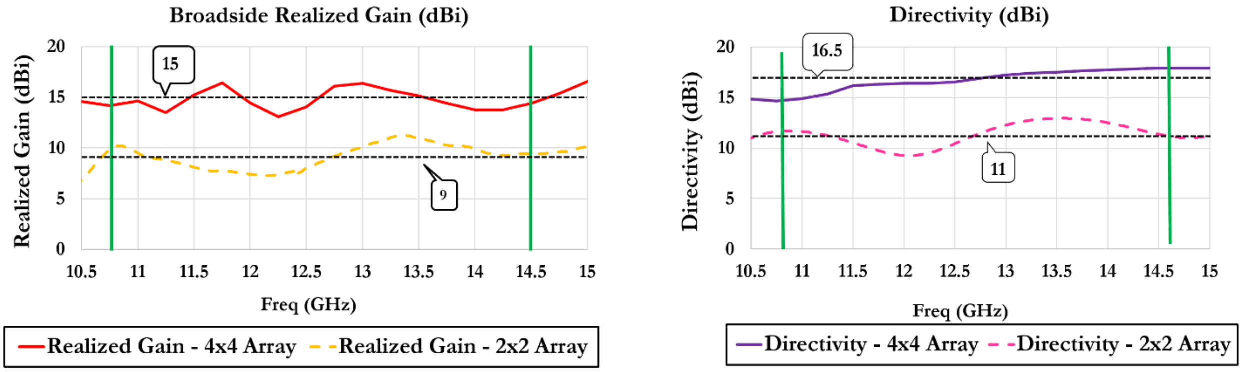

a) b)

Figure 113 Simulated performance of the complete 4x4 array with its feeding network (continuous line) and the 2x2 array with its feeding network (dashed line): a) broadside realized gain versus frequency, b) directivity versus frequency.

III.5.7 4x4 array with horn-like DRWG

The matching represents the main drawback of the designed 4x4 array with its feeding network, so we decided to taper the open-ended DRWG along the E-plane, as shown in Figure 114 [54].

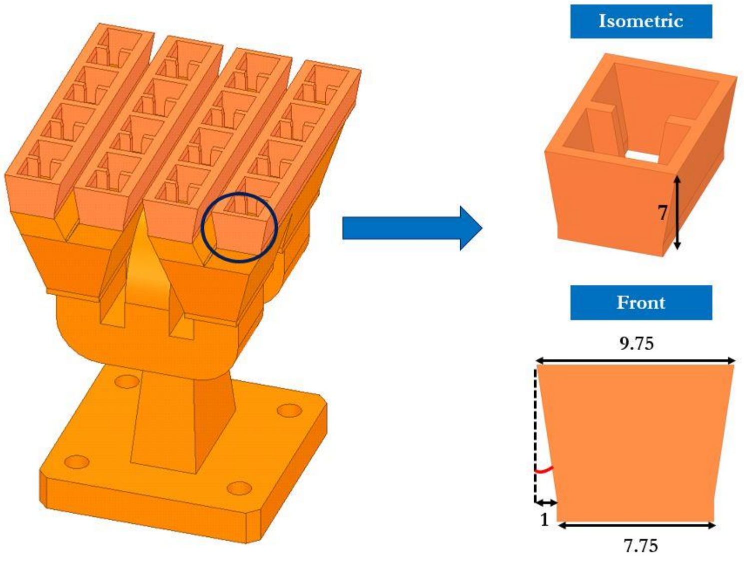

Figure 114 3D view of the 4x4 array with horn-like DRWGs, dimensions in mm.

The resulting radiating element has a height of 7 mm with a maximum difference of 2 mm between the top and bottom width with an optimal angle of 33°. Figure 115 shows the comparison of the simulated reflection coefficient and broadside realized gain of the design with horn-like DRWG antennas versus the previous one. Performance are comparable with improvements at lowest and highest frequencies, where the broadside realized gain increases of 0.6 and 1.4 dB, respectively.

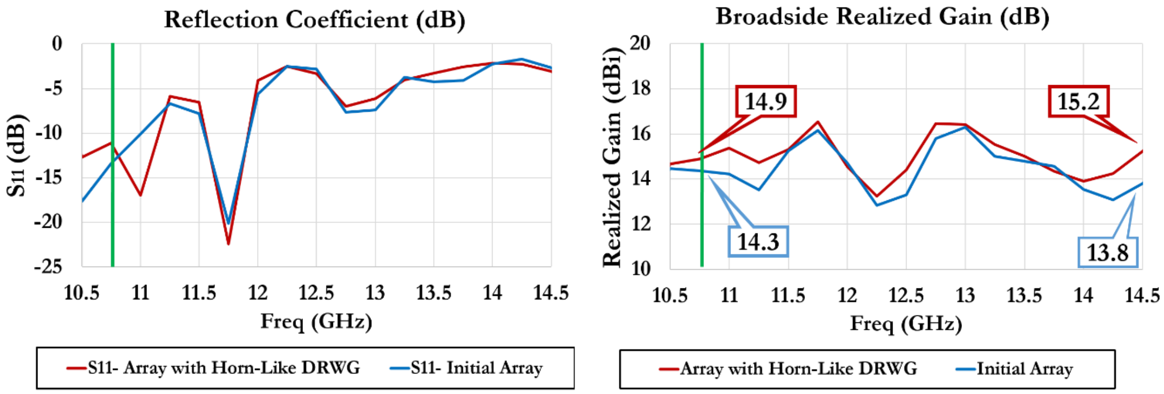

a) b)

Figure 115 Simulated performance of the 4x4 array with horn-like DRWGs versus frequency, compared with those of the initial array: a) reflection coefficient, b) broadside realized gain.

III.5.8 4x4 array with horn-like DRWG and parasitic patches

The goal is to further improve the performance of the array by adding a parasitic patch for each antenna as shown in Figure 116. The idea is to leverage the patch designed for the ACPA design working at Ku- band developed in Chapter 2. The same substrate as before is used, being NELCO 4000 – 13 Si EP (εr =3.7, tg(δ) =0.009), and the idea is to choose thinnest PCB as possible, being 100 µm in this case. The thickness of the PCB for the ACPA was 2.3 mm, so we proceed suspending the substrate over an air gap with a thickness optimized via simulation and set it equal to 3 mm. The dimensions of the square patch are 4.4 mm x 4.4 mm, as in the ACPA case. The simulated reflection coefficient and total efficiency are plotted versus frequency in Figure 117 a) and b), respectively, and compared with the previous solution without patches. Performance is consistency improved at high frequencies, notably the matching results in 8 dB better at 12.75 GHz and 7 dB better at 14.25 GHz. We underline an absolute increase of the 49% concerning the total efficiency at 14 GHz. Figure 118 shows the simulated broadside realized gain and directivity versus frequency, compared with those of the previous design without patches. The minimum value of the broadside realized gain is 14 dBi at 12 GHz and the overall performance of the previous solution is improved especially at high frequencies, where we have an increase of 3.65 dB at 14.25 GHz. The directivity stays between 15 and 18 dBi, practically unaltered if compared to the design without patches.

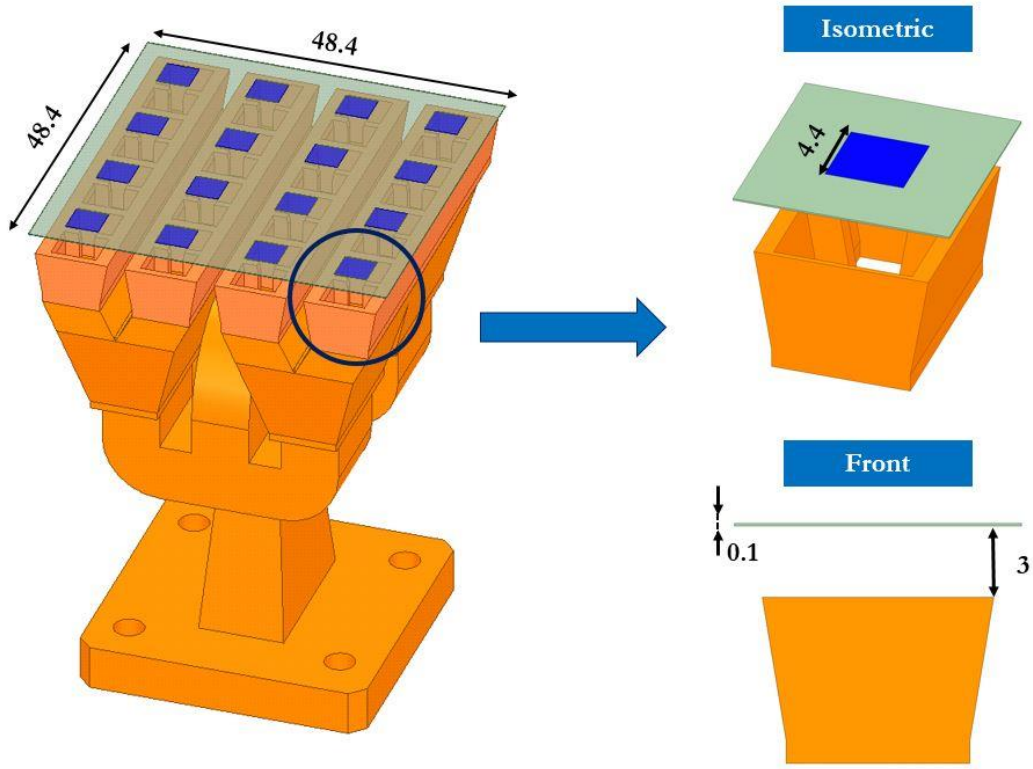

Figure 116 3D view of the 4x4 array with horn-like DRWGs and parasitic patches, dimensions in mm.

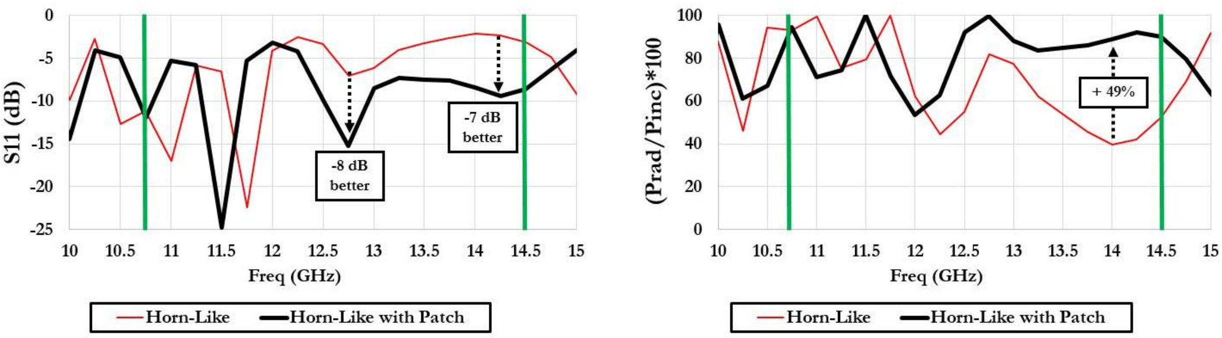

a) b)

Figure 117 Simulated performance of the 4x4 array with horn-like DRWGs and parasitic patches versus frequency, compared with the previous solution without patches: a) reflection coefficient, b) total efficiency.

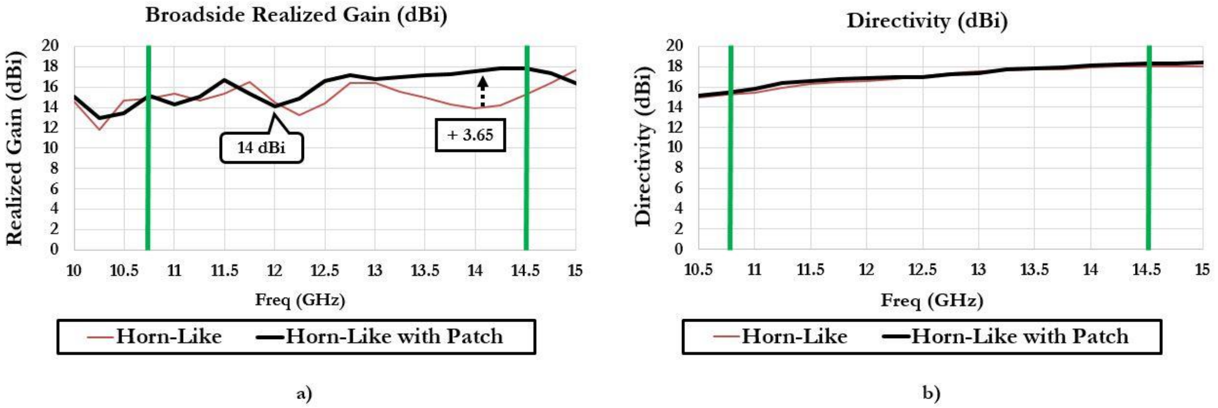

Figure 118 Simulated performance of the 4x4 array with horn-like DRWGs and parasitic patches versus frequency, compared with the previous solution without patches: a) broadside realized gain, b) directivity.

III.1 Pros and cons of proposed solution

It is interesting to underline that ~11.7 dBi of measured gain are obtained in broadside direction at 14.5 GHz (Sat-Com-On-The-Move Tx band) for the fabricated 2x2 DRWG antenna array. The Tx gain of a compact slotted waveguide array-based antenna panel of a commercial user terminal was given in Chapter 1 at the same frequency, being equal to 36 dBi. Hence, the same value was envisaged for a possible consumer-friendly Sat-Com-On-The-Move user terminal to be realized leveraging our antenna solution working at Ku-band. An antenna array created leveraging the 2x2 DRWG antenna unit cell designed in this chapter may guarantee 33 dBi of gain, if composed by 512 elements, or 36 dBi, if composed by 1024 elements, being in line with the mentioned specification. Two of the advantages of the proposed solution are related to the wide operational BW guaranteed using a compact radiating element and the possibility to achieve ±45° of electronic steering in elevation, guaranteeing a maximum scanning loss of 1dB. This allows to create a single Rx/Tx panel, instead of splitting the functions into two distinct panels, with the consequent benefits in terms of cost and form factor for the complete user terminal. Moreover, the leveraged DMLS fabrication process would allow to realize the antenna panel with its DRWG-based feeding network in a single block, without the needs for the various fabrication and assembly steps that would be required by the tradition metal machining methods. Another appealing feature of this solution is the possibility to envisage the design of a large array working at Ku-band that would not be affected by the losses associated to a microstrip line feeding network at these frequencies. At the same time, only one polarization is supported while two orthogonal linear ones are needed in order to satisfy the requirements of the Sat-Com-On-The-Move applications at Ku-band. The mechanical constraints due to the chosen fabrication method and previously discussed in this chapter represents a challenge if the modification of the radiating element and of the related feeding network are envisaged in order to support a double orthogonal polarization. The same challenges will need to be overcome in order to prototype the 4x4 array with the related complex feeding network.

IV. INNOVATIVE 3D-PRINTED WIDEBAND AND HIGH-EFFICIENCY KA- BAND ANTENNA ARRAY

In the previous chapter we have presented the design of wideband and high-efficiency 2x2 and 4x4 double ridged waveguide antenna arrays for Sat-Com-On-The-Move applications at Ku- band, to be used as unit cells for the development of large arrays. The objective was to realize a compact user's terminal able to guarantee the same performance as a traditional reflector–based solution with a price affordable by mass-consumers. The possibility to leverage an additive manufacturing technique like DMLS has allowed to fabricate the 2x2 antenna array and the relative feeding network as a single block paving the way to apply the same technique for bigger and larger prototypes.

The objective of this chapter is to propose a similar approach for SOTM applications at Ka- band (18-31 GHz). We begin with the introduction of the challenges related to the development of wideband antennas for high-efficiency phased arrays working at Ka-band and the possibility to leverage the results obtained at Ku-band underlining the main differences between the two cases. The computation of the array inter-element distance needed to guarantee ±45° of grating lobes–free steering at 31 GHz represents the starting point of our development, as it defines the form factor of the single radiating element. Hence, the development of a single high-efficiency and wideband double ridged waveguide antenna to work at these frequencies is presented. The integration strategy and the development of a 2x2 array leveraging the designed radiating element are also presented. A particular attention is given to the study of a feeding network able to fit the mechanical constraints of the envisaged fabrication process while respecting the previously determined form factor for the 2x2 array configuration. The simulated performance of the complete design is presented. Finally, the prototyping by DMLS and the relative issues are discussed, as well as the measurements of the fabricated samples. The last part of the chapter proposes the benchmarking of our development with existing high-efficiency antenna arrays for SOTM applications at Ka-band and the discussion of the advantages and the drawbacks of our proposed solution.

IV.1 Bandwidth challenges of Ka-band antennas

The development of a low-cost and low-profile full-duplex user's terminal for SOTM applications with a single antenna panel for transmission and reception requires radiating elements able to cover 53% of fractional bandwidth at Ka-band (18 – 31 GHz). This represents a challenge from the perspective of the design of a phased array antenna. The ACP antennas developed in Chapter 2 show functionalities over such a wide frequency range, but they could not be integrated in a large array able to satisfy the gain requirements of the communication with LEO orbit satellites. As discussed in Chapter 2, the emerging surface wave phenomena would drastically deteriorate the functionalities of such an array. Moreover, the losses associated to a theoretical microstrip feeding network for a large array would be unbearable at these frequencies. As far as the author knows, there are no examples in the literature or commercial solutions of such phased arrays able to guarantee the full-duplex functionalities through a single panel with low-cost structure. Hence, we considered the double ridged waveguide antenna as a candidate to propose a phased array solution whose operational bandwidth, efficiency and scanning capabilities would together represent a major innovation in the field.

IV.2 Opportunity to leverage DRWG antenna array solution validated at Ku-band.

Considering the results obtained in Chapter 3, the logical approach would be to scale the 2x2 solution validated at Ku-band in order to work at Ka-band, where the fractional bandwidth is incremented of > 20% if compared to the Ku- case. The versatility of the DRWG design allows to design a radiating element complying with the new requirements as we detail in the next paragraph. The main drawback concerns the cavity-based power divider: Figure 119 shows the cavity-based power splitter for the Ku- band and the best solution obtained for Ka-band. In order to be able to compare the designs, we normalize the dimensions to the wavelength corresponding to the central frequency of each bands. Once all the design parameters discussed in Chapter 3 are optimized via simulations, an iris is added inside the cavity along the H-plane and optimized. Ku- and Ka- designs have comparable form factors, while the iris is the biggest one allowed by the fabrication process design rules. Figure 120 a) shows the 5-port model of the 1:4 uniform power divider integrating the cavity for the Ka-band. Figure 120 b) illustrates the simulated matching staying around -5 dB with a peak at 21 GHz and the transmission coefficient from port 1 to port 2 with maximum losses of 8.3 dB at lower frequencies. If we consider that the matching was well below -11 dB along the whole bandwidth and the maximum losses were 6.4 dB for each output port at Ku-band, we realize that the design is not working at Ka-band. Considering the central role played by this component in the integration strategies of both the 2x2 and the 4x4 arrays developed at Ku-band, it is evident that the development of the 2x2 unit cell at Ka-band requires a different integration strategy for the feeding network and poses more challenges.

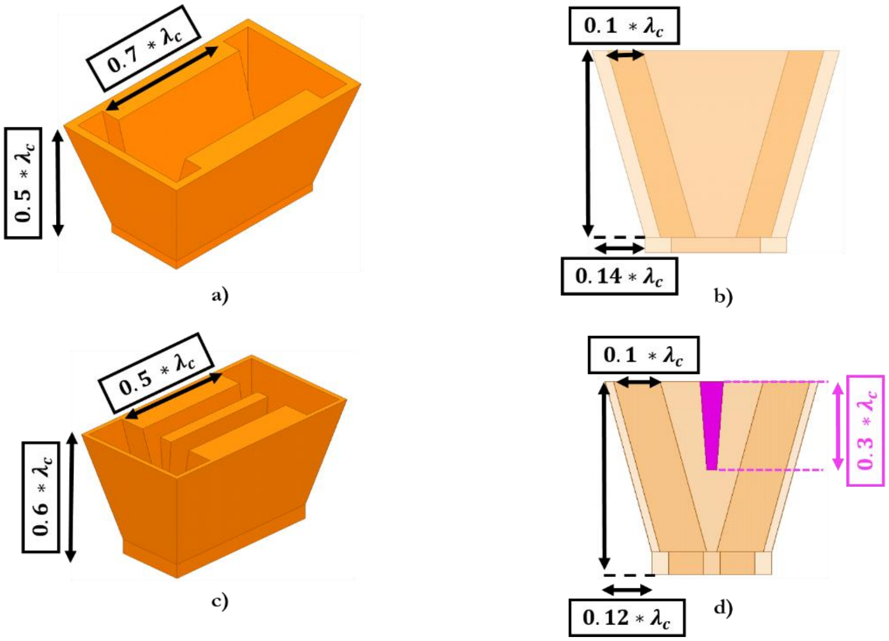

Figure 119 Ku- cavity with ridges(dimensions normalized to the central wavelength at 12.6 GHz): a) Isometric view, b) Transparent side-view. Ka- cavity with ridges (dimensions normalized to the central wavelength of at 24.5 GHz): c) Isometric view, d) Transparent side-view and highlighted iris.

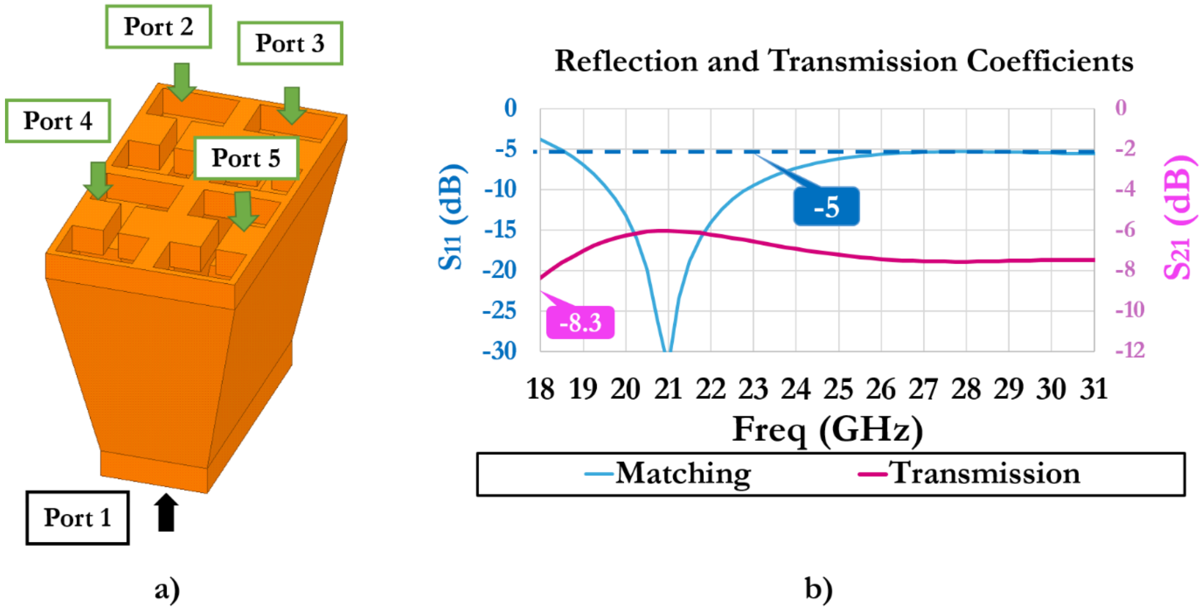

Figure 120 Four-way power divider integrating the cavity with ridges at Ka- band: a) 5-port model, b) simulated reflection coefficient and transmission coefficient from port1 to port 2 versus frequency.

IV.3 Open-ended Ka-band DRWG antenna design

The starting point of the design is represented by the calculation of the inter-element distance required to create a final large array able to electronically steer ± 45° in elevation at the highest frequency of interest (31 GHz), avoiding the apparition of grating lobes. We can apply the formula [5] seen the in Chapter 3 and evaluate this distance to be equal to 5.7 mm, setting the maximum allowed surface for a single antenna to be equal to (5.7 * 5.7) mm^2. As done in Chapter 3, we take into account that the antennas integrated in the final array will share adjacent walls characterized by a minimum thickness of 0.5 mm, defined by fabrication constraints. We design a corresponding rectangular WG with a maximum dimension of 5.2 mm to be used as reference for further developments as we can see in Figure 121 a). The normalized propagation constant of the fundamental mode of this WG is plotted versus frequency in Figure 121 b). It is evident that this device cannot work in the envisaged frequency band.

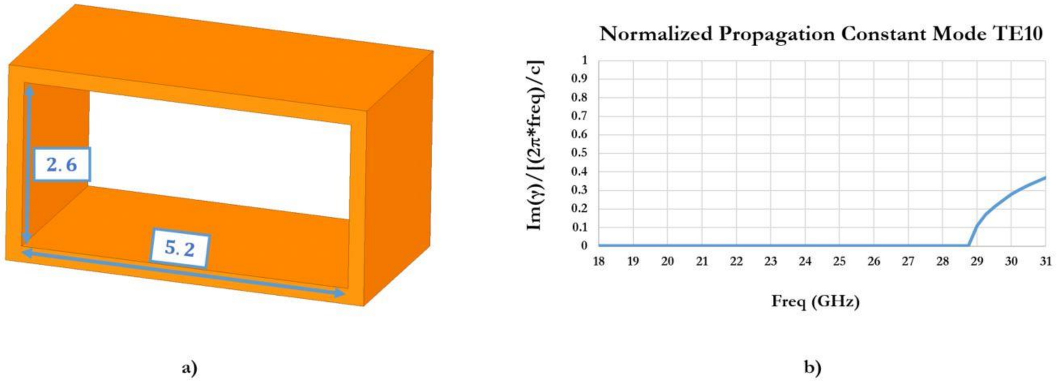

Figure 121 Rectangular WG with maximum dimensions allowed by the inter-element spacing for the final array: a) isometric view with dimensions in mm, b) normalized propagation constant of the TE_{10} mode in the WG.

IV.3.1 DRWG design

The DRWG is designed using the design curves from [75] illustrated in Chapter 3. The objective is to lower the cut-off frequency of the fundamental TE_{10} mode and widen the operational bandwidth of the rectangular WG shown in Figure 121 a) while keeping the same form factor. Taking into account the will to operate between 18 and 31 GHz, we target a lower cut-off wavelength for the TE_{10} mode of 20 mm, corresponding to a frequency of 15 GHz. The $\frac{\lambda_{c\,TE10}}{a}$ value is obtained using 5.2 mm as a value and results to ~4. The calculated value is used to determine form factor of the ridges of the DRWG as shown in Figure 122 a). Hence, we obtain $s = 0.45 * a = 2.3\ mm$ and $d = 0.2 * b = 0.6\ mm$. Starting from these values, we use the design curves in Figure 122 b) to calculate the bandwidth of the designed device, defined as the ration between the cut-off wavelength of the fundamental mode and the first higher order mode. This ratio results equal to 3.7, corresponding to a bandwidth of more than 30 GHz and suggests that the DRWG should operate from 15 GHz up to 45 GHz avoiding the apparition of any higher order mode.

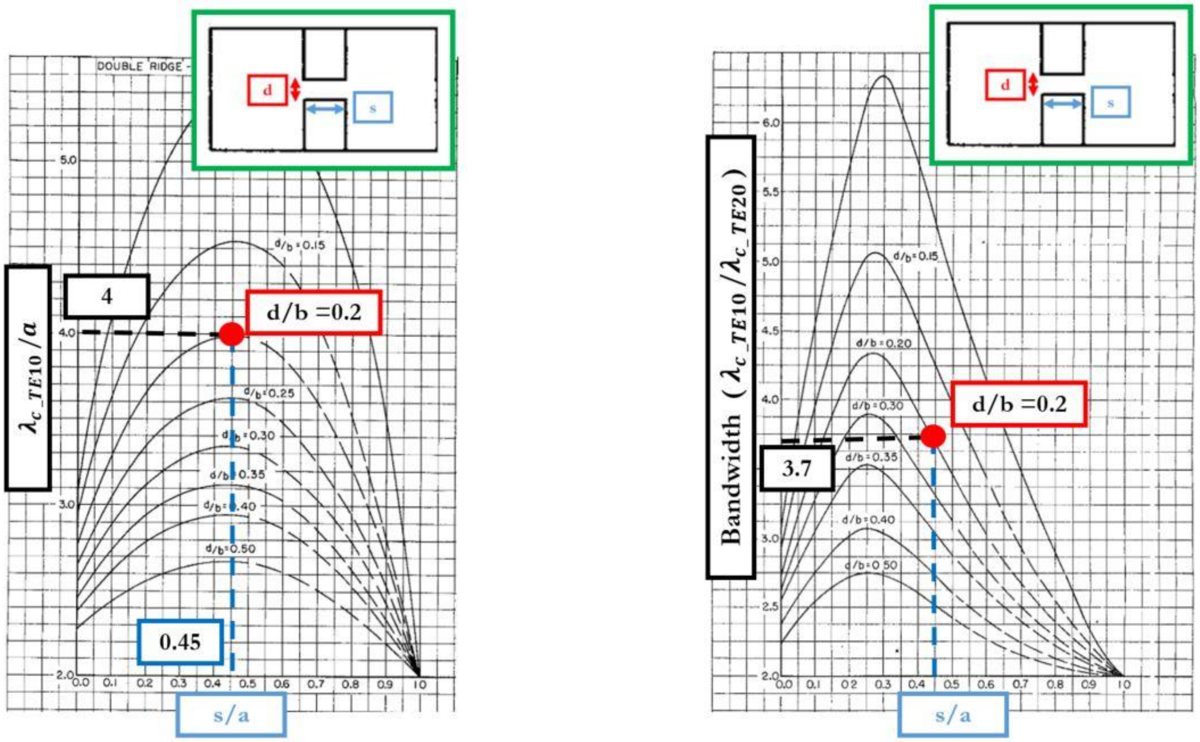

a) **b)**

Figure 122 Design of the DRWG using curves from [75]: a) cut-off wavelength of the fundamental TE_{10} mode, normalized to *a,* as a function of the ridge width *s,* normalized to *a,* and for various inter-ridge distances *d*, normalized to *b*, b) BW as a function of ridge width *s,* normalized to *a,* for various inter-ridge distances *d*, normalized to *b*.

Figure 5 shows the section of the designed DRWGs with relative dimensions in mm and the simulated normalized propagation constant of the fundamental TE_{10} mode as a function of frequency compared with the previously designed rectangular waveguide. The design is effective, as the obtained DRWG actually works in the band of interest. The next step is the simulation of the device in an open-ended configuration, in order to assess performance in the case of radiation. Results are given in Figure 124 for the frequency range of interest: the matching stays between -2.8 and -1.5 dB and the total efficiency between 28% and 50%. The broadside realized gain has a minimum of -1 dBi at 18 GHz and a maximum of 3.5 dBi at 31GHz with a directivity staying between 4.6 and 6.5 dBi. It is evident that if we want to cover the whole 50% of fractional BW at Ka-band we need a more complex design able to match the impedance of the open air over such a wide range of frequencies.

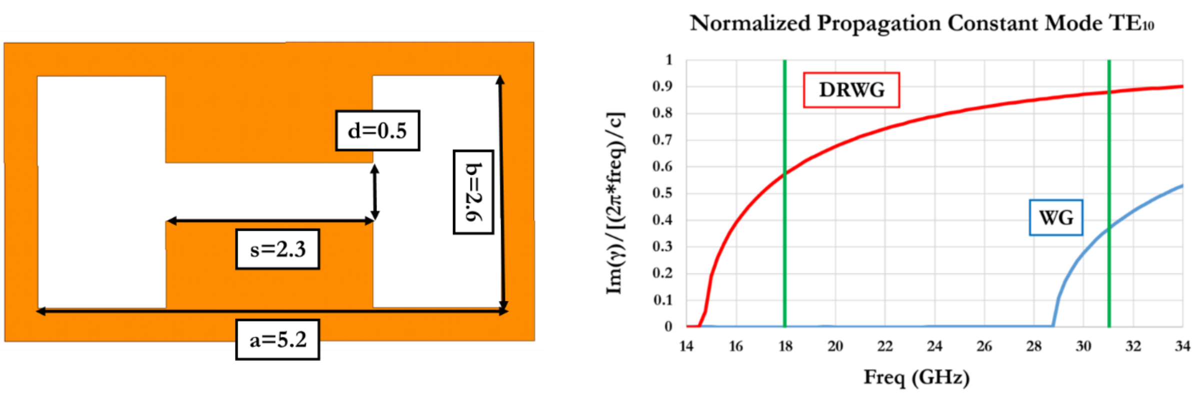

a) b)

Figure 123 Designed DRWG: a) top-view with dimensions in mm, b) normalized propagation constant of the TE_{10} mode versus frequency compared with the previous rectangular WG with an equivalent section.

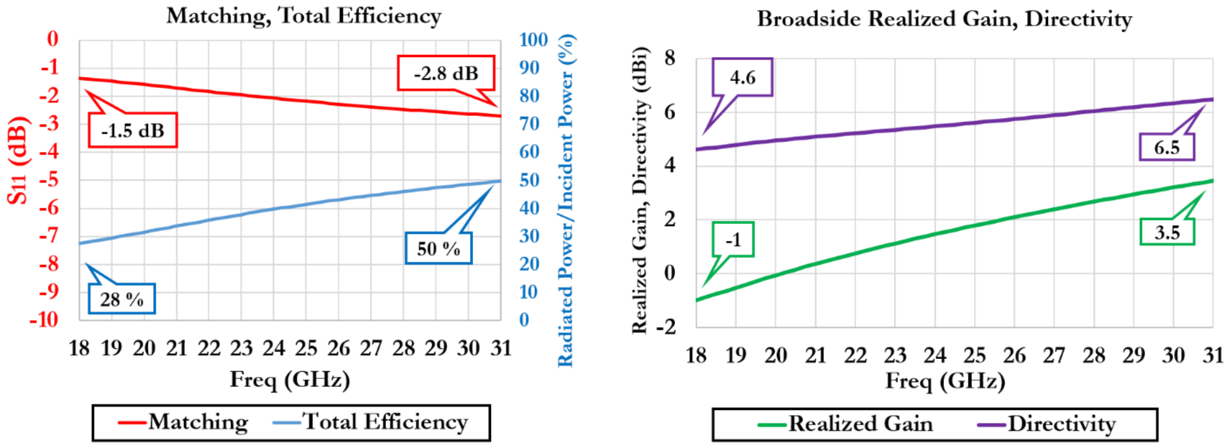

a) b)

Figure 124 Simulated performance of the designed DRWG simulated in open-ended configuration: a) reflection coefficient, total efficiency, b) broadside realized gain, directivity.

IV.3.2 Horn-like DRWG

The performance of the designed DRWG in open-ended configuration is strongly limited by the reflection coefficient staying between -2.8 and -1.5 dB as shown in Figure 124 a). We proceed increasing the section of the double ridged waveguide up to the maximum surface allowed by the design constraints for the final array, similarly to the radiating elements of the 4x4 array in Chapter 3. The various dimensions are optimized by simulation obtaining the model shown in Figure 125, being composed by a DRWG characterized by a height of 1 mm and a horn-like DRWG characterized by a height of 10 mm.

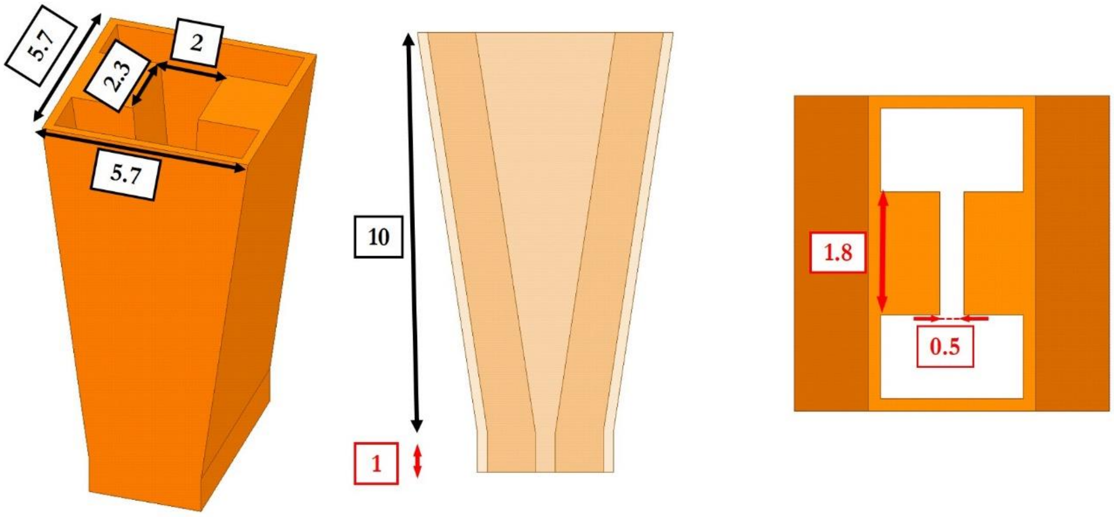

a) b) c)

Figure 125 Designed horn-like DRWG with dimensions in mm: a) isometric view, b)transparent front view, c) bottom view.

The designed horn-like DRWG is simulated in open-ended configuration and Figure 126 a) shows the simulated reflection coefficient versus frequency that stays below -5 dB along the whole bandwidth except for an increase at -3 dB around 18 GHz. The total efficiency oscillates around 80% in the frequency range of interest. Figure 126 b) shows the simulated broadside realized gain versus frequency reaching a minimum value of 1.1 dBi at 18 GHz and a maximum of 6.1 dBi at 31 GHz. The simulated directivity is plotted in the same figure achieving a minimum of 4.4 dBi at 18 GHz and a maximum of 6.5 dBi at 31 GHz. The simulated performance of the previous DRWG is strongly improved considering that for example the reflection coefficient stood between -2.8 and -1.5 dB and the total efficiency between 28% and 50%. Nevertheless, performance is still limited at low frequencies.

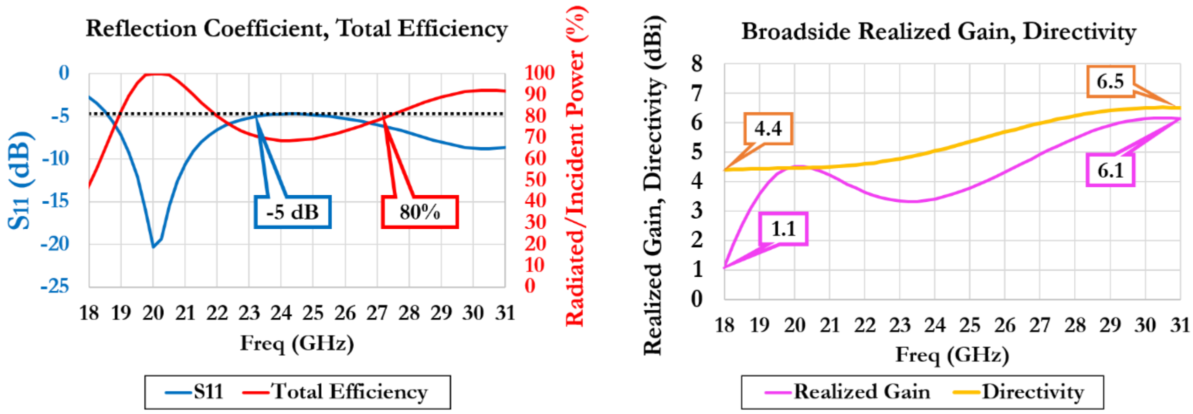

a) b)

Figure 126 Simulated performance of the designed horn-like DRWG in open-ended configuration: a) reflection coefficient and total efficiency, b) broadside realized gain and directivity.

IV.3.3 Horn-like DRWG with parasitic patch

The objective is to furtherly improve the performance of the horn-like DRWG in order to achieve satisfying performance at the lowest frequencies of the BW of interest. We propose the same approach followed in the case of the 4x4 array at Ku-band when we added parasitic patches over a suspended substrate. A square patch is added on a NELCO 4000 – 13 Si EP substrate (ε_r =3.7, tg(δ) =0.009) with a thickness of 0.1 mm, separated by an air gap of 2 mm from the top of the open end of the DRWGs. Once the thickness and the surface of the substrate are fixed, the dimension of the patch and the thickness of the air gap become the most important design parameters. Simulations indicate that the best results are obtained for an air gap thickness of 2 mm and patch dimensions of (2.8 x 2.8) mm^2. The final model is shown in Figure 127 a). The simulated reflection coefficient and total efficiency are plotted in Figure 127 b) versus frequency and the same curves for the previous horn-like DRWG are superimposed. The reflection coefficient of the actual configuration stays below -5 dB along the whole bandwidth of interest improving the previous one, especially at lowest frequencies. The total efficiency now oscillates around 90%. The simulation of such a high-efficiency and symmetric structure can lead to punctual numerical errors, such as the radiated power results higher than the incident one, as highlighted in Figure 127 b). The exchanges with the HFSS support engineers allowed to confirm the correctness of the simulation setup, rather than indicating that the error is related to a software issue they are actually dealing with.

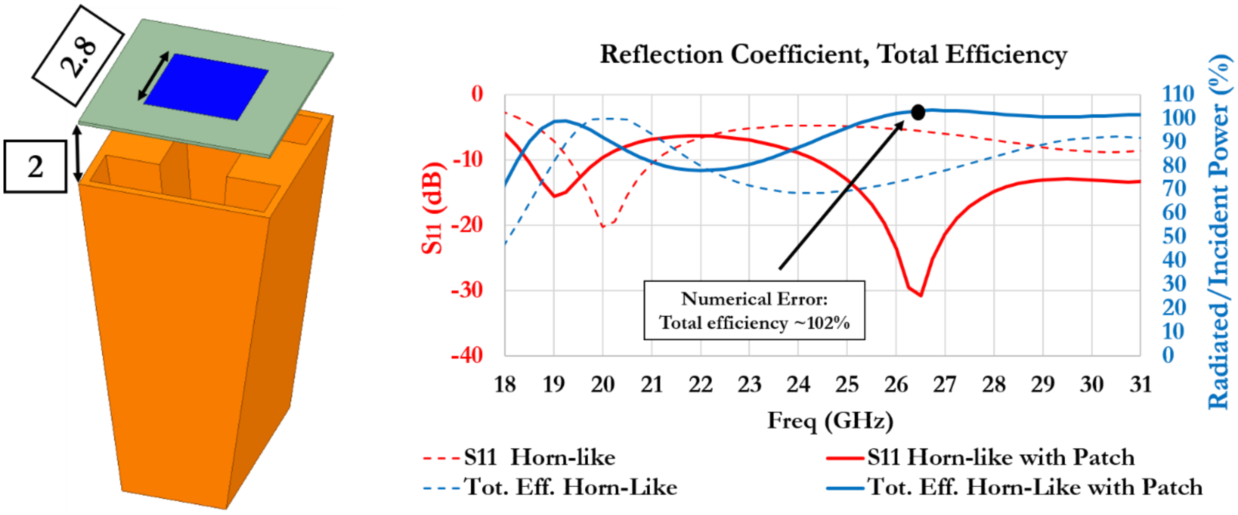

a) b)

Figure 127 Designed horn-like DRWG with patch: a) isometric view with dimensions in mm, b) simulated reflection coefficient and total efficiency versus frequency, compared with the performance of the horn-like DRWG.

The improvements in terms of matching between the initial open-ended DRWG, the horn-like one and the solution with the suspended patch can be appreciated on a smith Chart in Figure 128. As we can see, the use of the patch offers manages to create a second resonance within the bandwidth of interest, which helps to improve the overall matching of the device at these frequencies.

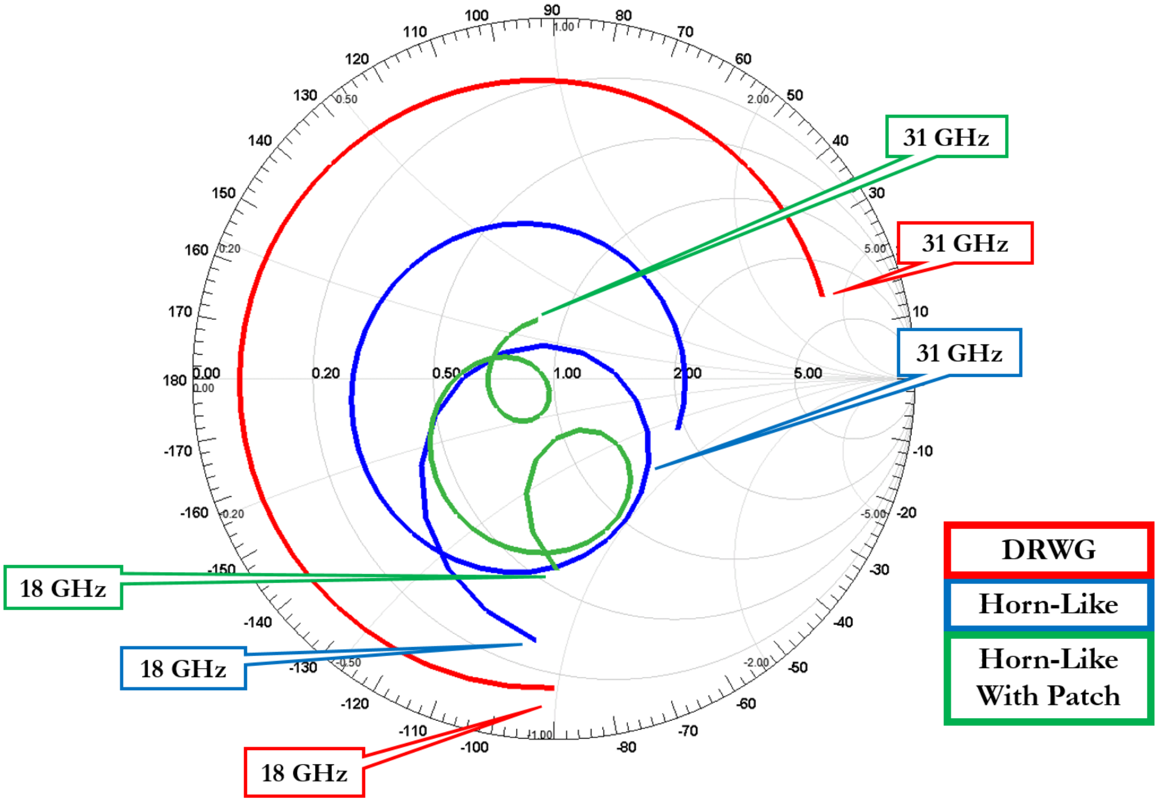

Figure 128 Simulated S_{11} plotted on a smith chart for the open-ended DRWG, horn-like DRWG and horn-like DRWG with suspended patch at Ka-band.

The simulated broadside realized gain and directivity of the solution with patch are plotted in Figure 129 a) versus frequency and compared with those of the horn-like DRWG. The directivity is improved by 1 dBi in the range of interest while the broadside realized gain has an average increment of 2 dBi that reaches 2.5 dBi at lowest frequencies. The previously noticed numerical error around 26.5 GHz is evident in this graph, too. As we can see, the realized gain of the model with patch results higher than the directivity around this frequency. Figure 129 b) shows an example of the 3-D radiation pattern of the realized gain at 31 GHz. The realized gain radiation patterns at 18, 24 and 31 GHz are shown in Figure 130 for both the E- and the H-planes.

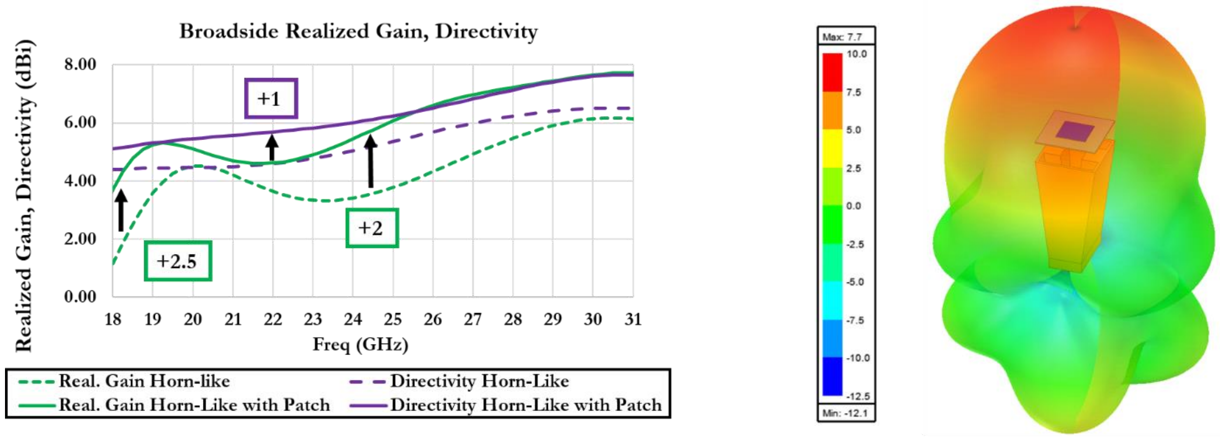

a) b)

Figure 129 Simulated performance of the horn-like DRWG with patch: a) broadside realized gain and directivity versus frequency, compared with horn-like DRWG, b) 3-D radiation pattern of the realized gain at 31 GHz.

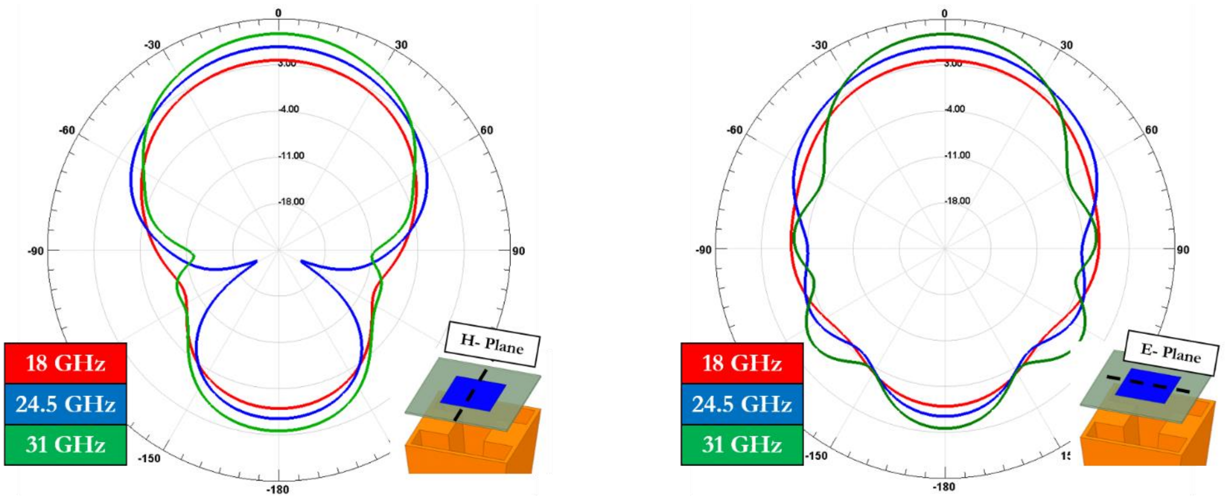

a) b)

Figure 130 Simulated realized gain patterns at 18, 24.5, 31 GHz in dBi: a) H-plane, b) E-plane.

IV.4 Innovative 2x2 Ka-band antenna array

The objective is now to create a 2x2 sub-array with corporate feeding network leveraging the designed horn-like DRWG antenna with parasitic patch, to be used as unit cell for the development of large arrays. Taking into account the (5.7 x 5.7) mm^2 available single antenna, a simple calculation gives us the theoretical maximum surface allowed for the development of the 2x2 unit cell, being equal to (11.7 x 11.7) mm^2.

IV.4.1

IV.4.2 2x2 Horn-like DRWG antennas with parasitic patches

The developed horn-like DRWG antenna with parasitic patch is simulated in a 2x2 array configuration in order to assess the initial performance of the array before designing the relative feeding network. The HFSS model can be seen in Figure 131 a). The S-parameters of the four ports are symmetric and the simulated S_{11}, S_{21}, S_{31} and S_{41} are shown in Figure 131 b) versus frequency. The reflection coefficient stays below -5 dB along most of the frequency band. The port-to-port isolation with adjacent antennas stays below -10 dB, being maximized for the one aligned in the H-plane (port 3). The port-to-port isolation with the non-adjacent antenna (port 4) is below –20 dB except at lower frequencies where it raises up to -17 dB.

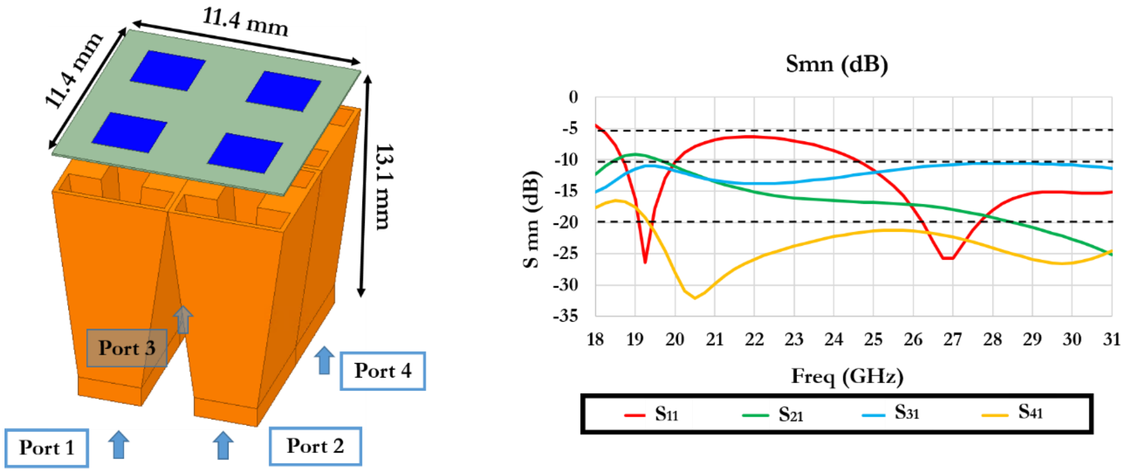

a)

Figure 131 2x2 array of horn-like DRWG antennas with patches: a) isometric view, b) simulated s-parameters of port 1 versus frequency at Ka-band.

Figure 132 shows the simulated broadside realized gain and directivity versus frequency, overlapped with those of the single antenna. Results are obtained feeding all the elements with the same amplitude and phase excitation. The resulting directivity of the array stays between 8.3 and 12 dBi, with an average increment of 4.6 dB if compared to the single antenna. The broadside realized gain of the array stays between 5.7 and 11.2 dBi with an average increment of 5.3 dB if compared to the single antenna. It is interesting to notice that the achieved increment results lower than the theoretical array factor of 6 dB in both cases. Nevertheless, this behavior can be explained taking into account that the theoretical value is given under the hypothesis of a perfect isolation between the radiating elements, which is not our case.

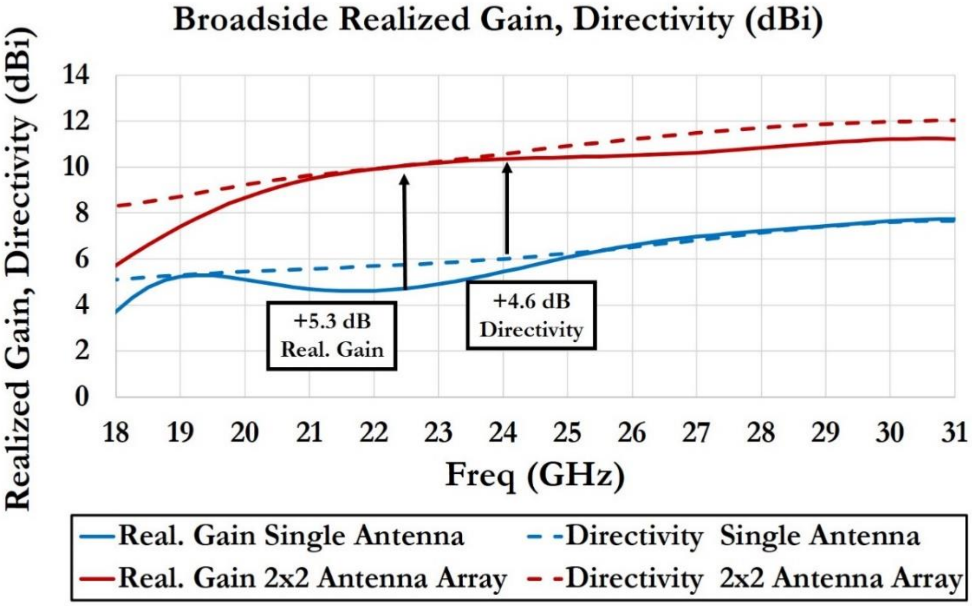

Figure 132 Simulated broadside realized gain and directivity of the 2x2 array of horn-like DRWG antennas with patches versus frequency at Ka-band, compared with those of the single antenna.

IV.4.3 Feeding network overall strategy

According to the impossibility to use a cavity-based approach to realize a compact four-way power divider and exploit the feeding network integration scheme of the 2x2 sub-array working at Ku-band, a different strategy must be proposed. We could theoretically use two levels of tee-junctions, as done for the connection between the DRWG transition and the 4 sub-arrays in the feeding network of the 4x4 array at Ku-band. A flange and a transition from DRWG to standard WG, being WR-42 in this case, are required in order to allow the connection of the fabricated prototypes to the test equipment during measurements. The signal coming from the WR-42 transition could be equally split in two using a H-plane tee-junction for realizing the first level of the power divider. Hence, each of the signals coming from this level may be equally split in two using an E-plane tee-junction. The principle of the envisaged integration scheme is shown in Figure 133 a), requiring additional 90° bends at the outputs of the tee-junctions, both in E- and H- planes, to connect the different blocks. The drawback of this approach is that the maximum dimension of the block composed by the tee-junction for the H-plane with two 90° H-bends is 16.6 mm, resulting in a size bigger than the 11.7 mm maximum allowed horizontal dimension for the unit cell. Figure 133 b) shows the model of the most compact H-plane DRWG tee-junction with 90°bends we managed to design to work at these frequencies.

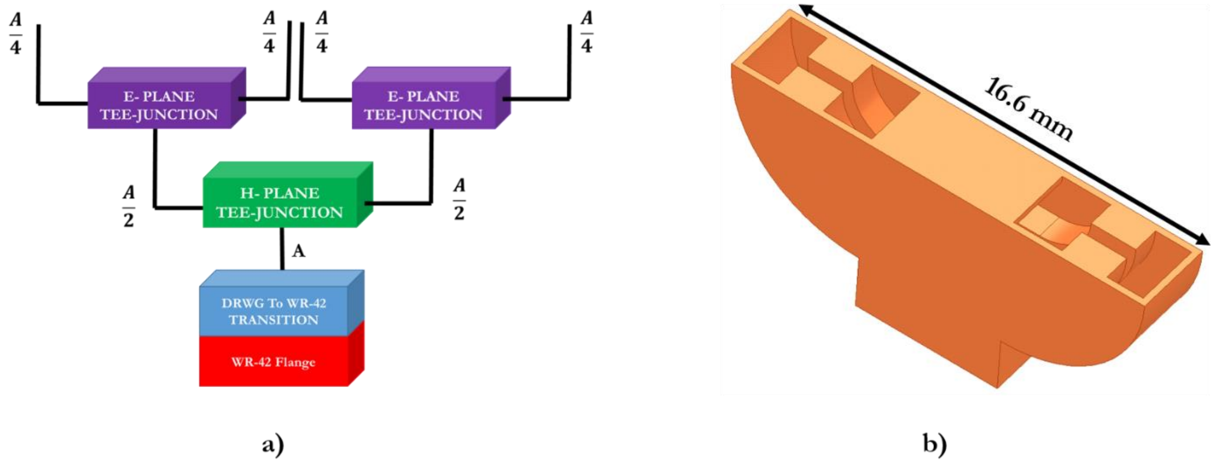

Figure 133 a) 2x2 feeding network integration scheme using H- and E- planes tee-junctions as power divider, b) model of a tee-junction for the H-plane with 90° H-bends working at Ka-band.

Spacing was not an issue at Ku-band as tee-junctions were used to connect 4 unit cells in the 4x4 array. Accordingly, the maximum horizontal dimension allowed for the design of the tee-junction for the H-plane was given by the sum of the maximum horizontal dimensions of two adjacent unit cells. Finally, an integration scheme for the complete Ka- 2x2 array is proposed in Figure 134: a four-way power divider is created using 3 DRWG tee-junctions for the E-plane disposed on two distinct levels with relative DRWG 90° bends and a section of DRWG connections.

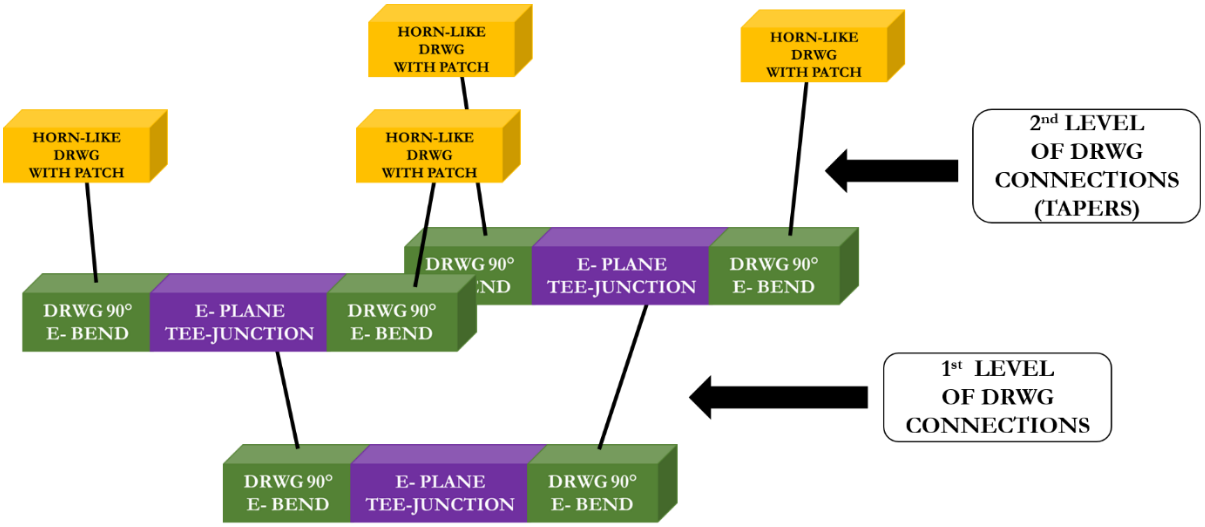

Figure 134 Integration scheme of the complete 2x2 unit cell with feeding network, using only DRWG tee-junctions for the E-plane in order to create the four-way power divider.

IV.4.4 DRWG tee-junction for the E-plane

The DRWG tee-junction for the E-plane represents the fundamental component of the envisaged feeding network for the 2x2 array. An initial design is obtained crossing two DRWGs in the E-plane, as shown in Figure 135 a) and b). Simulated S_{11}, S_{22} and S_{21} are shown in Figure 14 c). The simulated reflection coefficient is pretty symmetric with a value of about -9 dB along the whole bandwidth. The simulated transmission coefficient from port 1 to port 2 is lower than -3.5 dB along the whole bandwidth of interest with maximum losses of 3.65 dB at the lowest frequencies. Simulations show that the performance of port 2 and 3 is symmetric. We want to improve the performance of the design reducing the transmission losses and the mismatching at the input port. The tee-junction is optimized adding an iris along the H-plane at the input arm as proposed in [87]. The design can be appreciated in Figure 136 a) where the iris is put in evidence and the relative dimensions, optimized via simulations, are given in mm. The simulated S_{21} is given in Figure 136 b) versus frequency: performance is improved moving from losses higher than 3.5 dB along the whole bandwidth in the previous design to less than 3.3 dB. The simulated S_{11} and S_{22} are given in the same graph: S_{11} stays between -21.7 at lowest frequencies and -9.7 dB at highest ones, improving the previous case where it was equal to – 9 dB along the whole bandwidth. The obtained S_{22} has a maximum of -7 dB at the low edge of the band being worse than the previous design, and a minimum of -9.7 dB at the high edge of the band, where it is improved of 0.7 dB if compared to the case without iris.

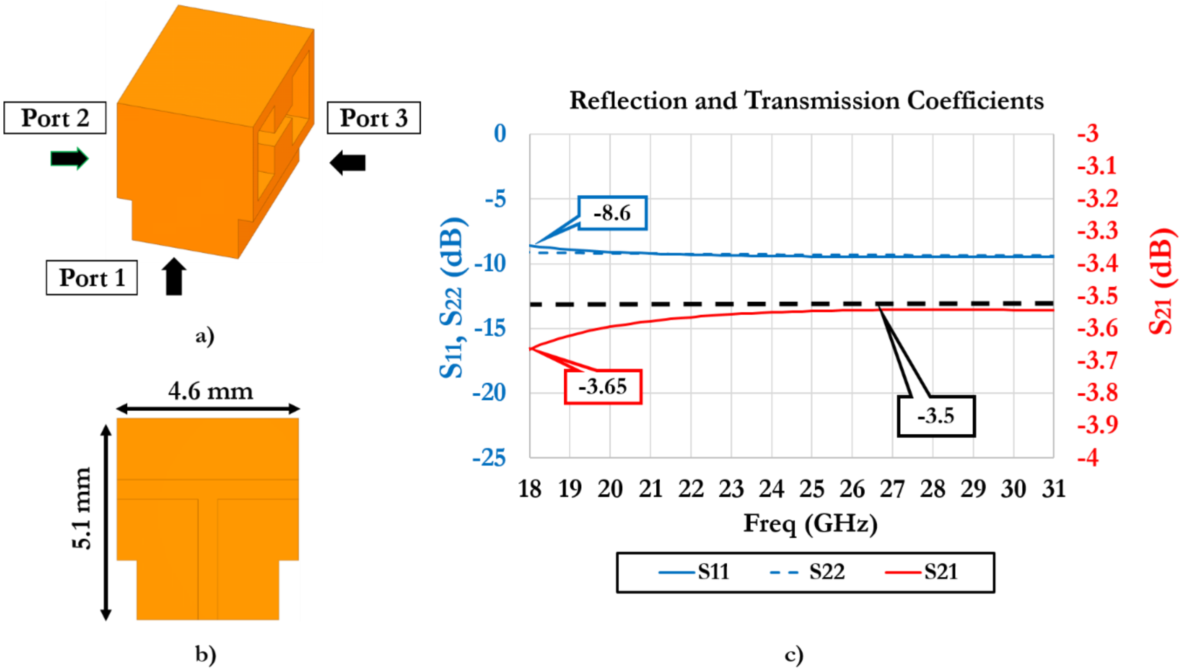

a)

b)

c)

Figure 135 Initial design of DRWG tee-junction for the E-plane working at Ka-band: a) isometric view, b) front cut with dimensions, c) simulated reflection coefficient and transmission coefficient versus frequency at Ka-band.

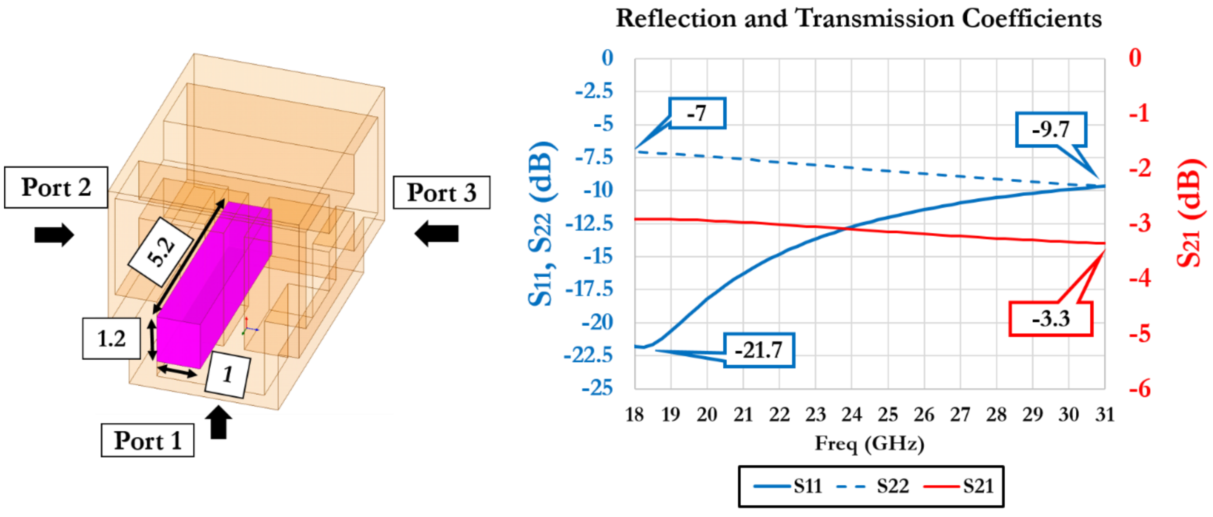

a) b)

Figure 136 DRWG tee-junction for the E-plane with iris: a) transparent isometric view highlighting the inner iris, dimensions in mm , b) simulated S_{11}, S_{22} and S_{21} versus frequency at Ka- band.

The simulated S_{11} of the designs with and without iris are shown in Figure 137 a) on a smith chart, confirming that the matching is strongly improved in the lowest part of the band by adding the iris. The phases of the transmission coefficients of the model with iris are plotted in Figure 137 b) versus frequency confirming the correct functionality of the design.

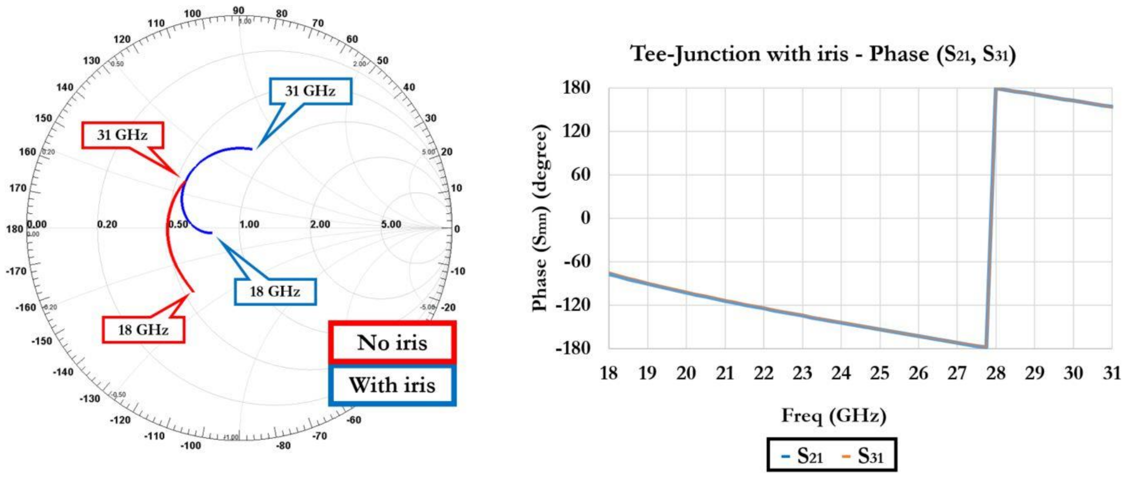

a) b)

Figure 137 a) Simulated S_{11} of the tee-junctions for the E-plane at Ka-band (with and without iris) on a smith chart, b) phase of the S_{21} and S_{31} coefficients of the tee-junction with iris versus frequency.

IV.4.5 DRWG 90° bend for the E- plane

A DRWG 90° bend working at Ka-band is designed following the same method applied in Chapter 3. The model is shown in Figure 138 a), while the simulated reflection coefficient stays between -36 and -28.7 dB with maximum transmission losses of 0.01 dB at 18 GHz (Figure 138 b). This performance give us the possibility to envisage the assembly of 2 of these bends with each tee-junction for the E-plane, as depicted in Figure 134, without consistent degradations of its performance.

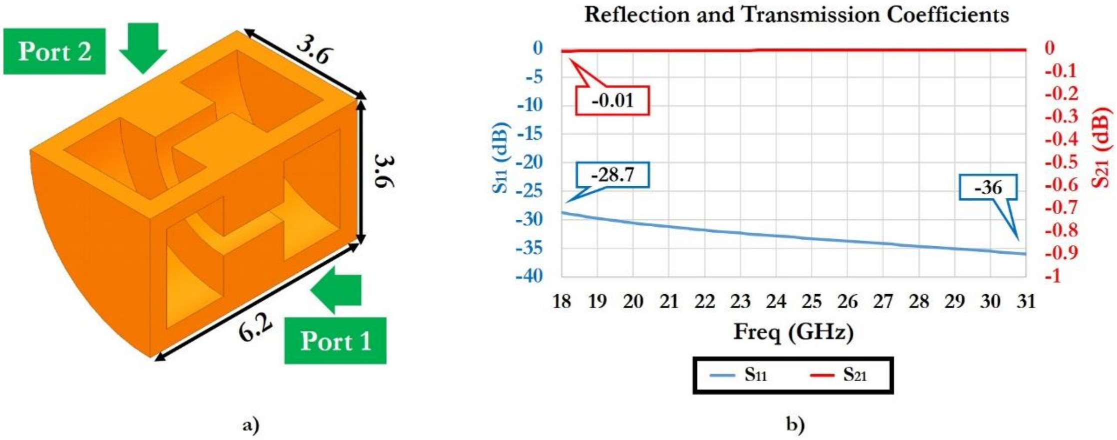

Figure 138 Designed DRWG 90° bend for the E-plane: a) isometric view with dimensions in mm, b) simulated S_{11} and S_{21} versus frequency at Ka-band.

IV.4.6 DRWG tee-junction for the E-plane with 90° bends

The designed DRWG tee-junction for the E-plane is assembled with two DRWG 90° bends for the E-plane as we can see in Figure 139 a) and b). It is interesting to underline that the maximum dimension is 10.8 mm in this case, being compatible with the maximum form factor of (11.7 x 11.7) mm^2 set for the 2x2 unit cell. The simulated S_{11}, S_{22} and S_{21} are plotted versus frequency and compared with the performance of the single tee-junction in Figure 139 c). As we can see, the effect of the assembly is such that we have an improvement of the reflection coefficient up to -1.5 dB around 22 GHz, while the S_{22} slightly deteriorates with a maximum increase of 0.7 dB around 20 GHz. Transmission losses are practically unaltered if compared to the single tee-junction. The aim of this design step is to validate a block to be re-used for the development of the complete feeding network for the 2x2 unit cell.

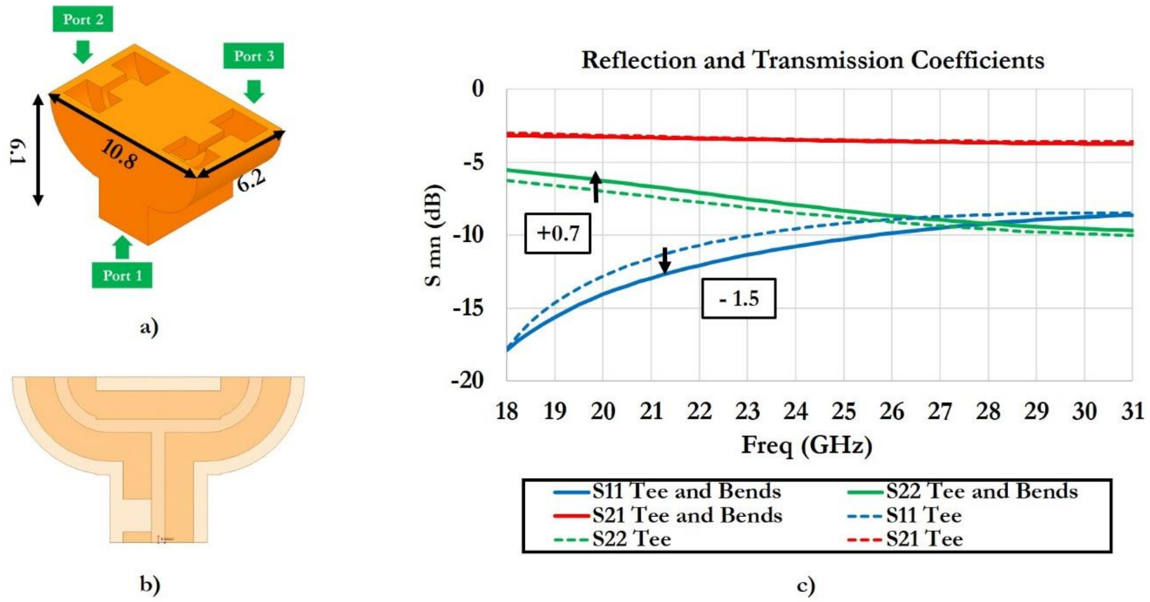

a)

b)

c)

Figure 139 Assembled DRWG tee-junction with 2 DRWG 90° bends for the E-plane: a) isometric view with dimensions in mm, b) transparent side-view, c) simulated S_{11}, S_{22} and S_{21} versus frequency at Ka-band for the assembled tee-junction with 2 DRWG 90° bends and for the single tee-junction.

IV.4.7 Four-way power divider design

The design of the four-way power divider requires to integrate 3 tee-junctions for the E-plane with the relative bends, to be placed on two different layers, and connected by a complex DRWG section, as depicted in Figure 134.

IV.4.7.a DRWG Connection

The design of the DRWG connection between the two levels of tee-junctions represents a challenge. We have to connect two DRWG sections aligned along their E-plane in the first level with other two aligned along their H-plane in the second level, while being constrained by the maximum surface allowed for the unit cell. Moreover, it is fundamental to underline that the inner volumes of the DRWGs used for this purpose must not overlap, in order to allow their fabrication and keep their correct functionality. Hence, we envisage the DRWG connection scheme in Figure 140. The 3-D model of the designed structure is shown in Figure 141 from different views.

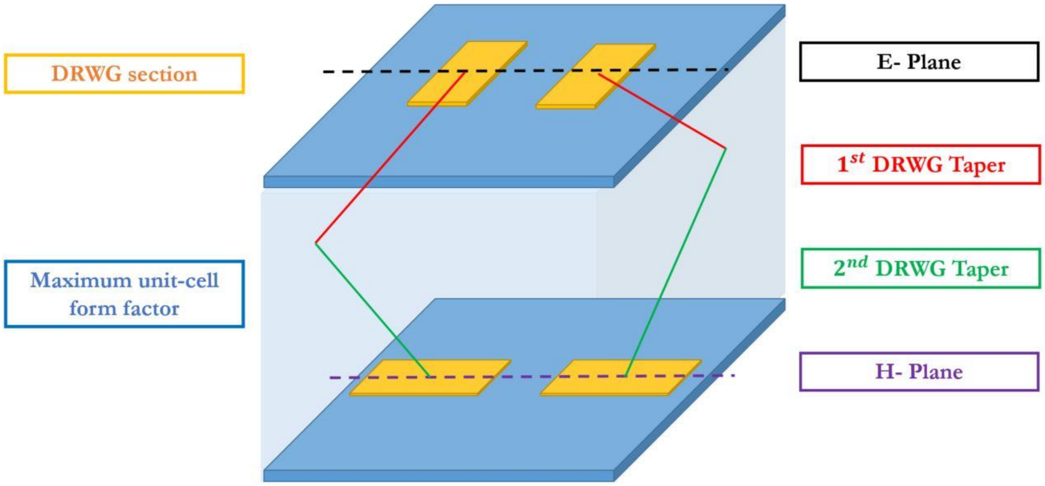

Figure 140 Envisaged DRWG connection scheme for the uniform 1:4 power divider.

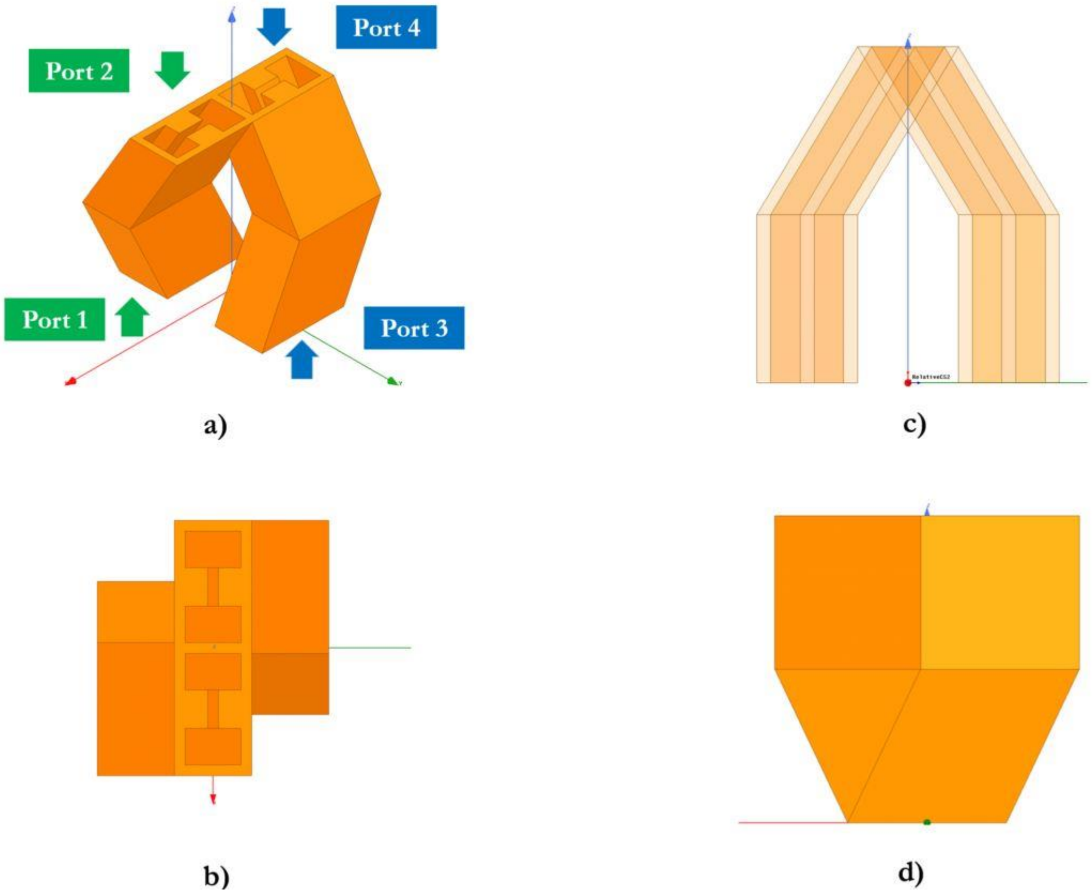

Figure 141 Designed DRWG connection for the uniform 1:4 power divider: a) isometric view, b) top-view, c) transparent front-view, d) right view.

The shown model is simulated in HFSS and the performance of the two arms are exactly symmetric. Figure 142 a) shows the simulated S_{11} versus frequency, resulting to be lower than -10 dB along most of the frequency range. The S_{21} reaches its minimum value of -0.5 dB at 18 GHz. Figure 142 b) illustrates a smith chart where the reflection coefficient is plotted for port 1 and port 3, confirming the symmetry of the performance.

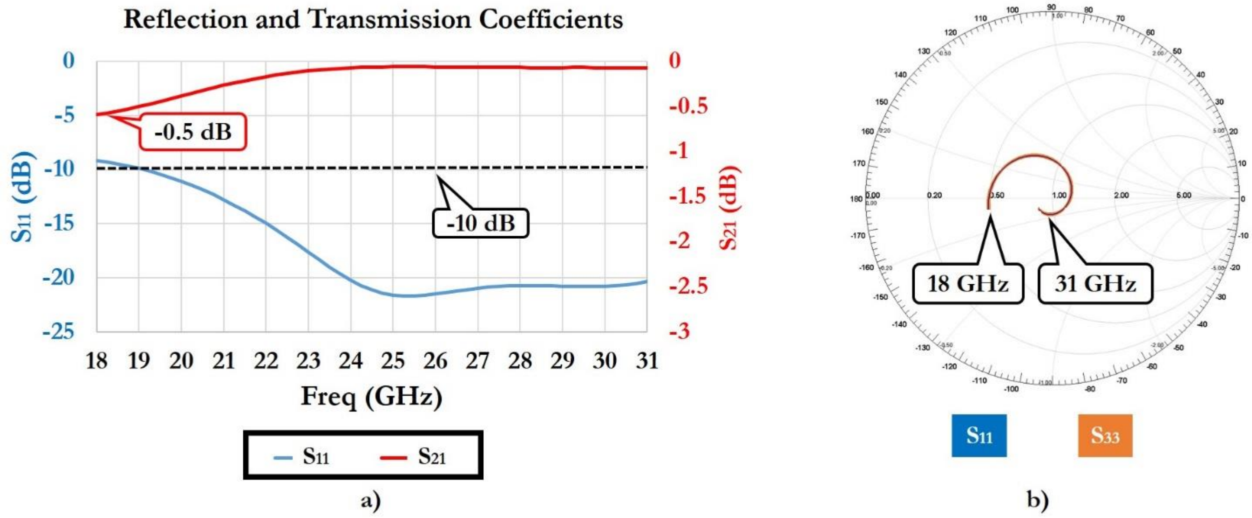

a)

b)

Figure 142 Simulated performance of the DRWG connections: a) S_{11} and S_{21} versus frequency, b) smith chart of the S_{11} and S_{33}.

IV.4.7.b Assembled four-way power divider

The complete design of the 1:4 power divider is assembled by leveraging the previously developed DRWG tee-junction and bend for the E- plane and the described DRWG connection section obtaining a 5-ports model to be simulated in HFSS. The model has a profile height of 24.2 mm, being illustrated in Figure 143 in terms of isometric and transparent front-view. Figure 144 a) shows the simulated reflection coefficient at the input port and the transmission coefficients at the four output ports versus frequency. The matching stays below -5 dB along most of the bandwidth and the transmission coefficients are practically the same oscillating around the value of -6 dB which guarantees a symmetric four-way power-splitting of the signal. Figure 144 b) illustrates the S_{11} plotted on a smith chart for the described design.

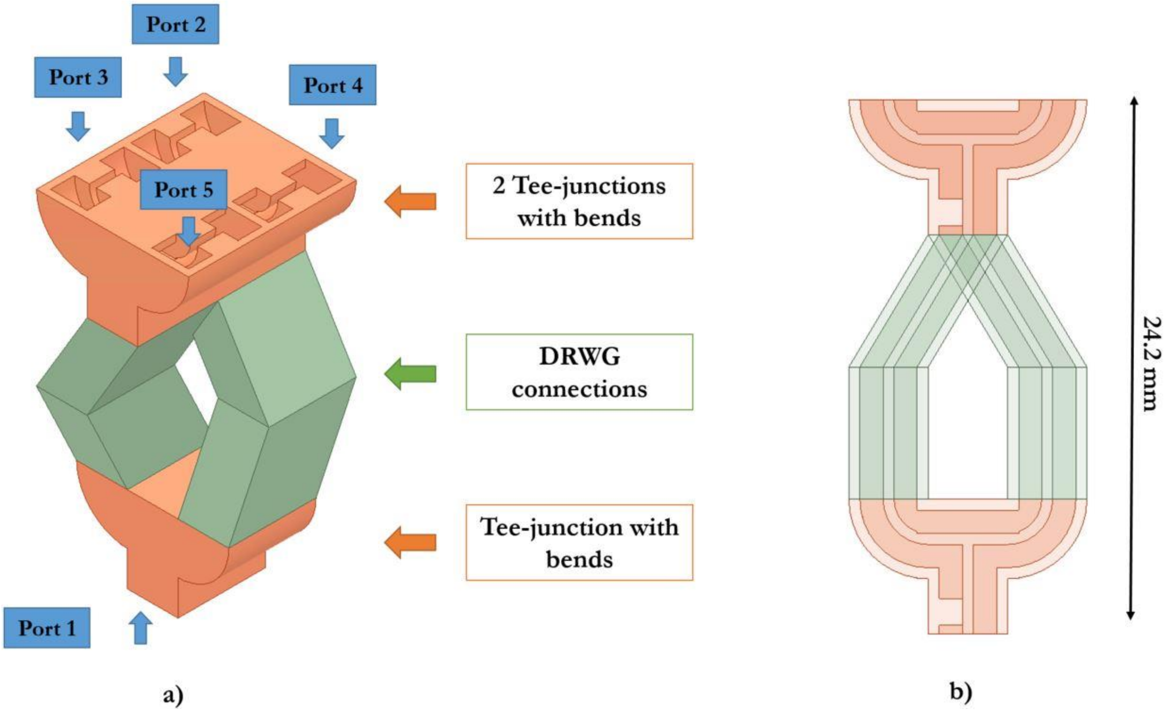

Figure 143 Assembled 1:4 power divider: a) isometric view, b) transparent front-view.

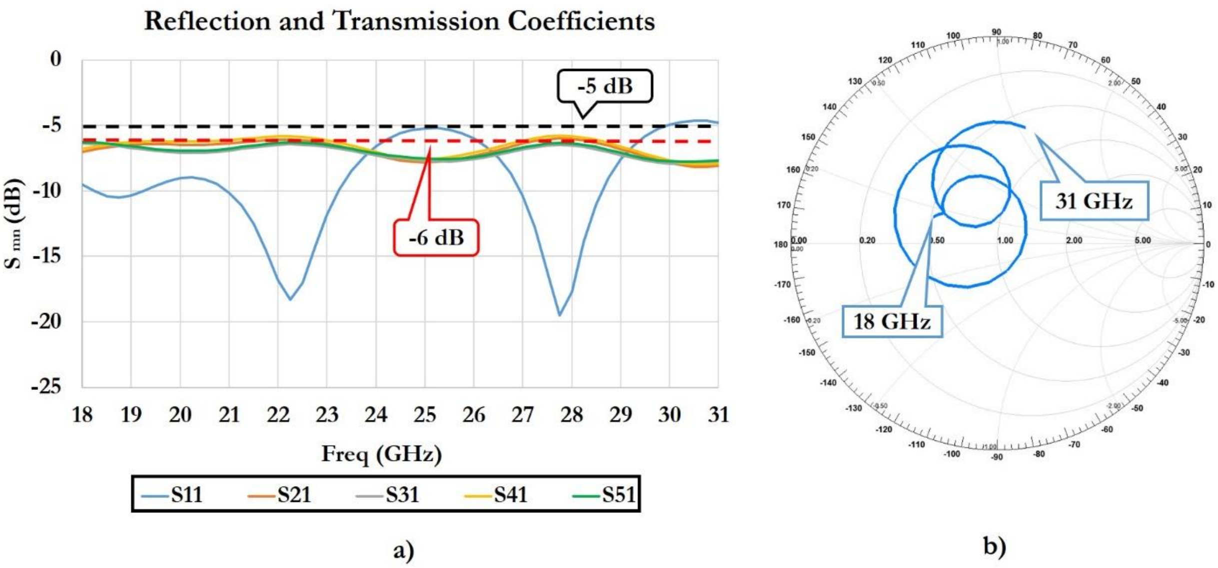

Figure 144 Simulated performance of the assembled 1:4 power divider: a) simulated reflection coefficient and transmission coefficients versus frequency at Ka-band, b) smith chart of the S_{11} at Ka-band.

IV.4.8 DRWG Tapers

A section of DRWG tapers is required to connect the designed 1:4 power divider to the 4 DRWG antennas, respecting the inter-element distance required for the final array. Figure 145 shows the designed model, being composed of 4 tapered DRWGs. A central part is added in order to fill the void we would have between them and improve the mechanic robustness of the structure. Figure 146 shows the simulated reflection coefficients at the four input ports versus frequency, resulting to be lower than -50 dB along the whole Ka-band in all cases. The transmission coefficients are plotted in the same graph versus frequency, resulting in being symmetric and with a minimum level of -0.01 dB.

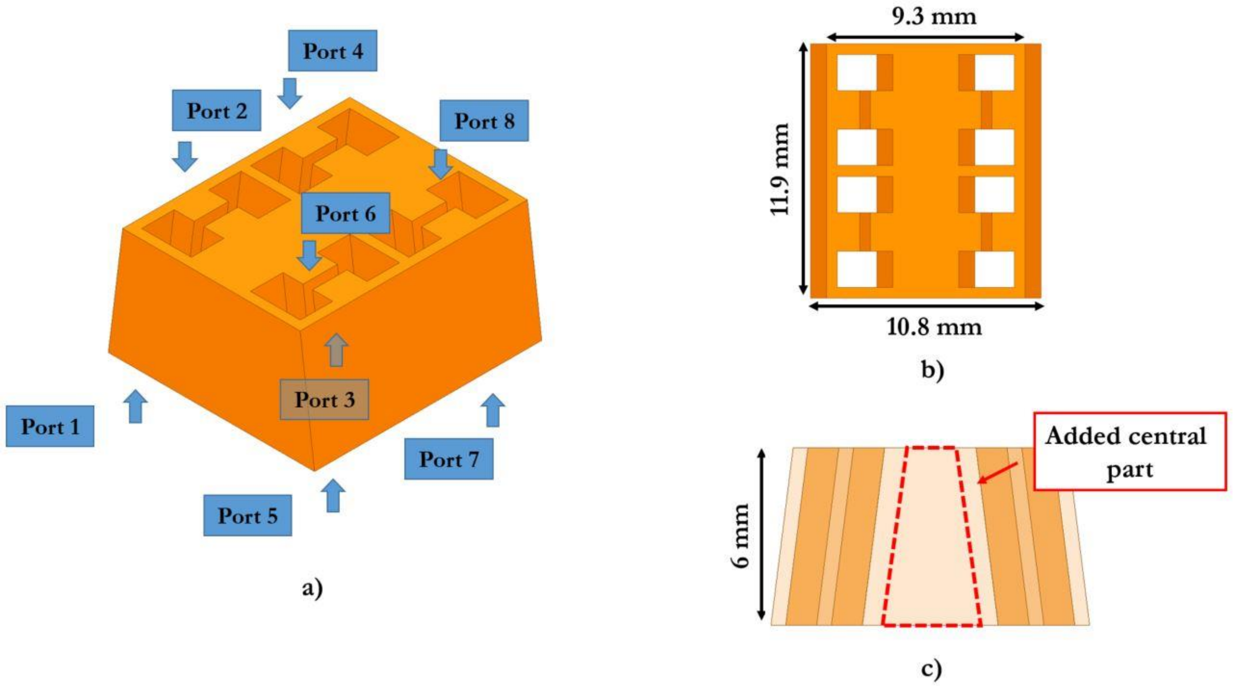

Figure 145 Designed DRWG taper block to connect the power divider to the antennas while respecting the required inter-element distance for the final array: a) isometric view, b) top view, c) transparent side-view with indication of the part added to fill the void between the DRWGs.

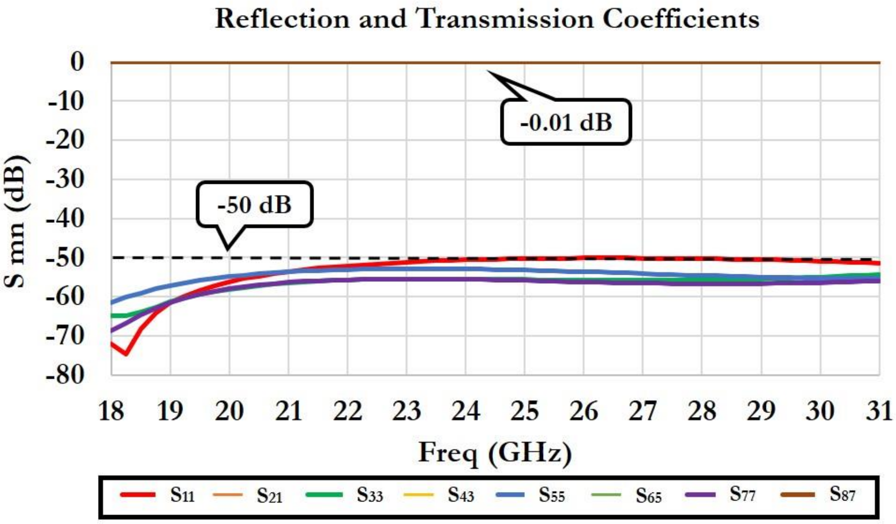

Figure 146 Simulated reflection coefficients and transmission coefficients of the taper block versus frequency.

IV.4.9 Four-way power divider with tapers and 2x2 antenna array

The designed four-way power divider is assembled with the obtained DRWG tapers and the 2x2 array of horn-like DRWG antennas with patches. The model is shown in Figure 147 from various perspectives, highlighting the different blocks.

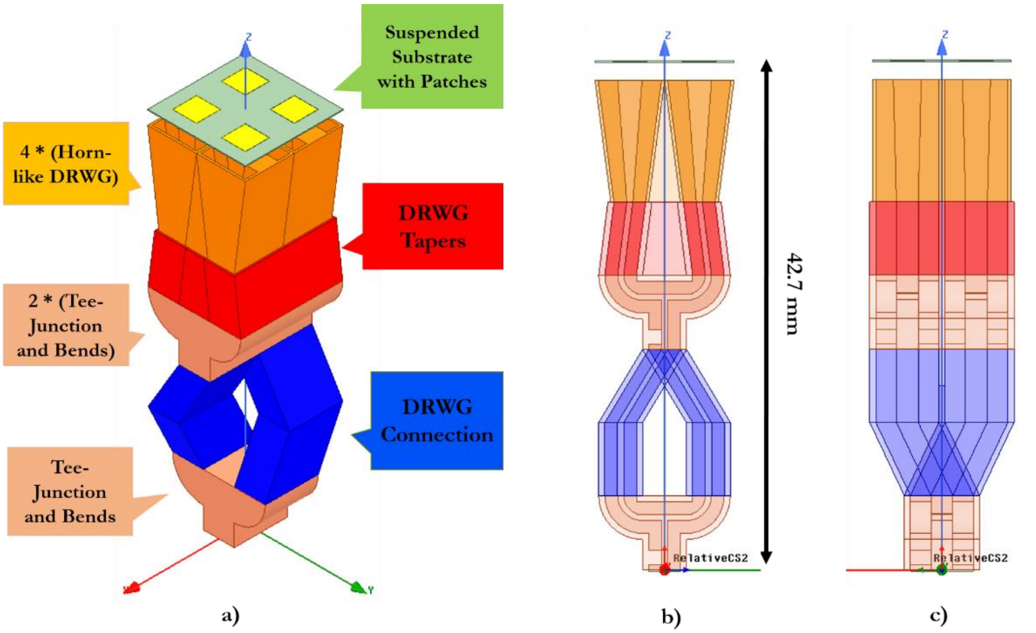

Figure 147 Assembled model of the four-way power divider with DRWG tapers and 2x2 horn-like DRWG antennas with patches: a) isometric view, b) transparent front-view, c) transparent side-view.

The assembled model is simulated with HFSS and the performance is compared with those of a fictitious 2x2 antenna array without any feeding network. Figure 148 a) shows the simulated reflection coefficient and the total efficiency versus frequency at Ka-band. The obtained matching stays below -5 dB along most of the Ka-band resulting in a maximum deterioration of 20 dB at 27 GHz and improvement of – 6 dB at 22 GHz, if compared to the 2x2 antenna array without feeding network. The simulated total efficiency stays between 55 and 94 % with a maximum improvement of 24% at 22.25 GHz and decrease of 37% at 29.5 GHz, always compared to the 2x2 array without feed. The simulated broadside realized gain stays between 4.8 and 11.7 dBi with a maximum improvement 1.3 dBi at 19 GHz and decrease of 1.9 dBi at 20.25 GHz. The simulated directivity stays between 8.35 and 12.4 dBi, resulting practically unaltered from the previous case. These results show that the design of such a feeding network with a large fractional operational bandwidth is particularly critical at these frequencies, especially if we want to respect the discussed array design and fabrication constraints. Moreover, it is evident that the feeding network will limit the overall performance of the unit cell.

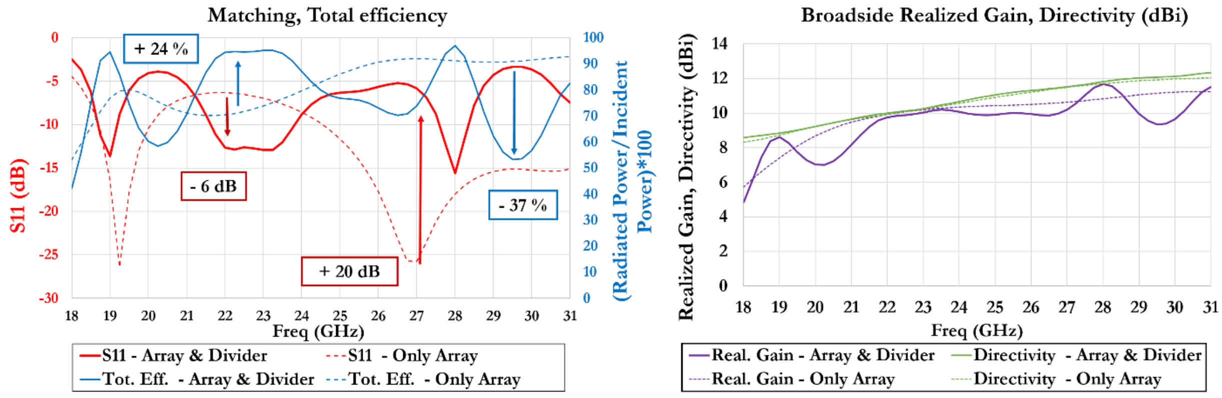

a) b)

Figure 148 Simulated performance of the assembled model of the power divider with DRWG tapers and 2x2 antennas versus frequency, overlapped with those of the single 2x2 antenna array: a) reflection coefficient and total efficiency, b) broadside realized gain and directivity.

IV.4.10 WR-42 flange with DRWG-to-WR-42 transition

A standard rectangular waveguide flange and a transition from a standard waveguide to the DRWG section are needed in order to allow the connection and the test of the complete 2x2 array with feeding network. Concerning the choice of the standard waveguide flange, we underline that it does not exist such a component meant to cover the wide operational bandwidth of interest (18-31 GHz) as we can see from the table in Table 16 [89].

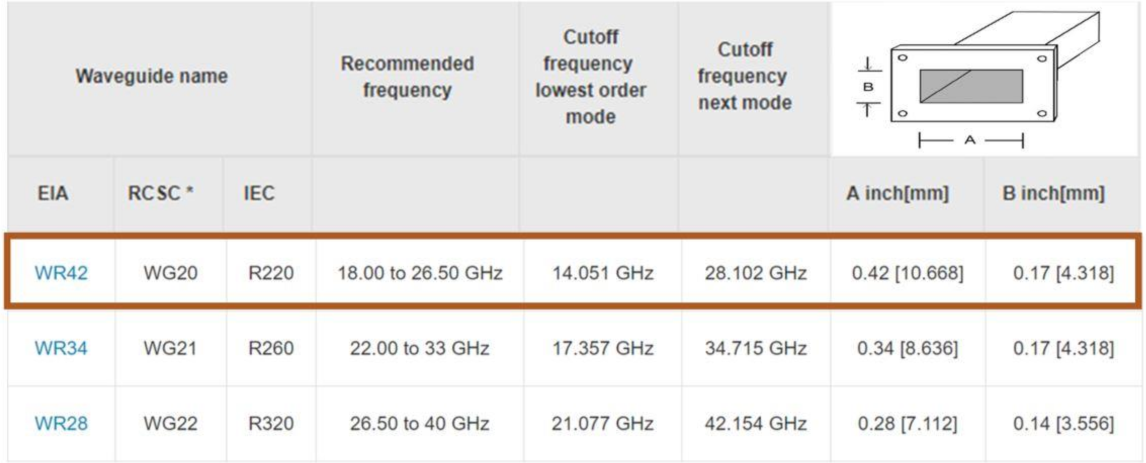

Waveguide name			Recommended frequency	Cutoff frequency lowest order mode	Cutoff frequency next mode		
EIA	RCSC *	IEC				A inch[mm]	B inch[mm]
WR42	WG20	R220	18.00 to 26.50 GHz	14.051 GHz	28.102 GHz	0.42 [10.668]	0.17 [4.318]
WR34	WG21	R260	22.00 to 33 GHz	17.357 GHz	34.715 GHz	0.34 [8.636]	0.17 [4.318]
WR28	WG22	R320	26.50 to 40 GHz	21.077 GHz	42.154 GHz	0.28 [7.112]	0.14 [3.556]

Table 16 Dimensions and operational bandwidths of the standard waveguides operating around Ka-band with reference picture of a rectangular WG, from [89], where the WR-42 line is highlighted.

A waveguide with the dimension of the standard WR- 42 is designed and simulated in HFSS. Figure 149 shows the simulated normalized propagation constants of the modes TE_{10} and TE_{20} versus frequency. The cut-off of the first higher order mode is at 28 GHz, starting to be assessed at very high edge of the bandwidth of interest. Hence, using the WR-42 standard WG for the whole Ka-band is considered as an opportune trade-off between functionality and design complexity. In fact, the alternative would be to use two different waveguides (i.e. WR-42 from 18 up to 26.5 GHz and WR-28 from 26.5 up to 31 GHz) and a diplexer, requiring designing this last component.

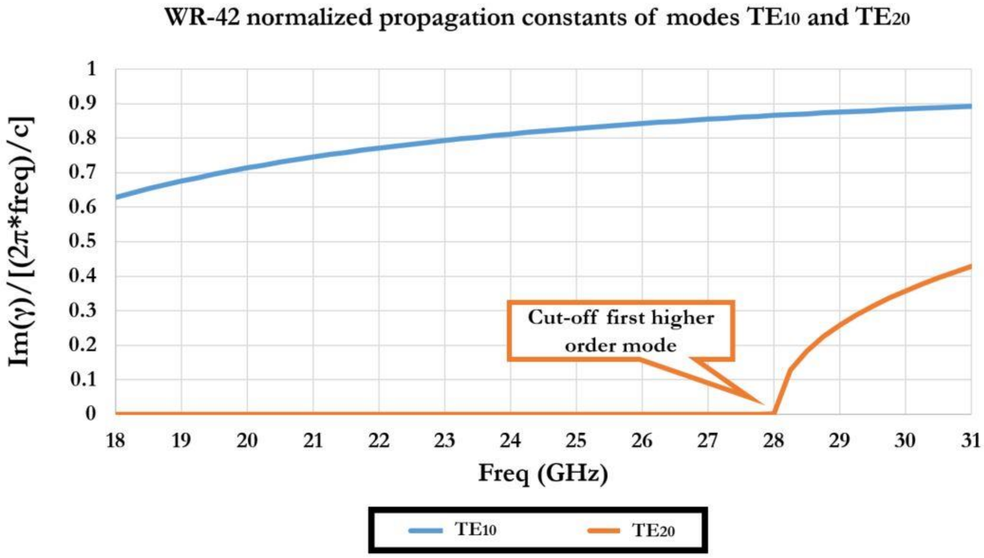

Figure 149 Simulated normalized propagation constant of the first two modes propagating in a rectangular waveguide with standard WR-42 section versus frequency.

The transition is designed starting from the section of the DRWG by chamfering the walls and progressively reducing the thickness of the inner ridges, until the section of a standard rectangular WR-42 waveguide is obtained. The height of the transition is set as design parameter and the value of 24 mm, corresponding to the double of the center wavelength of the operational BW at 24.5 GHz, is found to be the optimum trade-off between achieved performance and form factor. The assembled model of the flange with the transition is shown in Figure 150 a) and b), while the simulated performance is plotted in Figure 150 c) in terms of S_{11} and S_{21} versus frequency. Transmission losses stay below 0.5 dB along most of the bandwidth with a reflection coefficient that is lower than -10 dB. Frequencies lower than 18.5 GHz witness the worst performance with a reflection coefficient lower than -5 dB reaching -3.8 dB at 18 GHz, and transmission losses higher than 1.5 dB, reaching 2.9 dB at 18 GHz.

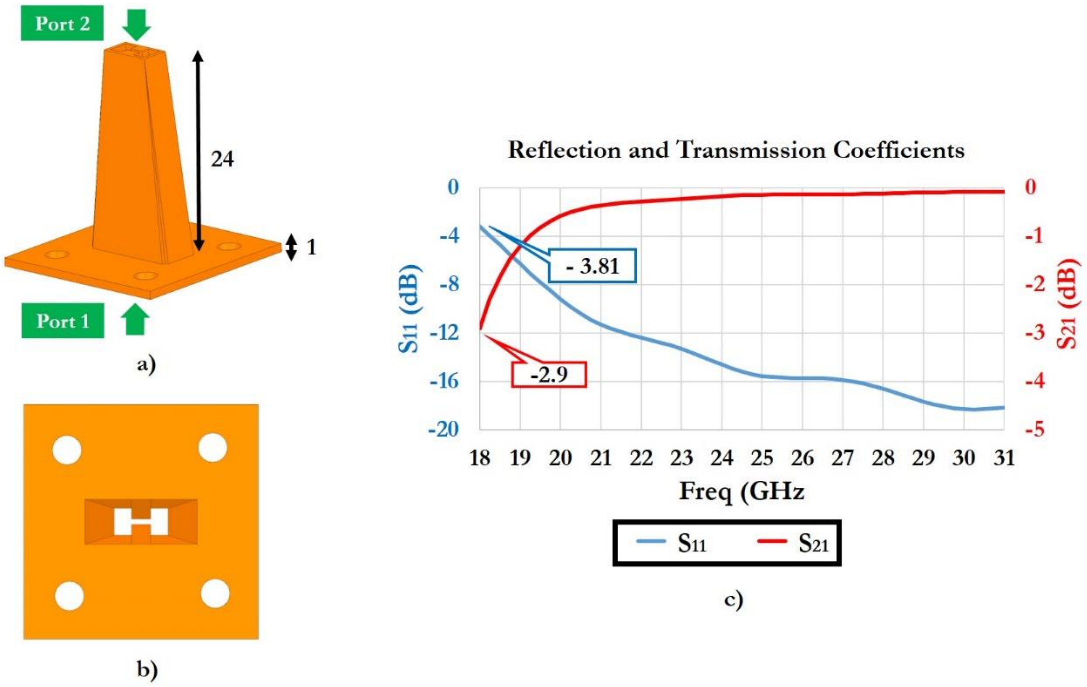

3

Figure 150 Designed WR-42 flange with DRWG-to-WR-42 transition: a) isometric view with dimensions in mm, b) bottom view, c) Simulated S_{11} and S_{21} versus frequency at Ka-band.

IV.4.11 Simulation of the complete 2x2 array

The complete model of the 2x2 antenna array with feeding network and WR-42 flange is assembled using all the previously developed blocks, to be simulated in HFSS. Figure 151 shows the assembled 3-D model with the indication of the different parts. The overall height is 66.8 mm, which is comparable to the 59 mm of the 2x2 unit cell with feeding network and flange realized to work at Ku-band in Chapter 3. Figure 152 a) shows the simulated reflection coefficient versus frequency, being lower than -5 dB along most of the bandwidth, achieving -12 dBi around 27.5 GHz and being minimum in the frequency range of interest. Performance is deteriorated below 18.25 GHz with a maximum return loss of 0.9 dB at 18 GHz. The simulated total efficiency versus frequency is plotted on the same graph showing a similar response, resulting higher than 60% at almost all frequencies with a maximum of 93% around 27.5 GHz and a minimum of 16% at 18 GHz. The simulated S_{11} plotted on a smith chart is given in Figure 152 b). The scattering matrixes of the various components are extracted from HFSS simulations and used to define a circuit model of the complete array with feeding network in ADS. The obtained ADS schematic is shown in Figure 153. Figure 154 shows the simulated reflection coefficient versus frequency, in ADS and HFSS. The objective is to assess the correctness of the ADS results, envisaging the possibility to design a larger structure using similar blocks. This kind of quick simulation would speed up the overall design flow, allowing evaluate the achievable levels of reflection coefficient during the initial design steps. Unfortunately, the differences between the results of the HFSS and the schematic simulation results reach -13 dB at 19 GHz and -9 dB at 22.5 dB. The complicated structure leads to non-negligible electromagnetic and wave interactions between the components of the complete array that cannot be modeled using the schematic simulation, especially at low frequencies. Taking into account the last consideration and the very wide fractional bandwidth (53%), we can appreciate an acceptable agreement between the results obtained in the two cases.

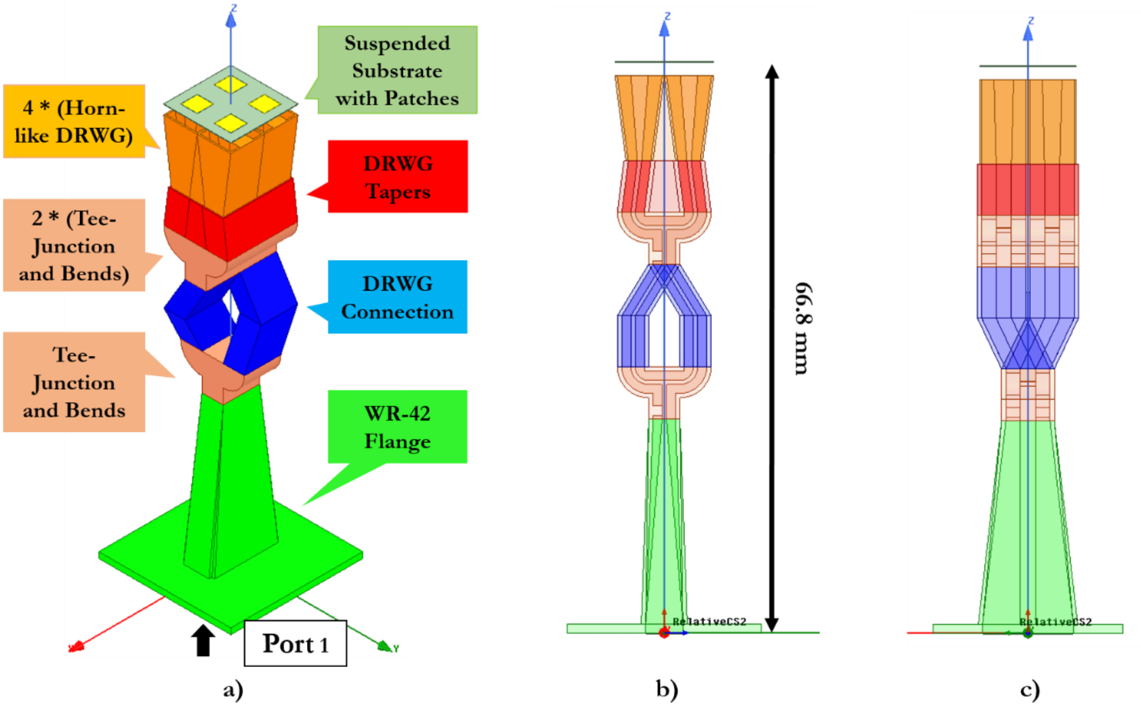

Figure 151 Assembled model of the complete 2x2 antenna array with feeding network and WR-42 flange: a) isometric view with indication of the different components, b) transparent front-view, c) transparent side-view.

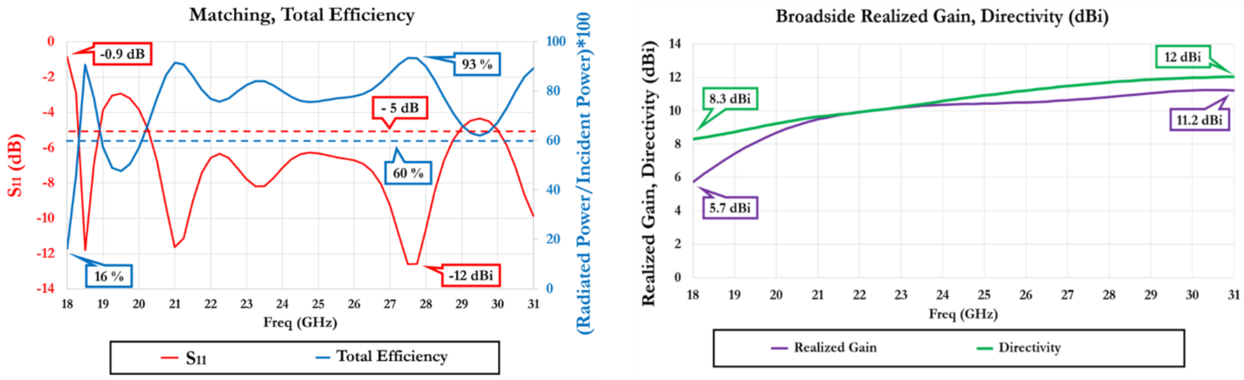

a)

b)

Figure 152 Simulated performance of the 2x2 array with feeding network and flange versus frequency at Ka-band: a) reflection coefficient and total efficiency, b) simulated S_{11} plotted on smith chart.

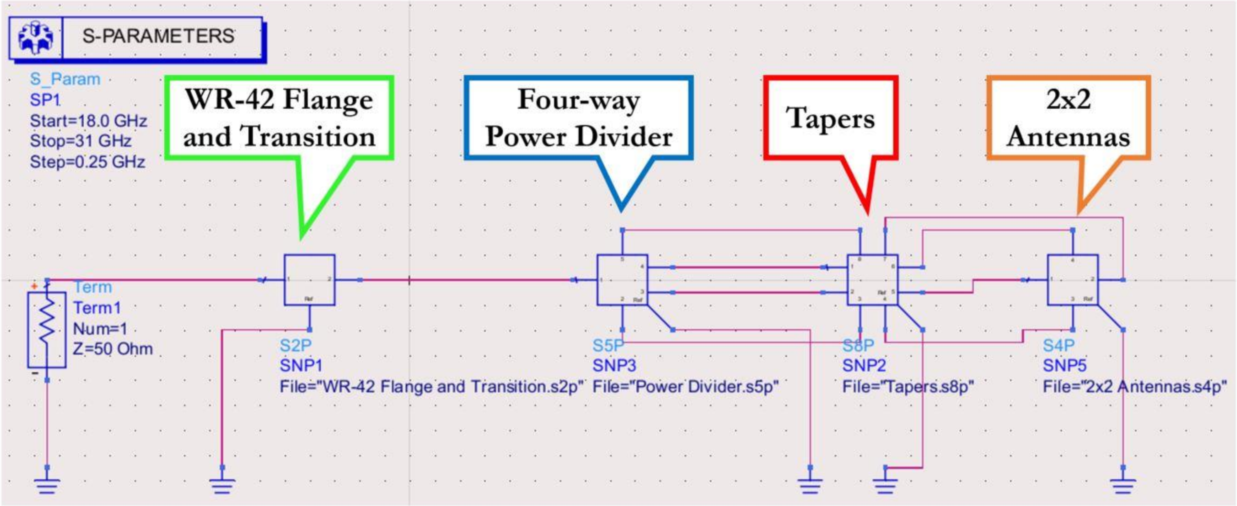

Figure 153 ADS schematic of the complete unit cell, realized using the S-parameters of the different components extracted from the HFSS simulations.

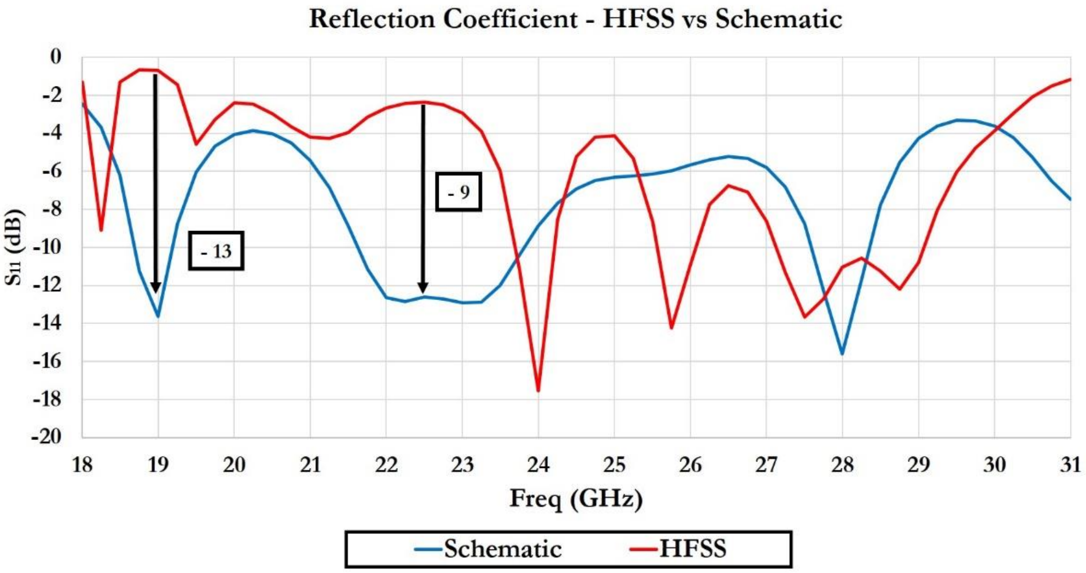

Figure 154 Simulated reflection coefficient of the complete 2x2 array versus frequency, in ADS and HFSS.

Figure 155 shows the simulated broadside realized gain versus frequency in HFSS, ranging from 5.7 up to 11.2 dBi, and the directivity, ranging from 8.3 up to 12 dBi. Figure 156 shows the simulated radiation patterns of the realized gain at 19, 27.5 and 31 GHz, for both the H- and the E- planes.

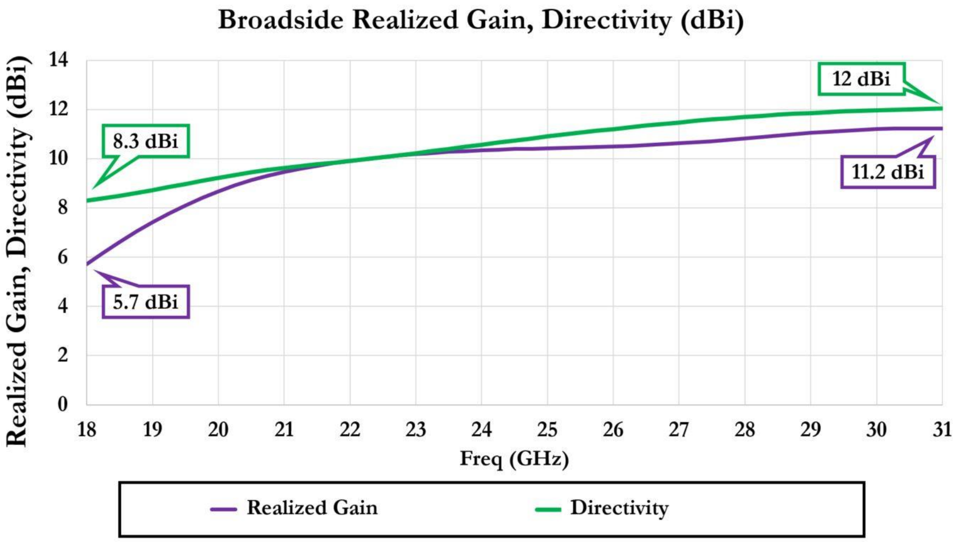

Figure 155 Simulated broadside realized gain and directivity of the 2x2 array with feeding network and flange versus frequency.

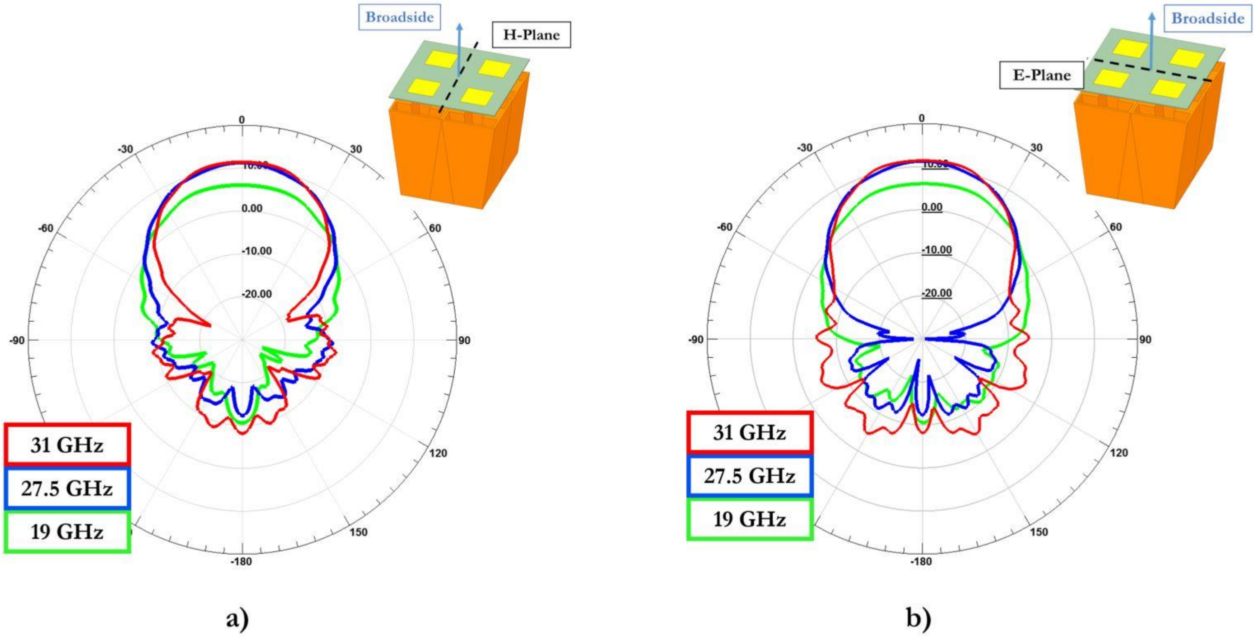

Figure 156 Simulated radiation patterns in terms of realized gain at 19, 27.5 and 31 GHz: a) H-plane, b) E-plane.

IV.4.12 Prototyping by DMLS technology

The objective is to use the DMLS fabrication technology to realize the prototypes of the unit cell working at Ka-band, as done for the Ku-band prototypes. As discussed in Chapter 3, the most important constraint is to avoid any surface to be parallel to the fabrication support in the direction of 3-D printing. Once the manufacturer provides its feedback about the optimal direction and the eventual angle of inclination of the fabrication supports, the initial design must be adapted to comply with the requirements of the process. Figure 157 shows the optimal 3-D printing direction: the model must be fabricated starting from the horn-like DRWGs towards the flange. Particulars of the tee-junction with bends are highlighted, the component must be modified to comply the fabrication constraints: the surfaces parallel to the printing supports and the bends must be replaced with 45° chamfers. Moreover, we envisage to elaborate a strategy in order to prototype the patches without the need to pass through the standard PCB fabrication, but directly integrating them in the metal structure of the unit cell. The recommendations of the additive manufacturing process engineers become fundamentals to correctly modify the design and evaluate the best option, as it will be furtherly discussed.

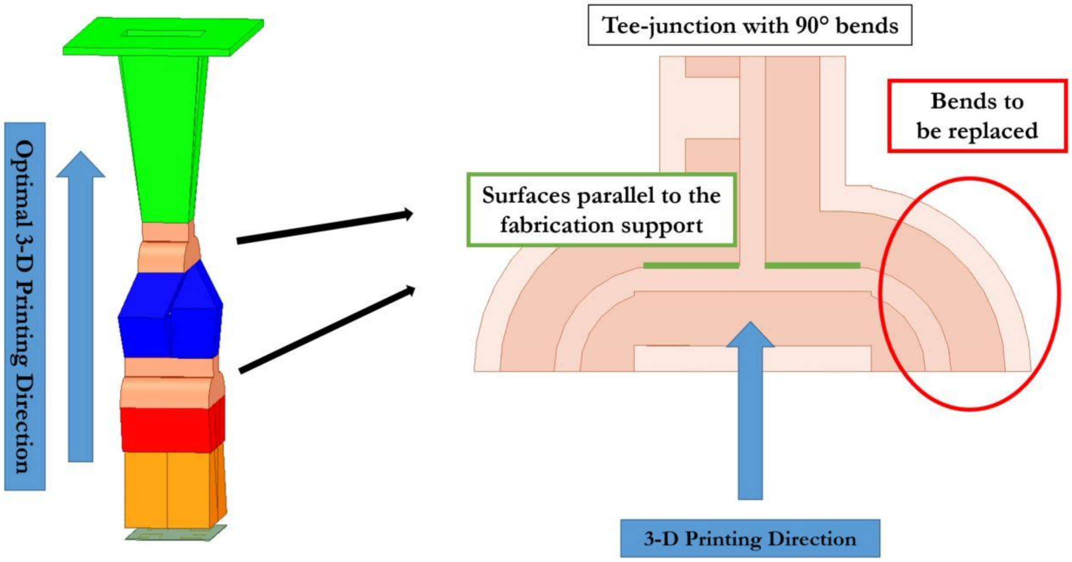

Figure 157 Optimal 3-D printing direction for the DMLS prototyping of the 2x2 array working at Ka-band with particulars of the tee-junction with bends, to be modified in order to comply the fabrication constraints.

IV.4.12.a Modified tee-junction with DRWG 90° bends

The tee-junction and the DRWG 90° bends must be modified replacing the surfaces parallel to the fabrication support in the direction of 3-D printing and the rounded bends with 45° chamfers. This will allow each sintered layer to mechanically support the next ones during the process of additive manufacturing, as explained in Chapter 3. The 3-D models of both the initial tee-junction and the modified one for the fabrication are shown in Figure 158, highlighting the modification of the iris of the input arm and the use of 45° chamfers instead of the rounded and parallel surfaces. Figure 159 a) shows the simulated S_{11} versus frequency, for both the initial design and the one modified for fabrication. The overall matching is improved in the last case, being improved of up to 17 and 16 dB at 20 and 25 GHz, respectively. Figure 159 b) shows the related smith charts. Figure 160 illustrates the simulated transmission losses of the modified design versus frequency overlapped with those of the initial design, resulting reduced along the whole bandwidth of interest with a maximum decrease of 0.6 dB around 27 GHz. We can explain this behavior looking Figure 158 c) and f): the 45° chamfers designed over each iris and those created in order to replace the rounded surface create a smoother transition between the modified tee-junction input and output ports. Hence, the propagation of the electromagnetic waves withstands less abrupt discontinuities if compared to the initial design, leading to such improvements of the performance. Figure 161 illustrates the simulated magnitude of the currents inside a cross section of the tee-junction at 20 GHz for both the initial and the modified tee-junction design, in order to validate the correctness of the previous hypothesis. It is worth to underline the benefits of having the chamfers designed on top of the iris, that lead to higher current values in this part of the structure.

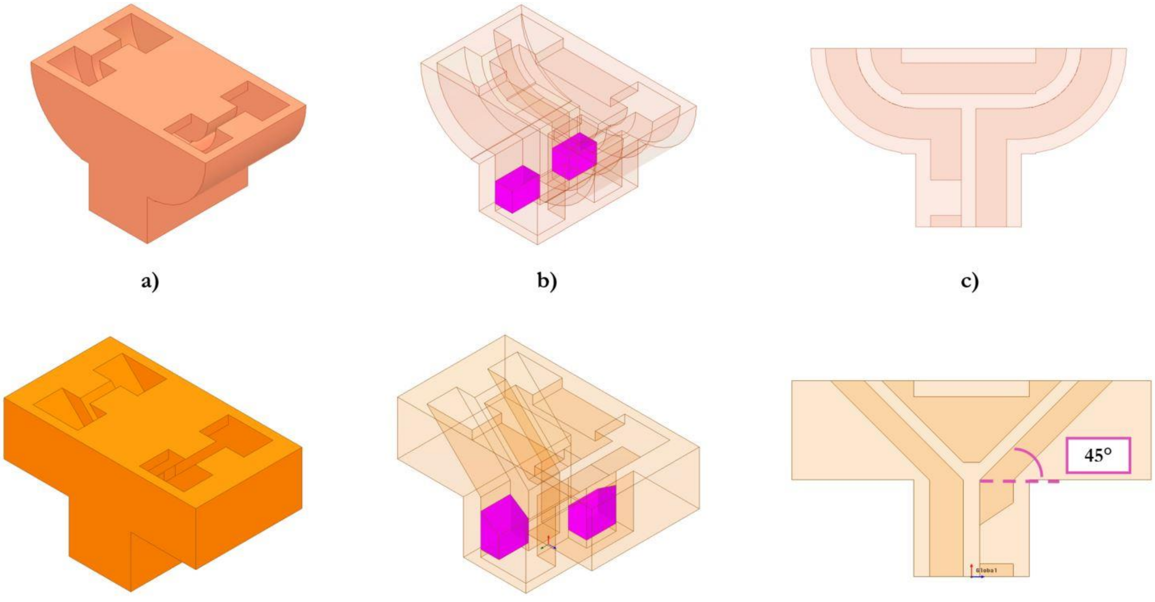

a) b) c)

d) e) f)

Figure 158 Initial tee-junction with 90°bends: a) isometric view, b) transparent isometric view with highlighted iris, c) transparent front-view. Modified tee-junction with 90° bends for fabrication: d) isometric view, e) transparent isometric view with highlighted iris, f) transparent front-view.

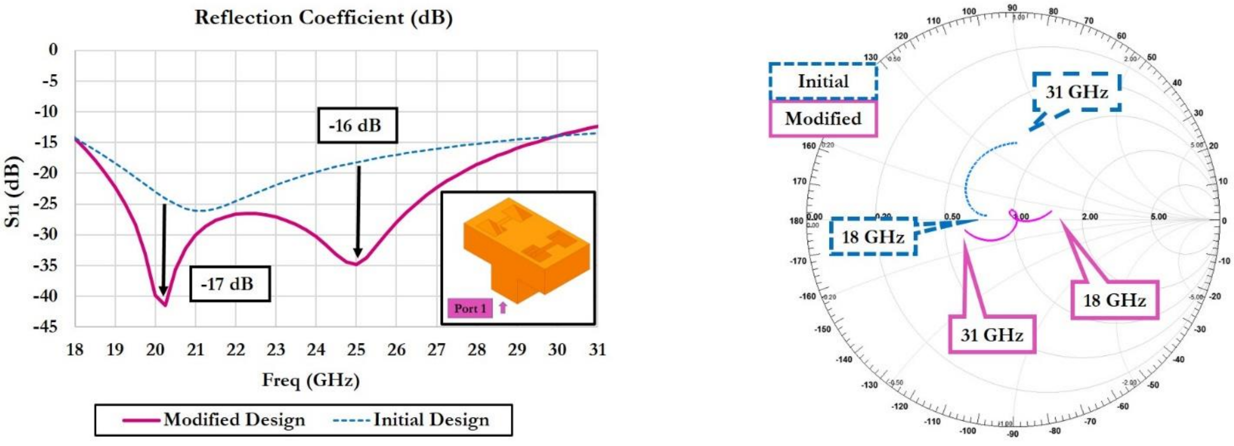

a) b)

Figure 159 a) Simulated reflection coefficient of the modified tee-junction for fabrication versus frequency at Ka-band, compared with the initial design and b) related smith charts.

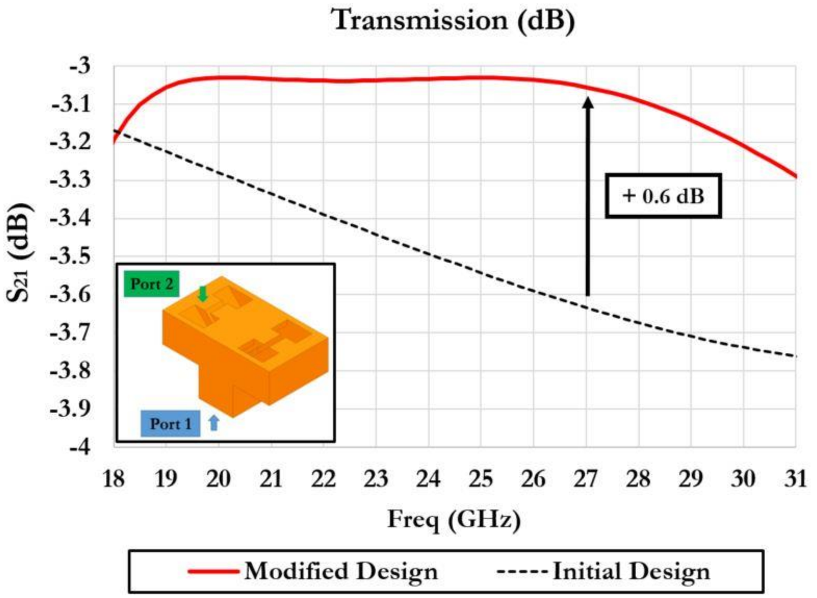

Figure 160 Simulated S_{21} versus frequency for both the initial and the modified tee-junction with bends.

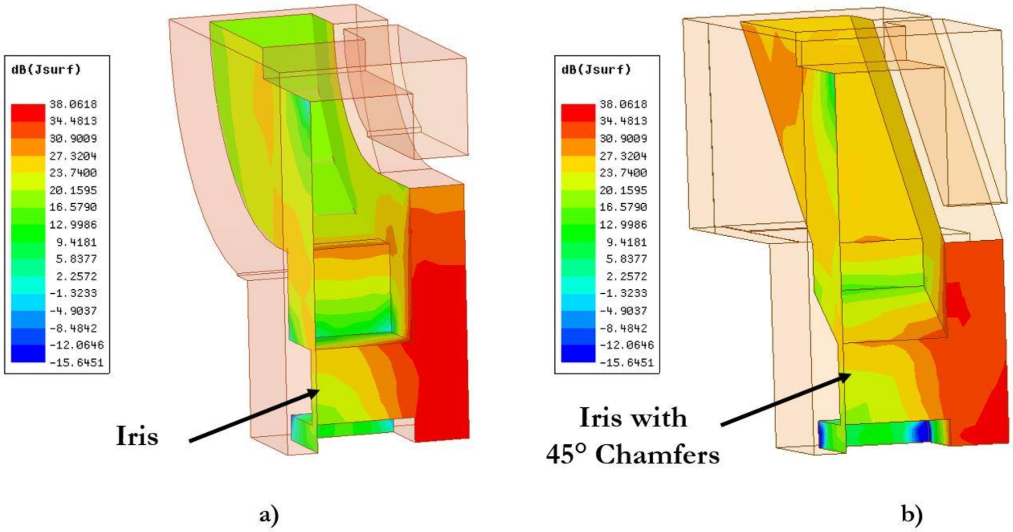

Figure 161 Simulated magnitude of the currents inside a cross section of the tee-junction at 20 GHz: a) initial design, b) modified design for fabrication.

The obtained tee-junction with bend is finally integrated in the feeding network of the unit cell replacing the previous block. The whole unit cell comprising of DRWG connections, antennas, flange and transition is simulated. The aim is to assess the impact of the modifications of the tee-junctions and the bends over the behavior of the complete structure. Figure 162 shows the simulated reflection coefficient and total efficiency of this new design versus frequency, overlapped with the performance of the unit cell integrating the initial tee-junction. As we can see, the reflection coefficient and the total efficiency of the new design oscillates around -5 dB and 90% respectively. The performance of the previous design is generally improved, confirming the advantages of the modifications made to the components in order to comply with the requirements of the fabrication process.

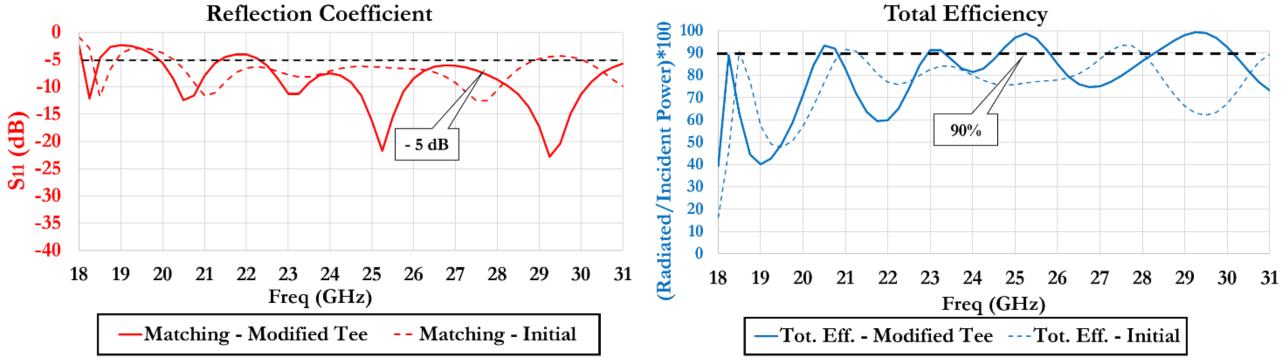

a) b)

Figure 162 Simulated performance of the complete model of the unit cell with the modified tee-junction for fabrication, overlapped with those of the unit cell integrating the initial tee-junction with bends versus frequency: a) reflection coefficient, b) total efficiency.

IV.4.12.b Patch prototyping

The following idea is to directly realize the patches as part of the metal structure and be able to completely leverage the benefits of the additive manufacturing building everything in a single piece. The design of supports able to connect the parasitic patches to the edges of the horn-like DRWG antennas is required. Considering the problem from the electromagnetic perspective, a proper air gap must be introduced to keep the envisaged functionalities of the parasitic elements while getting rid of the dielectric substrate. Moreover, the supports are required to lay in the middle of the edges of the patches along the H-plane, in order to do not modify the overall impedance matching. The previous consideration is true in this particular case, as the antennas operate with a single linear polarization. Figure 163 shows how we may theoretically integrate the patch into the metal structure of the single antenna.

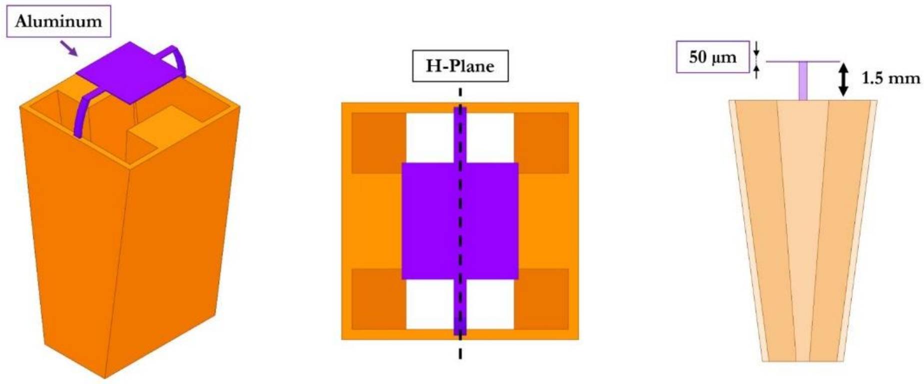

a) b) c)

Figure 163 Ideal integration scheme of the patch in the metal structure without altering the EM performance: a) isometric view; b) top-view, c) transparent side-view.

The challenges come from the mechanical constraints linked to the targeted fabrication process: as we already discussed, the structure will be fabricated from the top (antennas) to the bottom (WR-42 flange). This implies that the elements printed at the very beginning of the process, being the parasitic patches in this case, are meant to withstand all the remaining parts during the progressive fabrication process. Hence, the exchanges with the fabrication engineers and the optimization by simulation lead to two options for the fabrication: a model with patches and supports designed to have a minimum thickness of 1 mm for each layer of aluminum and a model without patches, as shown in Figure 164 a) and b).

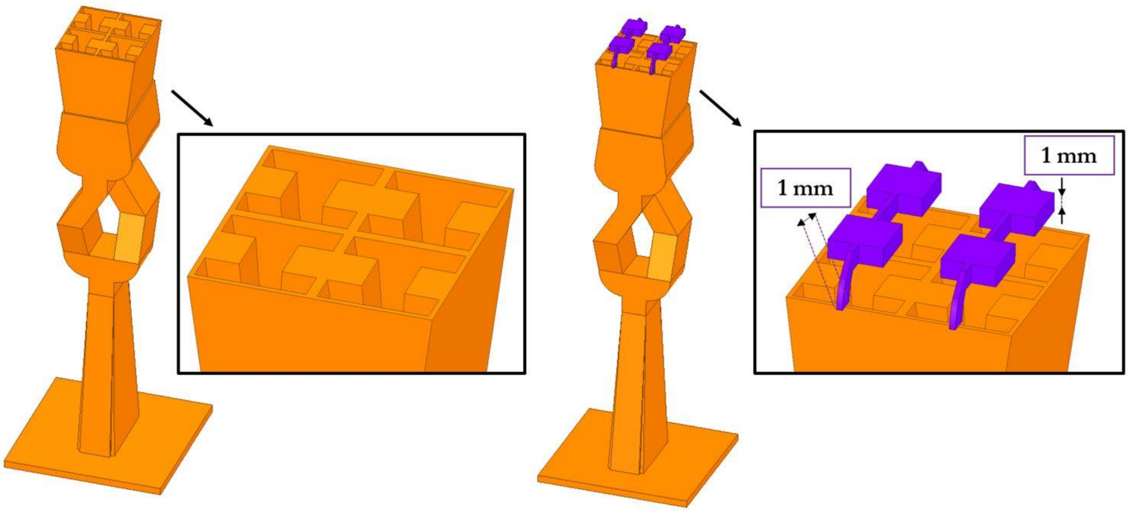

a) b)

Figure 164 Best models for DMLS additive manufacturing: a) unit cell without patches and particular of the horn-like DRWG antennas, b) unit cell with very thick patches and supports and particular of the horn-like DRWG antennas with the parasitic elements.

A simulation step is required to assess and compare the performance of the two designs. The modifications to the response of the design due to the removal of the patches are consistent. Hence, we consider worth to analyze the results highlighting the bands used for Rx and Tx for the Sat-Com-On-The-Move applications at Ka-band, corresponding to (18 – 21) GHz and (27.5 – 31) GHz, respectively. Figure 165 shows the simulated reflection coefficient and total efficiency of the 2 models., resulting almost equivalents in the frequency ranges of interest. Figure 165 a) shows that the reflection coefficient oscillates around -5 dB increasing at very low frequencies for both the simulated design and withstanding a degradation around 31 GHz, only for the model without patches. The performance of the model with patches is strongly preferable in the central part of the band, but it will not be taken into account for this comparison according to the chosen criteria. Figure 165 b) shows the simulated total efficiency with an analog behavior: the values oscillate around the 80% dropping at very low frequencies for both cases and at 31 GHz, only for the model without patches. Figure 166 b) illustrates the simulated broadside realized gain with a similar drop at very low frequencies for two models and another one around 31 GHz for the model without patches, while Figure 166 a) shows the simulated directivity being equivalent in the two cases. Finally, the model without patches is chosen as the model with patches do not guarantee a consistent improvement of the performance in the Rx and Tx frequency ranges.

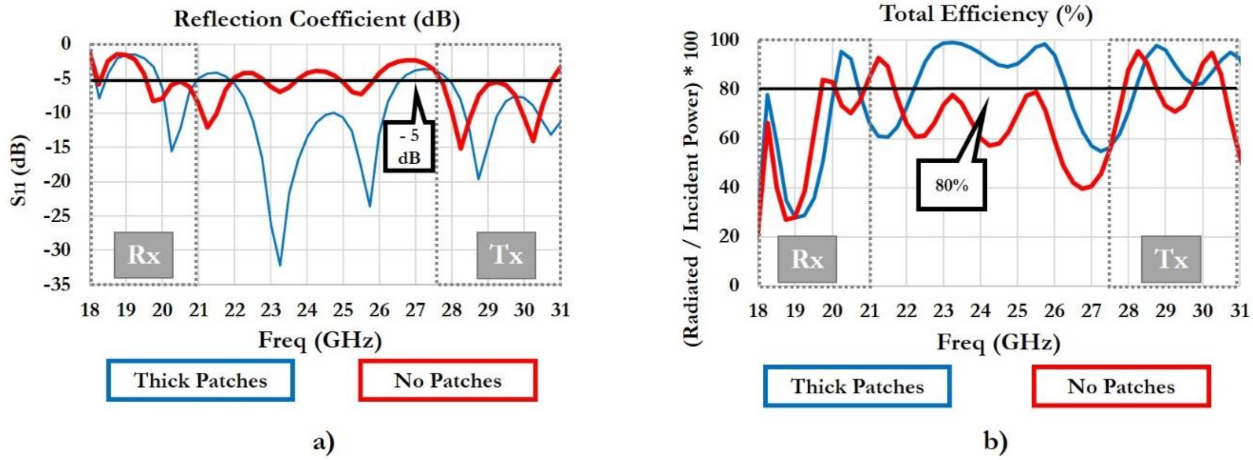

a) b)

Figure 165 Simulated performance of the designs with and without patches versus frequency: a) reflection coefficient, b) total efficiency.

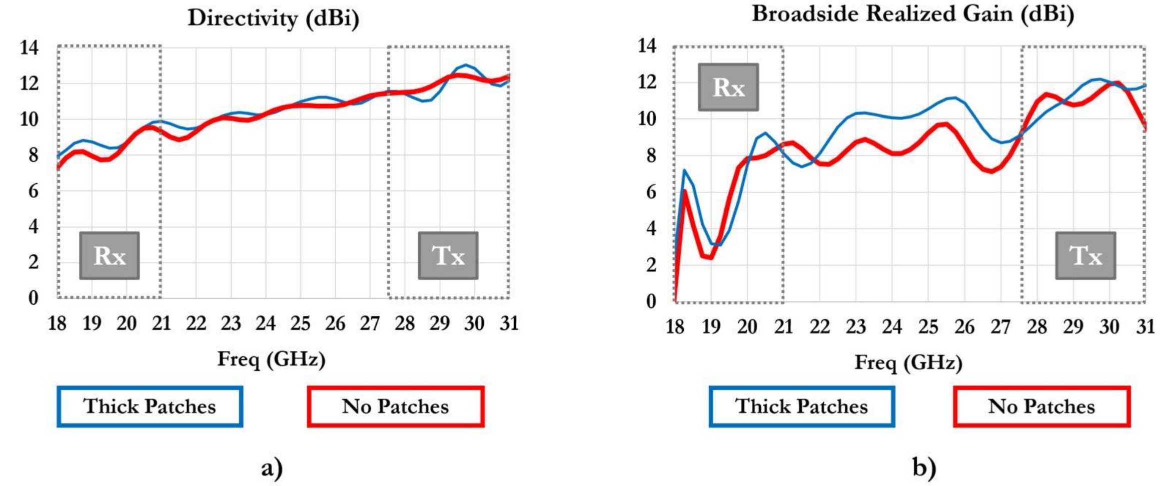

a) b)

Figure 166 Simulated performance of the designs with and without patches versus frequency: a) directivity, b) broadside realized gain.

IV.4.12.c Fabricated Samples

Following the previous considerations, three samples have been fabricated at Initial Prodways France by DMLS technology. Figure 167 a) and b) show the pictures of one these samples from the antennas and flange side, respectively.

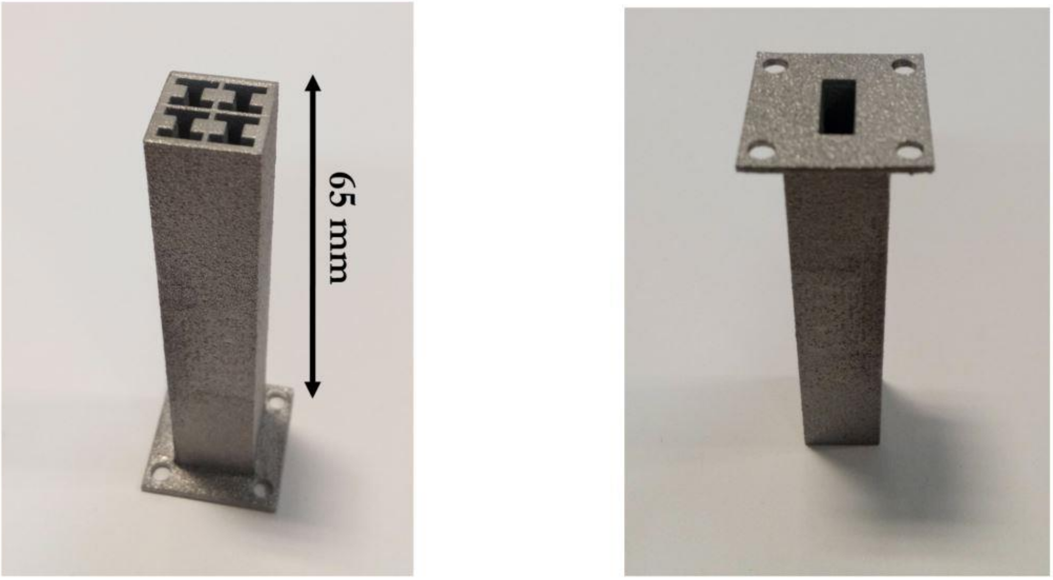

a) b)

Figure 167 Picture of a fabricated 2x2 DRWG antenna array sample in isometric view from : a) DRWG antennas side, b) WR-42 flange side.

IV.4.13 Measurements

The fabricated antenna arrays have been tested in the facilities of the University of Oviedo, leveraging the expertise of Prof. Jaime Laviada Martinez and Guillermo Alvarez Narciandi. The reflection coefficient of the prototypes has been measured using an Agilent PNA-X N5247A [49]. The measured S_{11} is plotted in Figure 168 versus frequency for all the samples, being compared with the simulated one. We underline the reception and transmission bandwidths for Sat-Com-On-The-Move applications at Ka-band for sake of readability. As we can see, the measured reflection coefficient is lower than the simulated one for all the samples both at Rx frequencies, from 18 to 21 GHz, and at Tx frequencies, from 27.5 up to 29 GHz. The measured reflection coefficient is consistently worse than the simulated only between 29 and 30.5 GHz.

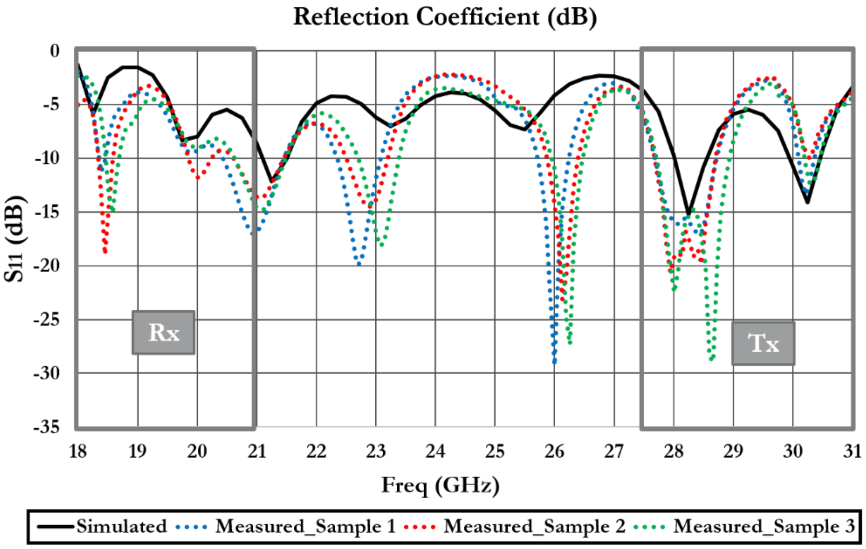

Figure 168 Simulated and measured reflection coefficient of the prototypes versus frequency.

Considering that the behavior of the samples is reproducible and the complex shape of feeding network, we can hypothesize that this behavior is related to the inaccuracy of the fabrication process, leading to unexpected losses within the structure. Concerning the surface roughness that could introduce additional losses not taken into account by the simulations, the arithmetic average roughness (R_a) guaranteed by the manufacturer is equal to 15 μm. Its impact over the performance can be evaluated computing the skin depth effect at the highest frequency of interest (31 GHz) using the following formula from [90]:

$$Skin\ Depth = \delta_s = \sqrt{\frac{\rho}{\pi f \mu_0 \mu_r}} \tag{6}$$

The parameters used in the formula are the electrical resistivity of the $AlSi_{10}Mg$ cast alloy (ρ), its relative permeability (μ_r), the permeability constant (μ_0) and the frequency (f). The computed skin depth value is equal to 633 μm and the resulting normalized average roughness (R_a/δ_s) is slightly above the 2%, which suggests that its impact over the behavior of the structure is negligible [90]. It is worth to underline that the electrical resistivity of the $AlSi_{10}Mg$ cast alloy has been taken from [91]. The other electrical properties of the material are subject to variations during the additive manufacturing process and they are not provided by the manufacturer in our case. It would be interesting to characterize the samples in terms of conductor losses per meter. An experimental method allowing to evaluate them is provided in [92], requiring to characterize a waveguide of fixed length in terms of reflection and transmission coefficients. Unfortunately, only the samples of the complete 2x2 DRWG antenna array with feeding network are available in our case. Moreover, the inner surfaces of the prototypes are characterized by tapers, 45° chamfers and irises, which makes impossible to fairly approximate the overall structure with an equivalent length, so the method provided in the mentioned reference results not applicable.

Figure 169 shows the simulated and measured S_{11} of the prototypes plotted on a smith chart. The charts are split among Rx and Tx Sat-Com-On-The-Move frequencies at Ka-band, in order to ease the fruition of the information for the reader. The analysis of these results confirms the previous considerations.

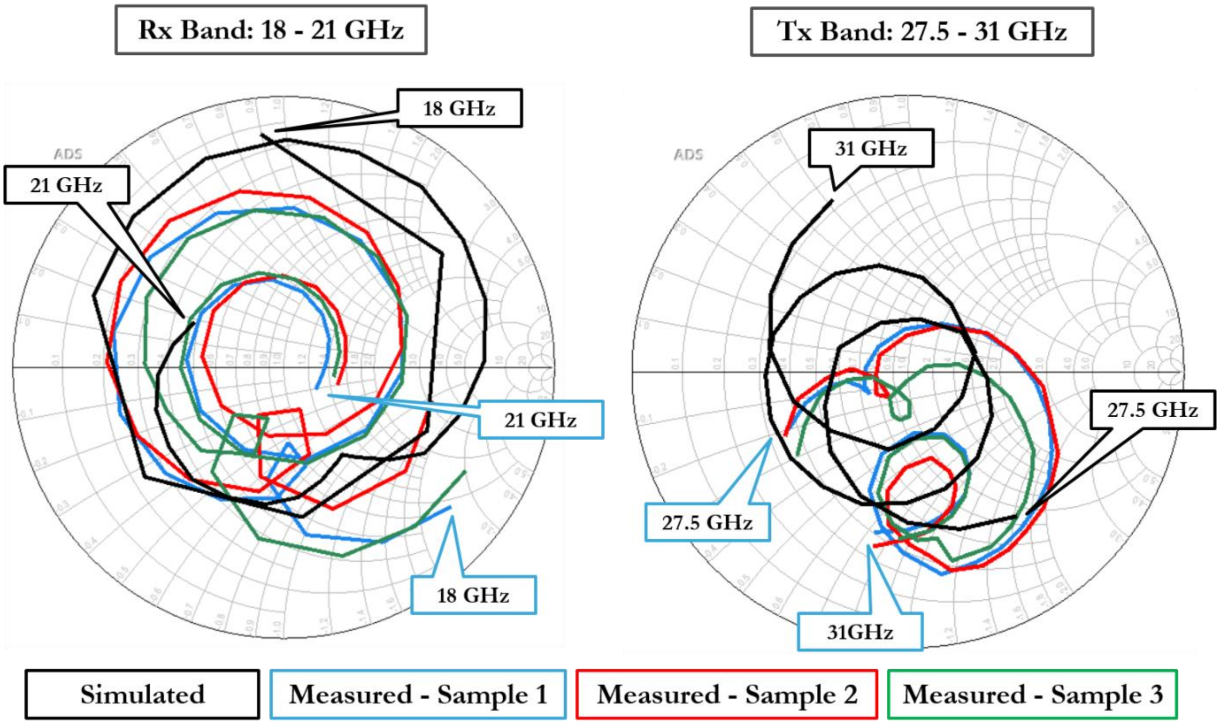

Figure 169 Simulated and measured S_{11} of the prototypes for Rx and Tx Sat-Com-On-The-Move frequencies at Ka-band plotted on a smith chart.

The radiation properties of the samples are measured in the anechoic chamber of the University of Oviedo using the same equipment as described in Chapter 2. Figure 170 a) shows the mounting of the AUT and the probe in the anechoic chamber, Figure 170 b) shows the AUT over the mechanic support in the anechoic chamber without absorbers and the measurement reference system.

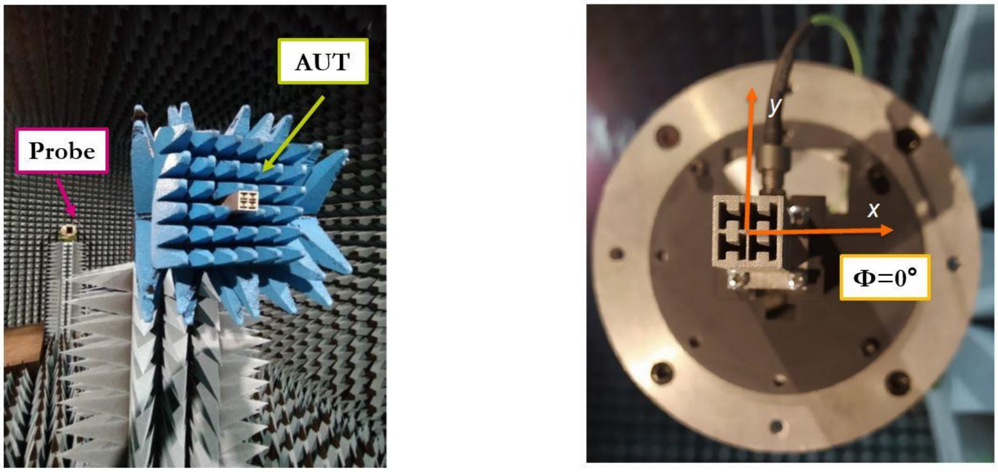

a) b)

Figure 170 a) Picture of the AUT and of the probe in the anechoic chamber, b) picture of the AUT over the mechanic support in the anechoic chamber without absorbers, showing the measurement reference system.

Figure 171 shows the measured and simulated peak realized gain versus frequency for all the samples. We have a good agreement between measurement and simulation at Rx frequencies, while consistent differences are found at Tx ones. We can hypothesize that the roughness of the samples may play a major role determining these differences at the highest frequencies of interest. Also, the flanges of the prototypes are not perfectly flat, and this causes a mechanical mismatching for the connection to the measurement equipment, whose impact is reasonably stronger at high frequencies.

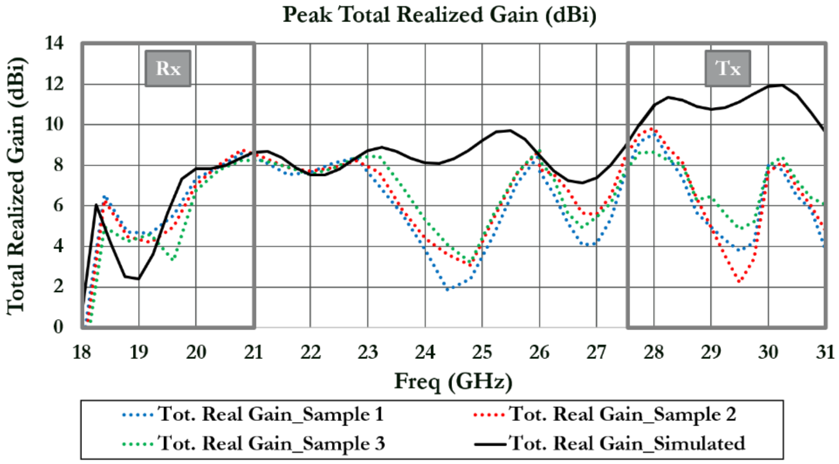

Figure 171 Measured and simulated peak realized gain for the different samples versus frequency.

Figure 172 a) and Figure 173 a) illustrate the simulated and measured ϕ and θ components of the realized gain of one sample for ϕ=0° as a function of θ at 19.2 and 21.2 GHz. Figure 172 b) and Figure 173 b) show the normalized ϕ component of the realized gain (notably representing the co-pol) of one sample for ϕ=0° as a function of θ at 19.2 and 21.2 GHz. These frequencies belong to the Rx sub-band (18 - 21 GHz) with a minor exception for the 21.2 GHz case. It is interesting to underline the good agreement between the simulated and measured radiation patterns, particularly concerning the co-pol. The measured cross-pol is found to be higher than the simulated one.

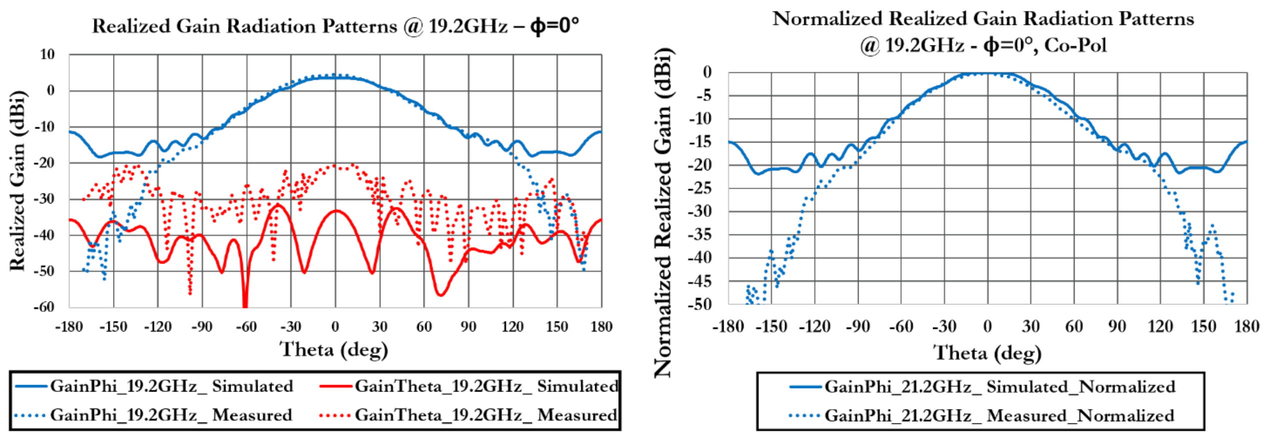

a) b)

Figure 172 Simulated and measured realized gain for ϕ=0° as a function of θ at 19.2 GHz: a) ϕ and θ components of realized gain, b) normalized ϕ component of realized gain.

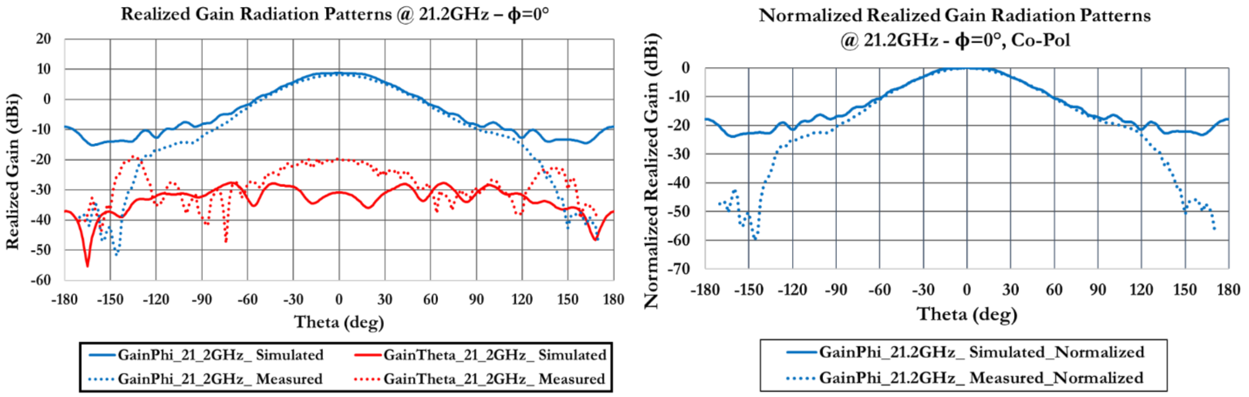

a) b)

Figure 173 Simulated and measured realized gain for ϕ=0° as a function of θ at 21.2 GHz: a) ϕ and θ components of realized gain, b) normalized ϕ component of realized gain.

The same curves given in the previous two figures are illustrated in Figure 174 and Figure 175 at 27.5 and 30 GHz. These frequencies belong to the higher sub-band of interest (Tx) and we appreciate a good agreement between the simulated and measured main lobes for the co-pol, in each case. The measured cross-pol is found to be higher than the simulated one in both cases, instead.

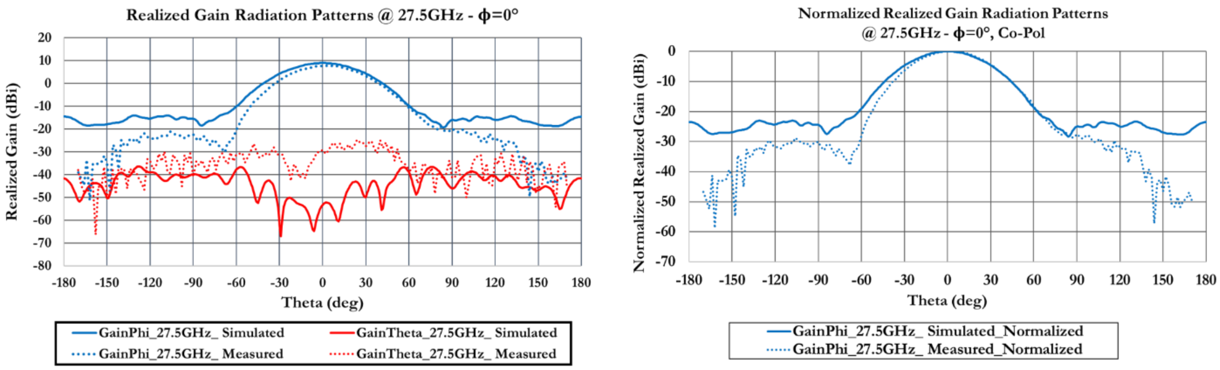

a) b)

Figure 174 Simulated and measured realized gain for ϕ=0° as a function of θ at 27.5 GHz: a) ϕ and θ components of realized gain, b) normalized ϕ component of realized gain.

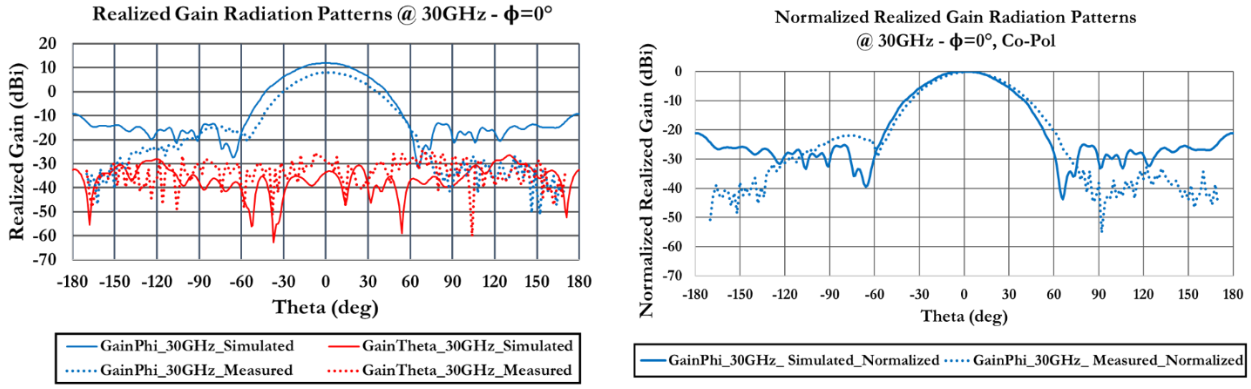

a) b)

Figure 175 Simulated and measured realized gain for ϕ=0° as a function of θ at 30 GHz: a) ϕ and θ components of realized gain, b) normalized ϕ component of realized gain.

IV.4.14 Benchmarking

It is not possible to make an exhaustive comparison of simulation or test results with any high-efficiency 2x2 antenna array working at the same frequencies. Up to our knowledge, there are not enough data in literature about such a small array configuration allowing to perform a consistent benchmarking. Table 17 gives a comparison of the measured peak gain, bandwidth, fractional bandwidth and polarization of our 2x2 array prototype with some of the high-efficiency antenna arrays for Sat-Com-On-The-Move applications at Ka-band. Unfortunately, the data given in the related publications are restrained to the measurements of larger array configurations, so the presented measured peak realized gain values have been extrapolated by the application of the array factor formula. It is worth to underline that this kind of extrapolation leads to values that are generally lower than those that could be obtained analyzing a 2x2 unit cell by itself. Even taking into account the limitation of this approximation, it is evident that the proposed solution outer performs the reviewed prototypes in terms of targeted operational bandwidth, while paying in terms of achievable realized gain.

Antenna Type	Measured Peak Realized Gain (dBi) - 2x2 Array	Bandwidth	Fractional Bandwidth	Polarization
SLOTTED WAVEGUIDE ARRAY - 2 Antenna Panels: 1 Rx and 1 Tx (J. I. Herruzo et al., "Low-Cost Ka-band Switchable RHCP/LHCP Antenna Array for Mobile SATCOM Terminal", Transaction on Antennas and Propagation, vol. 66, n. 5, May 2018)	13.3 (Rx)* 12.2 (Tx)*	Rx: (19.7 – 21.2) GHz Tx: (29.5 – 31) GHz	Rx: 7% Tx: 5%	Single Right- or Left-Handed Circular Polarization.
DRWG Single Panel for Rx/Tx (This Work)	8.6 (Rx) 9.6 (Tx)	Rx/Tx: (18 - 31) GHz	~ 50%	Single Linear
CONTINUOUS TRANSVERSE STUB ARRAY (M. Ettorre et al., "Continuous Transverse Stub Array for Ka-Band Applications," IEEE Transactions On Antennas and Propagation, Vol. 63, No. 11, November 2015)	21.6 (Tx Gain)*	Tx: (27.5 – 31) GHz	12%	Single Linear (Circular if polarizers are integrated)

Table 17 Measured peak realized gain, bandwidth, fractional bandwidth and polarization of the fabricated 2x2 DRWG array working at Ka-band, compared to the most relevant high-efficiency antenna arrays working at Ka- band reported in literature in 2x2 configuration [34], [63]. *Peak values have been extrapolated by mean of the array factor formula from the measurements performed over larger arrays: the slotted waveguide array panels consist of 576 elements for the Rx and 1326 elements for Tx, the continuous transverse stub array consists of 16 elements.

IV.5 Pros and Cons of the proposed solution

The analysis of the advantages and he drawbacks of the proposed 2x2 DRWG antenna array solution must be done taking into account the will to bring Sat-Com-On-The-Move technologies from being restricted to high-end and military users to the consumer mass-market. As described in the previous chapters, this purpose leads to a strong need to replace the traditional reflector-based user terminals with innovative low-cost and low-profile solutions. Our prototypes offer the advantage of a very wide operational bandwidth (the benchmark proposed in Table 17 clearly identifies this feature, if compared to state-of-the-art), guaranteed by the open-ended DRWG antenna design. Moreover, the use of waveguide-based antennas and feeding network guarantees high-efficiency when operating at Ka-band, avoiding the losses that would be associated to a microstrip feeding network for a microstrip patch antenna array working at these frequencies. The fabrication by 3-D printing allows to realize the complete array with its feeding network in a single piece without the need for a further assembly step (i.e. requiring soldering or screws), reducing the overall cost of the process and the weight of possible large antenna array, if the appropriate material is chosen. Finally, the choice of an inter-element distance able to guarantee ±45° of electronic steering avoiding grating lobes would allow to realize a user's terminal requiring a mechanical steering only for the azimuth plane. This set of features would allow to propose a single high-efficiency Rx/Tx antenna panel with an appealing scanning range. Nevertheless, the use of a DRWG antenna design over such a large operational bandwidth brought to mismatching issues over the wide targeted bandwidth. As seen in this Chapter, a horn-like configuration exploiting all the surface available for the unit cell has been required in order to improve this aspect. The drawback is that once all the available surface is exploited it becomes difficult to modify the design in order to support a second linear orthogonal polarization and create circular ones, as required by Sat-Com-On-The-Move at Ka-band, by mean of the electronics. Moreover, Table 17 underlines that the achievable realized gain of our prototypes is lower than that of the other reviewed solutions. Taking into account that this kind of telecommunications has already been developed only for high-end and military customers, we can take as example the Leonardo TST-301 military user's terminal implementing a foldable reflector and declaring a nominal Tx gain of 46.8 dBi [93]. If our prototypes were used for the same application, a large antenna array of 2048 elements would have been required to achieve the same level of gain. This would represent an issue in terms of size and cost of the final product, even if the comparison is made with a military product, whose electrical specifications are usually more stringent than those for civil applications. It is interesting to underline that the researches made about the possibility to integrate a parasitic patch in this Chapter suggest that we can strongly improve the performance of the 2x2 unit cell and improve the realized gain of about 4 dBi along the whole frequency range. As a direct consequence of that, the number of elements of an array able to satisfy the requirements of the previous example could be halved from 2048 to a maximum of 1024. Consequently, a very interesting line for the future developments consists in the investigation of the possibilities related to the integration of this kind of parasitic elements, in order to be fabricated by metal 3-D printing in a single block with the DRWG antennas and the related feeding net

V. CONCLUSIONS AND PERSPECTIVES

The results proposed in this manuscript must be analyzed taking into account the demand for compact and low-cost innovative Sat-Com-On-The-Move user's terminals. The objective is to make this technology affordable for the mass-consumers overcoming the size and price issues of the actually available solutions.

V.1 Conclusions

The results given in Chapter 2 suggest that it is possible to design two different low-cost wideband aperture coupled patch antennas supporting double linear polarizations, to be fabricated in standard PCB technology and working at Ku- and Ka- bands. Each one could allow to perform both Rx and Tx functions for Sat-Com-On-The-Move communications in the respective frequency bands. A user's terminal integrating this kind of antenna would be relieved from the need to exploit two distinct antenna designs for these purposes (which represents a fundamental bottleneck in order to decrease the price of the commercial low-profile user's terminal). The impact over the price and the form factor of the resulting products would be straightforward. The matching, gain and front-to-back ratio of these radiators could be furtherly improved adding a parasitic patch and/or an additional bottom ground layer acting as back-reflector, making a trade-off over the final complexity and the price of the designs [42]. Nevertheless, the levels of gain required by these kinds of application would still require large antenna arrays in order to be achieved. That would be possible only in the case of the Ku- ACP antenna, as the dimension of the radiating patch results equal to 0.22*λ at the highest frequency of interest (14.5 GHz). Considering the Ka-case, the size of the cavity is ~1.4*λ at the highest frequency of interest (31 GHz), so the minimum achievable inter-element distance for an eventual array is such as its functionalities would be compromised by the generation of grating lobes, even in the case of a fixed-beam configuration.

The results given in Chapter 3 illustrate that a 2x2 DRWG antenna array working at Ku- band for Sat-Com-On-The-Move can be fabricated by metal 3-D printing. The achieved operational bandwidth corresponds to the double of best examples of high-efficiency antenna array that can be found in literature allowing to perform both Rx and Tx functions for these applications. The radiating elements are dimensioned in order to allow to electronically scan ±45° in elevation, thus avoiding the apparition grating lobes. This would allow to create a user's terminal with a single antenna panel and a requiring mechanical steering only in the azimuth plane, always taking into account the requirement of LEO mobile satellite telecommunications. The benefits in terms of price, complexity and form factor of the resulting CPE would be immediate. On the other side, the input matching of the antenna array represents one of the major drawbacks of the design. The performance is compromised by the need to comply with the mechanical constraints of the chosen 3-D fabrication process that oblige to add inner chamfers having a degenerative effect over the response of the device itself. This limitation might be overcome by future developments able to exploit more sophisticated metal 3-D printing technologies relaxing parts of these mechanical constraints. The second main limitation of the design is represented by the possibility to support single linear polarization which may be overcome exploiting the space available in the unit cell in order to modify the design and thus, support a second linear orthogonal polarization.

Taking into account the advantages and the drawbacks of the proposed Ku-band unit cell, we can consider that a large 16*32DRWG antenna array design exploiting this solution (see Figure 176 a)) would achieve a Tx broadside realized gain comparable with that of a commercial low-profile and high-efficiency Sat-Com-On-The-Move user's terminal like Sanetel T65 [25]. Figure 176 b) illustrates the simulated realized gain at 14.5 GHz as a function of θ for ϕ=90°, obtained when feeding all the unit cells with the same amplitude and phase. Unfortunately, such a configuration would not allow to perform the elevation beam steering envisaged for LEO Sat-Com-On-The-Move applications. In fact, it is not possible to guarantee the required uniform phase shift between the DRWG antennas in adjacent rows as each feed corresponds to an 2x2 antenna configuration.

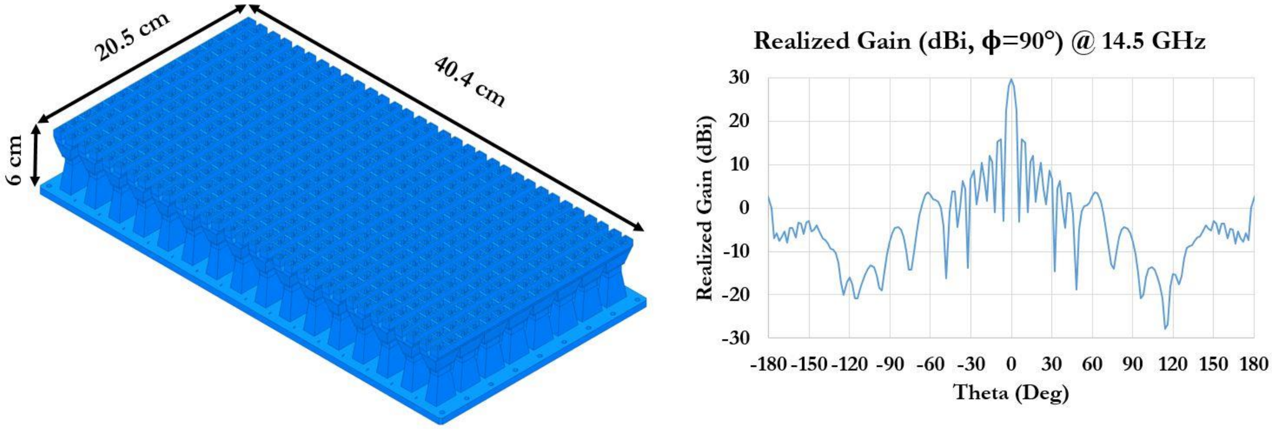

a) b)

Figure 176 a) Isometric view of a 16x32 antenna array working at Ku-band, obtained using the 2x2 DRWG antenna array with feeding network proposed in Chapter 3 as unit cell, b) simulated realized gain at 14.5 GHz as a function of θ for ϕ=90°, obtained when feeding all the unit cells with the same amplitude and phase.

Hence, we proceed designing a 16x32 DRWG antenna array without flanges and feeding networks, such as it is possible to control the amplitude and the phase of the excitation for each radiating element. The designed array, shown in Figure 177 a), is simulated steering the beam in the E-plane (ϕ=90°). All the elements are fed with the same amplitude's excitation. All the elements in a row are fed with the same phase, while a uniform phase shift is applied between rows. Figure 177 b) shows the simulated realized gain curves in the E-plane @ 14.5 GHz, as a function of θ for various steering angles, from

0° to 47°. It is interesting to see that grating lobes start to arise when pointing angle is at 47° (appearing at -75°). Taking into account that the array is envisaged to be used in 45° tilted antenna panel in order to perform a full electronic steering in elevation in a range of ±45°, these results can be considered as satisfying. It is interesting to underline that the symmetry of the design finally guarantees the possibility to steer ±47° in elevation. Figure 178 shows the simulated broadside realized gain and the side lobe level (SLL) of the 32x16 DRWG antenna array at 14.5GHz, as a function of the steering angle. Here we define the SLL as the ratio of the peak realized gain of the first side lobe over the peak realized gain of the overall radiation pattern. The maximum scanning losses are equal to 1.75 dB with an average SLL of -13 dB that reaches a maximum of ~-10 dB when steering the beam at 42°.

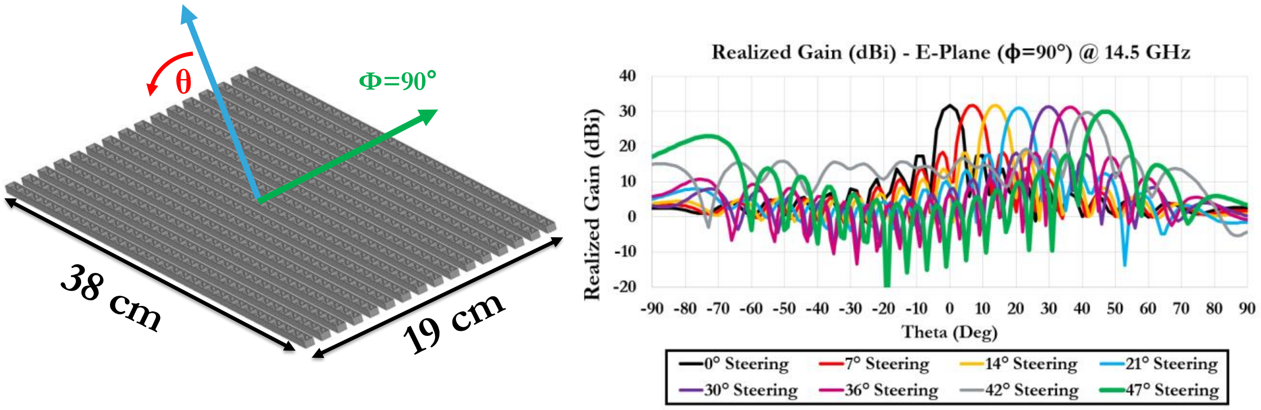

a) b)

Figure 177 a) Designed 16x32 DRWG antenna array working at Ku-band, b) simulated realized gain curves in the E-plane @ 14.5 GHz, as a function of θ for various steering angles.

Figure 178) Simulated broadside realized gain and side lobe level of the 32x16 DRWG antenna array at 14.5GHz as a function of the steering angle, according to the reference system provided in Figure 177 a).

Table 18 shows the comparison of the Sanetel T65 user's terminal for Sat-Com-On-The-Move at Ku-band and the one that could be realized using the designed 16x32 DRWG antenna array. The user terminal integrating our solution would include an antenna panel tilted of 45°, providing a ±45°electronic steering in elevation and a complete mechanical steering in azimuth. Eleven centimeters of additional thickness are taken into account in the comparison of Table 18 for our envisaged solution in order to accommodate mechanics and feeding networks. The profile height for the envisaged user's terminal without radome results 5 cm lower. The weight is given assuming that the 16x32 DRWG antenna array has to be fabricated by DMLS in $AlSi_{10}Mg$ material and excluding the radome, the mechanics and the feeding network. We move from the 54 kg for the complete Sanetel T65 solution to ~1 kg for our single antenna panel. Even taking into account all the given assumptions, rather than the necessity to modify the design in order to support a double linear polarization feature, we can hypothesize that our solution would outerperform the commercial one. It is worth to point out that the will to provide very wideband performance obliges to make a trade-off in terms of achievable gain. Hence, the gain of our solution results lower than the Sanetel T65 one. Nevertheless, we underline that the information about the number of the elements composing the antenna panel of this last solution was not given in the associated datasheet, so the values provided in Table 18 are purely indications [25]. Finally, Figure 179 offers a comparison of the shapes of the two solutions in order to help to visualize their form factor.

User Terminal	Broadside Gain @ 14.5 GHz [dBi]	Profile Height [m]	Surface [m^2]	Weight [kg]
Sanetel T65	**36.2**	**0.3**	**1.3**	**54**
16x32 DRWG*	**31.7**	**0.25**	**0.44**	**~ 1**

Table 18 Comparison of commercial Sanetel T65 Sat-Com-On-The-Move complete user's terminal for Ku-band (including radome and mechanics)and of the one that could be realized using the designed 16x32 DRWG antenna . * The array is tilted of 45° in elevation, in order to use a full electronic scan approach in this plane, given surface takes into account the required mechanical 360° rotation in the azimuth plane. Gain and weight are those of the 16x32 DRWG antenna array without radome, mechanics and feeding network. The profile height includes additional 11cm of thickness in order to accommodate mechanics and feeding network.

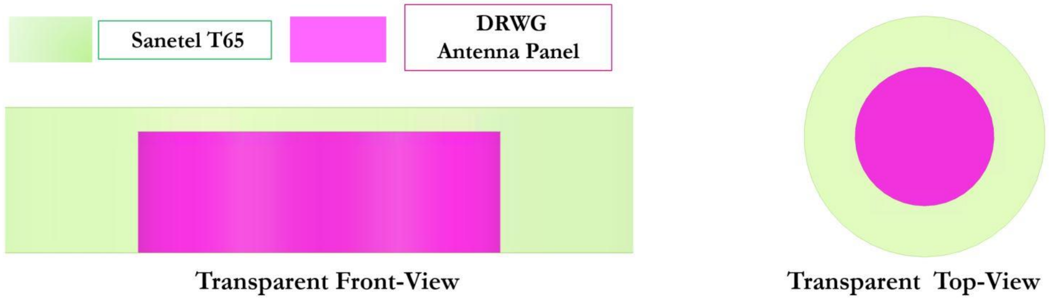

Figure 179 Comparison of the shapes of the Sanetel T65 and of the 32x16 DRWG antenna array depicted in Table 18 (without radome): a) transparent front-view, b) transparent top-view .

The results given in Chapter 4 suggest that a design similar to the Ku- 2x2 DRWG unit cell could be proposed in order to work at Ka-band and cover a fractional bandwidth of ~50%, such as both Rx and Tx functions for Sat-Com-On-The-Move applications could be performed at these frequencies. The wideband performance represents a strong innovation, if compared to the state-of-the-art: the best reviewed solution offers the 12% of operational fractional bandwidth [34]. The second interesting innovation comes from the possibility to realize the high-efficiency metal antenna array with the related feeding network in a single piece by DMLS 3-D printing. Nevertheless, the measurements confirm the matching issues already appreciated at Ku-band, being related to the wide operational bandwidth to be covered and especially to the need to comply with the mechanical constraints of the fabrication process. Moreover, the disagreements between measurement and simulation results suggest that the fabrication accuracy has a higher impact when working at higher frequencies than Ku- ones. On top of that, the model to be fabricated includes more complicated shapes than the previous one. A more sophisticated fabrication process with relaxed mechanical constraints would directly improve the achievable performance. Taking into account that the actual commercial Ka-band Sat-Com-On-The-Move user's terminals target high-end users and usually integrate reflector antennas, we consider not worth to propose a comparison like the one offered for the Ku- development.

V.2 Perspectives

The perspective of this work would be to realize a user's terminal demonstrator for LEO Sat-Com-On-The-Move communications, to be comprehensive of a Rx/Tx antenna panel, control electronics and rotary mechanics. Regarding the antenna panel, the Ku- and Ka-band DRWG radiating elements developed in the previous chapters would need modifications in order to support a second orthogonal linear polarization. The objective is to allow the generation of a double orthogonal polarization by mean of the electronics, as required by Sat-Com-On-The-Move applications. This would allow to electronically generate a double circular polarization in the Ka- case. Nevertheless, the Ku- case represents the most suitable choice for the development of a demonstrator, due to the form factor of the single DRWG antenna developed in Chapter 3. That last could be modified moving to a squared quadruple-ridged waveguide (QRWG) configuration, in order to support a second orthogonal linear polarization. Figure 180 shows a possible integration scheme for the envisaged demonstrator.

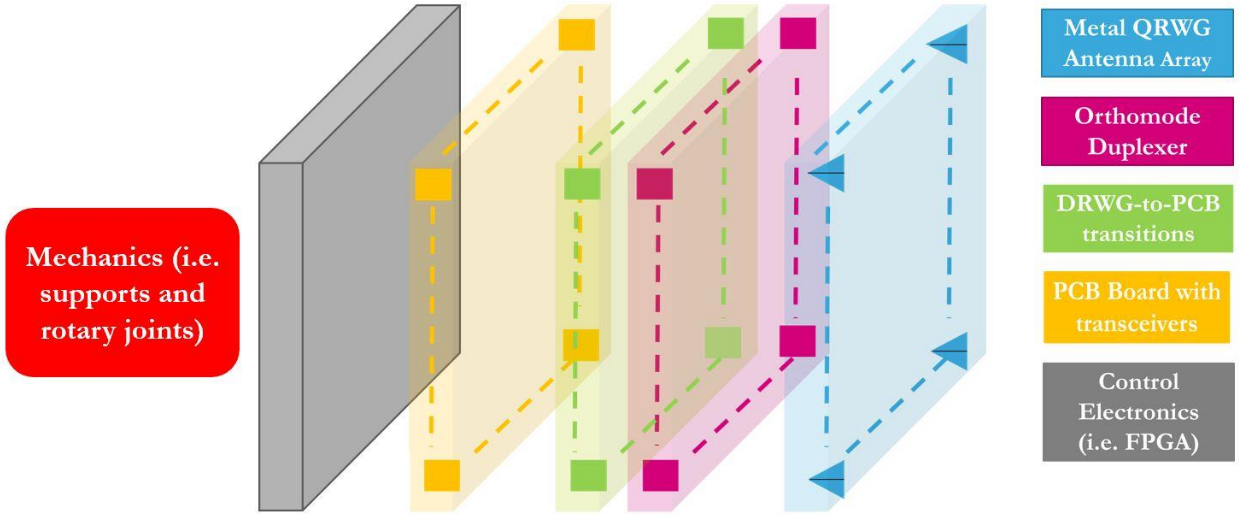

Figure 180 Possible integration scheme for full demonstrator working at Ku-band, to be realized in continuation of this work.

Focusing on the antenna panel, we underline that the radiating element modification may theoretically be done without infringing the form factor limits that allow to set the inter-element distance required for an antenna array that could be electronically steered ±45° at 14.5 GHz avoiding grating lobes. Once that will be done, the design and the fabrication of a large QRWG antenna array should be anticipated by the design, fabrication and test a smaller one (i.e. 4x4 or 8x8) [94]. The experience acquired in this work suggests that this intermediate step may be done in terms of a fixed beam antenna array solution with the related feeding network. This would allow to validate all the aspects related to the fabrication and the measurements. Concerning the fabrication, the mechanical constraints of DMLS fabrication led to degenerative effects in terms of matching and achievable gain of the Ku-band 2x2 DRWG antenna array proposed in Chapter 3. This was due to the necessity to add inner chamfers acting as inner supports for the structure during its fabrication. Envisaging the use of QRWG antennas with more complicated shapes to be realized by metal 3-D printing, an important improvement would come from the possibility to exploit fabrication technology with relaxed mechanical constraints. Moreover, the simulations of the 4x4 Ku-band DRWG antenna arrays highlighted the benefits of adding parasitic patches, in terms of achievable matching and realized gain over the wide operational bandwidth. This would be suitable even in the case of the antenna panel for the demonstrator, requiring the use of a metal 3-D printing technology allowing to print the patches in the same block as the antennas. A viable alternative would be to realize them on a very thin PCB board, to be assembled to the metal antenna panel afterwards. The final large array would comprehend the QRWG radiating elements without a waveguide-based feeding network, in order to allow the control of the amplitude and phase' excitation for each element. Such feature would allow to define customized excitation laws by the control electronics, allowing either to steer the beam and dynamically to control the characteristics of the generated beam in function of the steering angle (i.e. SLL). In fact, an important requirement for a LEO Sat-Com-On-The-Move user terminal is to comply with the ETSI mask in terms of equivalent power flux density (EPFD) produced by the user' terminal in uplink. More information about the way to calculate this figure of merit can be found in [95]. Considering that the spectrum results shared with Geo-stationary systems in a real scenario, it becomes crucial to avoid to interference with them. Detailed information about the subject can be found in the license application provided by SpaceX to the Federal Communications Commission of the United States in order to obtain the approval for the deployment of its non-geostationary satellite system [96]. The design of a metal wideband orthomode transducer would be crucial. Such device should able to guarantee -40 dB of isolation between the orthogonally polarized signal paths, in order to be in line with the state-of-the-art [7]. An important challenge would be linked to the need for a compact device design, possibly complying with the requirements of the targeted metal 3-D printing fabrication process. That should be characterized by a QRWG arm at the input of the antenna and two DRWG output arms, corresponding to the two orthogonal linear polarizations. The next step would be the design of a layer of DRWG-to-PCB transitions, required in order to connect each output arm of the transducer to the electronics. This would represent a design challenge, taking into account the geometry of this kind of radiating element and the need to realize a compact device, able to minimize the transmission losses at these frequencies. Hypothesizing to correctly satisfy all these demands, a system architecture recalling that of the Phasor user's terminal reviewed in Chapter 1 could be envisaged. A PCB board should be designed to be placed on the back of the antenna panel, such as each antenna would be associated to a transceiver. A particular attention would be required for the design of the associated filters to be used for the Tx and Rx chain, respectively. A FPGA-based digital beamforming technique at baseband is therefore envisaged in order to perform the beam steering in elevation and dynamically adjust the characteristics of the beam in function of the pointing angle. Finally, the envisaged approach would to assembly the antenna panel with the electronics, being tilted by 45°, and to fix them on a rotary joint. Hence, the boresight direction of the phased array would correspond to an angle of 45° in elevation, allowing to achieve an electronic steering of (0, 90)° in this plane avoiding grating lobes, up to 14.5 GHz. A scanning range of (0, 360)° in azimuth should be obtained by mechanical steering.

A similar demonstrator could be theoretically realized integrating the designed Ku-band ACP antenna, instead of the envisaged QRWG one. The planar radiating element is already designed in order to support a dual linear polarization. The major drawback is actually represented by the achieved port-to-port isolation of the fabricated samples, as shown in Chapter 3. The information given in [97] suggest that a dual polarization microstrip aperture coupled patch could achieve a port-to-port isolation higher than 50 dB. The approach provides a metal ground layer with quasi-cross shaped coupling slots and two orthogonal fork-shaped feeding lines with U-shaped stubs, as shown in Figure 181 a). The first feeding line (and the related substrate) is placed below the metal ground layer, while the second one (and the related substrate) is placed above, as shown in Figure 181 b). The ACP antenna developed in [98], whose transparent top-view and cross-section are shown in Figure 181, offers a -10 dB impedance FBW of ~18% around the center frequency of 3.5 GHz with a maximum measured gain of 9.6 dBi. Moreover, the proposed stack-up includes two different dielectric materials exploited for the feeding lines and the patch sun substrate, respectively, rather than a layer of air. Hence, the first challenge would be to prove the possibility to modify the Ku-band ACP antenna proposed in this thesis, in order to achieve the 30% of -10 dB impedance FBW at these frequencies while guaranteeing at least 40 dB of port-to-port isolation. Such design would require taking a particular attention to the complexity of the final stack-up in a low-cost perspective.

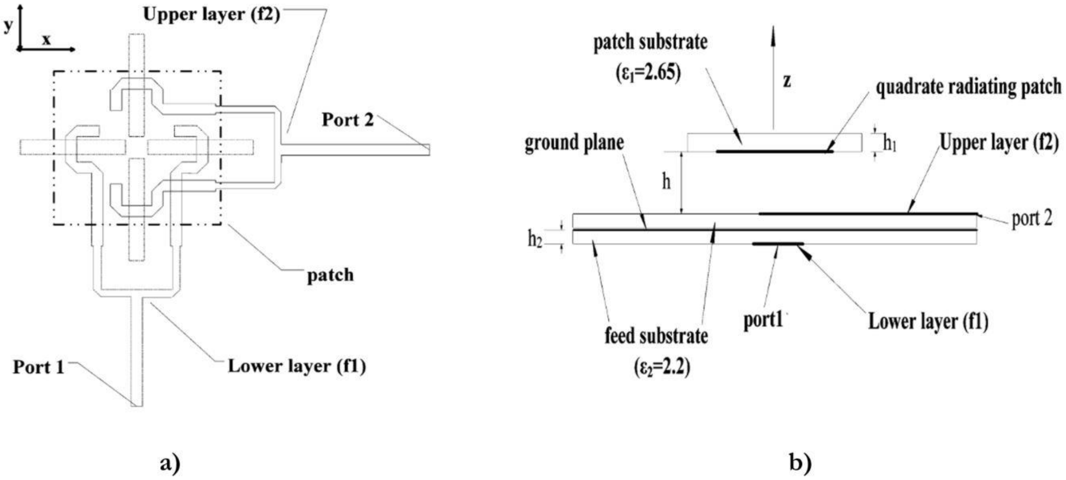

Figure 181 Dual polarization microstrip ACP antenna with high port-to-port isolation, from [8]: a)transparent top-view, b) cross-section.

If a satisfying trade-off between performance and cost of the antenna solution is achieved, then a large antenna panel could be theoretically realized in PCB technology. Hence, it would be possible to realize a demonstrator with an approach similar to the one depicted in Figure 180. The advantage is that there would be no need for a layer of waveguide-based duplexers and the related transitions towards the PCB board. This would relieve from the associated transition losses and from a challenging task in terms of mechanical integration. A microstrip-based orthomode duplexer in standard PCB technology would be required, instead.

A theoretical comparison between the two envisaged demonstrators should be done based on the achievable complexity, cost and performance of the complete solutions. To give an example: the possibility to obtain a (0, 90)° grating-lobe free electronic beam-steering in elevation should be proven in both cases, for both polarizations and at the highest frequency of interest. Not being able to satisfy this condition would require complicating the overall mechanical scanning system, with the consequent effects in terms of complexity and cost of the final solution, and this may be the reason for choosing one of them over the othe

Bibliography

[1] "Global mobile data traffic from 2017 to 2022 (in exabytes per month)." [Online]. Available: https://www.statista.com/statistics/271405/global-mobile-data-traffic-forecast/. [Consulted: 06-March-2020]

[2] J. Foust, "SpaceX's Space-Internet Woes," *IEEE Spectr.*, vol. 56, pp. 50–51, 2019.

[3] S. Borisov and A. Shishlov, "Antennas for Satcom-on-the-Move, Review," Proceedings of 2014 International Conference on Engineering and Telecommunication, Moscow, Russia, 2014, pp. 3–7.

[4] A. Anwar, "Military Satellite Terminals RF Technology Trends and Outlook," Microwave Journal, vol. 10, 2019. Online]. Available: www.microwavejournal.com/articles/31920-military-satellite-terminals-rf-technology-trends-and-outlook. [Consulted: 2-december-2019]

[5] "Satellite frequency bands." [Online]. Available: https://www.esa.int/Applications/Telecommunications_Integrated_Applications/Satellite_frequency_bands. [Consulted: 06-March-2020]

[6] T. Rossi et al., "Experimental Italian Q/V band satellite network," Proceedings of IEEE Aerospace Conference, Big Sky, USA, 2009, pp. 1–9.

[7] "How have c-band satellite services improved our world." [Online]. Available: https://www.ses.com/blog/how-have-c-band-satellite-services-improved-our-world. [Consulted: 06-March-2020]

[8] "Satcom frequency bands and how they affect maritime users." [Online]. Available: https://marlink.com/satcom-frequency-bands-and-how-they-affect-maritime-users/.[Consulted: 06-March-2020]

[9] C. Hudson, "Ku-band vs. Ka-band – What's the Real Story?," 2012. [Online]. Available: https://www.intelsatgeneral.com/blog/ku-band-vs-ka-band-whats-real-story/.

[10] D. Venugopal, M. G. Chandrasekhar, K. S. Mohanavelu, and K. Narayanan, "Ka-band satellite communication systems - applications and configurations," Proceedings of International Astronautical Congress, Jerusalem, Israel, pp. 3698–3702.

[11] H. Jameson, "Beyond Ka-: supporting future telecommunications." [Online]. Available: http://interactive.satellitetoday.com/via/january-2017/beyond-ka-supporting-future-telecommunications/. [Consulted: 06-March-2020]

[12] G. Codispoti et al., "RF technologies for the ground segment of future Q/V band satellite systems," Proceedings of Ka and Broadband Communications Conference, Trieste, Italy, 2017. [Online]. Available: http://proceedings.kaconf.org/papers/2017/ka1_4.pdf. [Consulted: 8-december-2019].

[13] Y. Lee and J. P. Choi, "Performance Evaluation of High-Frequency Mobile Satellite

Communications," IEEE Access, vol. 7, pp. 49077–49087, 2019.

[14] Telesat, "Real-Time Latency Rethink Possibilities with Remote Networks," 2018. [Online]. Available: https://www.telesat.com/sites/default/files/telesat/brochures/telesat_leo_-_real-time_latency_rethink_the_possibilities_with_remote_networks.pdf. [Consulted: 06-March-2020]

[15] I. Del Portillo, B. G. Cameron, and E. F. Crawley, "A technical comparison of three low earth orbit satellite constellation systems to provide global broadband," Proceedings of International Astronautical Congress, Bremen, Germany, 2018, pp. 1–12.

[16] N. Panagiotarakis, I. Maglogiannis, G. Kormentzas, and T. De Cuyper, "An Overview of Major Satellite Systems Key Satellite Communication The Major Satellite Systems," Proceedings of 2nd International Conference on Multimedia, Internet and Video Technologies, Skiathos, Greece, pp. 2451-2455, 2002.

[17] T. Taleb, N. Kato, and Y. Nemoto, "Recent trends in IP/NGEO satellite communication systems: transport, routing, and mobility management concerns," IEEE Wireless Communications, vol. 12, no. 5, pp. 63–69, 2005. [18] Eutelsat, "Eutelsat Satellites." [Online]. Available: https://www.eutelsat.com/en/satellites.html. [Consulted: 06-March-2020]

[19] Eutelsat, "Eutelsat Fact Figures." [Online]. Available: https://news.eutelsat.com/documents/eutelsat-facts-and-figures-83987. [Consulted: 06-March-2020]

[20] Intelsat, "Intelsat Fleet." [Online]. Available: http://www.intelsat.com/global-network/satellites/fleet/. [Consulted: 06-March-2020]

[21] Intelsat, "The Intelsat Epic NG Platform : High Throughput , High Performance to Support Next-Generation Requirements Intelsat," 2013. [Online]. Available: http://www.intelsat.com/wp-content/uploads/2016/03/Intelsat-Epic-Positioning-6493-wp.pdf. [Consulted: 06-March-2020]

[22] Satellite Industry Association, "Summary of the state of the Satellite Industry 2019," 2019. [Online]. Available: https://www.sia.org/wp-content/uploads/2019/05/2019-SSIR-2-Page-20190507.pdf. [Consulted: 06-March-2020]

[23] "DRS Ku-Band On-the-move antenna system." [Online]. Available: https://www.leonardodrs.com/media/1813/x38v_cotm_datasheet.pdf. [Consulted: 06-March-2020]

[24] "v85NX - 85cm Ku-Ka Convertible Maritime VSAT Antenna System Datasheet." [Online]. Available: https://www.digisat.org/v85nx-ku-ka-maritime-vsat-antenna. [Consulted: 06-March-2020]

[25] "SANETEL-T65 Datasheet." [Online]. Available: http://www.sanetel.com/upload/editor/files/T65 Brochure.pdf. [Consulted: 06-March-2020]

[26] Gogo, "Gogo 2Ku Specifications: High-performance inflight connectivity." [Online]. Available: http://static1.squarespace.com/static/57b203af5016e15b4c5dfac1/t/57b20ec215d5db405ffc

1f6d/1471286985901/Gogo+2KU.pdf. [Consulted: 06-March-2020]

[27] “Phasor SpecSheet.” [Online]. Available: http://www.phasorsolutions.com/fdownload.php?path=block/subPages/17/Phasor Spec Sheet (March 2017).pdf. [Consulted: 06-March-2020]

[28] K. Kirchoff and M. Zeweri, “Flat Panel Electronically Scanned Antenna Advantages,” in Proceedings of Inmarsat Developer Conference, London, UK, 2007, pp. 1–28. [29] “Kymeta mtenna flat panel vsat system.” [Online]. Available: https://www.satphonestore.com/solutions/critical-communications/news-and-media/kymeta-mtenna-flat-panel-vsat-system.html. [Consulted: 06-March-2020]

[30] “Kymeta expands distribution network to support remote alternative energy facilities.” [Online]. Available: https://www.windpowerengineering.com/kymeta-expands-distribution-network-support-remote-alternative-energy-facilities/. [Consulted: 06-March-2020]

[31] D. De Wet, “The why and how of High Throughput Satellites.” [Online]. Available: http://marketingspread.co.za/2016/11/22/the-why-and-how-of-high-throughput-satellites/. [Consulted: 06-March-2020]

[32] Y. Guan, F. Geng, and J. H. Saleh, “Review of high throughput satellites: Market disruptions, affordability-throughput map, and the cost per bit/second decision tree,” IEEE Aerospace Electronic Systems Magazine, vol. 34, no. 5, pp. 64–80, 2019.

[33] “Satellite Connectivity.” [Online]. Available: https://www.iis.fraunhofer.de/en/ff/kom/satkom/satellite_iot.html. [Consulted: 06-March-2020]

[34] M. Ettorre, F. F. Manzillo, M. Casaletti, R. Sauleau, L. Le Coq, and N. Capet, “Continuous Transverse Stub Array for Ka-Band Applications,” IEEE Transactions on Antennas and Propagations, vol. 63, no. 11, pp. 4792–4800, 2015.

[35] “Mini Cooper.” [Online]. Available: https://www.dimensions.guide/element/mini-cooper. [Consulted: 06-March-2020]

[36] Berginsight, “Insurance Industry Standards for Vehicle Tracking.” [Online]. Available: http://www.lbsinsight.com/filearchive/4/418/Insurance Industry Standards for Vehicle Tracking.pdf. [Consulted: 06-March-2020]

[37] “Taipan-48 Datasheet.” [Online]. Available: https://www.emsolutions.com.au/downloads/datasheets/Taipan_48_XKa_190602A.pdf. [Consulted: 06-March-2020]

[38] F. Tiezzi, S. Vaccaro, D. Llorens, C. Dominguez, and M. Fajardo, “Applications of hybrid phased array antennas for mobile satellite broadband communication user terminals,” in Proceedings of 7th European Conference on Antennas and Propagation, Gothenburg, Sweden, 2013.

[39] M. Kacar, C. Perkowski, P. Deffenbaugh, J. Booth, G. Mumcu, and T. Weller, “Wideband Ku-band antennas using multi-layer direct digital manufacturing,” in Proceedings of 2017 Antenna and Propagation International Symposium, San Diego, USA, 2017, pp. 1243–1244.

[40] P. Gorski, J. S. Silva, and J. R. Mosig, “Wideband, low profile and circularly polarized K/Ka

band antenna," in Proceedings of 9th European Conference on Antennas and Propagation, Lisbon, Portugal, 2015, pp. 11–13.

[41] H. Liu, A. Qing, Z. Ding, C. Zhang, and Y. Guan, "Multilayer Circularly Polarized Planar Aperture-Coupled Antenna for Satellite Applications," in Proceedings of 2018 Antenna and Propagation International Symposium, Boston, USA, 2018, pp. 349–350.

[42] F. Klefenz and A. Dreher, "Aperture-coupled stacked microstrip antenna with dual polarization and low back-radiation for X-band SAR applications," in Proceeding of RAWCON 2000, Denver, USA, pp. 179–182, 2000.

[43] A. S. Hussam, F. Mohmmad, W. M. Abdel-Wahab, G. Rafi, and S. Safavi-Naeini, "A 4×4 circularly polarized aperture coupled antenna array for Ka-band satellite communication," in Proceedings of 2015 Antenna and Propagation International Symposium, Vancouver, Canada, 2015, pp. 1896–1897.

[44] D. M. Pozar, "Microstrip Antenna Aperture-Coupled To A Microstripline," Electron. Lett., vol. 21, no. 2, pp. 49–50, 1985.

[45] V. Rathi, G. Kumar, and K. P. Ray, "Improved coupling for aperture coupled microstrip antennas," IEEE Trans. Antennas Propag., vol. 44, no. 8, pp. 1196–1198, 1996.

[46] T. Brauner, R. Küng, R. Vogt, and W. Bächtold, "5-6 GHz Low-Noise Active Antenna Array for Multi-Dimensional Channel-Sounding," in Proceedings of the 2003 SBMO/IEEE MTT-S International Microwave and Optoelectronics Conference, Foz do Iguacu, Brazil, 2003, pp. 297–301.

[47] F. Croq and A. Papiernik, "Stacked slot-coupled printed antenna," IEEE Microw. Guid. Wave Lett., vol. 1, no. 10, pp. 288–290, 1991.

[48] "Hirose HK-LR-SR2, DataSheet." [Online]. Available: https://www.digikey.fr/product-detail/fr/hirose-electric-co-ltd/HK-LR-SR2/H125497-ND/6679766. [Consulted: 06-March-2020]

[49] "N5247A PNA-X Microwave Network Analyzer, 67 GHz." [Online]. Available: https://www.keysight.com/en/pdx-x201825-pn-N5247A/pna-x-microwave-network-analyzer-67-ghz?pm=spc&nid=-32497.1150178&cc=FR&lc=fre. [Consulted: 06-March-2020]

[50] K. K. Sood, F. Klefenz, and A. Dreher, "Experimental Ka-band array elements for ATM-SAT terminal antenna," Asia-Pacific Microw. Conf. Proceedings, APMC, p. 34, 2000.

[51] M. M. Nikolić, A. R. Djordjević, and A. Nehorai, "Microstrip antennas with suppressed radiation in horizontal directions and reduced coupling," IEEE Trans. Antennas Propag., vol. 53, no. 11, pp. 3469–3476, 2005.

[52] H. Kim, K. Yeon, W. Kim, and C. S. Park, "Design and implementation of electromagnetic band-gap embedded antenna for vehicle-to-everything communications in vehicular systems," ETRI J., vol. 0, no. December 2018, pp. 1–8, 2019.

[53] A. Bisognin, "Evaluation of low loss organic technologies and 3D-printing plastic technologies in order to develop innovative antenna solutions in the 60 GHz - 140 GHz frequency band," Université de Nice - Sophia Antipolis, 2015.

[54] N. Nachabe, “Evaluation of 3D printing technologies for the development of wide-band directive antennas for millimeter wave backhaul links in E and V frequency bands,” Université Côte d’Azur, 2018.

[55] E. Lacombe, “Evaluation of silicon photonic technology for the development of innovative 40 Gbps wireless link above 200 GHz,” Université Côte d’Azur, 2018.

[56] E. Levine, G. Malamud, S. Shtrikman, and D. Treves, “A study of Microstrip Array Antennas with Feeding Network,” IEEE Trans. Antennas Propag., vol. 37, no. 4, pp. 426–434, 1989.

[57] “Microwave Horn Antenna.” [Online]. Available: https://www.electronics-notes.com/articles/antennas-propagation/horn-antenna/basics-primer.php. [Consulted: 06-March-2020]

[58] J. Reifenhäuser, “Investigation of a Plastic Printed Slotted Waveguide Antenna for Airborne SAR Applications,” B.S. Thesis, German Aerospace Center - Microwaves and Radar Institute, 2019, pp 7-17. [Online]. Available: https://elib.dlr.de/122382/1/Bachelor%20Thesis%20Jan%20Reifenh%C3%A4user.pdf.

[59] A. Valero-Nogueira et al., “Switchable RHCP/LHCP slotted waveguide array antenna for SATCOM on-the-move applications in Ka-band,” Proceedings of the 8th European Conference on Antennas and Propagation, The Hague, Netherlands, 2014, pp. 2047–2051.

[60] D. Gonzalez-Ovejero, J. I. Herranz-Herruzo, A. Valero-Nogueira, and J. V. Balbastre-Tejedor, “Design of radome-covered slot-array antennas loaded with parasitic dipoles for circular polarization at Ka band,” Proceedings of the Second European Conference on Antennas and Propagation, Edinburgh, UK, 2007, pp. 2047–2051.

[61] “Slotted Waveguide Antennas.” [Online]. Available: http://www.antenna-theory.com/antennas/aperture/slottedWaveguide.php. [Consulted: 06-March-2020]

[62] “LOCOMO - LOw COst and compact Ka-band MObile satcom terminal.” [Online]. Available: https://artes.esa.int/projects/locomo. [Consulted: 06-March-2020]

[63] J. I. Herranz-herruzo, A. Valero-nogueira, M. Ferrando-rocher, and B. Bernardo-clemente, “Low cost switchable RHCP / LHCP Antenna for SOTM Applications in Ka-band,” Poceedings of the 9th European Conference on Antennas and Propagation, Lisbon, Portugal, 2015, pp. 210–212.

[64] “NEW ANTENNA FOR SOTM APPLICATIONS SUCCESSFULLY DEVELOPED.” [Online]. Available: http://www.iteam.upv.es/2016/12/21/desarrollo-con-exito-de-una-nueva-antena/. [Consulted: 06-March-2020]

[65] F. F. Manzillo, “Wideband and flat multibeam antenna solutions for ultrafast communications in millimeter band,” PhD thesis, Université Rennes 1, 2017. [Online]. Available: https://tel.archives-ouvertes.fr/tel-01766807/document.

[66] M. Ettorre, F. F. Manzillo, M. Casaletti, R. Sauleau, L. Le Coq, and N. Capet, “Continuous Transverse Stub Array for Ka-Band Applications,” IEEE Transactions on Antennas and Propagation, vol. 63, no. 11, pp. 4792–4800, 2015.

[67] T. Sikina, D. McKay, K. Komisarek, and B. Porter, “Variably inclined continuous transverse stub-2 antenna,” Proceedings of the IEEE International Symposium on Phased Array

Systems and Technology, Boston, USA, 2003, pp. 435–440.

[68] R. B. I. S. Otto, I. Nistal, S. Holzwarth, O. Litschke, "Planar Satcom Antenna Systems in Ka-Band," Proceedings of the 25th ESA Antenna Workshop on Satellite Antenna Technology, Noordwijk, The Netherlands, 2012. [Online]. Available: https://pdfs.semanticscholar.org/b77f/a363170960a7f4733306b6295b3c0fa58b40.pdf

[69] I. Nistal-González et al., "Planar Phased Array Antenna for Nomadic Satellite Communication in Ka-Band," Proceedings of European Microwave Week 2014, Roma, Italy, pp. 396–399.

[70] K. S. Son, S. Y. Hwang, C. G. Park, and J. W. Yu, "Waveguide slot array in-motion antenna for receiving both RHCP and LHCP using single layer polarizer," Proceedings of Asia-Pacific Microwave Conference, Yokohama, Japan, 2006, vol. 1, pp. 331–334.

[71] A. Guennou-Martin et al., "Design and manufacturing of a 3-D conformal slotted waveguide antenna array in Ku-band based on Direct Metal Laser Sintering," Proceedings of 2016 IEEE International Conference on Antennas and Applications, Syracuse, USA, 2017, pp. 1–4.

[72] G. L. Huang, S. G. Zhou, and T. H. Chio, "Waveguide-Fed Cavity Backed Slot Antenna Array with high efficiency in the Ku-band," Proceedings of 2012 IEEE International Symposium on Antennas and Propagation, Chicago, USA, 2012, pp. 1–2.

[73] A. F. Yagli et al., "An antenna array for Ku band satellite reception," Proceedings of 2015 International Review of Progress in Applied Computational Electromagnetics, Williamsburg, USA, pp. 1–2, 2015.

[74] M. J. González et al., "Low cost and compact Ka-band mobile satcom terminal," in Proceedings of the 8th European Conference on Antennas and Propagation, The Hague, Netherlands, 2014, pp. 1229–1232.

[75] S. Hopfer, "The Design of Ridged Waveguides," *IRE Trans. Microw. Theory Tech.*, vol. 3, no. 5, pp. 20–29, 1955.

[76] T.Chen, "Calculation of the Parameters of Ridge Waveguides," *IRE Trans. Microw. Theory Tech.*, vol. 5, no. 1, pp. 12–17, 1957.

[77] D. M. Pozar, Microwave Engineering. Wiley, 2004, pp. 158-159.

[78] "Grating Lobes." [Online]. Available: https://www.microwaves101.com/encyclopedias/grating-lobes. [Consulted: 06-March-2020]

[79] "FABRICATION ADDITIVE MÉTAL." [Online]. Available: https://www.initial.fr/impression-3d-metal/fusion-metal-dmls/. [Consulted: 06-March-2020]

[80] J. R. Fisher, "Phased Array Feeds for Low Noise Reflector Antennas," 1996.

[81] Y. Miura, J. Hirokawa, M. Ando, Y. Shibuya, and G. Yoshida, "Double-layer full-corporate-feed hollow-waveguide slot array antenna in the 60-GHz band," IEEE Transactions on Antennas and Propagation, vol. 59, no. 8, pp. 2844–2851, 2011.

[82] "Standard Flange Details." [Online]. Available: https://www.maurymw.com/Precision/WR112_WR34_Drawings.php. [Consulted: 06-

March-2020]

[83] B. A. Fulcher, D. K. Leigh, and T. J. Watt, "Comparison of AlSi10Mg and Al 6061 Processed Through DMLS," Proceedings of the 25th Solid Freeform Fabrication Symposium, Austin, USA, 2014, pp. 404–419.

[84] "Direct Metal Laser Sintering." [Online]. Available: https://www.custompartnet.com/wu/direct-metal-laser-sintering. [Consulted: 06-March-2020]

[85] A. Arboleya, Y. Alvarez, and F. Las-Heras, "Millimeter and submillimeter planar measurement setup," in Proceedings of 2012 IEEE International Symposium on Antennas and Propagation, Chicago, USA, 2012, pp. 1–2.

[86] "Standard Waveguide Horns." [Online]. Available: https://nardamiteq.com/docs/WAVEGUIDEHORNANTENNAS_STANDARD_GAIN_HORNS_2.60_TO_40_GHZ.PDF. [Consulted: 06-March-2020]

[87] J. Ruiz, P. Soto, V. E. Boria, and A. A. S. Bias, "Compensated double-ridge waveguide E-plane and H-plane T-junctions," in Proceedings of 2015 Mediterranean Microwave Symposium, Lecce, Italy, 2015.

[88] "Waveguide Junctions." [Online]. Available: https://www.electronics-notes.com/articles/antennas-propagation/rf-feeders-transmission-lines/waveguide-junctions.php. [Consulted: 06-March-2020]

[89] "Rectangular Waveguide Sizes." [Online]. Available: https://www.everythingrf.com/tech-resources/waveguides-sizes. [Consulted: 06-March-2020]

[90] "Skin Depth." [Online]. Available: https://www.microwaves101.com/encyclopedias/skin-depth. [Accessed: 02-Mar-2020]. [Consulted: 06-March-2020]

[91] C. Silbernagel, I. Ashcroft, P. Dickens, and M. Galea, "Electrical resistivity of additively manufactured AlSi10Mg for use in electric motors," Addit. Manuf., vol. 21, no. March, pp. 395–403, 2018.

[92] B. Zhang et al., "Metallic 3-D Printed Antennas for Millimeter- and Submillimeter Wave Applications," IEEE Trans. Terahertz Sci. Technol., vol. 6, no. 4, pp. 592–600, 2016.

[93] "Leonardo TST-301 B." [Online]. Available: https://www.leonardocompany.com/documents/20142/3163259/TST301B_LQ_mm08603_.pdf?t=1542796661540. [Consulted: 06-March-2020]

[94] H. A. Wheeler, "A Systematic Approach to the Design of a Radiator Element for a Phased-Array Antenna," Proc. IEEE, vol. 56, no. 11, pp. 1940–1951, 1968.

[95] ITU, "ITU Article 22_Space services." [Online]. Available: https://life.itu.int/radioclub/rr/art22.pdf.

[96] M. Albulet, "Attachment A to the FCC's License Approval for SpaceX Non-Geostationary Satellite System," 2017. [Online]. Available: https://fcc.report/IBFS/SAT-MOD-20181108-00083/1569860.pdf.

[97] P. K. Verma and R. Kumar, "Realization of Ku-Band Ortho Mode Transducer with High Port to Port Isolation," vol. 74, no. January, pp. 111–115, 2018.

[98] J. Lu, Z. Kuai, X. Zhu, and N. Zhang, "A High-Isolation Dual-Polarization Microstrip Patch Antenna With Quasi-Cross-Shaped Coupling Slot," *IEEE Trans. Antennas Propag.*, vol. 59, no. 7, pp. 2713–2717.

List of Publications

Invited Talk:

- F. Filice, Nour Nachabe, Frédéric Gianesello & Cyril Luxey. "3D-Printed Double-Ridged Waveguide Array Antenna targeting High-Efficiency Ku-band SatCom on The Move Applications", Ansys Innovation Conference 2019, Paris, France, 2019.

Conferences:

- F. Filice, Nour Nachabe, Frédéric Gianesello & Cyril Luxey, "Antenne Patch alimentée par fente en technologie PCB fonctionnant dans la bande 18 GHz – 31 GHz", 21èmes Journées Nationales Microondes , Caen, France, 2019.
- F. Filice, Nour Nachabe, Frédéric Gianesello & Cyril Luxey, "3D-Printed Double-Ridged Waveguide Array Antenna targeting High-Efficiency Ku-band SatCom on The Move Applications ", AP-S 2019, Atlanta, USA, 2019.
- F. Filice, Nour Nachabe, Frédéric Gianesello, Guillermo Alvarez Narciandi, Jaime Laviada Martinez, Fernando Las-Heras & Cyril Luxey, "3D-Printed High-Efficiency 2x2 and 4x4 Double-Ridged Waveguide Arrays for Ku-band SatCom on The Move Applications", EuCAP 20, Copenhagen, Denmark, 2020. Accepted conference paper.
- F. Filice, Nour Nachabe, Frédéric Gianesello, Guillermo Alvarez Narciandi, Jaime Laviada Martinez, Fernando Las-Heras & Cyril Luxey, "Wideband aperture coupled patch antenna for Ka-band exploiting the generation of surface waves", AP-S 20, Copenhagen, Canada, 2020. Submitted conference paper.